SEARCH FOR FIRST-GENERATION LEPTOQUARKS IN THE JETS AND MISSING TRANSVERSE ENERGY TOPOLOGY IN PROTON-ANTIPROTON COLLISIONS AT CENTER-OF-MASS ENERGY 1.96 TeV

By

DMITRI TSYBYCHEV

A DISSERTATION PRESENTED TO THE GRADUATE SCHOOL
OF THE UNIVERSITY OF FLORIDA IN PARTIAL FULFILLMENT
OF THE REQUIREMENTS FOR THE DEGREE OF
DOCTOR OF PHILOSOPHY

UNIVERSITY OF FLORIDA

2004

TABLE OF CONTENTS

page

ACKNOWLEDGMENTS iii

LIST OF TABLES vii

LIST OF FIGURES ix

ABSTRACT xvi

1 INTRODUCTION 1

1.1 The Standard Model 2
1.1.1 Quarks and Leptons 3
1.1.2 Symmetry and Unification 4
1.1.3 Electroweak Theory 5
1.1.4 Quantum Chromodynamics 8
1.2 Beyond the Standard Model 8
1.2.1 Grand Unification 10
1.2.2 Supersymmetry 11
1.3 Experimental High-Energy Physics 12

2 LEPTOQUARK PHENOMENOLOGY 15

2.1 Leptoquark Models 15
2.1.1 Pati-Salam $SU(4)$ Color Symmetry 15
2.1.2 The $SU(5)$ GUT Models 16
2.1.3 Leptoquarks in SUSY Models 16
2.2 Leptoquark Production at the Tevatron 17
2.2.1 Production Diagrams 17
2.2.2 Leading Order Cross Section and NLO Corrections 20
2.2.3 Experimental Signatures 23
2.3 Current Leptoquark Search Limits 23
2.3.1 Non-Hadron Collider Searches 24
2.3.2 Run I Tevatron Results 25
2.3.3 Run II Searches 26

3 EXPERIMENTAL APPARATUS 28

3.1 The Accelerator Complex 28
3.1.1 The Proton Source 28
3.1.2 The Antiproton Source 29

3.1.3 The Main Injector 30
3.1.4 The Tevatron 30
3.2 The CDF Detector 31
3.2.1 Calorimetry 35
3.2.2 Tracking System 39
3.2.3 Muon Detectors 43
3.2.4 Trigger System and Data Acquisition 45
3.3 The Cherenkov Luminosity Monitor 49
3.4 Luminosity Measurement 53
3.4.1 The CLC Acceptance 54
3.4.2 Counting of Empty Bunch Crossings 57
3.4.3 Counting of Hits and Particles 60

4 EVENT RECONSTRUCTION 63

4.1 Jets 63
4.1.1 Jet-Clustering Algorithm 63
4.1.2 Jet Energy Corrections 65
4.2 Missing Transverse Energy 69
4.2.1 Missing Transverse Energy Reconstruction 69
4.2.2 Resolution 70
4.2.3 Missing-E_{T} Corrections 73
4.3 Tracking 77
4.4 Lepton Reconstruction 79
4.4.1 Electrons 80
4.4.2 Muons 81

5 TRIGGER PATH AND EVENT PRESELECTION 82

5.1 Missing Transverse Energy Trigger 82
5.1.1 Level-1 Trigger 82
5.1.2 Level-2 Trigger 84
5.1.3 Level-3 Trigger 84
5.2 Data Samples 84
5.2.1 Inclusive Missing Transverse Energy Sample 85
5.2.2 Inclusive Jet Sample 85
5.2.3 Inclusive Lepton Samples 86
5.2.4 Standard Ntuple 87
5.2.5 Good Run Requirement 88
5.3 Instrumental Background 88
5.4 Initial Data Selection 91
5.5 Trigger Efficiency 96

6 STANDARD MODEL BACKGROUND 103

6.1 Electroweak Background 103
6.2 Multi-Jet QCD Background 105
6.3 The $t\bar{t}$ Background 106
6.4 Detector Simulation 106

7 LEPTOQUARK SELECTION CUTS 108

7.1 Signal Monte Carlo 108
7.2 Signal and Background Kinematical Distributions 108
7.3 Acceptance 114
7.4 Cut Optimization 115

8 BACKGROUND NORMALIZATION, CONTROL REGIONS, SYSTEMATIC UNCERTAINTIES 128

8.1 Electroweak Background Normalization 128
8.2 Multi-Jet QCD Background Normalization 135
8.2.1 Method-1 135
8.2.2 Method-2 143
8.2.3 Multi-jet QCD Background Contribution in the Signal Region 149
8.3 Control Regions and Background Normalization Cross-Check. . . 151
8.4 Systematic Uncertainties 151
8.4.1 Luminosity Measurement Uncertainty 152
8.4.2 Jet Energy Measurement Uncertainty 152
8.4.3 Initial- and Final-State Radiation Uncertainty 152
8.4.4 Parton Distribution Function Uncertainty 153
8.4.5 Uncertainties on the Signal Acceptance 153
8.4.6 Uncertainties on Background Prediction in Signal and Control Regions 155

9 RESULTS 156

9.1 Control Regions 156
9.2 Leptoquark Acceptance and Background Prediction in the Signal Region 158
9.3 Projected Limits 163
9.4 Signal Region 166
9.5 Search Limits 168
9.6 Conclusion 171

REFERENCES 174

BIOGRAPHICAL SKETCH 179

LIST OF TABLES

Table		page
1-1	Known quarks and leptons of the Standard Model.	4
1-2	Gauge bosons of the Standard Model.	5
2-1	Quantum numbers of scalar (S) and vector (V) leptoquarks.	18
2-2	Lower limits on the first-generation scalar leptoquark mass from Tevatron, LEP and HERA experiments.	25
3-1	Summary of the CDF calorimeter subsystem properties.	37
3-2	The $p\bar{p}$ cross section for various inelastic processes at $\sqrt{s} = 1.96$ GeV at the Tevatron.	56
3-3	Acceptances for CLC and CLC plus plug detectors calculated for different inelastic processes.	57
3-4	Probability to have zero hits in both CLC modules.	59
4-1	Average missing-E_{T}, average scalar $\sum E_{\mathrm{T}}$ and average missing-E_{T} significance and RMS of distributions from `JET50` data for uncorrected and corrected jet energies.	76
5-1	Event reduction in missing E_T sample.	97
5-2	Parametrization of the missing-E_{T} trigger efficiency.	100
6-1	List of MC background samples used, number of events generated, leading-order cross section, and equivalent integrated luminosity.	105
7-1	Loose central and plug electron identification cuts used for electron veto.	116
7-2	Loose central muon identification cuts used for muon veto.	116
8-1	Tight and loose central electron selection cuts for $Z \to e^+e^-$ candidate events.	129
8-2	Total efficiency for tight and loose electron identification cuts in data and Monte Carlo	134
8-3	Four kinematic regions of the `MET45` data sample defined by the azimuthal angular separation and missing-E_{T}.	135

8-4 Definition of "QCD-like" regions. 137

8-5 Number of events in the four kinematic regions from `MET45` data. . 139

8-6 Estimated number of QCD events in region (D) for different definitions of the low missing-E_{T} region, and the "QCD-like" region. . . 140

8-7 Fit parameters for final cut efficiency function from `JET20` and `JET50` samples. 146

8-8 Predicted number of QCD multi-jet events in the signal region by Method-2. 150

8-9 Definition of 7 control regions with large missing-E_{T}. 151

8-10 Systematic uncertainties on the acceptance of the first-generation scalar leptoquark signal (for leptoquark mass of 100 GeV). 154

9-1 Comparison of the number of expected events from Monte Carlo with the number observed in data for the seven control regions. . . 158

9-2 Acceptance of the first-generation scalar leptoquark signal as a function of mass, as well as the number of events expected in 191 pb^{-1}. 163

9-3 Number of expected events from various Standard Model sources in the leptoquark signal region. 163

LIST OF FIGURES

Figure		page
1-1	Evolution of the gauge coupling constants in the Standard Model.	10
2-1	Leading-order Feynman diagrams for leptoquark pair production at the Tevatron.	19
2-2	Feynman diagrams for the leptoquark pair production at the Tevatron due to the gluon-quark subprocesses.	21
2-3	Renormalization/factorization scale dependence of the leptoquark pair-production cross-section at the Tevatron energy $\sqrt{s} = 1.8$ TeV.	22
2-4	Ratio of the NLO to LO cross sections for scalar leptoquark production for both CTEQ4 and CTEQ5.	22
2-5	Next-to-leading order cross section for scalar leptoquark production.	23
2-6	Ratio of the NLO cross section for scalar leptoquark production at $\sqrt{s} = 1.96$ TeV to $\sqrt{s} = 1.8$ TeV as a function of leptoquark mass.	26
2-7	Run I limits from CDF and DØ on scalar leptoquarks in the β vs. mass plane.	27
3-1	A Schematic view of the Fermilab Accelerator complex	29
3-2	Isometric view of the CDF detector.	33
3-3	Elevation view of one half of the CDF II detector.	34
3-4	The R-z cross section view of new end plug calorimeter.	39
3-5	Longitudinal view of the CDF tracking volume.	41
3-6	The CDF Silicon vertex detector.	42
3-7	Central outer tracker.	44
3-8	The CDF II map of the central muon system coverage in η-ϕ plane.	45
3-9	The CDF II data flow.	46
3-10	The CDF II L1/L2 trigger systems.	47
3-11	The Cherenkov Luminosity Counters in CDF.	49

3-12 The Assembly drawing for one module of the CDF Cherenkov Luminosity Counters. 50

3-13 Number of photoelectrons produced by single particles traversing the full length of the CLC counters measured for all 96 counters. . 51

3-14 Simulated amplitude distribution for a particle from minimum bias $p\bar{p}$ interactions in the Cherenkov counter. 53

3-15 Amplitude distribution of Cherenkov counters normalized to single particle peak from $p\bar{p}$ collisions. 54

3-16 Amplitude distribution for one of the Cherenkov counters from $p\bar{p}$ collisions after an isolation cut. 55

3-17 Average number of counters hit in the $p\bar{p}$ collision in the two CLC modules as a function of the amplitude threshold. 56

3-18 Real-time insatantaneous and integrated $p\bar{p}$ luminosities for a typical Tevatron store. 60

3-19 Average number of hits in CLC. 62

4-1 The CDF event display of the di-jet event. 64

4-2 Relative jet energy corrections. 68

4-3 Missing-E_{T} distribution in minbias events. 71

4-4 Distributions of the x and y components of the missing-E_{T} in minbias events. 72

4-5 Missing-E_{T} resolution as a function of total transverse energy. . . . 73

4-6 Uncorrected missing-E_{T} and missing-E_{T} after applying corrections from the case 2. 75

4-7 Uncorrected total scalar E_{T} and total scalar E_{T} after applying corrections from the case 2. 76

5-1 Transverse view of two wedges in the plug calorimeter. 83

5-2 Total integrated luminosity recorded by CDF 85

5-3 Event display of the typical beam halo muon bremsstrahlung in the calorimeter. 89

5-4 Azimuthal angle distribution of the missing-E_{T} in the inclusive `MET45` sample. 90

5-5 Event display of the typical cosmic ray event. 91

5-6 Distribution of the number of vertices in the MET45 sample. 92

5-7 Event electromagnetic fraction distribution. 93

5-8 Distribution of the event electromagnetic fraction versus missing-E_{T} in JET50 data. 94

5-9 Event charge fraction distribution for JET50 data sample and QCD di-jet Monte Carlo sample. 95

5-10 Distribution of the event charge fraction versus missing-E_{T} in JET50 data. 96

5-11 Distributions of event electromagnetic fraction and event charge fraction for MET45 data. 97

5-12 Distribution of the event charge fraction versus event electromagnetic fraction in the inclusive MET45 data sample. 98

5-13 Missing-E_{T} distribution for the events from the inclusive MET45 data sample. 99

5-14 Total scalar transverse energy distribution for the events from the inclusive MET45 data sample. 100

5-15 Missing-E_{T} distribution in the high-p_{T} electron sample. 101

5-16 Efficiency of the MET45 trigger as a function of offline missing-E_{T} from the high-p_{T} electron sample. 102

5-17 Efficiency of the MET45 trigger as a function of offline missing-E_{T} from the high-p_{T} muon sample. 102

7-1 Kinematic distribution of quarks from leptoquark decay. 109

7-2 Vector sum of the transverse momenta from the two neutrinos from the leptoquark decays. 110

7-3 Missing-E_{T} distribution for the pair production of first generation leptoquarks ($m_{\mathrm{LQ}} = 100$ GeV/c^2) compared to the missing-E_{T} distributions for the dominant Standard Model background processes. 111

7-4 Comparison of the E_{T} distributions for the first-leading jet (J1) for leptoquark pair production and for the dominant Standard Model processes. 111

7-5 Comparison of the E_{T} distributions for the second-leading jet (J2) for the leptoquark pair production and for the dominant Standard Model processes. 111

7-6 Pseudo-rapidity distribution of the first-leading jet (J1) for the leptoquark pair production and for the dominant Standard Model processes. 112

7-7 Pseudo-rapidity distribution of the second-leading jet (J2) for the leptoquark pair production and for the dominant Standard Model processes. 112

7-8 Distribution of the azimuthal angular separation between the first- and second-leading jets for the leptoquark pair production and for the dominant Standard Model processes. 113

7-9 Distribution of the azimuthal angular separation between the directions of the first leading jet and the missing-E_{T} for leptoquark pair production and for the dominant Standard Model processes. . 113

7-10 Distribution of the minimum azimuthal angular separation between the directions of the jets and the missing-E_{T} direction for the leptoquark pair production and for the dominant Standard Model processes. 114

7-11 Distribution of the number of tracks in central jets for leptoquark pair production and for the dominant Standard Model processes. . 114

7-12 Optimization of the cut on the azimuthal angle between the first-leading jet and the missing-E_{T} direction in ϕ 117

7-13 Optimization of the cut on the azimuthal angle between the first- and second-leading jets. 118

7-14 Optimization of the cut on the transverse energy of the first-leading jet. 119

7-15 Optimization of the cut on the transverse energy of the second-leading jet. 120

7-16 Optimization of the cut on the pseudo-rapidity of the first-leading jet. 121

7-17 Optimization of the cut on the pseudo-rapidity of the second-leading jet. 122

7-18 Optimization of the cut on the pseudo-rapidity of the third-leading jet. 123

7-19 Optimization of the cut on the minimum azimuthal separation between any jet and missing-E_{T} direction. 124

7-20 Final optimization of the cut on the azimuthal angle between the first- and second-leading jets. 125

7-21 Optimization of the cut on the minimum number of tracks in the selected central jets. 126

8-1 Invariant mass distribution of electron pairs. 130

8-2 Number of jets in inclusive $Z \to e^+e^- +$ jets sample. 131

8-3 Z boson p_{T} distribution in $Z \to e^+e^- +$ jets sample. 132

8-4 Missing-E_{T} distribution in $Z \to e^+e^- +$ jets sample. 133

8-5 Transverse energy distribution for the first and second leading jets in inclusive $Z \to e^+e^- +$ jets sample. 134

8-6 Comparison of the shapes of the missing-E_{T} distributions for "non-QCD-like" region to several different definitions of the "QCD-like" regions. 140

8-7 Comparison of the shapes of the missing-E_{T} distributions for "non-QCD-like" region to several different definitions of the "QCD-like" regions. 141

8-8 Ratio of the missing-E_{T} distribution of "QCD-like" (defined as "q11") to the "non-QCD-like". 142

8-9 Ratio of the number of events in "non-QCD-like" region to the number of events in the "QCD-like" region as a function of the missing-E_{T}. 143

8-10 Number of vertices of class 12 or higher in `JET20` sample. 144

8-11 Comparison of the missing-E_{T} distributions for the events with one and only one vertex and events with two or more vertices in `JET20` sample. 144

8-12 Ratio of the number of events in "non-QCD-like" region to the number of events in the "QCD-like" region as a function of the missing-E_{T} in `JET20` for events with only one vertex of class 12 or higher. 145

8-13 Efficiency of the azimuthal angular separation cuts as function of the missing-E_{T} in `JET20` sample. 147

8-14 Efficiency of the azimuthal angular separation cuts as function of the missing-E_{T} in `JET50` sample. 148

8-15 Efficiency of the azimuthal angular separation cuts as function of the missing-E_{T} of a QCD MC sample 149

8-16 Missing-E_{T} distribution from the inclusive missing-E_{T} data sample, all selection cuts are applied, except the number of jets requirement and azimuthal angular separation cuts. 150

9-1 Comparison of the number of events observed in data with the number expected from Standard Model sources. 157

9-2 Missing-E_{T} distribution in the electroweak-like control region for data (solid points) compared to Standard Model expectation (shaded histogram). 159

9-3 Jet multiplicity distribution in the electroweak-like control region for data (solid points) compared to Standard Model expectation (shaded histogram). 159

9-4 The leading-jet E_{T} distribution in the electroweak-like control region for data (solid points) compared to Standard Model expectation (shaded histogram). 160

9-5 The second-leading jet E_{T} distribution in the electroweak-like control region for data (solid points) compared to Standard Model expectation (shaded histogram). 160

9-6 The third-leading jet E_{T} distribution in the electroweak-like control region for data (solid points) compared to Standard Model expectation (shaded histogram). 161

9-7 The ϕ difference between the two highest E_{T} jets in the electroweak-like control region for data (solid points) compared to Standard Model expectation (shaded histogram). 161

9-8 The ϕ difference between the leading-jet and the missing-E_{T} direction in the electroweak-like control region for data (solid points) compared to Standard Model expectation (shaded histogram). . . 162

9-9 The minimum ϕ difference between any jet and the missing-E_{T} direction in the electroweak-like control region for data (solid points) compared to Standard Model expectation (shaded histogram). . . 162

9-10 Expected cross section upper limit for scalar leptoquark production. 166

9-11 Missing-E_{T} distribution in the leptoquark signal region. 167

9-12 The leading-jet E_{T} distribution in the leptoquark signal region for data (solid points) compared to Standard Model background (yellow histogram). 168

9-13 The second leading jet E_{T} distribution in the leptoquark signal region for data (solid points) compared to Standard Model background (yellow histogram). 169

9-14 The third leading-jet E_{T} distribution in the leptoquark signal region for data (solid points) compared to Standard Model background (yellow histogram). 169

9-15 The ϕ difference between the two highest E_{T} jets in the leptoquark signal region for data (solid points) compared to Standard Model background (yellow histogram). 170

9-16 The ϕ difference between the leading-jet and the MET direction in the leptoquark signal region for data (solid points) compared to Standard Model background (yellow histogram). 170

9-17 The minimum ϕ difference between any jet and the MET direction in the leptoquark signal region for data (solid points) compared to Standard Model background (yellow histogram). 171

9-18 The upper limit on the cross section times squared branching ratio for scalar leptoquark production in missing-E_{T} plus jets signature. 172

Abstract of Dissertation Presented to the Graduate School
of the University of Florida in Partial Fulfillment of the
Requirements for the Degree of Doctor of Philosophy

SEARCH FOR FIRST-GENERATION LEPTOQUARKS
IN THE JETS AND MISSING TRANSVERSE ENERGY TOPOLOGY
IN PROTON-ANTIPROTON COLLISIONS
AT CENTER-OF-MASS ENERGY 1.96 TeV

By

Dmitri Tsybychev

April 2004

Chair: Darin E. Acosta
Cochair: Jacobo Konigsberg
Major Department: Physics

We performed a search for the pair production of first-generation leptoquarks using 191 pb^{-1} of proton-antiproton collision data recorded by the CDF experiment during Run II of the Tevatron. The leptoquarks are sought via their decay into a neutrino and quark, which yields missing transverse energy and several high-E_{T} jets. Several control regions were studied to check the background estimation from Standard Model sources, with good agreement observed in data. In the leptoquark signal region, 124 events were observed with 118.3 ± 14.5 expected from background. Therefore, no evidence for leptoquark production was observed, and limits were set on the cross section times the squared branching ratio. Using the next-to-leading order cross section for leptoquark production, we excluded the mass interval 78 to 117 GeV/c^2 at the 95% confidence level for 100% branching ratio into neutrino plus quark.

CHAPTER 1
INTRODUCTION

High energy physics is the study of elementary particles and their interactions. At present we believe that matter consists of two types of matter units called leptons and quarks. All of the variety of the objects that we see around us is made of just three of these building blocks: the up quark, the down quark and the electron. In addition to those particles there are two more generation of quarks and leptons, with increasing mass. All our current knowledge about elementary particles and their interactions is combined into a collection of theories called the Standard Model (SM). Particles interact with each other by exchanging force-carrying particles that are bosons. The are four type of forces; however the SM incorporates only three of them: the electromagnetic force, the weak force and the strong force. The fourth force, gravity, most commonly encountered in everyday life, is not incorporated in the theory yet. Its carrier has not been observed either.

Although the Standard Model has proved to accurately describe all known phenomena of elementary particles with high precision, there are several questions that can not be answered without going beyond it. For example, we do not know why particles have masses (or the masses they do) and why there are three generation of particles. Possible extensions to the SM are proposed to resolve those outstanding problems.

Leptoquarks are hypothetical particles that are predicted in many extensions to the Standard Model of particle physics. The remarkable similarities between quarks and leptons may imply that a more fundamental theory exists where quarks and leptons interrelated, which could give rise to particles (i. e. leptoquarks) with quantum numbers of both — leptons and quarks.

High energy physics suggests that particle physics is intimately connected with the early history of the Universe. It is believed that right after the Big Bang, the Universe was so hot that it was essentially just a soup of the elementary particles. Therefore, probing matter at smaller and smaller scales allows us to effectivaly travel back in time and see how the Universe looked like at the beginning of the Big Bang.

Search for first-generation leptoquarks in jets and missing transverse energy topology is performed using the CDF detector at the Tevatron accelerator at the Fermi National Accelerator Laboratory. The Tevatron collides beams of protons and anti-protons at a center-of-mass energy of 1.96 TeV, the highest in the world. It has restarted colliding beams on March 1, 2001 after a major upgrade. It is expected to deliver up to 100 times more data than in Run I by 2009. The CDF experiment has an ambitious physics program including searches for the physics beyond the Standard Model. This program should benefit from the increased center-of-mass energy and the increased amount of the data.

1.1 The Standard Model

The Standard Model is a theoretical framework that attempts to provide a fundamental basis for a description of all the complexity of the observable phenomena by a relatively small set of equations. It represents a unified description of the electromagnetic, weak and strong forces in the language of quantum gauge theories. Halzen and Martin [1] and Aitchison and Hey [2] give a nice introduction to this. In such theories, each particle type is understood as a quantum excitation of some field. There are two type of fields — matter fields and force fields. The particles associated with those fields are distinguished by the spin they possess, which is the amount of intrinsic angular momentum in units of $\hbar$. The matter particles are spin $\frac{1}{2}$, and so they are fermions and thus obey the Pauli exclusion

principle. The force particles are bosons, that is, they possess integer spin, and obey Bose-Einstein statistics.

As the Mendeleev periodic table predicts the properties of the new elements, so does the Standard Model of elementary particles. The Standard Model showed a remarkable success over the past 30 years in predicting new data, from observation of gauge bosons [3]-[6] to the discovery of the top quark [7].

1.1.1 Quarks and Leptons

The experimental evidence shows that nuclei and atoms are built of fundamental particles [8]. Those fundamental particles so far do not appear to have internal structure and carry different quantum charges that determine what type of interactions they participate in. Leptons carry integer electric charge in units of electron charge (e), while quarks carry fractional electric charge ($+2/3$ or $-1/3$ in units of electron charge). Each particle has an anti-particle with quantum charges opposite to the particle charges. There are two types of these fundamental building blocks: quarks and leptons.

$$\text{quarks} \quad \begin{pmatrix} u \\ d \end{pmatrix} \begin{matrix} \text{up} \\ \text{down} \end{matrix} \qquad \begin{pmatrix} c \\ s \end{pmatrix} \begin{matrix} \text{charm} \\ \text{strange} \end{matrix} \qquad \begin{pmatrix} t \\ b \end{pmatrix} \begin{matrix} \text{top} \\ \text{bottom} \end{matrix}$$

$$\text{leptons} \quad \begin{pmatrix} e \\ \nu_e \end{pmatrix} \begin{matrix} \text{electron} \\ \text{neutrino} \end{matrix} \qquad \begin{pmatrix} \mu \\ \nu_\mu \end{pmatrix} \begin{matrix} \text{muon} \\ \text{muon neutrino} \end{matrix} \qquad \begin{pmatrix} \tau \\ \nu_\tau \end{pmatrix} \begin{matrix} \text{tau} \\ \text{tau neutrino} \end{matrix}$$

In the Standard Model they are grouped into three generations according to their quantum numbers and masses, which are called isodoublets (isodoublet refers to weak interaction structure). Table 1-1 summarizes properties of the known quarks and leptons.

Table 1-1: Known quarks and leptons of the Standard Model. Masses are given in GeV/c^2 except where indicated otherwise.

Quarks				Leptons			
Charge 2/3		Charge –1/3		Charge –1		Charge 0	
Mass		Mass		Mass		Mass	
u	$0.0015 - 0.0045$	d	$0.005 - 0.0085$	e	0.511 MeV/c^2	ν_e	< 3 eV/c^2
c	$1.0 - 1.40$	s	$0.080 - 0.155$	μ	0.106	ν_μ	< 0.19 MeV/c^2
t	174.3	b	$4.0 - 4.5$	τ	1.777	ν_τ	< 18.2 MeV/c^2

Source: Particle Data Group [8].

1.1.2 Symmetry and Unification

Symmetry plays an important role in physics. Symmetries are transformations that leave the physics laws for a system invariant. For example, rotational symmetry is represented as an invariance under the redefinition of the spatial coordinates by rotating the axes. Such invariance leads to the conservation of the total angular momentum. In addition to continuous space-time symmetries and discrete symmetries (such as space inversion, or parity, time reversal), there is another type of symmetry in the particle theories: field redefinition. For example, the electric field does not depend on the constant term added to the electric field potential. Such a symmetry is called gauge symmetry. A particle, generally, could be represented as a complex field. The complex phase of such a field may depend on space and time coordinates. The requirement that the transformation of such a field does not depend on the local complex phase is known as local gauge invariance.

The requirement that the Standard Model Lagrangian is invariant under local gauge transformations leads to conservation of particle charges and other quantum numbers. Symmetry transformations mathematically are described by group theory, where particles are combined together into multiplets and their transformations can be described in matrix representation form. Gauge invariance is based on the group of special unitary transformations denoted by $SU(n)$, where n is the number of dimensions in the gauge charge space. The Standard Model

includes three gauge invariant field theories: quantum electrodynamics (QED), quantum chromodynamics (QCD) and electroweak theory. It does not incorporate gravity. The complete symmetry of the Standard Model can be given by the $U(1)_Y \times SU(2)_L \times SU(3)_C$, where Y refers to hypercharge, L— to weak isospin and C— to color charge. In a gauge field theory, interactions between particles are mediated by force-carrying particles called gauge bosons. The number of bosons is determined by the number of the generators associated with the theory group and is equal to $n^2 - 1$. Bosons have integer spin (1) and include: photons (γ), intermediate gauge bosons ($W^{\pm}$,Z^0) and gluons (g). The gauge boson in its turn could be neutral (i.e., a photon) or carry a charge, conserved under given symmetry ($W\pm$,Z^0 in electroweak theory and gluon in QCD). The properties of the gauge bosons are summarized in table 1-2. Maxwell formulated the theory of

Table 1-2: Gauge bosons of the Standard Model.

Force	Relative strength	Gauge boson	Mass (GeV/c^2)	Range
Strong	~ 1	g	0	$\sim 10^{-15}$ m
Electromagnetic	$\sim 1/137$	γ	0	infinite
Weak	$\sim 10^{-5}$	$W^{\pm}$ Z^0	80.423 ± 0.039 91.1876 ± 0.0021	$\sim 10^{-18}$ m

electromagnetism, by combining two seemingly different phenomena of electricity and magnetism. Later, the quantum electrodynamic theory was combined with theory of weak interactions which led to the electroweak theory of the Standard Model.

1.1.3 Electroweak Theory

Quantum Electrodynamics (QED) was the first gauge invariant field theory based on the U(1) group. The requirement that the Lagrangian in QED is invariant under local phase change leads to interaction between the carrier of the electromagnetic field (the photon) and charged fermions (quarks or leptons) and

the conservation of the electric charge. Both quarks and leptons act as sources of the electromagnetic field. The strength of the interaction is determined by the dimensionless coupling constant[1] :

$$\alpha = \frac{e^2}{4\pi}, \tag{1-1}$$

A great achievement for quantum field theory was that QED could be renormalized. An electron in QED can spontaneously emit a virtual photon. Such a photon could produce an electron-positron pair, and this process could repeat itself indefinitely, so that the initial electron will be surrounded by a "cloud" of electron-positron pairs. The positrons will be closer to the initial electron, since the opposite charges attract, and therefore the electron charge will be "screened". The "bare" electron charge e_0 will be increasing with decreasing distance to the electron. Therefore, the calculation of the bare charge e_0 becomes divergent. However it is possible to redefine e_0 in terms of effective charge e at some large scale, and such a procedure is called renormalization. Since the electromagnetic coupling constant is proportional to the electric charge therefore the coupling strength is reduced at larger distances (lower energies). Thus, α depends on the energy scale associated with interaction.

Glashow [9], Weinberg [10] and Salam [11] proposed a new theory, which unified the electromagnetic force with the weak force, first observed in nuclear β decays, and was based on the $SU(2) \times U(1)$ gauge group. In the combined electroweak theory there are four gauge bosons: W^+, W^0 and W^- of the weak isospin group $SU(2)$ and B^0 of the weak hypercharge group $U(1)$. The left-handed helicity fermions are combined into isodoublets, which correspond to the pairs

[1] throughout this dissertation the natural system of units is used, where $\hbar = c = 1$

of quarks and leptons within each generation. The $W^{\pm}$ gauge bosons transform one particle of the isodoublets into another. It occurs when a fermion emits or absorbs a real or virtual $W^{\pm}$ boson. The combination of W^0 and B^0 creates the gauge boson of QED—the photon—and a weak neutral current carrier—the Z^0 boson. The requirement for the electroweak theory to be gauge invariant implies that gauge bosons remain massless. In reality only the photon is massless. The weak interactions were observed to occur at much smaller distances compared to the electromagnetic, therefore the $W^{\pm}$ and Z^0 bosons should have mass. Explicit mass terms are not gauge invariant and can not simply be added to the Lagrangian without violating renormalizability of the theory. That means that underlying symmetry is broken.

The Higgs mechanism provides spontaneous symmetry breaking of the electroweak theory[12], leaving the Lagrangian invariant under the gauge transformations. It introduces an additional scalar field, which is associated with a new particle — the Higgs boson. The scalar field has a non-zero expectation value and the $W^{\pm}$ and Z^0 gauge bosons acquire mass through the interaction with this field. The leptons and quarks also acquire mass through the interaction with the Higgs field. The strength of the particle couplings to this field determines the masses of the fermions. It was proved that any spontaneously broken gauge theory could be renormalized [13]. However, to cancel triangle anomalies that appear in the renormalization procedure, the theory requires an equal number of lepton and quark generations and that the sum of electric charges of all fermions is zero. The electroweak force appears to be "broken" into two pieces — electromagnetic and weak — at low energies. However at energies $\approx M_Z$ they are unified with the same intrinsic coupling constant.

The discovery of the third generation of the leptons and quarks as well as W and Z bosons was a remarkable success in theoretical predictions of the electroweak theory.

1.1.4 Quantum Chromodynamics

Quarks are distinguished from leptons by possessing an additional type of charge (color) that allows them to interact strongly with each other. There are three different colors (three charges: red, green and blue), which reflects the underlying symmetry based on the $SU(3)$-color group. Hence, quarks of different color are combined into groups called triplets. The strong force is mediated by eight massless gluons. Unlike the photons, gluons carry charge; hence they also can interact with each other. As a consequence, the charge "screening" has a different effect, the color force between colored particles increases in strength with increasing distance. Therefore quarks and gluons do not appear as free particles. They exist only in colorless bound states—hadrons. This is also known as a color confinement. There are two types of hadrons: baryons, which consist of three quarks of different colors, resulting in a "white" color-neutral state, and mesons, which consist of quark anti-quark pair with opposite color charges. The color charge is conserved in the strong interactions. Another important aspect of QCD is that the strong coupling constant α_s becomes smaller at smaller distances (larger energy transfer in the associated interaction), which allows to use perturbative methods in many complicated QCD calculations. This is known as "asymptotic freedom."

1.2 Beyond the Standard Model

Despite the tremendous success of the Standard Model in explaining experimental data we believe that this model is incomplete for several reasons. To name a few:

- The Standard model does not include gravity.

- The cancellation of triangle anomalies in the Standard model is only possible if there are same number of generation of leptons and quarks. The Standard model does not explain why there are three generations of quarks and three generations of leptons and why they have the charges they have.

- There is no explanation of the mass difference within the same generation isodoublet. For example, why is the top quark mass so much larger than the other fermion masses?

- The Standard Model contains a large number of arbitrary parameters: six quark masses, three lepton masses (neutrinos are assumed massless in the SM), the electromagnetic and strong coupling constants α and α_s, the weak coupling constant $\sin^2\theta_W$, where the Weinberg angle, θ_W, is defined as $\cos\theta_W = \frac{M_W}{M_Z}$, the Z^0 boson mass M_{Z^0} and the Higgs boson mass M_H. The quark mass eigenstates need not be the same as the weak isodoublet eigenstates; therefore, the matrix relating these bases was defined for the six quarks [17, 18]. Four Cabbibo-Kobayshi-Maskawa mixing angles that determine mixing of the left-handed isodoublets into the quark mass eigenstates, which are also arbitrary parameters in the Standard Model.

- The Higgs mechanism, which provides Electroweak Symmetry Breaking (EWSB), is inserted by hand, to preserve the symmetry of the Standard Model Lagrangian. Moreover why there should be only one scalar field?

- Loop corrections make the Higgs mass calculations quadratically divergent and the mass integral requires a cut off at some scale Λ, which represents the scale where new physics occurs. So the Higgs mass is given by $m_H^2 = m^2 - g^2\Lambda^2$, where m is the bare Higgs boson mass parameter at the Λ scale and g is a dimensionless coupling constant. In order to get a m_H Higgs mass of the order 100 GeV/c^2 we will need a cancellation to 22 decimal places, which is very unnatural (the "naturalness" problem)

- Astrophysical observations show that there must be some additional, unseen mass, which is called dark matter.

All these facts suggest that there could be another theory beyond the Standard Model. There are two possible ways to extend the Standard Model:

- One is to include the existing particles and forces as a part of some bigger symmetry. By introducing *new* interactions, the fields and their interactions could be unified in one single theory. Examples of such theories include Grand Unified Theories (GUTs), Supersymmetry, String theory and Extra dimensions.

- The other is to consider *new* particles and *new* interactions. In these type of theories, the existing particles are composed of these new particles, in

the same way as hadrons consist of quarks. Examples of such models are compositeness, Technicolor. Even though these models are not completely ruled out by experimental data, they are not as appealing as the models of the first type, due to a limited parameter space and same fine tuning problems.

1.2.1 Grand Unification

The unification of the electromagnetic and weak force leads naturally to the idea of combining the electroweak and strong forces. In the Standard Model, the coupling strength in the strong and weak interactions decreases with increasing energy scale, whereas the coupling of the electromagnetic interaction increases. Figure 1-1 shows the evolution of the gauge coupling constants in the Standard Model from the experimentally measured values at the Z-mass pole. Thus, it

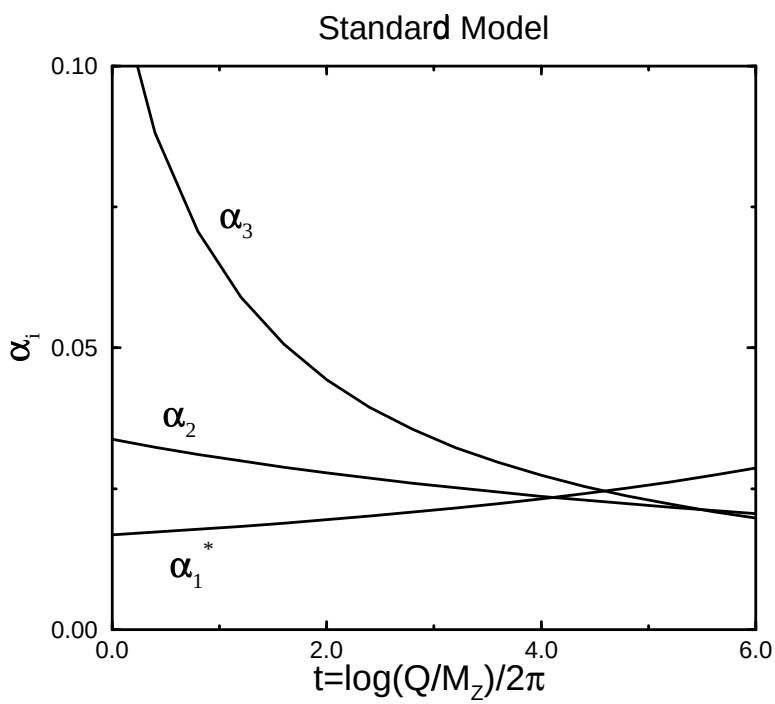

Figure 1-1: Evolution of the gauge coupling constants in the Standard Model from the experimentally measured values at the Z-mass pole [15].

becomes possible that at some larger energy scale they become equal. According to Grand Unified Theories, all three SM forces are a manifestation of a single force [14, 16]. The underlying symmetry of the GUT theory is spontaneously broken at some higher energy of the order $\sim 10^{16}$ GeV, and the single interaction is split into the three known interactions of the SM.

1.2.2 Supersymmetry

Supersymmetry (SUSY) is a type of symmetry that relates fermions to bosons [19, 20, 21]. The Minimal Supersymmetric extension of the Standard Model (MSSM) introduces "superpartners" for all particles of SM. Superpartners have the same quantum numbers as their SM counterparts except that their spin differs by one half.

- MSSM provides a solution to the naturalness problem, since there are boson-fermion pairs with identical couplings that make equal but opposite in sign contributions to the loop diagrams for the Higgs mass. These contributions cancel quadratic divergences and solve the "naturalness problem".
- A Heavy top quark plays an important role in the theory. Through loop corrections, it drives the Higgs vacuum expectation values to negative values, which allows a spontaneous breaking of electroweak symmetry.
- SUSY provides a framework for the unification of gravity with three other forces.

If Supersymmetry were an exact symmetry, then SM particles and their superpartners would have the same mass and they would have been discovered a long time ago. So far no such particles have been seen, which implies that Supersymmetry is also a broken symmetry, so that superparticle masses are heavier than observed so far. The effective scale of supersymmetry breaking is related to the Standard Model Higgs vacuum expectation value. The MSSM introduces two Higgs fields to generate masses for quarks and charged leptons and their corresponding superpartners as well as all other particle masses in the theory. They produce five total Higgs boson particles, two of which have charge. There are also

six new particles: 4 neutralinos (χ_i^0) and 2 charginos ($\chi_i^\pm$), which are superpartners to the gauge fields.

In the Standard Model, Baryon and Lepton numbers are conserved. Supersymmetry introduces a new quantum number — R-parity, defined as $R = (-1)^{3(B-L)+2S}$, where B = baryon number, L = lepton number and S = spin. From this formula, it follows that all the Standard Model particles have a $R = +1$, whereas all superparticles have $R = -1$. If R parity is conserved then the lightest supersymmetric particle (LSP) must be stable. All superparticles can be produced only in even numbers. Each superparticle should eventually decay into a state which contains odd number of LSPs. The LSP is thus a good candidate for the dark matter.

However MSSM itself introduces more than 100 new arbitrary parameters and by itself is not believed to be a complete theory, but a part of more general unified theory of everything. One such theory could be a super-string theory [22]. However, some assumptions can be made about particle masses and their supersymmetric couplings to the fields (for review, see for example [23]). Those assumptions form models of SUSY. Each model can have a different scenario of supersymmetry breaking and of communication of this breaking to the "visible" sector. Those SUSY models greatly reduce the number of the free parameters. The two most popular scenarios are gravity-mediated (SUGRA) and gauge-mediated supersymmetry breaking (GMSB).

1.3 Experimental High-Energy Physics

The "elementary" particle, in most cases, can be imagined as a point-like particle with charge and mass. The term elementary is due to historical reasons, before it was discovered that some of the elementary particles have internal structure and in their turn consist of the more fundamental particles. The most general way to study of elementary particles is to collide them head on and study

their remnants and decay products. If a high enough energy is reached, new particles of larger mass can be created. In elementary particle physics, energy is measured in electron-Volts (eV), the energy that an electron would achieve after it passes through a potential difference of 1 Volt. Modern experiments use particle beams of tens or hundreds of billion electron-Volts: GeV (1 GeV = 10^9 eV).

To achieve such high energies, particles are accelerated by the electromagnetic force. This requires that particles should have an electric charge and be stable. The particle energy is limited by the size of the accelerator and the strength of the magnets, which are needed to hold the particles in a stable orbit. Another limitation is energy loss through radiation.

Accelerators using protons (or anti-protons) as beam particles can reach higher energies than accelerators using electrons, which are limited by the energy loss through radiation. The most interesting type of collision is when the original particles annihilate and create new particles. However since the proton is a composite particle, only a fraction of the total proton energy is spent in the collision. The rest of the energy is carried away by constituent quark and gluons (partons). Such a collision is usually called a hard scattering. The goal of high energy experiments to collect such collisions, or events, and study the properties of the particles and their interactions. The remnant partons could participate in a secondary collision, which is called the underlying event. The fraction of the momentum carried by the parton participating in the hard scattering process is variable; and is parameterized by the parton-distribution functions.

There is a finite list of the particles that could be produced in $p\bar{p}$ interactions Each particle leaves a distinct signature in the detector, which allows its identification. Various types of detectors and techniques are used to measure particle momentum and energy. Total particle energy and momenta are conserved. Therefore, since before the collision occurred there was no energy imbalance in transverse

plane, same should be true after the collision. Weakly interacting particles (neutrinos, for example) escape detection; thus a large energy imbalance will be observed in collisions where such particles are produced. Such energy imbalance is called "missing transverse energy" or "missing-E_{T}". Therefore, the presence of such particles can be inferred through the measurement of the missing-E_{T}.

The total luminosity (L) of a collected data sample times the cross-section (σ) of a process under consideration gives the total number of events for such a process produced at the accelerator:

$$N = L \times \sigma. \tag{1-2}$$

In practice, usually a collision rate, or instantaneous luminosity ($\mathcal{L}$), is measured in terms of the effective area per unit time. Then the total luminosity of the sample is given by:

$$L = \int \mathcal{L} dt. \tag{1-3}$$

The cross-section (measured in barns — 10^{-24} cm^2) of a process is usually known from theoretical calculations, from another experiment, or may be the quantity under study.

Computer programs based on Monte Carlo techniques [8] are used to simulate different high energy processes (physics event generators) and particle interactions with detector material and detector response (detector simulation programs). The simulated events are used to test different hypotheses about particle interactions and verify the distribution of kinematical variables.

CHAPTER 2
LEPTOQUARK PHENOMENOLOGY

The remarkable symmetry between quarks and leptons in the Standard Model suggests that some more fundamental theory may exist, which allows interactions between them. Such interactions are mediated by a new type of particle, a leptoquark (LQ), which carries both lepton and baryon number. A leptoquark is a color-triplet boson with spin 0 or 1, and has fractional electric charge. The coupling between leptoquarks and fermions is given by a Yukawa coupling λ. Leptoquarks appear in many possible extension to the Standard Model and could be directly observed at current particle colliders. In this chapter, possible theoretical sources of the leptoquark pair production mechanism in $p\bar{p}$ collisions is discussed and the experimental signature for leptoquark search is presented. The current limits on the leptoquark mass from other searches are also presented.

2.1 Leptoquark Models

In GUT models leptoquarks appear as new gauge bosons and generally have a mass near the unification scale (10^{16} GeV) to avoid rapid proton decay. Theories with a leptoquark mass accessible at current accelerators must preserve lepton and baryon numbers.

2.1.1 Pati-Salam $SU(4)$ Color Symmetry

The unification of quarks and leptons may arise from the extension of the $SU(3)_C$ color group to the $SU(4)_C$ symmetry group of four colors, by adding lepton number as the fourth color to the three colors of the SM [16]. The leptoquarks in this type of model occur as exotic gauge bosons carrying both baryon and lepton quantum numbers. Therefore, quarks are allowed to decay directly into leptons.

The lack of observation of such decays in experiments implies that the leptoquarks in this model are very heavy (on the order of tens of TeV/c^2).

2.1.2 The $SU(5)$ GUT Models

GUT models postulate a unified gauge group with a single coupling constant [14]. The simplest unifying group that could include $SU(3)_C$, $SU(2)_L$ and $U(1)_Y$ is $SU(5)$. Under this group, quarks and leptons from the same generation are combined into one multiplet. The symmetry of the $SU(5)$ is spontaneously broken through the Higgs mechanism, giving rise to the strong, electromagnetic and weak interactions. Gauge bosons of the unified theory include leptoquarks, which mediate interaction between quarks and leptons within same multiplet. The decays, violating baryon number, are suppressed by assigning very high mass to such bosons ($M_{\mathrm{GUT}} \approx 10^{16}$ GeV/c^2)

2.1.3 Leptoquarks in SUSY Models

The squarks in supersymmetry models may appear as leptoquarks if R-parity is not conserved. In general MSSM, R-parity conservation is postulated to accommodate long proton life-time and conservation of lepton and baryon numbers. However, R-parity could be violated by adding a super-potential of the form to the Lagrangian of the supersymmetry model:

$$\mathcal{L}_{\not{R}} = \lambda_{ijk} L_i L_j E_k^c + \lambda'_{ijk} L_i Q_j D_k^c + \lambda''_{ijk} U_i^c D_j^c D_k^c, \tag{2-1}$$

where λ, λ' and λ'' are Yukawa tri-linear coupling constants, L_i and Q_i correspond to the lepton and quarks doublets and their superpartners, E_i^c, U_i^c, D_i^c the corresponding charge-conjugated doublets for the leptons, up and down quarks, respectively, and i, j, k are generation indexes. The second term allows a leptoquark-like interaction between leptons and quarks. In these models, squarks could be significantly lighter than the ones in unification theories (of the order of hundreds GeV/c^2).

2.2 Leptoquark Production at the Tevatron

In the general phenomenological framework of Buchmüller, Rückl, and Wyler [24], leptoquarks interact with a single generation of the SM model fermions via Yukawa couplings and are assumed to preserve the $U(1)_Y \times SU(2)_L \times SU(3)_C$ symmetry of the Standard Model. The lepton and baryon numbers are also conserved. In this model, leptoquarks are characterized by spin ($J = 0, 1$), weak isospin ($T = -1/2, 0, 1/2, 1$), and fermion number ($F = 0, 2$), defined as $F = L + 3B$, where L is lepton number (+1 for electrons) and B is baryon number (+1/3 for quarks). They are also distinguished whether they couple to the left (L) or right-handed (R) leptons. The leptoquark types and their properties are listed in Table 2-1 according to the notation adopted by the Hadron Elektron Ring Anlage (HERA) experiments. The table assumes charge conjugation and applies to the second and third generation leptoquarks with global replacement of first-generation fermions. Under these assumptions, only the masses and the Yukawa couplings of leptoquarks remain free parameters, since the coupling to the gauge bosons of the Standard Model are determined by the electric charge, isospin and the color charge.

Leptoquarks decay to a quark and a lepton. The branching ratio to a charged lepton(β) is either 1, 1/2 or 0.

2.2.1 Production Diagrams

Leptoquarks may be produced as a particle/anti-particle pair at the Tevatron, which is a proton/anti-proton collider. In this scenario, the production cross-section does not strongly depend on the lepton-quark-leptoquark Yukawa couplings and is completely determined by the strong coupling constant of the SM. The LQ pair-production process is similar to the QCD heavy-quark production process and to leading order occurs in the quark/anti-quark annihilation and gluon fusion:

$$q\bar{q} \rightarrow LQ + \overline{LQ} \tag{2-2}$$

Table 2-1: Quantum numbers of scalar (S) and vector (V) leptoquarks. The subscript indicates the weak isospin and the superscript indicates whether the leptoquark couples to the left or right leptons. Tilde denotes leptoquarks that differ by two units of hypercharge.

Type	Charge	Coupling	Branching Ratio	F
S_0^L	-1/3	$\lambda_{\rm L}(e_{\rm L}u),\ -\lambda_{\rm L}(\nu_e d)$	1/2	2
S_0^R	-1/3	$\lambda_{\rm R}(e_{\rm R}u)$	1	2
$\tilde{S}_0^R$	-4/3	$\lambda_{\rm R}(e_{\rm R}d)$	1	2
S_1^L	-4/3	$-\sqrt{2}\lambda_{\rm L}(e_{\rm L}d)$	1	2
	-1/3	$-\lambda_{\rm L}(e_{\rm L}u),\ -\lambda_{\rm L}(\nu_e d)$	1/2	2
	+2/3	$\sqrt{2}\lambda_{\rm L}(\nu_e u)$	0	2
$V_{1/2}^L$	-4/3	$\lambda_{\rm L}(e_{\rm L}d)$	1	2
	-1/3	$\lambda_{\rm L}(\nu_e d)$	0	2
$V_{1/2}^R$	-4/3	$\lambda_{\rm R}(e_{\rm R}d)$	1	2
	-1/3	$\lambda_{\rm R}(e_{\rm R}u)$	0	2
$\tilde{V}_{1/2}^L$	-1/3	$\lambda_{\rm L}(e_{\rm L}u)$	1	2
	+2/3	$\lambda_{\rm L}(\nu_e u)$	0	2
$S_{1/2}^L$	-5/3	$\lambda_{\rm L}(e_{\rm L}\bar{u})$	1	0
	-2/3	$\lambda_{\rm L}(\nu_e\bar{u})$	0	0
$S_{1/2}^R$	-5/3	$\lambda_{\rm R}(e_{\rm R}\bar{u})$	1	0
	-2/3	$-\lambda_{\rm L}(\nu_e\bar{u})$	1	0
$\tilde{S}_{1/2}^L$	-2/3	$\lambda_{\rm L}(e_{\rm L}\bar{d})$	1	0
	+1/3	$\lambda_{\rm L}(\nu_e\bar{d})$	0	0
V_0^L	-2/3	$\lambda_{\rm L}(e_{\rm L}\bar{d}),\ \lambda_{\rm L}(e_{\rm L}\bar{u})$	1/2	0
V_0^R	-2/3	$\lambda_{\rm R}(e_{\rm R}\bar{d})$	1	0
$\tilde{V}_0^R$	-5/3	$\lambda_{\rm R}(e_{\rm R}\bar{u})$	1	0
V_1^L	-5/3	$\sqrt{2}\lambda_{\rm L}(e_{\rm L}\bar{u})$	1	0
	-2/3	$-\lambda_{\rm L}(e_{\rm L}\bar{d}),\ -\lambda_{\rm L}(\nu_e\bar{u})$	1/2	0
	+1/3	$\sqrt{2}\lambda_{\rm L}(\nu_e\bar{d})$	0	0

$$g\bar{g} \rightarrow LQ + \overline{LQ} \tag{2-3}$$

The Feyman diagrams [1] for the pair-production of leptoquarks in the quark/anti-quark annihilation and in gluon fusion in the leading order calculations (LO) are shown in figure 2-1.

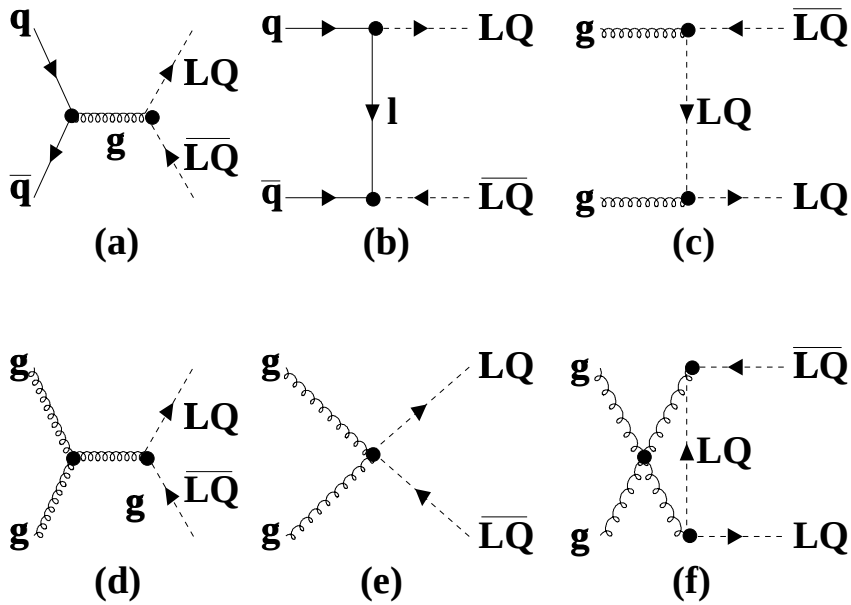

Figure 2-1: Leading-order Feynman diagrams for leptoquark pair production at the Tevatron.

The contribution to the total cross-section of the LQ pair-production through virtual lepton exchange can be neglected if the coupling strength to fermions in this process is assumed to be of the order of the electromagnetic coupling strength ($\lambda \approx 0.3$) or smaller. However, λ can not be infinitely small ($\lambda \sim 10^{-6}$), otherwise LQ will not decay inside the detector volume.

In the case of the vector leptoquarks, the production cross-section depends on the couplings to the SM gauge bosons. Since those couplings depend on the

[1] The Feyman diagram is a convenient way to graphically present terms in the perturbative expansion of the production cross-section.

specific model, usually some assumption should be made about the nature of the leptoquarks and the particular values of the couplings [24, 25, 26, 27]. The production cross-section for the vector leptoquark is typically larger than for the scalar leptoquarks, even for minimal vector couplings [28].

2.2.2 Leading Order Cross Section and NLO Corrections

In this search, we consider only the case of the scalar leptoquark pair-production at the Tevatron collider. In this case, the cross section of the processes is determined by the QCD couplings, as explained above, and at the parton level, in the Born approximation, this cross section is given by:

$$\sigma_{\mathrm{LO}}(q\bar{q}) = \frac{\pi\alpha_s^2}{\hat{s}}\frac{2}{27}\beta^3, \tag{2-4}$$

$$\sigma_{\mathrm{LO}}(gg) = \frac{\pi\alpha_s^2}{96\hat{s}}\left[\beta(41-31\beta^2)+(18\beta^2-\beta^4-17)\ln\frac{1+\beta}{1-\beta}\right], \tag{2-5}$$

where $\beta = \left(1-\frac{4M_{\mathrm{LQ}}^2}{\hat{s}}\right)^{\frac{3}{2}}$, M_{LQ} is leptoquark mass, and $\hat{s}$ is the squared center-of-mass energy of the process. The total production cross-section for $p\bar{p}$ collisions is obtained by convoluting the expressions for the partonic cross-sections from 2-4 and 2-5 with the parton-distribution functions of the proton and anti-proton [28].

The dependence of the theoretical calculation of the total production cross-section on the factorization and renormalization scales (both refer to be μ) could be significantly reduced, when higher-order QCD corrections are included into the calculations [29]. The renormalization scale is unknown and thus is a free parameter. Infinities could arise in the perturbative expansion of the invariant amplitude in the cross section calculation. A procedure called renormalization is used, to regulate these infinities and make the calculations finite. In such a procedure the expansion series is cut off at some high energy scale. The factorization scale sets the scale for evaluating the parton density functions and is also free parameter. The usual choice is to set the renormalization/factorization scale to the dominant scale of the physics process, in this case the leptoquark mass. Then, the variation of μ between

$2M_{\mathrm{LQ}}$ and $M_{\mathrm{LQ}}/2$ gives a theoretical uncertainty in the cross-section calculation (this is a convention to estimate the theoretical uncertainty).

The QCD radiative corrections to the order α_s include virtual corrections, the bremsstrahlung of gluons and additional contributions from the gluon-quark collisions. The inelastic Compton scattering processes, shown in Figure 2-2, contribute in the order of α_s^3 to the total cross-section.

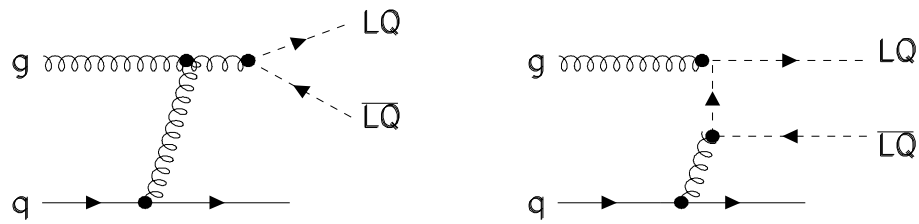

Figure 2-2: Feynman diagrams for the leptoquark pair production at the Tevatron due to the gluon-quark subprocesses.

The Figure 2-3 shows the dependence of the LO and next-to-leading order (NLO) cross-section calculations as function of μ [29]. The variation of μ between $M_{\mathrm{LQ}}/2$ and $2M_{\mathrm{LQ}}$ changes the LO cross-section calculation by 100%. However, for the same variation in μ, the scale dependence reduces significantly to only 30% for NLO calculations. Besides reducing the theoretical uncertainty of the calculation, the QCD radiative corrections enhance the LQ production cross-section for the nominal choice of $\mu \sim M_{\mathrm{LQ}}$ by 15% to 50% depending on the leptoquark mass. The ratio of the NLO to the LO cross section[2] as a function of leptoquark mass is shown on Figure 2-4 for two choices of parton density functions, CTEQ4 and CTEQ5 [30, 31].

[2] Programs to compute the cross-sections from these calculations have been obtained [32] from the authors [29].

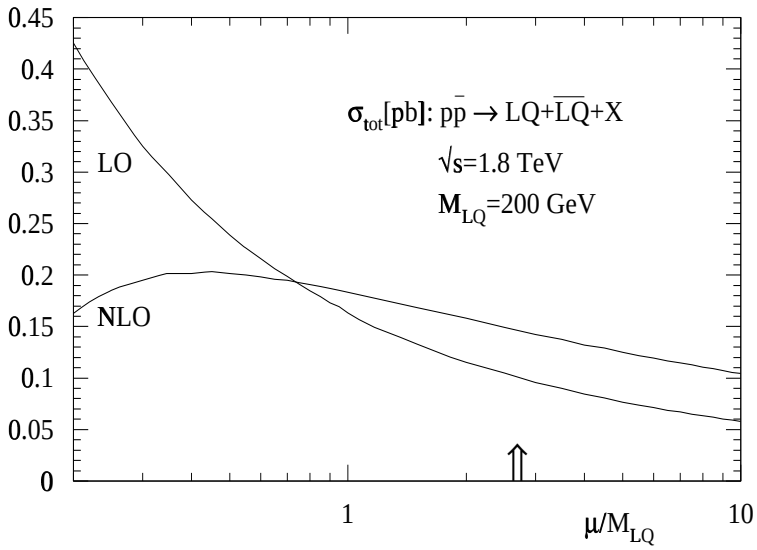

Figure 2-3: Renormalization/factorization scale dependence of the leptoquark pair-production cross-section at the Tevatron energy $\sqrt{s} = 1.8$ TeV. The arrow indicates the average invariant energy $< \hat{s} >^{1/2}$ in the hard subprocess [29].

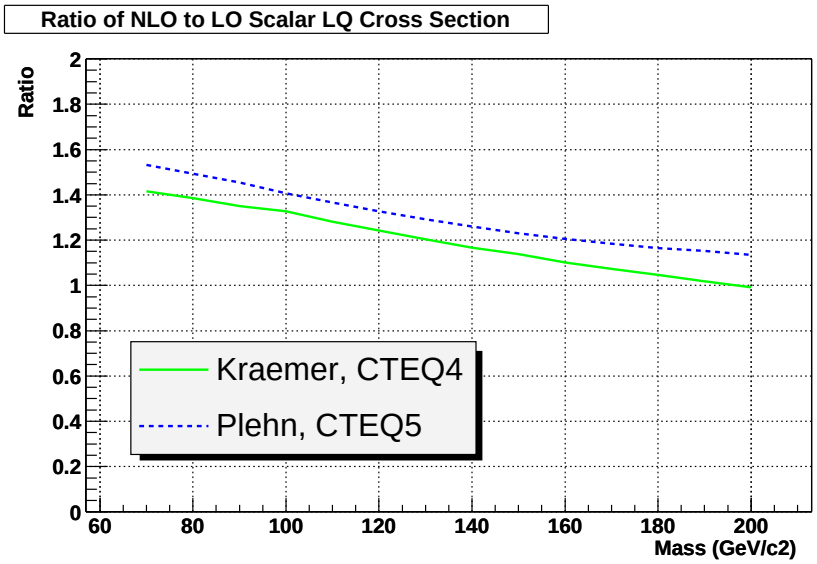

Figure 2-4: Ratio of the NLO to LO cross sections for scalar leptoquark production for both CTEQ4 and CTEQ5 [32].

Figure 2-5 shows the next-to-leading order cross section for scalar leptoquark production as a function of mass for 3 choices of the factorization/renormalization scale: $\mu = M_{\rm LQ}$, $\mu = 2M_{\rm LQ}$, and $\mu = 0.5M_{\rm LQ}$.

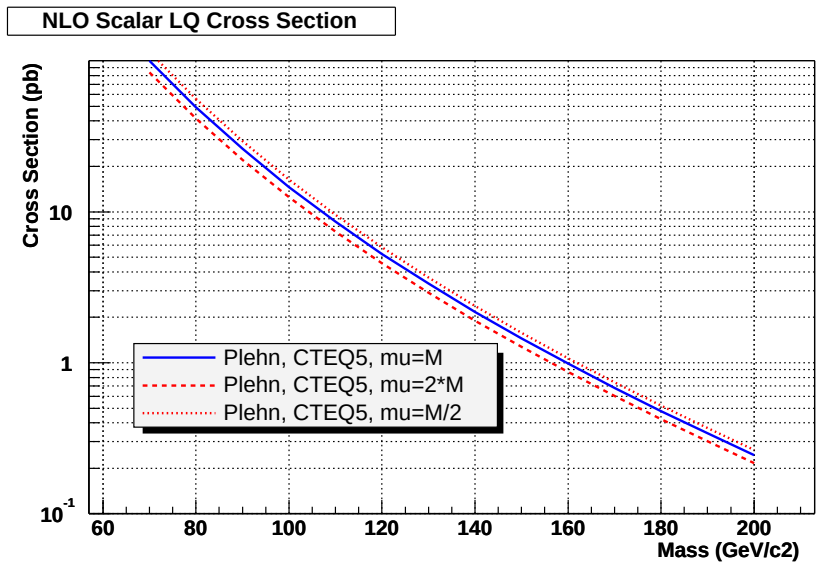

Figure 2-5: Next-to-leading order cross section for scalar leptoquark production for 3 choices of the factorization/renormalization scale: $\mu = M_{\rm LQ}$, $\mu = 2M_{\rm LQ}$, and $\mu = 0.5M_{\rm LQ}$. CTEQ5 parton densities are chosen.

2.2.3 Experimental Signatures

Each leptoquark decays into a lepton and a quark, thus three final states are possible for leptoquark pair production depending on the charged lepton branching ratio β: $ll+$ jets, $l\nu+$ jets, and $\nu\nu+$ jets, where l is a charged lepton and ν its associated neutrino. Since the neutrino can not be detected directly, its presence is inferred from the large missing transverse energy. Therefore, the experimental signature at the Tevatron could be two charged leptons plus two jets, charged lepton, missing-$E_{\rm T}$ plus two jets, or missing-$E_{\rm T}$ plus two jets.

2.3 Current Leptoquark Search Limits

Extensive experimental searches for all generations of leptoquarks were conducted at $p\bar{p}$,ep and e^+e^- high energy colliders. No evidence for such particles has yet been observed; therefore, lower limits on the leptoquark mass were placed

based on the search results. A comprehensive review of the leptoquarks searches at $p\bar{p}$ and ep colliders could be found in [33]. Current limits for the first-generation scalar leptoquark masses from different experiments are presented here.

2.3.1 Non-Hadron Collider Searches

At the HERA ep collider with $\sqrt{s} = 318$ GeV, leptoquarks could be produced singly in direct electron-quark interactions. If M_{LQ} is below the center-of-mass energy and Yukawa couplings are not too large (of electromagnetic order), the leptoquark could be produced as a narrow-width resonance. Therefore, a leptoquark could be observed as a narrow peak in the spectrum of lepton-jet invariant mass. The leptoquark signal can be further distinguished from the deep inelastic scattering background based on the difference in the angular distribution of the decay products. The H1 [34] and ZEUS [35] collaborations at HERA reported an excess of events beyond the Standard Model expectations observed in neutral-current deep inelastic scattering events at high Q^2 (large negative values of the squared four-momentum transfer). This excess occurred at a lepton-parton mass of $M \approx 200$ GeV$/c^2$, which could be due to the first generation leptoquark production. However, the significance of the excess has been reduced after both HERA experiments [36, 37] have more than doubled their data samples reported in these analyses.

The leptoquarks could be pair-produced at the Large Electron Positron collider (LEP) via electroweak processes if $M_{\mathrm{LQ}} < \sqrt{s}/2$. The OPAL collaboration has performed a search for three generation leptoquarks at the center-of-mass energy from 189 to 209 GeV, in the $ll+$ jets, $l\nu+$ jets, and $\nu\nu+$ jets channels. Single LQ production may occur when a beam electron interacts with quark or anti-quark, which are pair-produced from radiated photon. In this case LQs can be created up to the full center-of-mass energy and the leptoquark production cross-section depends on the Yukawa coupling λ.

The most recent results on the mass limits for the first-generation scalar leptoquark from HERA and LEP experiments [38, 39, 40] are summarized in Table 2-2.

Table 2-2: Lower limits on the first-generation scalar leptoquark mass from Tevatron, LEP and HERA experiments. Tevatron limits are independent of the Yukawa coupling λ, wheres LEP limits are presented for the $\lambda = \sqrt{4\pi\alpha_{em}} \approx 0.3$ and HERA limits are presented for $\lambda = 0.1$. A dash indicates that no limit could be set.

Type	Branching Ratio	Mass Limit (GeV/c^2)		
		Tevatron	LEP	HERA
S_0^L	1/2	204	196	276
S_0^R	1	242	196	273
$\tilde{S}_0^R$	1	242	183	248
$S_{1/2}^L$	1	242	185	282
	0	98	187	-
$S_{1/2}^R$	1	204	196	282
$\tilde{S}_{1/2}^L$	1	242	185	269
	0	98	89[a]	-
S_1^L	1	242	185	275
	1/2	204	196	275
	0	98	97[a]	-

[a] The limits derived for the leptoquark from pair-production processes.

2.3.2 Run I Tevatron Results

Searches for three generations of leptoquarks were performed by two experiments, D0 and CDF, at the Tevatron collider with $\sqrt{s} = 1.8$ TeV during Run I. The combined mass limit [43] of 242 GeV/c^2 for scalar leptoquarks with $\beta = 1$ from CDF and DØ ruled out a leptoquark interpretation of the HERA anomaly for large β. More recently, DØ has published [44] an improved limit on the search for first-generation leptoquarks in the $\nu\nu jj$ final state, and CDF has published [45] limits on a search for second- and third-generation leptoquarks in the MET plus heavy-flavor jets final state ($\nu\nu QQ$). Preliminary limits from searches by CDF for first-generation leptoquarks decaying in the $e\nu jj$ channel [46] and in the $\nu\nu jj$ channel [47] were never published, but are similar to the published DØ limits [44].

The results on the mass limits for the first-generation scalar leptoquark from the Run I Tevatron experiments are summarized in Table 2-2.

2.3.3 Run II Searches

The Tevatron is currently the highest energy accelerator in the world with $\sqrt{s} = 1.96$ GeV, which offers a unique opportunity for searches for new physics beyond the Standard Model.

Figure 2-6 shows the ratio of the cross sections for $\sqrt{s} = 1.96$ TeV and $\sqrt{s} = 1.8$ TeV. As can be seen, the increase in the center-of-mass energy increases the cross section by 30% for a mass of 100 GeV/c^2, which offers the possibility to set stronger limits on leptoquark production even for a data sample equivalent in size to Run I.

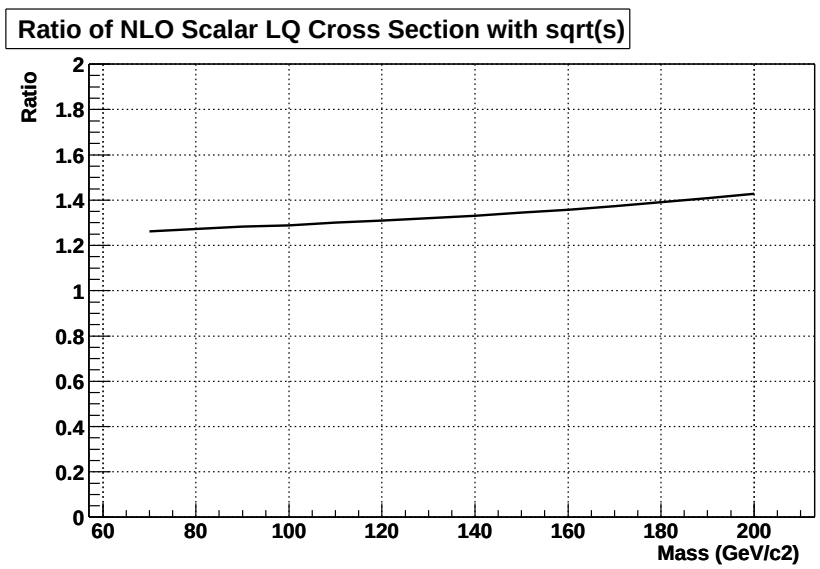

Figure 2-6: Ratio of the NLO cross section for scalar leptoquark production at $\sqrt{s} = 1.96$ TeV to $\sqrt{s} = 1.8$ TeV as a function of leptoquark mass.

Figure 2-7 shows the DØ combined limit for first-generation scalar leptoquarks in the β vs. mass plane. Also shown is the CDF limit from the published $eejj$ channel interpreted for values of β other than 1. The aim of this study is to improve the sensitivity near the $\beta = 0$ region by conducting a search for the

decay of first-generation leptoquarks in the $\nu\nu jj$ channel, that is, in the missing transverse energy and multi-jets channel.

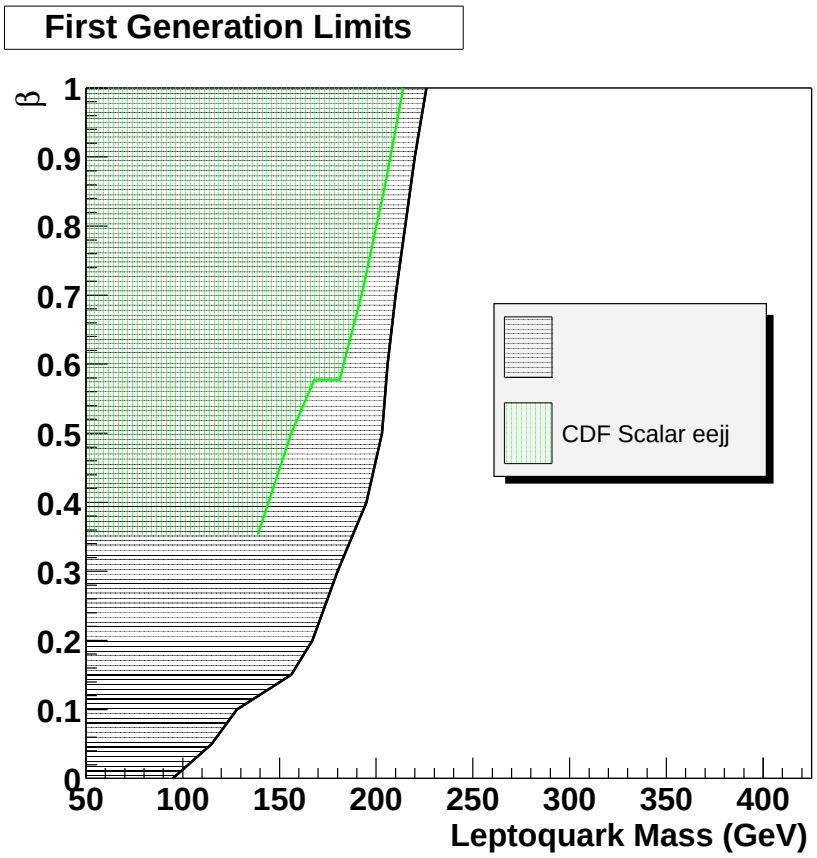

Figure 2-7: Run I limits from CDF and DØ on scalar leptoquarks in the β vs. mass plane.

CHAPTER 3
EXPERIMENTAL APPARATUS

This chapter briefly describes the Fermilab accelerator complex and the Collider Detector at Fermilab (CDF) detector. The CDF detector is a general purpose detector designed to study $p\bar{p}$ interactions. The Tevatron is a superconducting synchrotron that accelerates and collides beams of protons and antiprotons at a center-of-mass energy $\sqrt{s} = 1.96$ TeV. It is the highest energy collider in the world, and will remain so until Large Hadron Collider (LHC) at CERN starts operating in 2007 at a center-of-mass energy $\sqrt{s} = 14$ TeV.

3.1 The Accelerator Complex

The Fermilab accelerator complex consists of eight particle accelerators that are linked together to produce intense high energy beams of protons and antiprotons: the Cockcroft-Walton linear pre-accelerator, the Linear Accelerator (Linac), the Booster, the Debuncher, the Accumulator, the Main Injector, the Recycler and the Tevatron [48]. The Recycler was not used for the data collected for this analysis. Figure 3-1 shows a schematic view of the Fermilab Accelerator complex.

3.1.1 The Proton Source

The proton source consists of the Cockcroft-Walton pre-accelerator, Linac and Booster. The source of the protons is a bottle of hydrogen gas. At the first stage of acceleration hydrogen ions are created, consisting of two electrons and one proton. At the next stage, ions are accelerated in the Linac and reach an energy of 750 keV. At the end of the second stage, the ions are stripped of electrons by a carbon foil and injected into the Booster along with the existing proton beam and accelerated to an 8 GeV energy. The Linac and Booster provide a beam

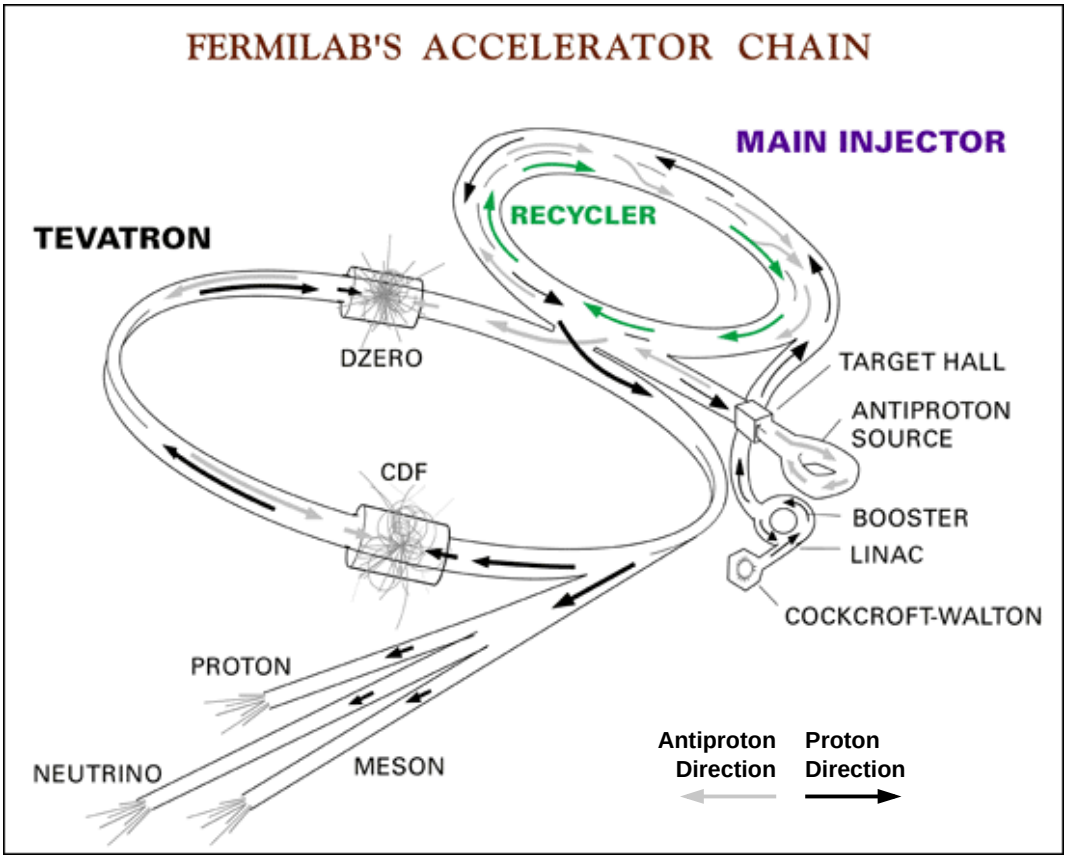

Figure 3-1: A Schematic view of the Fermilab Accelerator complex

with typically 6×10^{10} protons per bunch.[1] In another mode of operation the Linac/Booster can deliver a beam with an intensity up to 5×10^{12} protons per bunch to the Main Injector for antiproton production.

3.1.2 The Antiproton Source

The Antiproton source consists of two parts: the Accumulator and the Debuncher. Protons from the Main Injector with a beam energy of 120 GeV strike a nickel target, and antiprotons are selected from the collision products with an average energy of about 8 GeV. At the next stage the spread in the antiproton momenta is reduced in a small synchrotron—the Debuncher—and antiprotons are sent to the Accumulator. The Accumulator, a storage ring, collects antiprotons, up

[1] Throughout this dissertation the typical number quoted refers to the Tevatron running period, during which the data for this search were accumulated.

to a maximum of 140×10^{10} antiprotons. The antiproton accumulation process is referred as stacking. The antiproton stacking rate varies inversely with the stack size, starting from around 11×10^{10} hr^{-1} and falling to 6×10^{10} hr^{-1}. When the stack of antiprotons reaches the maximum, it is sent via the Main Injector to the Tevatron for the proton-antiproton collisions.

3.1.3 The Main Injector

The Main Injector is a large-aperture proton synchrotron that was specifically designed and built for Run II, which addresses the limitations of the Run I Main Ring accelerator. The Main Injector further accelerates particles and transfers beams to the Tevatron or fixed target experiments. It has four functions:

- It accelerates protons from 8 GeV to 150 GeV.
- It produces 120 GeV protons, which are used for antiproton production.
- It receives antiprotons from the Antiproton Source and increases their energy from 8 to 150 GeV.
- It injects protons and antiprotons into the Tevatron.

3.1.4 The Tevatron

The Tevatron is a proton-antiproton synchrotron collider situated in a 1 km radius tunnel. The Tevatron receives 150 GeV protons and antiprotons from the Main Injector and accelerates them to 980 GeV. In a typical store there are 36 proton and 36 antiproton bunches in the Tevatron, with a bunch spacing of 396 ns. The two beams circulating around the Tevatron in the opposite direction are focused and brought into collision in two points around the ring, denoted as B0, which hosts the CDF detector, and D0 with the DØ detector.

The shot setup (particle injection into the Tevatron) begins when the antiproton stack size is large enough in the Accumulator. First, seven proton bunches from the Booster are coalesced in the Main Injector into a single bunch of $\sim 300 \times 10^9$ particles. Then this large bunch is transfered into the Tevatron.

This process is repeated until 36 bunches of protons with an energy of 150 GeV are circulating in the Tevatron. At the next stage, seven to eleven antiproton bunches from the Accumulator are coalesced in the Main Injector into a single bunch with $\sim 30 \times 10^9$ particles and injected into the Tevatron up to a total of 36 bunches. About 90% of antiproton stack is used for the shot. The rest is usually saved for the next shot setup. When all proton and antiproton bunches are loaded into the Tevatron, they are accelerated to an energy of 980 GeV and brought into collision. However, at this point there is large radiation in the detectors due to the beam losses. So, the beams are "scraped", using special collimators, to remove the peripheral halo of particles from the beams. After the scraping is complete the data taking period begins. The typical period of data taking lasts for about 15 hours and is called a store. Over that period of time, the luminosity decays by an order of the magnitude due to the beam losses, $p\bar{p}$ interactions and beam-gas interactions. In parallel with $p\bar{p}$ collisions in the Tevatron, the new stacking period begins in the Accumulator to prepare for the next store. When a new, sufficiently large antiproton stack is collected, the current store is aborted and new bunches are injected into the Tevatron. The period of the down time between the store could be as short as 2 hours, and is usually used for the detector calibrations.

The typical Run IIa value for the initial luminosity is $4 \times 10^{31}\text{cm}^{-2}\text{sec}^{-1}$. The $p\bar{p}$ luminous region at CDF is roughly a Gaussian in z with a width $\sigma \sim 30$ cm.

3.2 The CDF Detector

The CDF experiment is a general purpose particle detector with azimuthal and forward/backward symmetry designed to study $p\bar{p}$ the interactions. The detector is used to measure the energy, momentum and if possible, type of particle over as large a solid angle as possible. This is achieved through the combination of different types of detectors dedicated to particular measurements. Closest to the beam pipe are the silicon vertex detectors surrounded by the charged-particle

tracking chamber to reconstruct particle momenta and the collision vertex. The tracking system is, in turn, surrounded by calorimeters, to measure particle energies, and by muon detectors. CDF has also a time-of-flight system for the identification of charged hadrons [49] and dedicated luminosity [50] and beam loss monitors [51].

The CDF detector has undergone a major upgrade for Run II [52]. The upgrade was necessary to accommodate the increase in the Tevatron luminosity as well as the shorter bunch-crossing time. Also, it reflects the experience gained from Run I physics analyses and detector operation, and thus includes additional detectors.

Figure 3-2 shows isometric view of the CDF detector. An elevation view of one half of the CDF II detector is shown in Figure 3-3. This analysis relies on central and plug electromagnetic and hadronic calorimeters, used for the jet reconstruction and energy measurement, as well as the missing transverse energy measurement. The combination of the tracking system together with calorimeter and muon systems is used for charged lepton identification. In this section, only a general description of the major components of the detector is given, with emphasis on details relevant to this analysis. The detector is described in more detail elsewhere [52, 53].

The coordinate system adopted to describe positions within the CDF detector is centered on the nominal collision point — at the center of the detector. The z-axis is directed along the direction of the proton beam, traveling clockwise in the Tevatron when viewed from above, and with the x-axis pointing radially outward and the y-axis pointing upward. It is convenient to use a cylindrical-like system of coordinates (z, ϕ, η), where the polar angle θ has been transformed into the

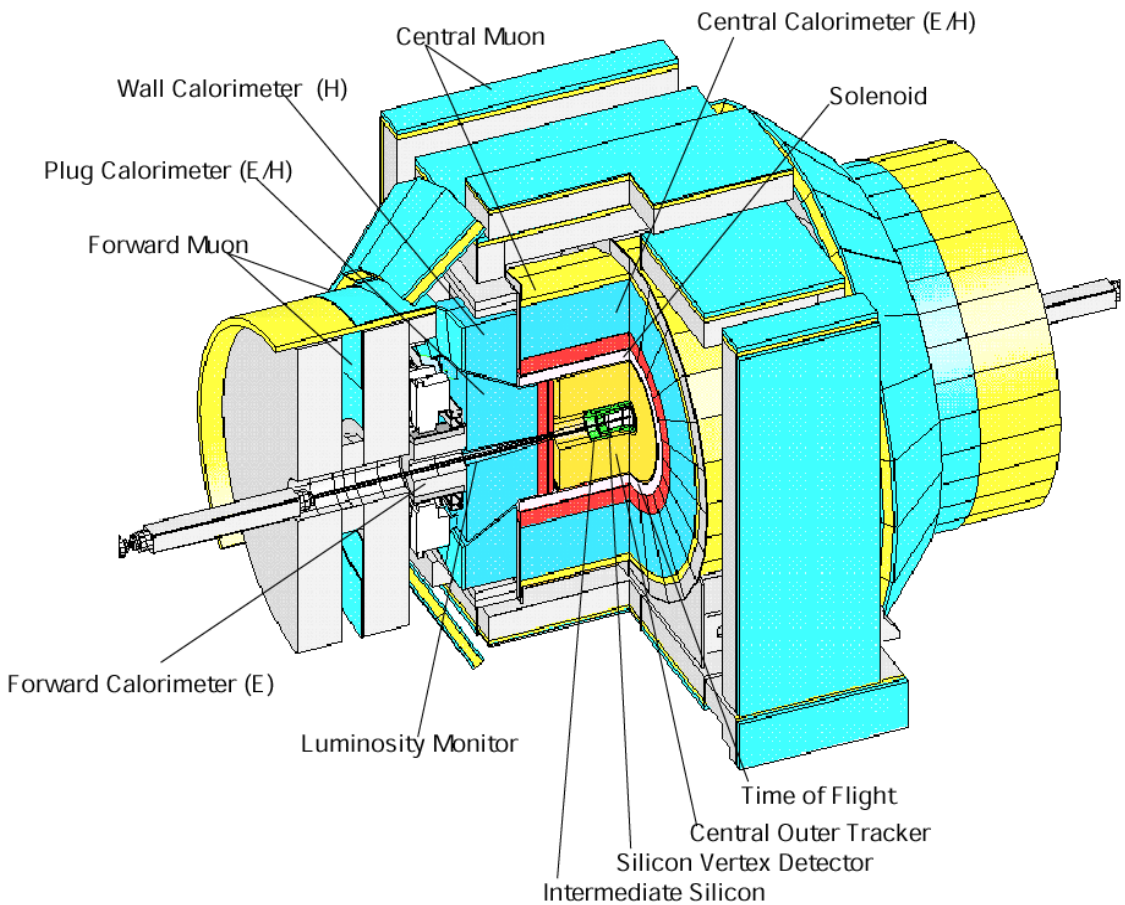

Figure 3-2: Isometric view of the CDF detector.

pseudorapidity η. The rapidity, y, is defined by:

$$y = \frac{1}{2} \ln \left(\frac{E + p_z}{E - p_z} \right), \tag{3-1}$$

where E and p_z are the particle energy and the z-component of the momentum, respectively. The rapidity shows how much the particle is boosted along the z-axis. The rapidity transforms as $y \to y - \tanh^{-1} \beta$, under a a Lorentz transformation in the z-direction to a frame with velocity β relative to the lab frame. Hence the shape of the rapidity distribution dN/dy is invariant under Lorentz transformation along the z-axis. The pseudorapidity, η, is approximately equal to the rapidity

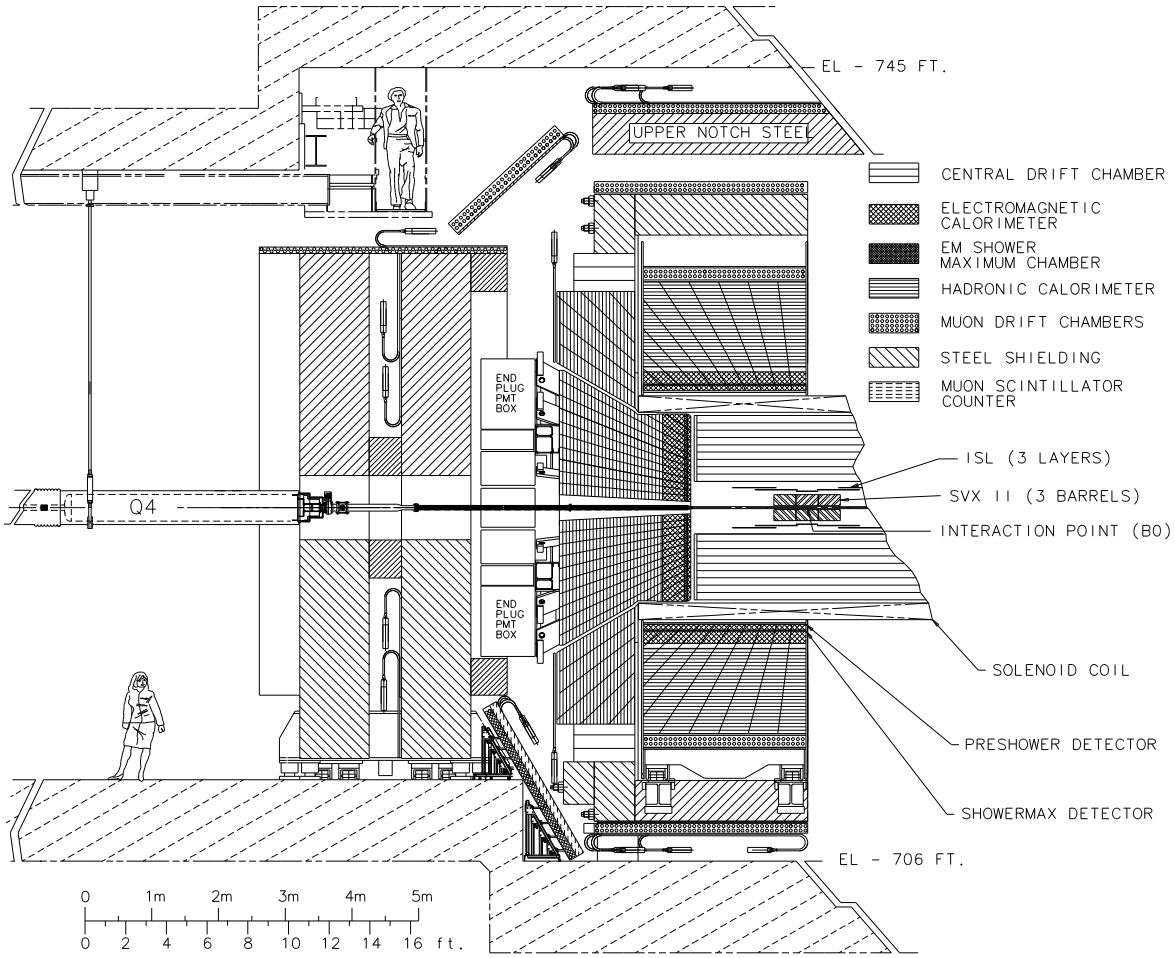

Figure 3-3: Elevation view of one half of the CDF II detector.

when $p \gg m$, and is defined as:

$$\eta = -\ln \tan \frac{\theta}{2} \tag{3-2}$$

It is important to note that two conventions to calculate the pseudorapidity are used at the CDF: detector pseudorapidity, usually denoted as η_{det}, which is measured with respect to nominal interaction point at $z = 0$, and the particle pseudorapidity, η, which measures the pseudorapidity with respect to the reconstructed $p\bar{p}$ interaction vertex.

3.2.1 Calorimetry

The CDF calorimeter detectors are used to measure the energy of charged and neutral particles produced in $p\bar{p}$ interactions. They also indirectly measure the transverse energy of weakly interacting particles, such as the neutrino, which escape the detector undetected, by measuring the imbalance in energy. Information from the calorimeter, along with tracking information is used in the particle identification.

The energy of a particle is measured by its total absorption in the calorimeter. When a particle traverses matter, it will generally interact and lose a fraction of its energy [54]. The interaction processes through which a particle loses its energy depends on the initial energy and the nature of the particle.

The principal source of energy loss by electrons (or positrons) above 100 MeV is photon radiation, or bremsstrahlung, whereas a high-energy photon loses its energy through the electron-positron pair creation process when interacting with nuclear electromagnetic field. The electrons and positrons generated in these processes may in turn lose energy by radiating more photons, thus producing an electromagnetic shower. The shower energy is eventually deposited in the calorimeter through ionization energy loss (electrons) or through Compton scattering or photoelectric processes (photons). As the shower develops in calorimeter material, the amount of energy deposited initially increases with detector depth. However, at some point the number of shower particles decreases and no further particle multiplication takes place. The depth at which this occurs is called the shower maximum. Beyond the shower maximum the energy deposited in a detector slice of given thickness gradually decreases. It is convenient to describe the shower development in a material-independent way. The radiation length (X_0) of a given material is defined as the distance over which a high-energy electron loses on average, $1-e^{-1}$ of its energy through bremsstrahlung [8].

Any charged particle traversing matter would lose its energy through ionization or photon radiation. However, for heavy charged particles the radiative energy loss starts to dominate at much higher energies, which is approximately higher by a factor $(m/m_e)^2$ (where m and m_e are the particle and the electron mass respectively) than that of for the electron.

The interaction of hadrons with matter is more complicated, since hadrons can undergo electroweak and strong interactions. In general, highly energetic hadrons lose their energy through inelastic collisions with the nuclei of the absorbing medium. The particles produced in such nuclear reactions may in turn lose their energy by ionization of the medium or induce a secondary nuclear reaction, thus causing a shower to develop. However, for hadrons the cross section for nuclear interactions is much smaller than for electromagnetic, thus hadrons travel greater distances before losing all of their energy. The nuclear interaction length λ_0 is defined as a mean free path for a hadron to undergo a nuclear inelastic interaction. However, because the multiplicity per interaction is higher for nuclear interaction versus electromagnetic, the depth in λ is shallower than in X_0.

All calorimeters utilize a sampling technique, where passive layers of absorber material are interchanged with active layers of scintillator (for the signal collection). The light from the scintillator plates is read out through wavelength-shifting (WLS) light guides by photo-multiplier tubes (PMTs). The energy resolution of the calorimeter, denoted as σ/E, is dominated by statistical sampling fluctuations and the photo-statistics of the PMTs, and is inversely proportional to the square root of the incident energy. It also includes a smaller constant term that comes from the non-uniform response of the calorimeter, calibration errors and electronics noise.

The complete CDF calorimeter system extends up to 5.2 in $|\eta|$ and provides 2π azimuthal coverage. The detectors are segmented in azimuth and pseudorapidity to form a projective tower geometry, pointing back to the nominal interaction point.

The CDF calorimeter system consists of an electromagnetic section followed by a hadronic section behind it (except forward calorimeter), and is separated into three detector regions according to the pseudorapidity coverage: central, plug and forward. The central region consists of the Central Electromagnetic Calorimeter (CEM) and the Central Hadronic Calorimeter (CHA). The plug region includes the Plug Electromagnetic Calorimeter (PEM) and the Plug Hadronic Calorimeter (PHA). The Endwall Hadronic Calorimeter (WHA) closes the gap between central and plug regions in the hadronic section of the calorimeter. The forward region consists only of an electromagnetic section, the Miniplug (MNP) [55], and is not used in this analysis. Thus, the calorimeter coverage relevant to this search extends up to $|\eta| < 3.6$

The η coverage, depth and resolution of the CDF calorimeter system are summarized in the Table 3-1.

Table 3-1: Summary of the CDF calorimeter subsystem properties. X_0 refers to the radiation length and λ_0 refers to the interaction length for the electromagnetic and the hadronic calorimeters respectively. Energy resolution is given for a single incident electron or photon (EM calorimeters) or pion (HAD calorimeters).

Calorimeter subsystem	η coverage	Depth	Energy resolution $\sigma(E)/E$
CEM	$\|\eta\| < 1.1$	18 X_0	$13.5\%/\sqrt{E_{\mathrm{T}}} \oplus 2\%$
PEM	$1.1 < \|\eta\| < 3.6$	21 X_0	$16\%/\sqrt{E_{\mathrm{T}}} \oplus 1\%$
CHA	$\|\eta\| < 0.9$	$4.5\lambda_0$	$75\%/\sqrt{E_{\mathrm{T}}} \oplus 3\%$
WHA	$0.7 < \|\eta\| < 1.3$	$4.5\lambda_0$	$75\%/\sqrt{E_{\mathrm{T}}} \oplus 3\%$
PHA	$1.2 < \|\eta\| < 3.6$	7 λ_0	$80\%/\sqrt{E_{\mathrm{T}}} \oplus 5\%$

Central calorimeters. The central calorimeters, CEM, CHA and WHA, are retained from Run I, but with upgraded front-end and data acquisition electronics to accommodate for the shorter bunch-crossing time in Run II.

The calorimeter has a cylindrical symmetry and is divided into two halves at $\eta = 0$. Both calorimeter halves have an 1 in thick iron end plate at $\eta = 0$, which form an uninstrumented region ("crack") in η coverage. The CEM calorimeter

covers region up to about $|1.1|$ in pseudorapidity on either side. Each calorimeter section is divided in projective towers with 15° in $\Delta\phi$ and 0.11 in $\Delta\eta$. One wedge module is notched to allow an access to the CDF superconducting solenoid ("chemney"). The CEM calorimeter is made of 0.5 cm thick plastic scintillator plates interspersed with 0.32 cm thick lead layers as an absorber. It provides $13.5\%/\sqrt{E} \oplus 2\%$ energy resolution for a single electron or photon at normal incidence. Embedded in each CEM module, at a depth of about 6 radiation lengths from the front face of the detector, is the Central Electromagnetic Shower maximum detector (CES). The CES is a combined strip/wire gas proportional chamber that measures the position and transverse shape of the electromagnetic showers in both z and r-ϕ directions. It gives a position resolution of 0.2 cm for electrons at 50 GeV.

The CHA is placed outside the CEM radially. It covers the pseudorapidity range $|\eta| < 0.9$ and the WHA calorimeter extends this coverage up to $|\eta| < 1.3$. The CHA consist of 1 cm thick scintillator layers interleaved with layers of 2.5 cm thick steel. The layers of the steel absorber serve as a return yoke for solenoid magnetic field. The end wall uses 5 cm thick absorber which reflects the fact that, that the total energy in this calorimeter is on average a factor $\sqrt{2}$ bigger than in the central one for the particles with the same transverse energy.

Plug calorimeters.The plug calorimeters, PEM and PHA, were replaced for Run II. Figure 3-4 shows an r-z cross section view of the CDF II end plug calorimeter.

The plug section covers the pseudorapidity range from $1.1 < |\eta| < 3.6$. Part of the detector at the lower rapidity range uses finer azimuthal segmentation, $\Delta\phi = 7.5°$, which was chosen to optimize electron/positron identification in b-quark jets.

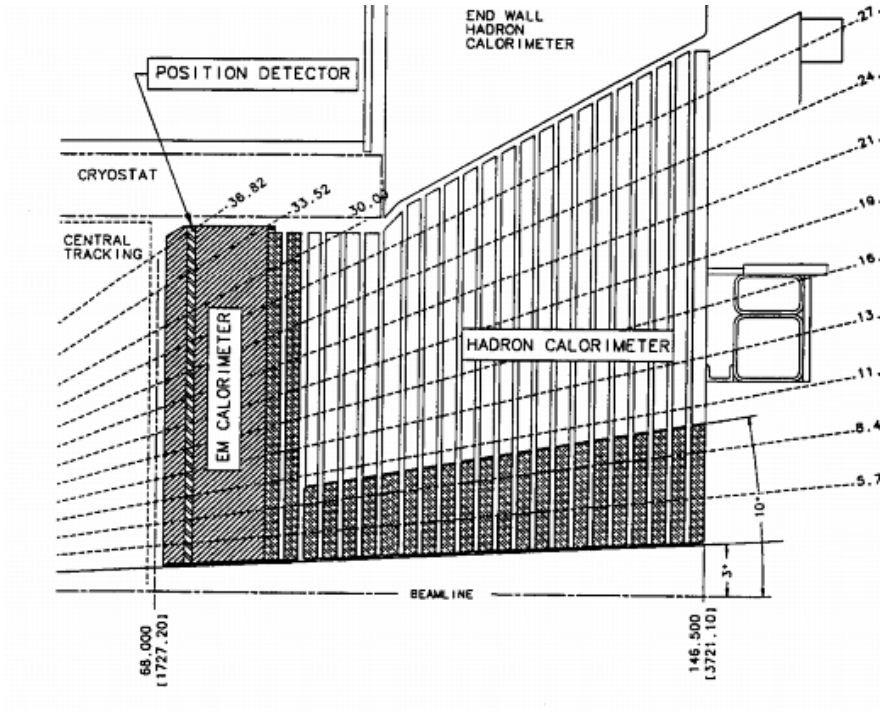

Figure 3-4: The R-z cross section view of new end plug calorimeter.

The PEM calorimeter is a lead/scintillator sampling type, with unit layers composed of 0.4 cm scintillator and 0.45 cm lead. The energy resolution of the detector is $16\%/\sqrt{E} \oplus 1\%$. It also includes a shower maximum detector (PES), at about 6 radiation length depth, made of 0.5 cm pitch scintillator strips and arranged in two layers. They are aligned at $+22.5°$ and $-22.5°$ with respect to radial dimension, to provide a two-dimensional position measurement.

The PHA is made of 0.6 cm thick scintillator layers and 5 cm thick iron layers and follows electromagnetic section.

3.2.2 Tracking System

An integrated tracking system at CDF is used for the reconstruction of trajectories of charged particles and their momenta, the reconstruction of the primary interaction vertex and for particle identification through the measurement of energy loss due to ionization (ionization density dE/dx). The CDF Run II integrated

tracking system builds on the success of the Run I system, which provided excellent particle momentum resolution and precise measurement of the track impact parameter, the distance of the closest approach to the nominal interaction point. The combination of those measurements allowes the identification of the secondary vertices in the jets and thus heavy flavor tagging. Since charm and bottom quarks have a long lifetime (for example, $c\tau = 317$ μm for the $D^{\pm}$ meson) compared to the light quarks, the average decay length will be relatively long. That will manifest as secondary vertices displaced as much as several hundred microns on average from the primary interaction vertex.

The charged-particle tracking system consists of a superconducting solenoid, multi-layer silicon detectors and a large open-cell drift chamber.

For the region $|\eta| < 1$, the combination of the silicon detectors and the Central Outer Tracker (COT) provide full 3D-track reconstruction. Because the tracking efficiency from the COT is reduced for $|\eta| > 1$, CDF relies on stand-alone silicon tracking for the region $1 < |\eta| < 2$. A diagram of the CDF integrated tracking system and its pseudorapidity coverage is shown on Figure 3-5.

The Solenoid. The tracking system resides inside a superconducting solenoid magnet, which produces a uniform 1.4 T magnetic field oriented along the z-axis in the tracking volume. The coil is 3 m in diameter and 5 m long. In addition to the precise momentum measurement, it allows to determine the sign of charged particles.

Silicon Detectors. The CDF silicon microstrip vertex detector consist of three separate subdetectors: Layer 00 (L00), Silicon Vertex Detector (SVX) and Intermediate Silicon Layers (ISL).

The silicon microstrip detectors are typically built of thin silicon wafers, with polarized p-n junctions. The surface of the wafers could be segmented into p^+ (or in case of two-sided silicon wafer n^+) strips, which are read out through implanted

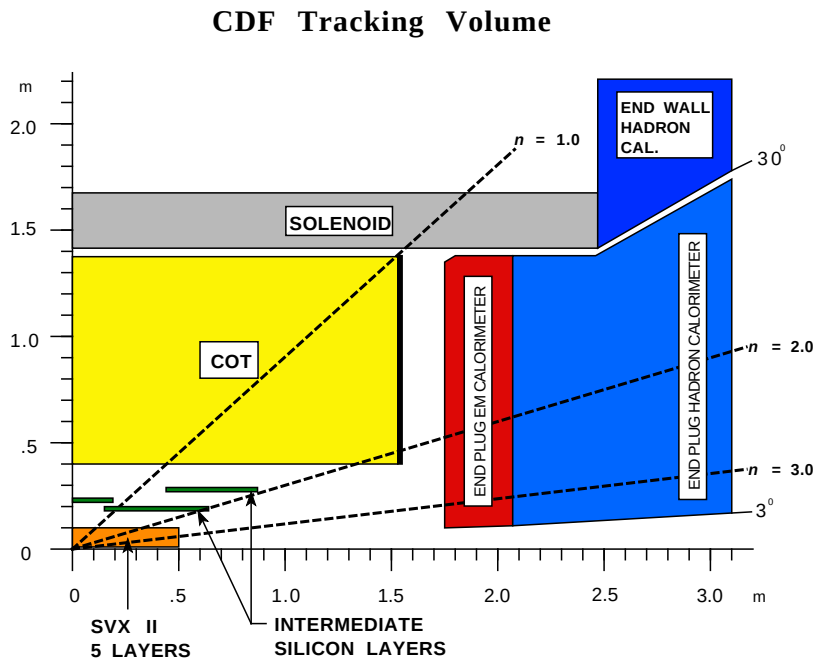

Figure 3-5: Longitudinal view of the CDF tracking volume. Coverage in pseudorapidity is shown for different tracking subsystems.

closely-spaced conducting strips. A reversed bias voltage depletes the bulk material from charge carriers. When a charged particle passes through the silicon layer it can create electron-hole pairs, which then drift and accumulate on the conducting strips, providing the position measurement along the axis perpendicular to the strips. In case of the double-sided silicon microstrip detector one side could be used for the charged particle position measurement in r-ϕ plane and the other in r-z.

Layer 00. The innermost layer of the silicon tracking system is Layer 00, which consists of a single-sided layer of radiation hard silicon mounted directly onto the beam pipe [56]. L00 has a strip separation of 25 μm and a 50 μm readout pitch. It serves two purposes: first, it improves the impact parameter resolution, especially for low momentum particles whose impact parameter resolution is degraded due to multiple scattering in the readout electronics and other support material of the detector. The second purpose is to extend the lifetime of the silicon tracking

system, since the performance of the inner layers of SVX is expected to degrade due to radiation damage.

Silicon Vertex Detector. The Silicon Vertex Detector, shown on Figure 3-6, is segmented into three barrels along the z-axis, with a total length of 96 cm. It is placed outside of the Layer 00 between the radii of 2.4 and 10.7 cm. Each barrel is divided into 12 wedges in ϕ, that support five layers of silicon microstrip detectors (Fig 3-6). All layers in the SVX are double-sided. One side in all layers is used to measure the position in r-ϕ. Three of the layers have a 90° stereo measurement on the other side, of three of the layers have a 90° stereo measurement, and the remaining two layers have small angle(1.2°) stereo. Custom designed chips that are placed on the surface of the silicon detectors read out the strips. The chips preamplify and digitize the signal. There are total of the 405,504 channels in the system.

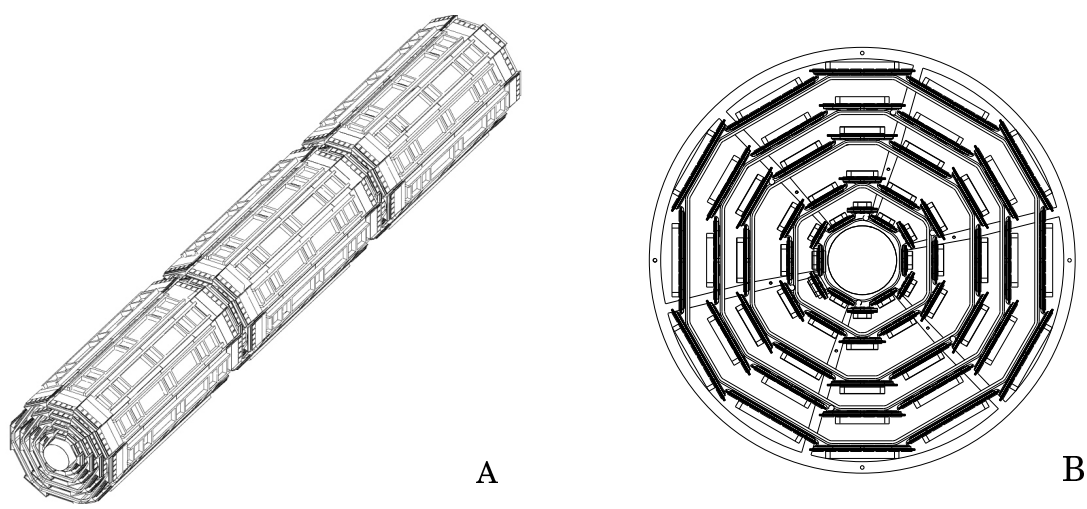

Figure 3-6: The CDF Silicon Vertex Detector. A) An isometric view of the three-barrel structure of SVX is shown. B) An end-view shows 5 layers of silicon divided into 12 wedges.

Intermediate Silicon Layers. The Intermediate Silicon Layers (ISL) include 3 layers of double-sided silicon with axial and small-angle stereo sides. They are placed just outside the SVX in radius. In central the region, $|\eta| < 1$, there is only

one layer at the radius of 22 cm. In the forward region ($|\eta| < 2$), where there is no COT coverage, it consists of two layers placed at radii 20 and 28 cm.

Central Outer Tracker. The big open cell drift chamber, the Central Outer Tracker, provides tracking in the central region at large radii, covering radii between 44 and 132 cm. It consists of 4 axial and 4 small angle ($\pm 3°$) stereo super-layers, providing charged-particle track position measurement in the r-ϕ and z planes respectively. Figure 3-7 shows an end-view of the COT detector with a layout of eight super-layers. Each super-layer, in turn, is divided in ϕ into separate cells. Such basic cell contains 12 sense wires (used for signal read out), alternating with potential wires; thus there are a total of 96 possible measurements per track. Figure 3-7 shows a diagram with layout of potential and sense wires. In axial layers the sense wires are parallel to the z-axis, whereas in stereo layers sense wires are tilted. The COT is filled with a mixture of gases $\mathrm{Ar} - \mathrm{Et} - \mathrm{CF}_4$ (50:35:15), which has a drift velocity of ~ 100 μm/ns. Charged particles passing through the gas ionize it. Free electrons drift to the sense wires, resulting in an avalanche at the wire surface. The position of the track is calculated from the sense wire position and drift velocity of electrons. Because of the crossed electric and magnetic fields in the drift regions, electrons will drift at a Lorentz angle of $\approx 35°$ with respect to the electric field. Thus, the cells are tilted by this amount with respect to the radial direction to provide a uniform readout time. The resolution on the track curvature is 0.68×10^{-4} cm^{-1}, which corresponds to a momentum resolution of $\delta p_{\mathrm{T}}/p_{\mathrm{T}}^2 \simeq 0.3\%(\mathrm{GeV}/c)^{-1}$ [52].

3.2.3 Muon Detectors

The muon detectors are located furthest from the interaction point. There are four systems of scintillators and proportional chambers that are used for the muon detection at CDF and that cover the region up to $|\eta| < 2$. The Run II upgrade

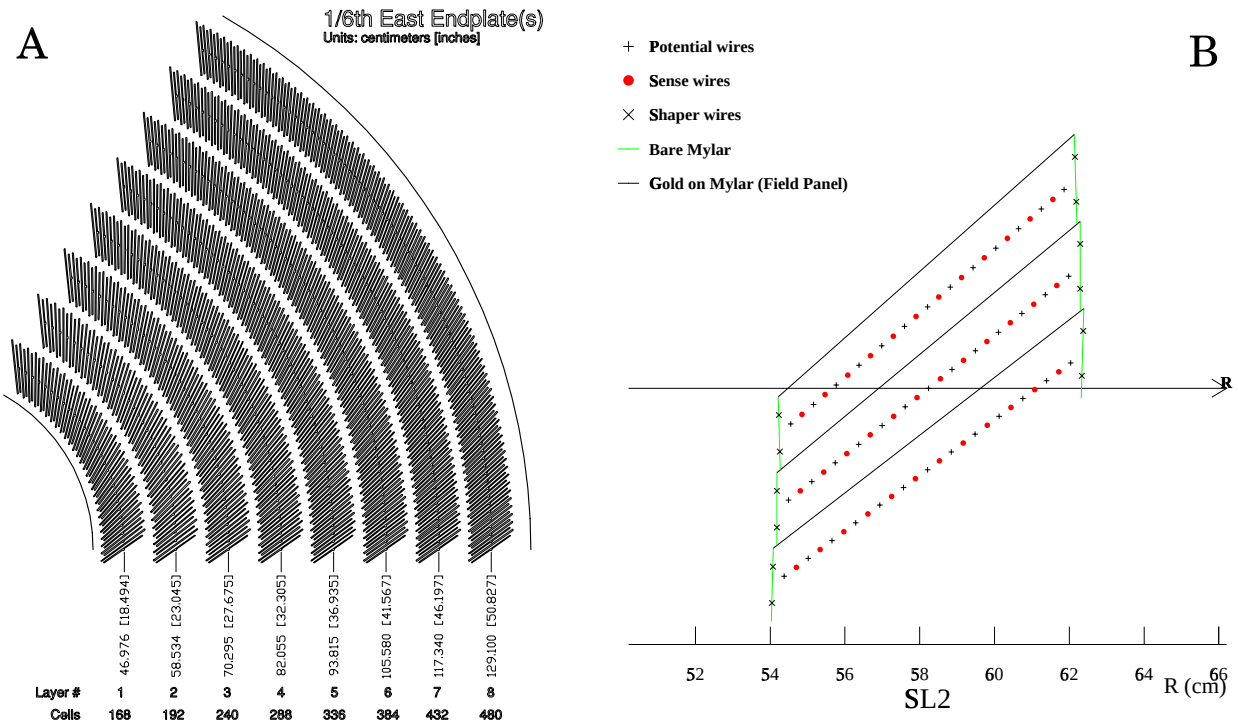

Figure 3-7: The Central Outer Tracker. A) one sixth of the detector is shown in end-view; odd-numbered superlayers are small-angle stereo layers and even-numbered superlayers are axial. B) the details of one cell of the detector is shown with layout of potential and sense wires.

closed the gaps in the solid angle for the existed systems in the central region. The Run I muon detectors were completely replaced in the forward region.

The central muon detector includes three subsystems : Central Muon Detector (CMU), Central Muon Upgrade (CMP) and Central Muon Extension (CMX). The central calorimeter and return yoke of the magnet serve as the hadron absorber for these systems. An additional layer of 60 cm of steel is placed in front of the CMP. Figure 3-8 shows the fiducial region in the solid angle for the central part of CDF. The intermediate angle muon system (IMU) identifies muons over a pseudorapidity range 1—1.5 using a 4-layer barrel made of drift tubes (BMU) and scintillators (WSU, BSU, TSU).

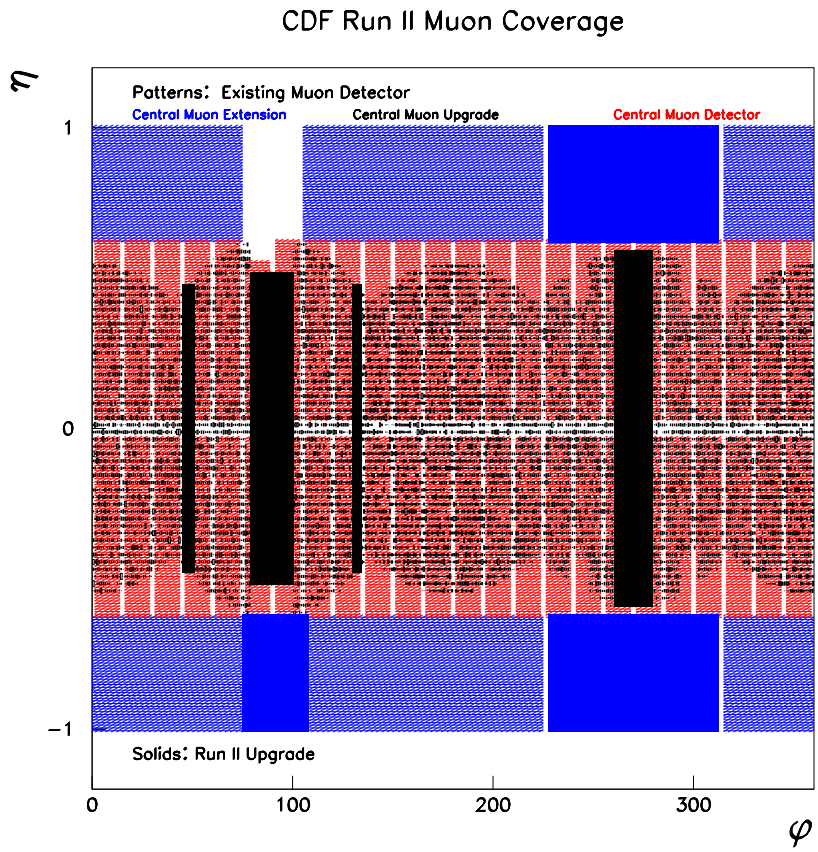

Figure 3-8: CDF II map of the central muon system coverage in η-ϕ plane. The hatched region shows the Run I detector and the solid region shows the solid angle coverage added for Run II.

3.2.4 Trigger System and Data Acquisition

The Tevatron Run II bunch spacing is 396 ns, which corresponds to a 1.7 MHz bunch-crossing rate. At a typical luminosity of 4×10^{31} cm^{-2}sec^{-1}, about 1 $p\bar{p}$ interaction occurs at CDF per bunch crossing on average. With a typical event size of 250 kB, the data acquisition system would have to record 435 GB of data per second. Most of $p\bar{p}$ collisions represent "minimum bias" events, events where $p\bar{p}$ inelastic scattering occurs with no significant energy flow in the direction transverse to the incoming particle direction. For example, such events occur six orders of magnitude more frequently than the processes of creation of W or Z bosons. Therefore, the detector has to be able to identify and retain sufficiently

interesting events from a million collisions per second for further analysis, while rejecting by about a factor of 10^5 of the less interesting collisions. This is achieved through a 3-tier trigger architecture. Each stage is designed in such a way as to provide a sufficient reduction in the rate and to allow for processing in the next level with minimal deadtime. The trigger must have a large rejection factor, but at the same time be highly efficient for a broad range of physics topics studied at CDF.

Figure 3-9 shows the functional block diagram of the data flow and figure 3-10 shows the block diagram of the first two levels of the trigger system. The

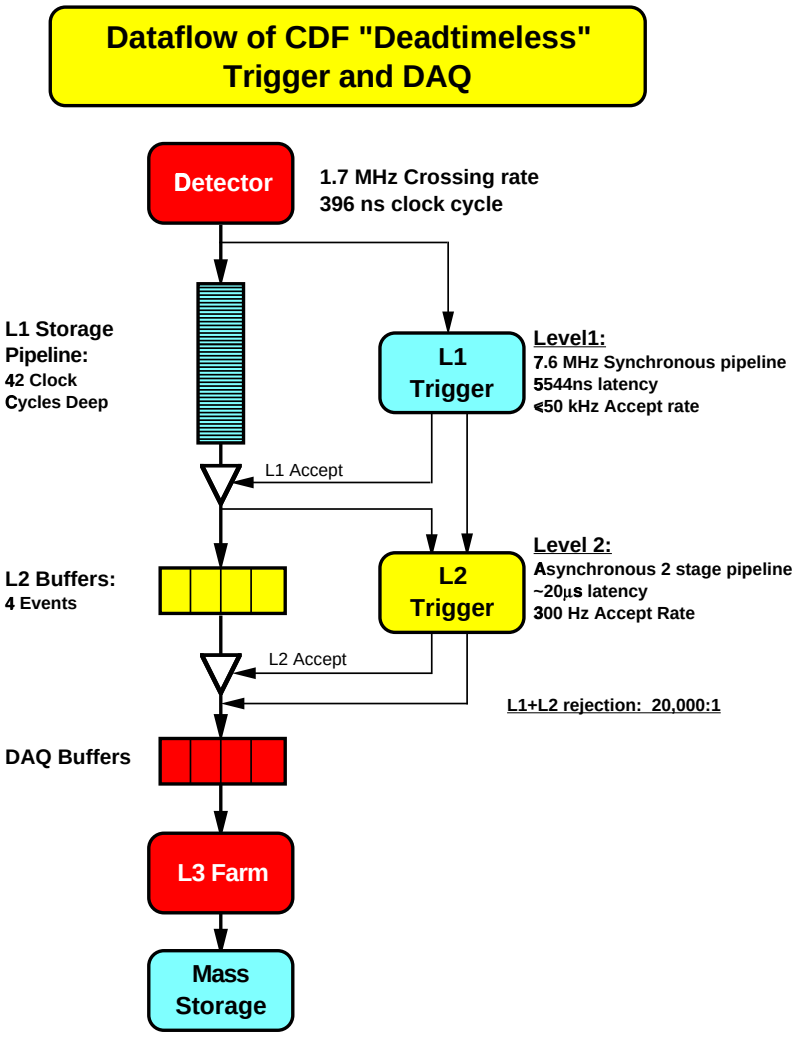

Figure 3-9: The CDF II data flow.

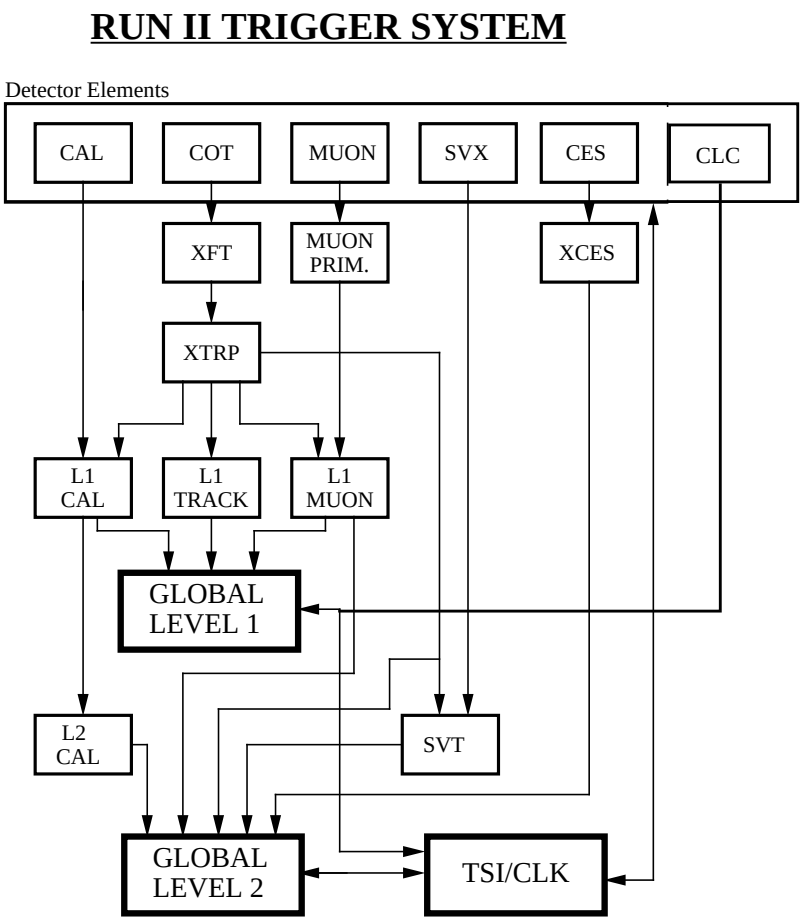

Figure 3-10: The CDF II L1/L2 trigger systems.

Level-1 (L1) and Level-2 (L2) trigger systems use only a subset of the data from an event to make a decision on whether to hold the event for subsequent processing or to reject it. The Level-1 and Level-2 trigger use custom hardware to do a limited event reconstruction, whereas Level-3 (L3) uses full event information and offline-like reconstruction software to make a final decision to write it on tape.

Data from the calorimeter, central tracking chamber, muon systems and Cherenkov Luminosity Counters (CLC) are sent to the L1 trigger system, which decides whether the event is interesting enough to hold it for Level-2. Level-1 is a deadtimeless synchronous electronic system, with a pipeline of 42 clock cycles

(at 132 ns clock). In Run II, CDF has the ability to reconstruct high p_{T} tracks by means of the Extremely Fast Tracker (XFT) [57] at L1, so its results can be used for the L1 trigger decision. The L1 trigger acceptance rate for the initial period of Run II was < 20 kHz.

Events accepted by the L1 trigger are moved to L2 system. All of the information used in the L1 decision is available at L2. The second level trigger is an asynchronous system composed of custom computing processors and uses 4 buffers to store an event information. Each buffer contains one event. The buffer is unavailable for an additional L1 accepts while L2 analyses the information. Therefore, if all buffers are full, the trigger incurs dead time, which is recorded during the run. The average decision time is about 25 μsec. The overall Level-2 acceptance rate is less than 300 Hz. The main limitations on the trigger bandwidth at the Level-2 are the silicon detector data readout and the relatively slow processing speed at Level-3.

For the first time in hadron-collider experiments, CDF implemented a trigger system — the Silicon Vertex Tracker (SVT) — that provides the capability to trigger on tracks with large impact parameters (typical threshold of > 100 μm). This enables one to collect large event samples enriched in heavy-quark content, the key for many new physics searches.

The Level-3 system consists of a farm of commercial CPUs running a version of the full reconstruction software as it is used offline. After an event is reconstructed, it is passed through a set of filters that decides whether the event should be sent for storage on tape based on the complete event information and the full resolution of the detector. The maximum output rate of L3 at present is 75 Hz. The main limitation is due to the low data-logging rate, with a typical value of 18 MB/s, but which also depends on the size of the event.

3.3 The Cherenkov Luminosity Monitor

The Cherenkov Luminosity Counters (CLC) are used at CDF in Run II to measure the luminosity. They allow a precise luminosity measurement at peak instantaneous luminosities up to 2×10^{32} cm^{-2}s^{-1}, corresponding to an average of six $p\bar{p}$ interactions per bunch crossing.

The detector consists of two modules which are located within the "3-degree holes" inside the forward and backward CDF plug calorimeters and covers the pseudorapidity range of $3.75 < |\eta| < 4.75$ (see Fig. 3-11). Each CLC detector

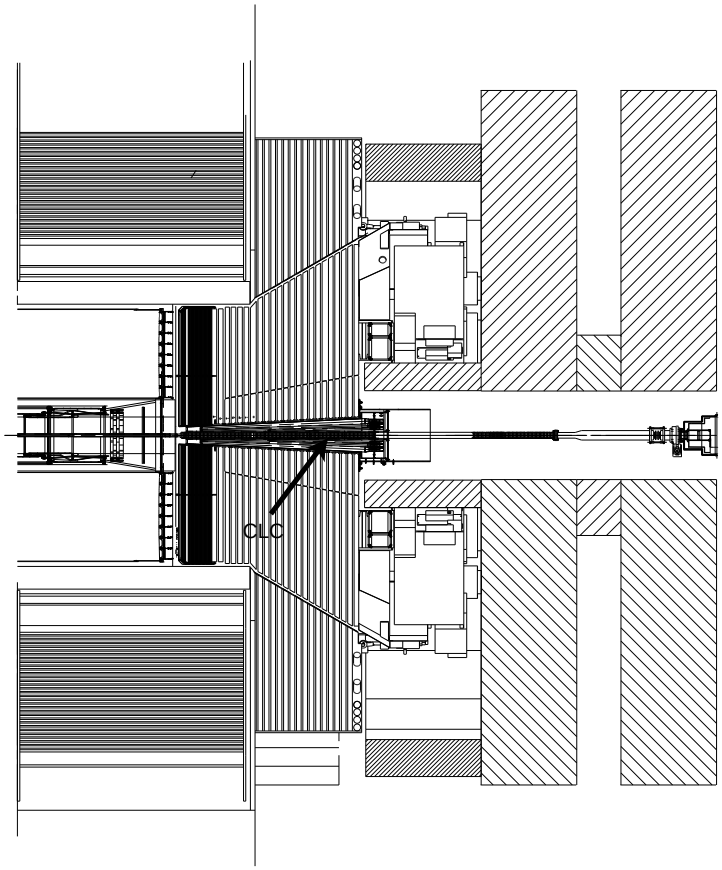

Figure 3-11: The Cherenkov Luminosity Counters in CDF.

module consists of 48 thin, long, gas-filled Cherenkov counters. These counters are arranged around the beam-pipe in three concentric layers, with 16 counters in each layer, and pointing to the center of the interaction region (see Fig. 3-12). They

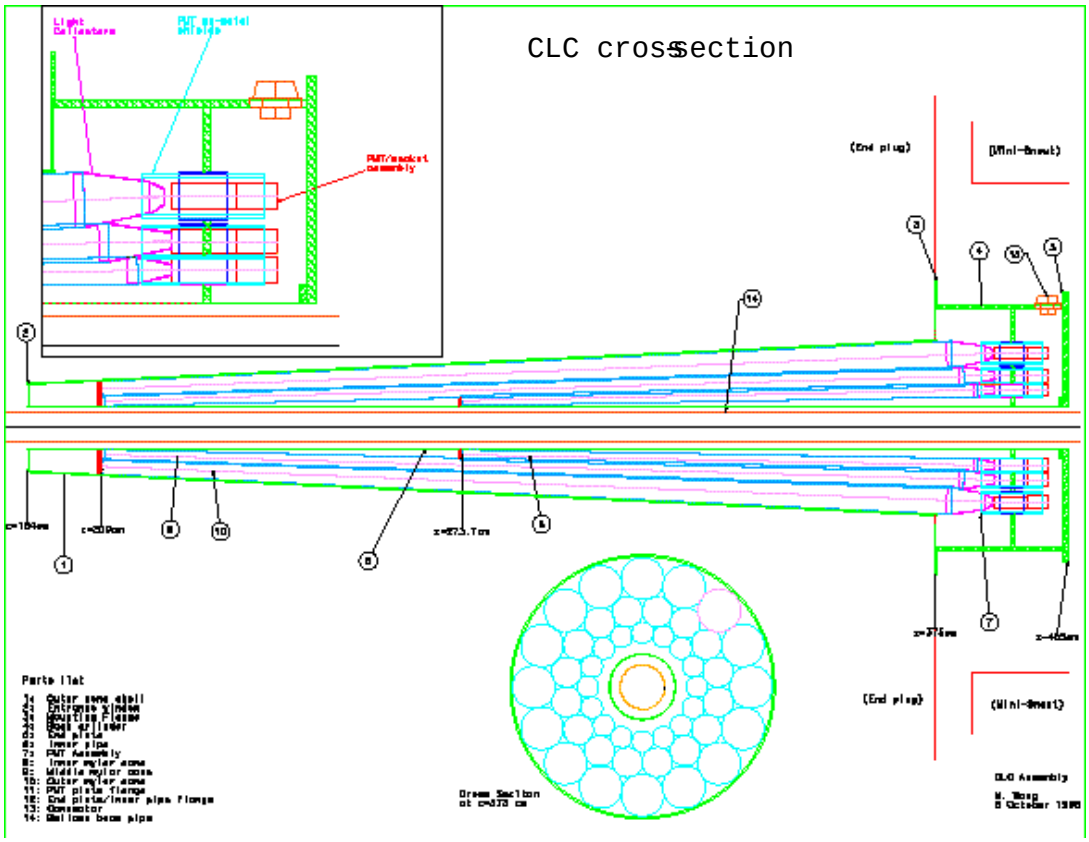

Figure 3-12: The Assembly drawing for one module of the CDF Cherenkov Luminosity Counters.

are built with reflective aluminized mylar sheets 0.1 mm thick and have a conical shape. The cones in two outer layers (furtherest away from the beam pipe) are about 180 cm long and the inner layer counters have length of 110 cm. The whole assembly is mounted inside a thin pressure vessel made of aluminum and filled with isobutane at 1.5 times the atmospheric pressure.

When a charged particle travels faster than the speed of light in a certain medium (i.e. $\beta = v/c > 1/n$, where n is the index of refraction of the medium) it emits Cherenkov radiation. This radiation is emitted at a Cherenkov angle $\theta_{\mathrm{C}} = \arccos(1/n\beta)$, with respect to the particle direction.

The isobutane is used as a radiator because it has a large index of the refraction (1.002145 at 1.5 atmospheric pressure) and good transparency for photons in

the ultra-violet part of spectra, where most of the Cherenkov light is radiated. The Cherenkov angle is 3.1° and the momentum threshold for Cherenkov emission is 9.3 MeV/c for electrons and 2.6 GeV/c for pions. The Cherenkov light is detected with fast, 2.5 cm diameter, photomultiplier tubes (Hamamatsu R5800Q). The tubes have a concave–convex, 1 mm thick, quartz window for efficient collection of ultra-violet part of Cherenkov spectra and operate at a gain of 1.5×10^5. Figure 3-13 shows the large light yield ($\sim$ 130 photoelectrons) for relativistic particles from $p\bar{p}$ collisions, traversing the full length of the counters. The CLC simulation is

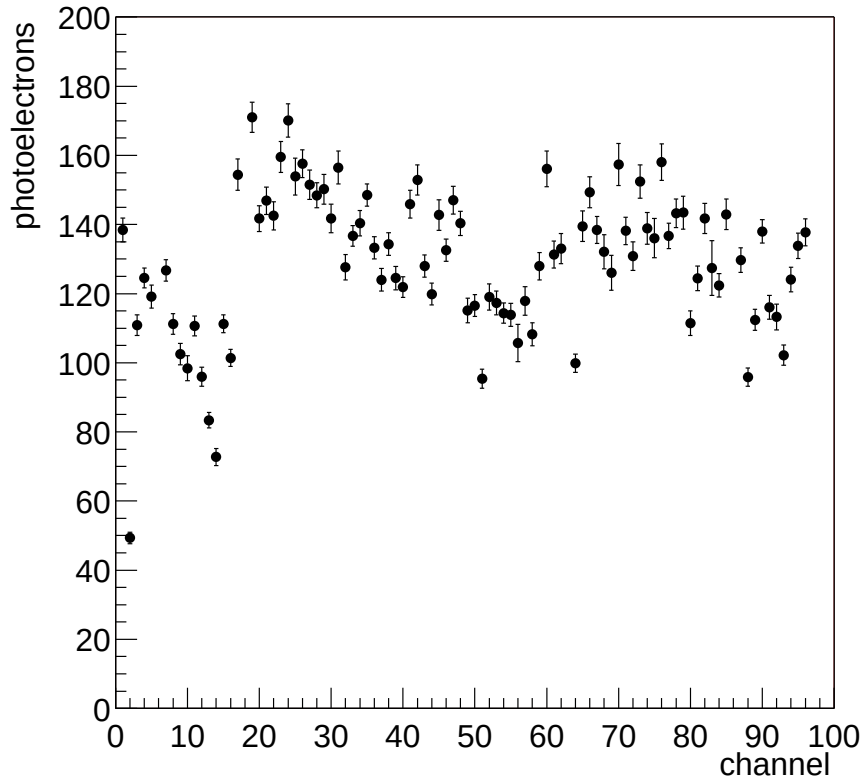

Figure 3-13: Number of photoelectrons produced by single particles traversing the full length of the CLC counters measured for all 96 counters.

based on the GEANT detector simulation program [58] and is an integral part of the CDF detector simulation program. It simulates Cherenkov photon radiation,

transports particles through the detector material, and simulates the PMT response and signal digitization [59, 60].

Particles coming directly from the $p\bar{p}$ interaction (primary particles) typically traverse the full length of a counter and generate a large amplitude PMT signal. Particles due to secondary interactions of particles in the detector material surrounding the CLC and beam-pipe, or particles coming from beam-halo interactions (secondary particles) traverse the counters at large angles, thus with shorter path lengths, and the Cherenkov photons from those particles suffer a larger number of the reflections. Therefore, the signal due to secondary particles is significantly smaller than that of primaries. Figure 3-14 shows the simulated amplitude distribution for a particle from minimum bias $p\bar{p}$ interactions in a Cherenkov counter (some of the passive detector material in front of the detector was not included in the simulation). Figure 3-15 shows the distribution of amplitudes in the counters normalized to single particle peak from $p\bar{p}$ collisions in data and in the full simulation of the detector, using the MBR event generator [61]. MBR is a CDF minimum bias event generator that includes diffractive processes and that has been tuned to reproduce CDF data. The distribution of amplitudes in the counters does not show a clear single particle peak, which is due to a considerable number of secondary particles coming from electromagnetic showers in the beam-pipe and vertex detector material. To suppress the showers and observe the single particle peak, an isolation cut is used which requires that amplitudes in the counters around a selected counter are less than 20 photoelectrons. Figure 3-16 shows the amplitude distribution for one of the CLC counters after applying such an isolation cut. The CLC is calibrated by measuring the mean single particle peak (SPP) for each individual counter. The width (rms) of the single particle peak is determined by the photoelectron statistics, light collection uniformity and the amplitude resolution of the photomultipliers. Figure 3-17 shows the average number of counters (hits)

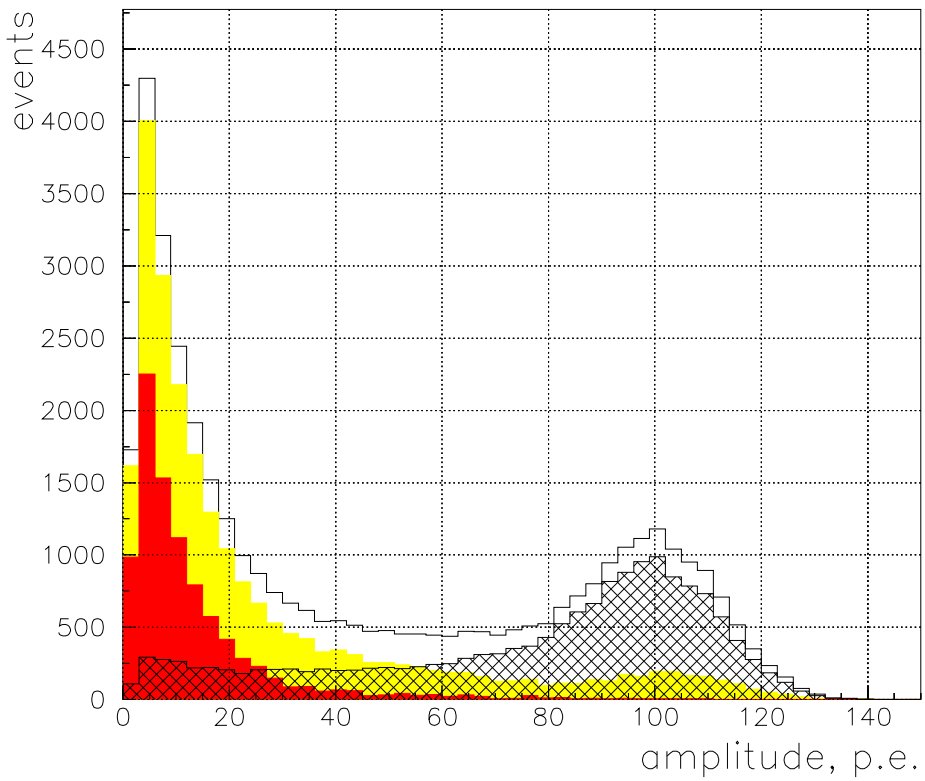

Figure 3-14: Simulated amplitude distribution for a particle from minimum bias $p\bar{p}$ interactions in the Cherenkov counter. The solid line corresponds to all particles and the hatched histogram corresponds to the primary particles. The yellow histogram is the contribution from all secondary particles and the contribution from the plug calorimeter is shown in the red histogram.

hit by particles from the $p\bar{p}$ collision in the two CLC modules as a function of the amplitude threshold used to count hits expressed in the single particle peak units.

The CLC detector is also used to provide a minimum bias trigger at CDF [62].

3.4 Luminosity Measurement

Since October 2000, the CLC has been consistently providing luminosity measurement for CDF and the Tevatron.

The total rate of $p\bar{p}$ interactions is given by:

$$\mu \cdot f_{BC} = \sigma_{tot} \cdot \mathcal{L}, \tag{3-3}$$

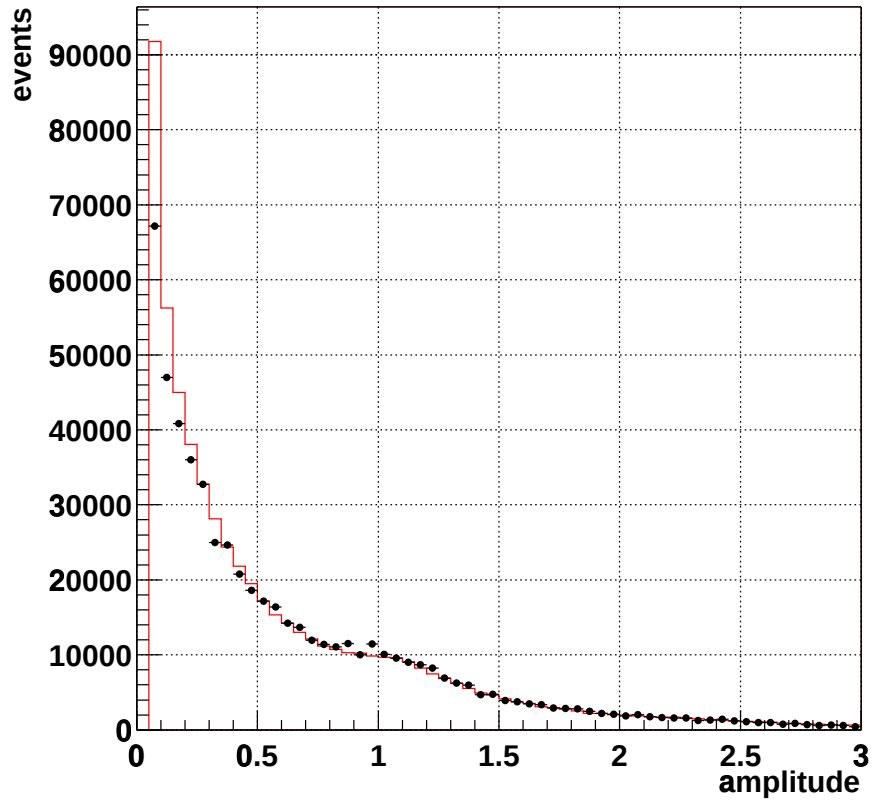

Figure 3-15: Amplitude distribution of Cherenkov counters normalized to single particle peak from $p\bar{p}$ collisions: solid histogram is data, dots are simulation.

where the σ_{tot} is the total $p\bar{p}$ cross-section at $\sqrt{s} = 1.96$ TeV, $\mathcal{L}$ is the instantaneous luminosity, f_{BC} is the rate of bunch crossings in the Tevatron, and μ is the average number of $p\bar{p}$ interactions in one crossing. Therefore, we need to measure the average number of interactions per bunch crossing in order to measure the luminosity.

3.4.1 The CLC Acceptance

Inelastic $p\bar{p}$ interactions that satisfy some selection criteria α to be registered in the CLC, have an effective cross-section σ_α. The CLC has zero acceptance for elastic $p\bar{p}$ interactions. The average number of inelastic interactions per bunch crossing, μ_α, satisfies

$$\mu_\alpha \cdot f_{BC} = \sigma_\alpha(\mu) \cdot \mathcal{L}, \tag{3-4}$$

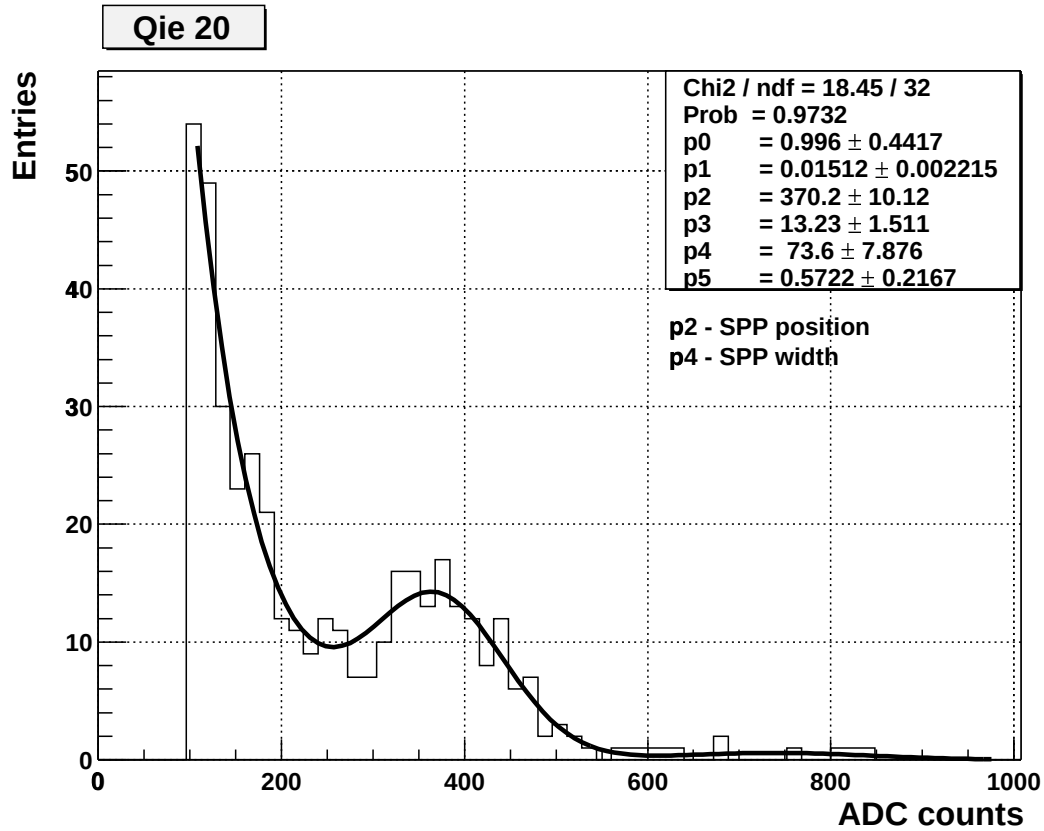

Figure 3-16: Amplitude distribution for one of the Cherenkov counters from $p\bar{p}$ collisions after an isolation cut: solid histogram is data, smooth curve is fit. One photo electron corresponds approximately to 4 ADC counts.

with

$$\sigma_\alpha(\mu) = \sigma_{\rm in}\epsilon_\alpha(\mu), \tag{3-5}$$

where $\epsilon_\alpha(\mu)$ is the probability to register a $p\bar{p}$ interaction in the CLC. For low luminosity ($\mu \to 0$), it is expected that $\epsilon_\alpha(\mu \to 0) = \epsilon_\alpha$, where ϵ_α is the CLC acceptance to a single inelastic $p\bar{p}$ interaction. The acceptance ϵ_α can be factorized as

$$\epsilon_\alpha = \frac{\epsilon_\alpha^{\rm h}\sigma_{\rm h} + \epsilon_\alpha^{\rm sd}\sigma_{\rm sd} + \epsilon_\alpha^{\rm dd}\sigma_{\rm dd}}{\sigma_{\rm in}}, \tag{3-6}$$

with

$$\sigma_{\rm in} = \sigma_{\rm h} + \sigma_{\rm sd} + \sigma_{\rm dd}, \tag{3-7}$$

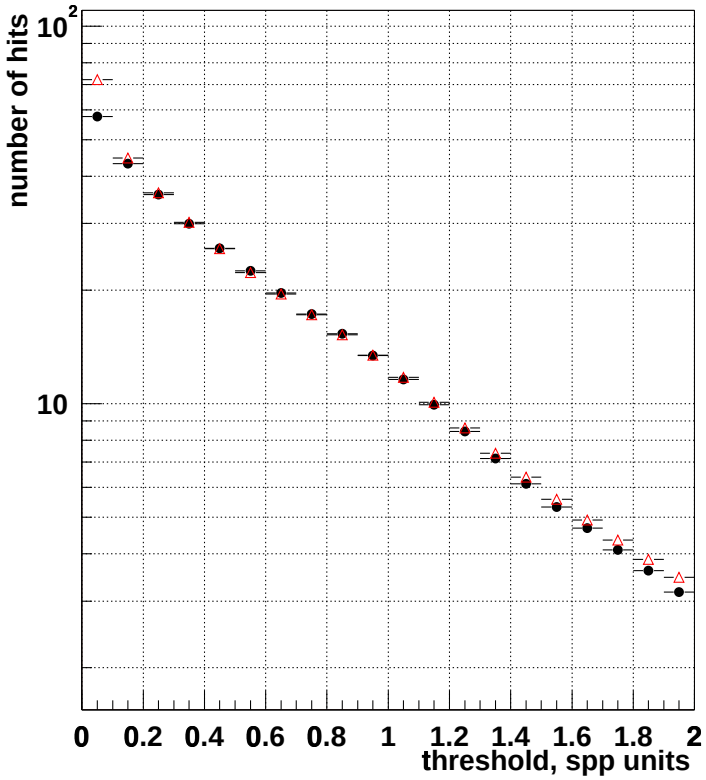

Figure 3-17: Average number of counters hit in the $p\bar{p}$ collision in the two CLC modules as a function of the amplitude threshold: open triangles are data; dots are simulation.

where $\sigma_{\rm h}$, $\sigma_{\rm sd}$, $\sigma_{\rm dd}$ are the hard core, single diffractive and double diffractive inelastic cross sections, respectively, and $\epsilon_\alpha^{\rm h}$, $\epsilon_\alpha^{\rm sd}$, $\epsilon_\alpha^{\rm dd}$ are their acceptances in the CLC. The $p\bar{p}$ cross sections for various inelastic process at $\sqrt{s} = 1.96$ GeV are listed in Table 3-2 as reported by the MBR generator.

Table 3-2: The $p\bar{p}$ cross section for various inelastic processes at $\sqrt{s} = 1.96$ GeV at the Tevatron.

	$\sigma_{\rm h}$	$\sigma_{\rm dd}$	$\sigma_{\rm sd}$	$\sigma_{\rm in}$
Cross Section (mb)	44.54 ± 1.3	10.30 ± 0.50	7.0 ± 0.5	61.8 ± 1.4

The CLC is most sensitive to the hard core $p\bar{p}$ interactions, with small contributions from diffractive processes, especially when an East-West coincidence

($\epsilon_{\rm EW}$) is required. Two methods are used to estimate the CLC acceptance to inelastic $p\bar{p}$ interactions. One method relys on CLC Monte Carlo simulation only, whereas the other uses a "reference detector" with an acceptance for hard core events close to 100%. In the latter method, we measure the ratio R of $p\bar{p}$ events detected in the CLC to those detected in the reference detector, then we have $\epsilon_\alpha = \epsilon_r R$, where ϵ_r is the acceptance of the reference detector. Using the CLC and the CDF plug calorimeters as a reference detector the combined acceptance for hard core interactions is about 97%, from simulation. We define a coincidence of the East and West detectors (EW) by requiring at least one counter in each CLC module with amplitude above a threshold of 0.5 single particle peak and the total energy in each plug above 3 GeV. Table 3-3 shows the acceptances for the different inelastic processes calculated using the MBR generator for the CLC only and CLC plus plug calorimeter. The CLC acceptance is most sensitive to the accurate modeling of $p\bar{p}$ interactions and the detector material.

Table 3-3: Acceptances for CLC and CLC plus plug detectors calculated for different inelastic processes. Only statistical errors are shown.

Method	$\epsilon^{\rm h}_{\rm EW}$ (%)	$\epsilon^{\rm dd}_{\rm EW}$ (%)	$\epsilon^{\rm sd}_{\rm EW}$ (%)	$\epsilon^{\rm tot}_{\rm EW}$ (%)
CLC only	88.6 ± 0.5	31.8 ± 0.7	9.1 ± 4	69.6 ± 0.2
CLC + plug	97.3 ± 0.2	44.7 ± 0.7	20.5 ± 0.6	79.3 ± 0.2

3.4.2 Counting of Empty Bunch Crossings

The number of $p\bar{p}$ interactions (n) in a bunch crossing follows Poisson statistics with mean μ:

$$\mathcal{P}_n(\mu) = \frac{\mu^n e^{-\mu}}{n!}. \tag{3-8}$$

Bunch crossings with $n = 0$ are empty and the probability of such , from simulation,empty crossings is:

$$\mathcal{P}_0(\mu) = e^{-\mu}. \tag{3-9}$$

By measuring the fraction of empty crossings we can find μ and thus the luminosity:

$$\mathcal{L} = \frac{f_{\mathrm{BC}}}{\epsilon_\alpha(\mu)\sigma_{\mathrm{in}}} \cdot \mu. \tag{3-10}$$

The determination of whether a bunch crossing is empty or not depends on the CLC selection criteria. We therefore define, the experimental probability of zero interactions ($\mathcal{P}_0^{\mathrm{exp}}$) to be a coincidence of two CLC modules. For a single $p\bar{p}$ inelastic interaction, we define:

- ϵ_0 — the probability to have no hits in either East or West CLC modules.
- ϵ_{E} — the probability to have at least one hit exclusively in the East module.
- ϵ_{W} — the probability to have at least one hit exclusively in the West module.

Then the probability, $\pi_0(k)$ to observe an empty crossing if there were k interactions in a bunch crossing is given by:

$$\pi_0(k) = (\epsilon_0 + \epsilon_{\mathrm{W}})^k + (\epsilon_0 + \epsilon_{\mathrm{E}})^k - (\epsilon_0)^k \tag{3-11}$$

The probability to detect an empty interaction when the average number of total $p\bar{p}$ interactions is μ can be obtained by summing over the Poisson distribution with mean μ but with weights given by Eqn. 3-11:

$$P_0^{\mathrm{exp}}(\mu) = \sum_{k=0}^{\infty} \mathcal{P}_k(\mu) \cdot \pi_0(k) = (e^{\epsilon_{\mathrm{E}}\mu} + e^{\epsilon_{\mathrm{W}}\mu} - 1) \cdot e^{-(1-\epsilon_0)\mu}. \tag{3-12}$$

Assuming that two CLC modules are identical, the experimental probability for a coincidence of two CLC modules to see an empty crossing reduces to:

$$P_0^{\mathrm{exp}}(\mu) = (2e^{\epsilon_1\mu} - 1) \cdot e^{-(1-\epsilon_0)\mu}, \tag{3-13}$$

where ϵ_1 is the probability to detect at least one hit exclusively in one module. In the low luminosity approximation, when $\mu \to 0$, we obtain:

$$P_0^{\mathrm{exp}}(\mu) = e^{-\epsilon_{\mathrm{EW}}\mu}, \tag{3-14}$$

where ϵ_{EW} is the CLC acceptance with East-West coincidence. The advantage of the empty bunch-crossing counting method is weak dependence of CLC acceptance to inelastic $p\bar{p}$ interactions on the counter amplitude threshold. The disadvantage is a very small probability of empty crossings at high luminosity, which becomes difficult to measure with precision due to the pile-up of multiple $p\bar{p}$ interactions (uncertainty in the acceptance is as large as the empty bunch crossings probability) and beam losses.

The luminosity is calculated on-line in a commercial CPU board running custom-designed program. A look-up table is used to measure the average number of interactions from the Eqn. 3-12 from the experimentally measured probability for a coincidence of two CLC modules. The signals from the CLC detector are digitized in ADMEM boards, and the number of hits is counted in each module (only 2 outer layers in each module are used online). A hit is counted if the signal in a counter is above a fixed, pre-set threshold (250 ADC counts). A collision is defined as a coincidence of one or more hits registered in both modules. The CLC acceptance for this 2 layer collision definition is $\epsilon_{\mathrm{EW}} = 0.602 \pm 0.024$. The probability to have zero hits in both CLC modules and the probabilities to have hits exclusively in one module are given in Table 3-4. We use 60.7 ± 2.4 mb for

Table 3-4: Probability to have zero hits in both CLC modules (only 2 outer layers in each module are used) and the probabilities to have hits exclusively in one module for inelastic $p\bar{p}$ interactions. Only statistical errors are shown.

	Probability
ϵ_0	0.112 ± 0.004
ϵ_{E}	0.143 ± 0.005
ϵ_{W}	0.147 ± 0.005

the total inelastic cross section at $\sqrt{s} = 1.96$ TeV [63] , which is the average of the two measurements of the total $p\bar{p}$ cross section at Tevatron from CDF [64]

and E811 [65] experiments, and agress with MBR cross section within errors. Figure 3-18 shows the online $p\bar{p}$ luminosity for a typical Tevatron store.

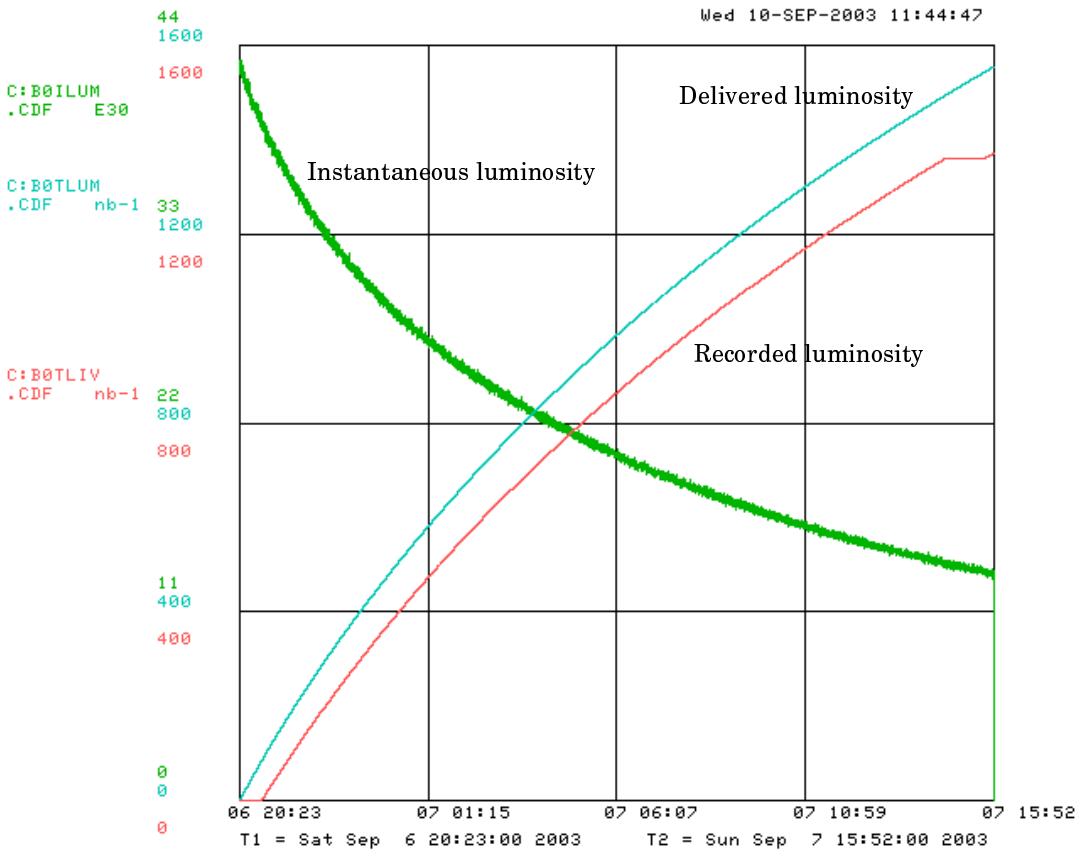

Figure 3-18: Real-time insatantaneous and integrated $p\bar{p}$ luminosities for a typical Tevatron store. Horizontal axis shows time and vertical axis shows instantaneous luminosity in units of 10^{30} cm^{-2} s^{-1} and integrated luminosity in units of nb^{-1}.

The systematic uncertainty of the luminosity measurement (6%) is dominated by the uncertainty on the acceptance ϵ_{EW} (4%) and the uncertainty on the measurement of the total $p\bar{p}$ inelastic cross section (3.9%).

3.4.3 Counting of Hits and Particles

In the Tevatron high luminosity regime up to 2×10^{32} cm^{-2} s^{-1}, where up to 6 $p\bar{p}$ interactions on average are expected per bunch crossing, the CLC hit counting method can be used to measure the luminosity. This method does not suffer from

the very low probability of empty crossings at high luminosity, which becomes very difficult to measure.

For a specific selection criteria α, which defines a collision and threshold on the amplitude of the CLC hits, the average number of $p\bar{p}$ interactions per bunch crossing can be estimated from:

$$\mu_\alpha = \frac{< N_\alpha >}{< N_\alpha^{\mathrm{s}} >}, \tag{3-15}$$

where $< N_\alpha >$ is the measured average number of $p\bar{p}$ collisions per bunch crossing and $< N_\alpha^{\mathrm{s}} >$ is the average number of hits from a single $p\bar{p}$ collision. $< N_\alpha^{\mathrm{s}} >$ can be measured from Monte Carlo simulation or directly from data at low luminosity ($\mu << 1$), when the fraction of multiple interaction in the same bunch crossing is very small. The CLC occupancy grows with luminosity and eventually saturates due to the finite number of counters. Therefore, an accurate measurement of the μ_α non-linearity is required. Figure 3-19 shows the average number of hits as a function of μ, calculated for a coincidence of two CLC modules and an amplitude threshold of 0.5 SPP. We observe an excellent agreement between the data and simulation. In order to construct bunch crossings with large μ for the current data, we have superimposed the counters response from many bunch crossings recorded at low luminosity. At $\mu = 5$ a correction of about 40% is needed to compensate for the non-linearity. Alternatively, we can count the actual number of the particles detected by the CLC. This is done by dividing a counter's amplitude by its SPP value and summing up the normalized amplitude A_p, which passed the selection criteria, over all counters. The number of the particles is proportional to the luminosity. We expect that the A_p does not saturate at high luminosity as it happens for hits. Figure 3-19 shows the total amplitude A_p (particles) as a function of μ. Approximately a 7% correction needs to be applied to the luminosity ($\mu = 5$),

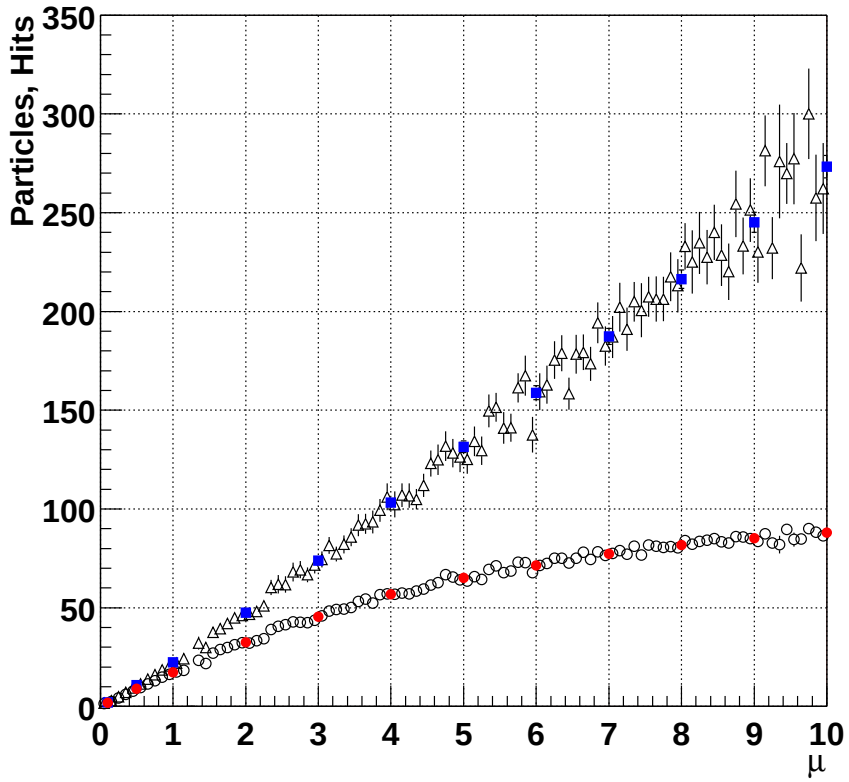

Figure 3-19: The average number of hits in CLC(data: open circles; simulation filled circles) and number of particles reconstructed from the total CLC amplitude (data: open triangles, simulation: filled squares) as a function of μ.

which is much smaller than the equivalent correction for the hit counting method.

This method is thus suitable for use at very high luminosities.

CHAPTER 4
EVENT RECONSTRUCTION

The experimental signature for a leptoquark decaying to a neutrino and quark is large missing transverse energy and several high E_{T} jets. In this chapter, we describe the algorithms and procedures used to reconstruct high-level objects from raw detector information, with emphasis on the missing-E_{T} and jet reconstruction.

4.1 Jets

Partons from the hard scattering produce a collimated cluster of stable particles, called jets. Jets are the product of the fragmentation, or hadronization, of colored partons—quarks or gluinos—into colorless hadrons. Experimentally, a jet is detected as a large energy deposit in a localized area of detector. Figure 4-1 shows a lego plot in $\eta - \phi$ plane of a typical di-jet event as it is interpreted by the CDF event display program. Two peaks on the plot represent the large energy deposition in the calorimeter from the jets.

4.1.1 Jet-Clustering Algorithm

CDF uses an iterative fixed cone algorithm (JETCLU) for jet identification [66]. The cone size R in η-ϕ space is defined by:

$$R = \sqrt{(\Delta\eta)^2 + (\Delta\phi)^2}, \tag{4-1}$$

where $\Delta\eta = \eta_c - \eta_{tow}$ and $\Delta\phi = \phi_c - \phi_{tow}$, with η_c and ϕ_c being pseudorapidity and azimuthal angle of the energy-weighted jet centroid and η_{tow}, ϕ_{tow} being the pseudorapidity and azimuthal angle of the i-th tower belonging to the jet.

The algorithm begins by creating a list of the seed towers from all the calorimeter towers with transverse energy above some fixed threshold (1 GeV). Starting with the highest-E_{T} seed tower, a precluster is formed by combining

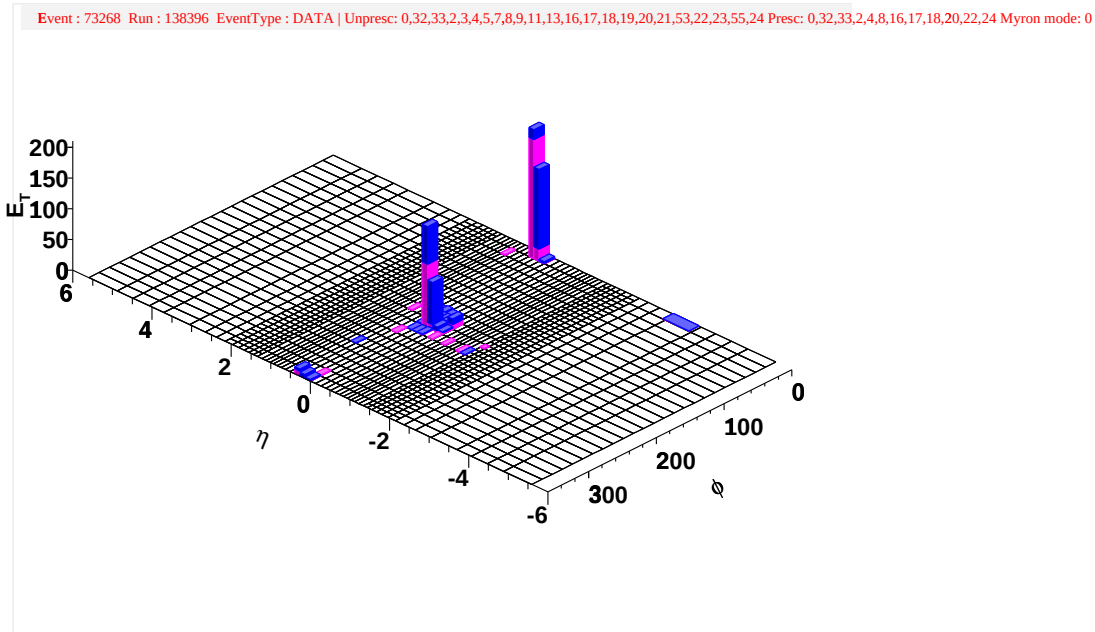

Figure 4-1: The CDF event display of the di-jet event. Two peaks on the plot represent the large energy deposition in the calorimeter from the jets. The height of the peaks is proportional to the energy deposition. The magenta corresponds to electromagnetic energy and blue corresponds to hadronic energy.

together all adjacent seed towers within a cone of radius R. This procedure is repeated, starting with the next unused seed tower, until the list is exhausted. The transverse energy-weighted centroid is then formed from the towers in the precluster and a new cone of radius R is formed around this centroid. All towers with energy above some lower threshold (> 100 MeV) within this new cone are then added to the cluster. Then, a new centroid is calculated from the set of towers within the cluster and a new cone drawn. This process is iterated until a stable solution is found, i.e., until the centroid of the energy deposition within the cone is aligned with the geometric axis of the cone. After all the initial clusters are found, the next step is to merge or separate overlapping clusters, since each tower may belong to only one jet (in reality, particles should not be assigned to more than one jet). Two clusters are merged if the total energy of the overlapping towers is greater than 75% of the energy of the smaller cluster. If the shared energy is

below this cut, the shared towers are assigned to the cluster that is closer in $\eta - \phi$ space. This process is iterated again until the list of clusters remains fixed. The towers in the clusters are assigned massless four-vector momenta separately for electromagnetic and hadronic components. The four-vectors have a magnitude equal to the energy deposited in the tower, and a direction defined by a unit vector pointing from the event vertex to the center of the calorimeter tower at the depth that corresponds to the shower maximum. A cluster four-vector is then defined by summing over the towers in the cluster:

$$E = \sum_{i=1}^{N} (E_i^{em} + E_i^{had}), \tag{4-2}$$

$$p_x = \sum_{i=1}^{N} (E_i^{em} \sin\theta_i^{em} \cos\phi_i^{em} + E_i^{had} \sin\theta_i^{had} \cos\phi_i^{had}), \tag{4-3}$$

$$p_y = \sum_{i=1}^{N} (E_i^{em} \sin\theta_i^{em} \sin\phi_i^{em} + E_i^{had} \sin\theta_i^{had} \sin\phi_i^{had}), \tag{4-4}$$

$$p_z = \sum_{i=1}^{N} (E_i^{em} \cos\theta_i^{em} + E_i^{had} \cos\theta_i^{had}), \tag{4-5}$$

where E_i^{em} (E_i^{had}), ϕ_i^{em} (ϕ_i^{had}) and θ_i^{em} (θ_i^{had}) are the raw jet energy, azimuthal and polar angles respectively for the i-*th* electromagnetic (hadronic) tower in the cluster. The jet transverse energy, pseudorapidity and azimuth angle are given by

$$E_{\mathrm{T}} = E \sin\theta, \qquad \eta = -\ln\tan\left(\frac{\theta}{2}\right), \qquad \phi = \arctan\left(\frac{p_y}{p_x}\right) \tag{4-6}$$

where

$$\theta = \arctan\left(\frac{\sqrt{p_x^2 + p_y^2}}{p_z}\right). \tag{4-7}$$

Jets with cone size of $R = 0.4$ are used in this analysis.

4.1.2 Jet Energy Corrections

The ultimate goal of the jet reconstruction algorithm is to determine the energies of the outgoing partons from the hard interaction. The cone clustering

algorithm gives a raw energy that is different from the energies of the initial partons before the hadronization. There are number of reasons for this difference that could be divided into two categories: instrumental and due to underlying physics processes. The instrumental effects include:

- Particles that shower in boundary regions of the calorimeter (the ϕ boundaries between modules in the central calorimeter and η_{det} boundaries between the two halves of the central calorimeter and between central and plug calorimeters), on average, have a smaller energy reported than for regions of uniform response.
- The calorimeter response is non-linear for low-energy charged pions ($E_{\mathrm{T}} <$ 10 GeV).
- Charged particles with transverse momenta below $\sim$ 400 MeV bend in the magnetic field and do not reach the calorimeter.
- The calorimeter response is changing with time due to radiation damage of the scintillator or aging of the PMTs.
- Intrinsic energy resolution of calorimeter.

The physical effects include:

- A fraction of the jet energy is carried away by muons or neutrinos, which deposit little or no energy in the calorimeter.
- Some of the particles may deposit energy outside the cone, since fixed cone algorithm is used.
- There could be additional energy in the calorimeter due to a soft underlying event interaction (energy not associated with the hard-scattering process) or an extra $p\bar{p}$ interaction in the same bunch crossing.

A standard procedure [66, 67] has been developed at CDF to correct jet energies to the parton level. It includes the following corrections:

- Relative jet corrections
- Raw energy scale corrections
- Multiple interaction corrections
- Absolute energy scale corrections
- Underlying event corrections
- Out-of-cone corrections

The combined correction factor is meant to reproduce the parton E_{T} correctly. However, this can be done only on average. The jet energy resolution, defined relative to the real parton E_{T}, depends on the fluctuations and not on the mean jet E_{T}. The jet energy resolution (rms) can be parametrized as $\sigma(E_{\mathrm{T}})/E_{\mathrm{T}} \approx 1/\sqrt{E_{\mathrm{T}}}$, and varies from 20% to 10% for the jets between 20 and 100 GeV [66]. The combined correction factor does not reduce the jet energy fluctuations. Since we will correct the raw missing-E_{T} for the jet energy corrections (see section 4.2.3, we may enhance the number of events in the tail of the missing-E_{T} distribution. In principle, in this analysis it is sufficient for us to use jets and missing-E_{T} based on the raw energy as measured by calorimeter. Therefore, in this analysis we use only first two corrections, which account for the non-linearity in the calorimeter response and set the energy scale in the central calorimeter.

Relative jet corrections. The relative jet corrections account for the difference in the calorimeter response in different fiducial regions. The corrections are obtained from a large di-jet sample of events with one of the jets in the central region of the calorimeter ($0.2 < |\eta| < 0.6$), where the detector response is flat as a function of η. Therefore, the jet from that region is used as a reference jet. The second jet is allowed to be anywhere in the calorimeter and is called the probe jet. Cuts are imposed to require that there be no additional jet activity in the events. In a perfect detector the jets should be balanced in E_{T}. Thus, scale factors are obtained by requiring that the jets balance each other in the transverse plane as a function of the p_{T} and η of the second jet. Figure 4-2 shows the relative jet energy corrections as a function of the calorimeter η and jet transverse energy (for the jets with $|\eta_{det}| < 2.5$).

Raw jet energy scale. The relative jet corrections take out the known η_{det} dependence of the calorimeter response. The raw jet energy scale can be calibrated

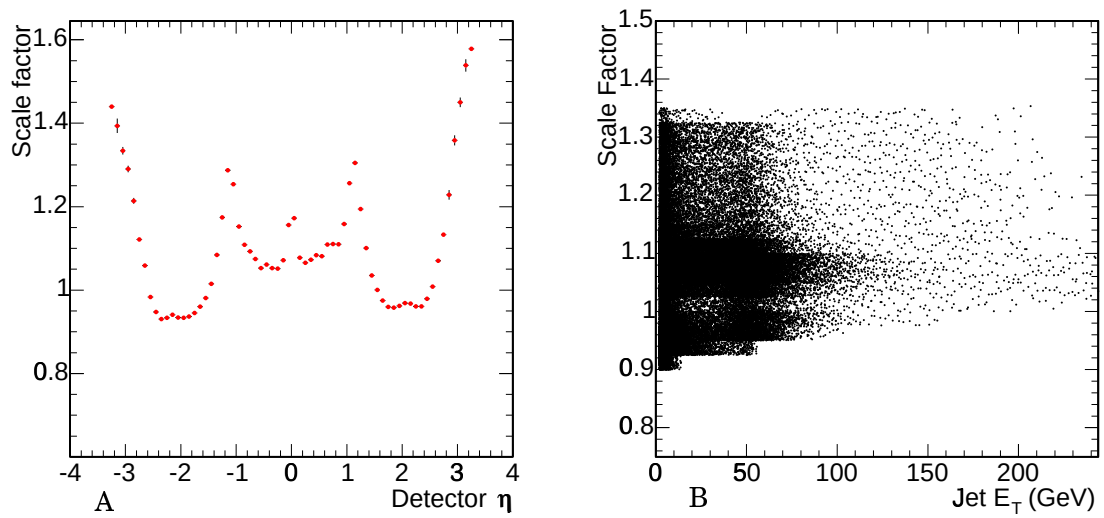

Figure 4-2: Relative jet energy corrections. A) Relative jet energy corrections as a function of the calorimeter η. B) Relative jet energy corrections as a function of jet transverse energy ($|\eta_{det}| < 2.5$).

using photon-jet balancing, since the photon is fully contained in the electromagnetic calorimeter and its energy is measured very precisely. The CEM energy scale is established by electrons from Z boson decays, which arise from a well known mass peak position and width. The CHA energy scale is established through muon energy response, which is consistent with that of minimum ionizing particle.

The corrected jet E_{T}, on average should balance the transverse momentum of the photon in di-jet like events, where one of the jets is a photon. The γ-jet balancing function for raw jets is defined by:

$$f_b = \frac{p_{\mathrm{T}}^{jet} - p_{\mathrm{T}}^{\gamma}}{p_{\mathrm{T}}^{\gamma}} \tag{4-8}$$

Ideally, photon-jet balancing results in Run II should be the same as in Run I. However, lower response was observed in Run II [68], therefore an additional scale factor was applied to correct raw jet energy back to Run I scale. The raw jet

energy scale factor is given by:

$$K_j = \frac{1+ < f_b^{Run\ I} >}{1+ < f_b^{Run\ II} >}, \tag{4-9}$$

and was measured to be 6.5%. This correction is important, since Monte Carlo simulation will be used for background normalization. Monte Carlo calorimeter simulation was tuned to test beam and Run I data.

4.2 Missing Transverse Energy

Energy and total momentum are always conserved, but since the CDF detector has a gap in a coverage around the beam pipe, some of the energy along the z-axis escapes in the beam pipe. Thus, we should observe conservation only in the transverse plane. Weakly interacting particles, such as neutrinos, never interact in the detector material and escape undetected, creating an imbalance in the measured transverse energy. Such imbalance in the transverse energy is proportional to the neutrino momentum and is called the missing transverse energy.

4.2.1 Missing Transverse Energy Reconstruction

The missing-E_{T} measurement is based on the central and plug calorimeters up to $|\eta| = 3.6$. The raw missing-E_{T} is defined as the negative vector sum of the transverse energy in the calorimeter:

$$\not{E}_x = -\sum_{i=1}^{N_{towers}} (E_i^{em} \sin\theta_i^{em} + E_i^{had} \sin\theta_i^{had}) \cos\phi_i, \tag{4-10}$$

$$\not{E}_y = -\sum_{i=1}^{N_{towers}} (E_i^{em} \sin\theta_i^{em} + E_i^{had} \sin\theta_i^{had}) \sin\phi_i, \tag{4-11}$$

where $E_i^{em,had}$ is the energy of the ith tower, θ_i is the polar angle of the line pointing from z-coordinate of event vertex to the center of the ith tower, and ϕ_i is defined by:

$$\phi_i = \frac{E_i^{em} \sin\theta_i^{em} \phi_i^{em} + E_i^{had} \sin\theta_i^{had} \phi_i^{had}}{E_i^{em} \sin\theta_i^{em} + E_i^{had} \sin\theta_i^{had}}. \tag{4-12}$$

$\phi_i^{em}, \phi_i^{had}$ is the center-of-gravity of energy for the electromagnetic and hadronic compartment in the tower, respectively. Only towers above a certain threshold enter the sum. The default thresholds used in calculation of missing-E_{T} is 0.1 GeV for all calorimeter components (CEM, PEM, CHA, WHA, PHA). The magnitude of missing-E_{T} is given by:

$$\not{E}_{\mathrm{T}} = \sqrt{\not{E}_x^2 + \not{E}_y^2}. \tag{4-13}$$

One also can define the missing transverse energy angle $\phi_{\not{E}_{\mathrm{T}}}$:

$$\phi_{\not{E}_{\mathrm{T}}} = \arctan \frac{\not{E}_y}{\not{E}_x} \tag{4-14}$$

Total scalar transverse energy ($\sum E_{\mathrm{T}}$) is defined as a sum of the transverse electromagnetic and hadronic energies over all towers above the given threshold.

4.2.2 Resolution

The missing-E_{T} measurement and resolution depends on the total energy deposited in the calorimeter and the events topology. The resolution is usually parametrized in terms of the total scalar E_{T} and measured in minbias events, where, on average, the energy deposition is expected to be uniformly distributed in ϕ, and thus no large intrinsic missing-E_{T} is expected.

If the x and y components of the missing-E_{T} are distributed as a Gaussian with $\sigma_x = \sigma_y = \sigma$ [69]:

$$\frac{dN}{d\not{E}_x} \simeq \exp\left(-\frac{\not{E}_x^2}{2\sigma^2}\right) \tag{4-15}$$

$$\frac{dN}{d\not{E}_y} \simeq \exp\left(-\frac{\not{E}_y^2}{2\sigma^2}\right), \tag{4-16}$$

then from Eq. 4-13 and since the x and y components of missing-E_{T} are independent

$$\frac{dN}{d\not{E}_{\mathrm{T}}^2} \simeq \exp\left(-\frac{\not{E}_{\mathrm{T}}^2}{a}\right), \tag{4-17}$$

with

$$\frac{1}{a} = <\not{E}_{\mathrm{T}}^2> = 2\sigma^2, \tag{4-18}$$

where $<\not{E}_{\mathrm{T}}^2>$ is the average squared missing-E_{T}. From this relation we define

$$\Delta = \sqrt{2}\sigma = \sqrt{<\not{E}_{\mathrm{T}}^2>}\,. \tag{4-19}$$

The missing-E_{T} resolution was measured in a sample of events collected by the minbias trigger [62]. In minbias events, the missing-E_{T} resolution is expected to scale as the square root of the total transverse energy in the event. Figure 4-3 shows the missing-E_{T} distribution in minbias events. Figure 4-4 shows the missing-E_{T} x and y component distributions for the minimum bias data sample. They are fit with two Gaussians. The small offset in x and y components is attributed to the beam axis being slightly offset from the nominal position (0,0) in the plane perpendicular to it.

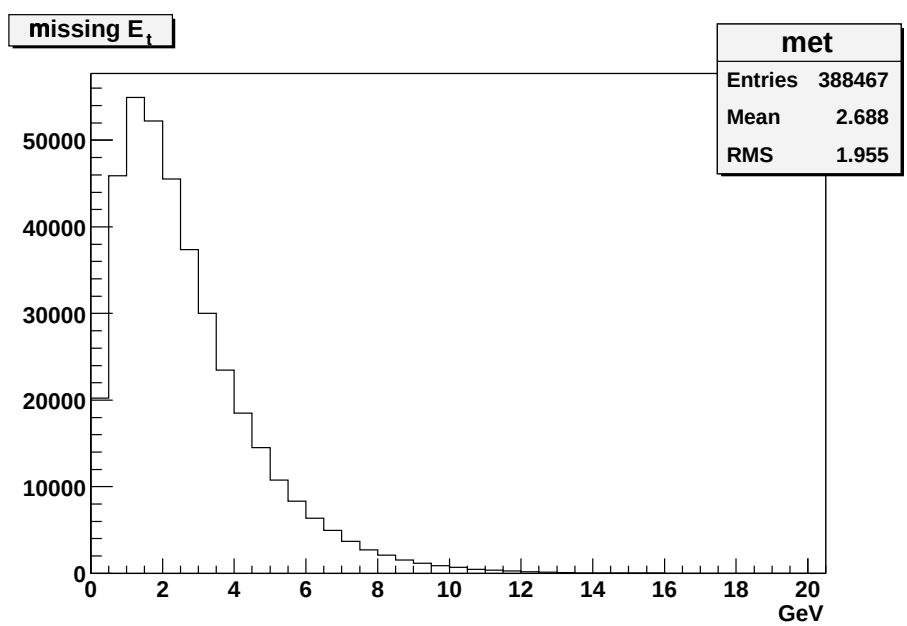

Figure 4-3: Missing-E_{T} distribution in minbias events.

Figure 4-5 shows the missing-E_{T} resolution as a function of total transverse energy. The distribution is fit with function

$$\Delta(\not{E}_{\mathrm{T}}) = p0 + p1\sqrt{\Sigma E_{\mathrm{T}}}. \tag{4-20}$$

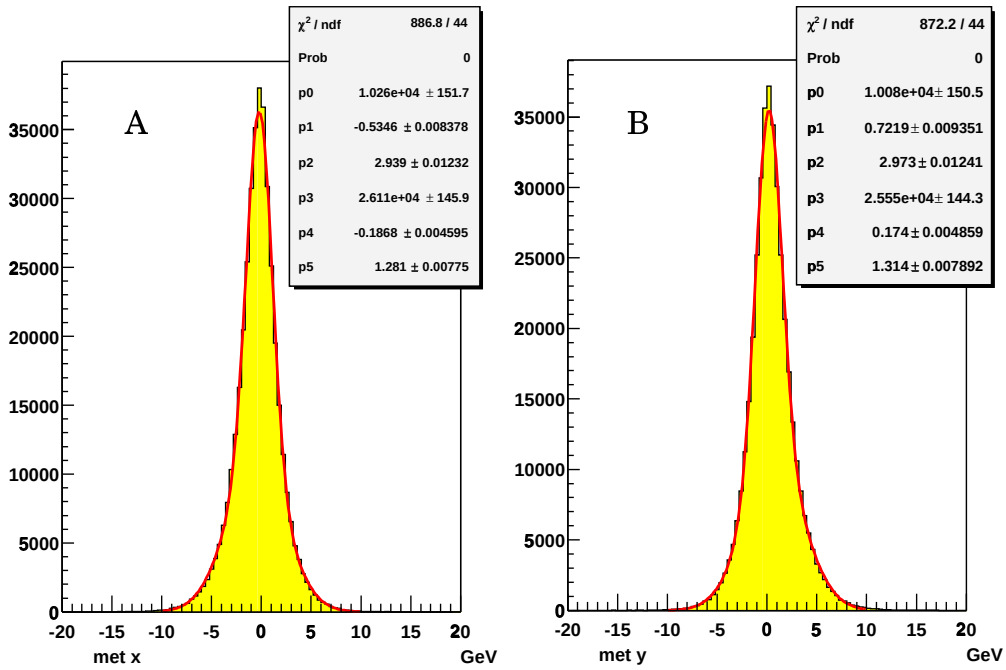

Figure 4-4: Distributions of the x and y components of the missing-E_{T} in minbias events. A) Distribution of the x component of the missing-E_{T} in minbias events. B) Distribution of y component of the missing-E_{T}.

Thus to a first order approximation, the missing-E_{T} resolution in minbias events is:

$$\Delta(\not{E}_{\mathrm{T}}) = -0.25 + 0.64\sqrt{\Sigma E_{\mathrm{T}}}. \tag{4-21}$$

The missing-E_{T} resolution scales as the square root of the total transverse energy as expected.

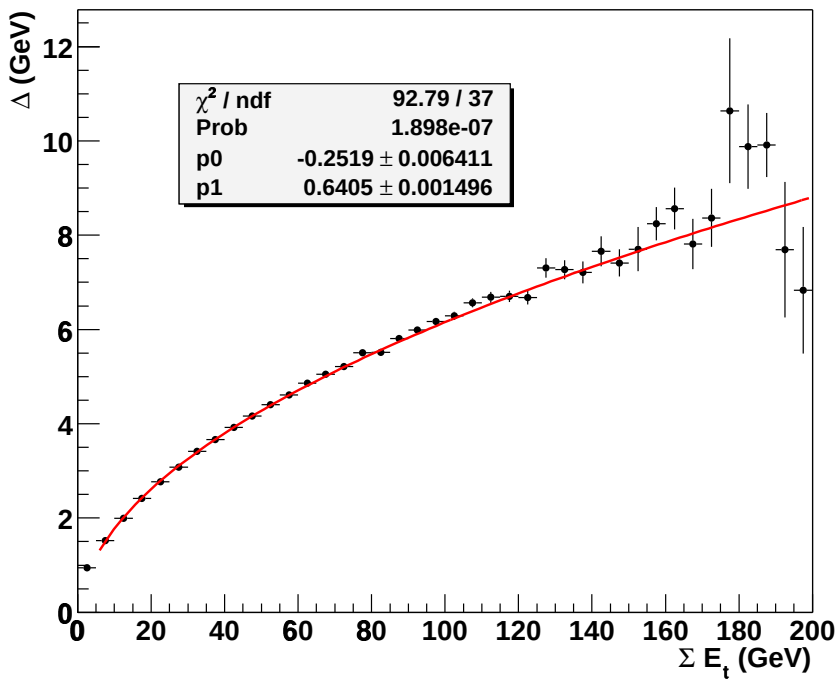

Figure 4-5: Missing-E_{T} resolution as a function of total transverse energy.

4.2.3 Missing-E_{T} Corrections

The missing transverse-energy in an event should only be due to weakly interacting particles escaping the detector. However, missing-E_{T} reconstruction does not give the real intrinsic missing-E_{T} in the event due to the same reasons as listed for jets. Therefore, the missing-E_{T} should also be corrected for the jet energy corrections, since the calorimeter towers associated with the jets are also used to calculate the missing-E_{T}.

The missing-E_{T} from equations 4-10, 4-11 can be rewritten as:

$$\vec{\not{E}}_{\mathrm{T}}(raw) = -[\sum_{clus} \vec{E}^{clus}(\text{ jet uncorr}) + \sum_{unclus} \vec{E}^{unclus}]_{\mathrm{T}}, \tag{4-22}$$

where $\sum_{clus} \vec{E}^{clus}$ is performed over towers that are associated with jets, with tower energies uncorrected, and $\sum_{unclus} \vec{E}^{unclus}$ is perfomed over towers that do not belong to any of the jets. Missing-E_{T} is then corrected for the jet energy corrections:

$$\vec{\not{E}}_{\mathrm{T}}(corr) = \vec{\not{E}}_{\mathrm{T}}(raw) - \sum_{i}^{N_{jets}} \Delta E_{i\ \mathrm{T}}^{jet} \hat{n}_i, \tag{4-23}$$

where $\Delta E_{i\ \mathrm{T}}^{jet}$ is the difference in the jet energy before and after corrections, and $\hat{n}$ is a unit vector pointing in the direction of the jet and sum is performed over all corrected jets.

An ideal energy correction mechanism should account for the non-uniform and non-linear detector response and give the real missing-E_{T} due to the weakly interacting particles. We use the missing-E_{T} significance, defined as

$$S = \frac{<\not{E}_{\mathrm{T}}>}{\sqrt{<\sum E_{\mathrm{T}}>}}, \tag{4-24}$$

as a criteria to choose which jet energy corrections to apply, where $<\sum E_{\mathrm{T}}>$ is average total scalar energy, and $<\not{E}_{\mathrm{T}}>$ is average missing-E_{T}. In the events where missing-E_{T} appears due to the calorimeter resolution effects the missing-E_{T} significance should be small, whereas in the events with the intrinsic missing-E_{T} the significance will be large. The missing-E_{T} should not scale as much as a $\sum E_{\mathrm{T}}$, if the jet correction mechanism works properly. Therefore the optimum correction level will give us minimal missing-E_{T} significance. Moreover, since the search described here selects large missing-E_{T}, it is important to apply corrections that correctly account for those effects and give a real intrinsic missing E_{T}, and minimize the tail at high missing-E_{T} from these artificial imbalances.

We use JET50 sample (see Section 5.2.2) to study jet energy corrections and their impact on missing-E_{T} measurement. We compare average missing-E_{T}, average scalar $\sum E_{\mathrm{T}}$ and average missing-E_{T} significance for the following cases:

- No jet energy corrections are applied (case 1).
- Relative jet energy corrections and raw jet energy scale corrections are applied (case 2).
- Multiple interaction corrections and absolute energy scale corrections are applied in addition to the corrections applied in case two (case 3).
- Underlying event corrections and out-of-cone corrections are applied in addition to the corrections applied in case three (case 4).

Only jets with uncorrected energies above 10 Gev are corrected.

Figure 4-6 compares the missing-E_{T} without corrections with missing-E_{T} after applying corrections from the case 2 to the jets and recalculating missing-E_{T}. Figure 4-7 compares the total scalar E_{T} without corrections with total E_{T} after applying corrections from the case 2 to the jets and recalculating transverse energy.

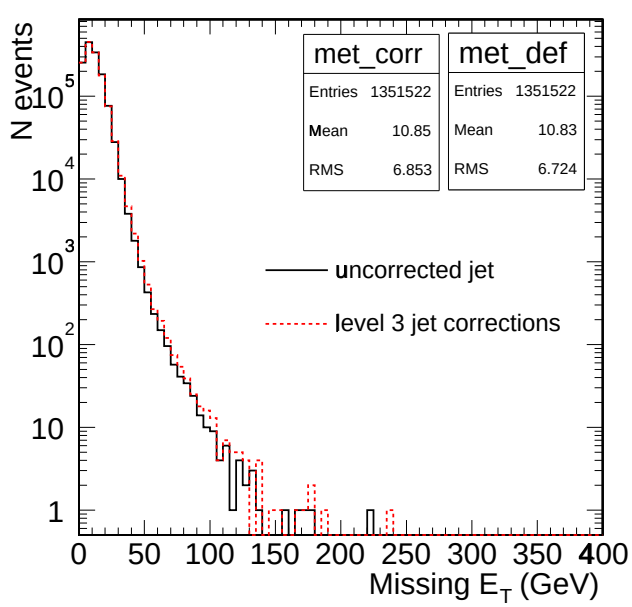

Figure 4-6: Uncorrected missing-E_{T} and missing-E_{T} after applying corrections from the case 2 (level-3) to the jets and recalculating missing-E_{T}.

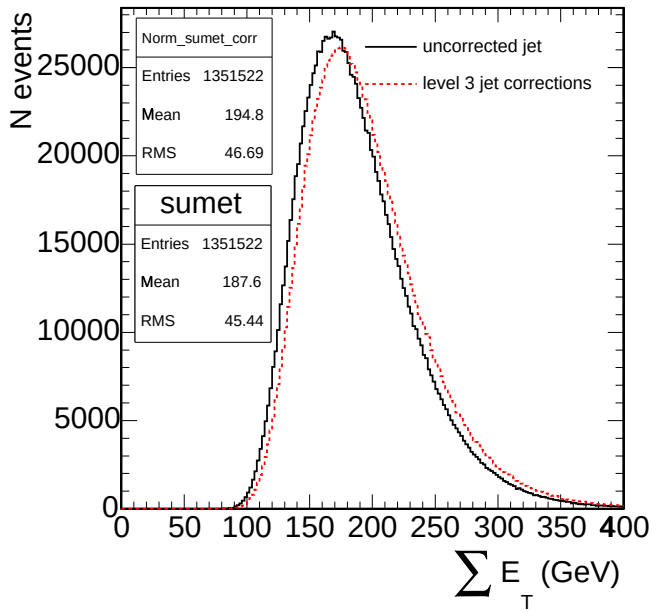

Figure 4-7: Uncorrected total scalar E_{T} and total scalar E_{T} after applying corrections from the case 2 (level-3) to the jets and recalculating transverse energy.

Table 4-1 shows average missing-E_{T}, average scalar $\sum E_{\mathrm{T}}$ and average missing-E_{T} significance for all four cases.

Table 4-1: Average missing-E_{T}, average scalar $\sum E_{\mathrm{T}}$ and average missing-E_{T} significance and RMS of distributions from `JET50` data for uncorrected and corrected jet energies.

Jets	Uncorrected Corrections	Case 2 Corrections	Case 3 Corrections	Case 4 Corrections
$< \not{E}_{\mathrm{T}} >$	10.83 ± 6.87	10.85 ± 6.85	12.38 ± 7.82	14.23 ± 8.73
$< \sum E_{\mathrm{T}} >$	187.6 ± 45.44	194.8 ± 46.69	214.8 ± 48.21	234.7 ± 49.57
S	0.79 ± 0.1	0.78 ± 0.1	0.84 ± 0.1	0.93 ± 0.1

The case 2 corrections give minimal missing-E_{T} significance. Therefore, we use jet energy corrections from case 2, which include relative jet energy corrections and raw jet energy scale corrections and correct the missing-E_{T} for the resulting difference in the jet energy. No further corrections can be made to single towers and this affects the resolution. We choose not to include the absolute jet energy corrections, underlying event corrections and out-of-cone corrections. Beside jets,

originating from leptoquark decay, there is an additional unclustered energy in the calorimeter due to recoil particles and underlying event. This energy will be undermeasured, if the particles in the underlying event have low momentum, and since the calorimeter response falls off at low energy. If we choose to include the absolute jet energy corrections, we would need to scale proportionally the unclustered energy, otherwise we would create artificial imbalance in the energy flow in the calorimeter. Scaling up the energy to compensate such an energy mismeasurement in unclustered energy, could result in enhancing of the number of events in the tail of the missing-E_{T} and degradation of the missing-E_{T} resolution. Out of cone energy is already included in the missing-E_{T} measurement, therefore special care needs to be taken to disentangle it from the unclustered energy. Furthermore, those corrections have not been yet measured in Run II.

4.3 Tracking

The ability to detect and reconstruct charged particle trajectories is an essential requirement for particle identification and momentum reconstruction. Precise, high efficiency tracking plays a central role at CDF for lepton and photon (no associated tracks) identification. It allows precise reconstruction of the track impact parameter, and thus the identification of heavy-flavor quarks in jets.

Charged particles traveling inside a uniform magnetic field have a helical trajectory. At CDF the following five parameters are used to describe the helix trajectory, where the axis coincides with z-axis of the detector:

- C - the half-curvature of the trajectory, with the same sign as the particle charge. It is proportional to the transverse momentum of the track.
- $\cot\theta_0$ - cotangent of the polar angle at the closest approach to the origin.
- ϕ_0 - the azimuthal angle at the closest approach to the origin.
- z_0 - the z position at the point of the closest approach to the helix origin.
- d_0 - the impact parameter, the distance of the closest approach in the transverse plane between the helix and the origin.

There are several tracking algorithms used at CDF for the track reconstruction, depending on the η region and the available detector information [70]. The most robust and precise tracking is provided by the "Outside-In" tracking algorithm, which uses both the COT and the Silicon detectors in the pseudorapidity region $|\eta| < 1$. In the forward region, the "Silicon Stand-Alone" tracking algorithm is used.

The "Outside-In" tracking algorithm starts with finding tracks in the COT, since the hit occupancy there is lower and tracks are more isolated than in the silicon. Two algorithms are employed: segment linking and histogram linking. The former, first reconstructs track segments in each superlayer and then tries to link them together through an iterative process into a single track. The latter combines one segment in the outermost available superlayer with the expected beam line position and tries to construct a reference track. The distances of the hits in the other superlayers from this reference track are filled into histogram, which is then used to determine track parameters. The COT tracking reconstruction efficiency was measured in data and found to be $\epsilon_{\mathrm{COT}} = 99.63^{+0.35}_{-0.4}\%$ [71] for isolated tracks with $p_{\mathrm{T}} > 5$ GeV/c.

At the second stage of reconstruction, a track found in the COT is then propagated into the silicon system. A road around a track is defined based on the errors on the COT track parameters. Then new hits are added if they lie inside this predefined road along the track. When a hit is added, the track parameters are recalculated and the search is performed again. The impact parameter resolution of COT + SVX tracks is found to be $\sigma(d_0) = 23 \pm 3$ μm [72].

Any remaining hits in the silicon detectors (after the second stage) are used for the silicon stand-alone tracking [70]. The tracks from the default track collection are used in this analysis, which includes tracks reconstructed by all algorithms.

Vertex reconstruction.

The transverse energy calculation of the calorimeter towers requires knowledge of the collision vertex location. The $p\bar{p}$ interaction region is spread out along the the beam line, forming approximately a Gaussian with a $\sigma \approx 30$ cm. Thus, a precise z position of the event vertex along the beamline is needed to correctly compute the transverse energy of jets as well as the missing transverse energy.

A highly efficient vertex algorithm (ZVertexColl) is used at CDF to accurately measure the z-position of all $p\bar{p}$ interactions that may have occured in one crossing. [73]. Fast, pre-tracking primary z-vertex finder algorithm, which uses a histogram method to reconstruct vertices from hits in the COT, the SVX and the ISL, forms a list of seed vertices. Then, the ZVertexColl algorithm uses pre-tracking seed vertices and tries to define a smaller set of vertices by applying more stringent requirements on the tracks associated with these vertices. Different quality flags are assigned to the vertices in the event, based on the number of the tracks with silicon/COT hits associated to the vertex. Higher quality is assigned to a vertex with more COT tracks, since tracks with COT hits have much better momentum resolution and less likely to be fake tracks. The vertex reconstruction efficiency was measured in QCD di-jet Monte Carlo events and was found to be 99.0 ± 0.7 for the vertices with two or more COT tracks.

4.4 Lepton Reconstruction

The final state for this analysis does not have any charged leptons. However, electroweak processes with charged leptons in the final state contribute the most to the background events. This is because identification is not always 100% efficient and because of the limited coverage of the detector. Thus, reconstruction of muons and electrons is briefly described here. Tau leptons are not directly identified in this analysis and their reconstruction is not discussed.

4.4.1 Electrons

Electrons deposit most of their energy in the electromagnetic calorimeter, thus the electron reconstruction algorithm looks for clusters of relatively large electromagnetic energy deposition in the calorimeter [74]. The algorithm starts with the creation of a list of seed towers. A tower is considered as a seed if the electromagnetic energy is greater than a threshold (2 GeV). Then the algorithm checks towers adjacent to the seed towers to see if they could be added to the cluster. In the CEM only towers with non-zero electromagnetic (EM) or hadronic (HAD) energy in the same ϕ wedge and nearest in η could be added to the seed tower to form a cluster. In the PEM a cluster consists of a seed tower and at most three adjacent daughter towers with transverse electromagnetic energy greater than a threshold (100 MeV). Finally, a list of the clusters is formed by requiring that each cluster has an electromagnetic E_{T} greater than 2 GeV and a hadron to EM energy ratio less than 0.125. The cluster is accepted regardless of hadron to EM ratio if the cluster energy (not transverse energy) is greater than 100 GeV.

Electron identification cuts. The electron candidates are selected from the list of the electromagnetic clusters using a set of stricter cuts. A central electron candidate is required to have a COT track associated with its electromagnetic cluster. The following variables are used to discriminate electrons against photons, prompt π^0, isolated charged hadrons and jets faking electrons [75]:

- The ratio of the cluster energy to track momentum (E/p).
- The ratio of hadronic energy to electromagnetic energy of the cluster (HAD/EM).
- A comparison of the lateral shower profile in the calorimeter cluster with that of test beam electrons (L_{shr}).
- The distance between the extrapolated track-position and the CES measurement in the $r-\phi$ and z views (Δx and Δz).

- A χ^2 comparison of the CES shower profile with those of test-beam electrons (χ^2_{strip}).
- The reconstructed track position in the z-direction (Z_0).
- The isolation, defined as the ratio of the additional transverse energy in a cone of radius $R = 0.4$ around the cluster axis to the transverse energy of the electron cluster (I).

4.4.2 Muons

Muons are reconstructed by matching stubs in one of the muon detectors with extrapolated COT tracks [76]. A stub is a collection of the hits that are linked together to form a muon track segment in the muon detectors. Relatively loose track-stub matching requirements, based on the matching distance between the extrapolated COT track and the track segment in the muons chambers, are used to form a muon collection. Also, muon candidates are formed from all the remaining high-p_{T} COT tracks ($p_{\mathrm{T}} > 10$ GeV), that are not matched to stubs in muon detectors. Usually they are required to be consistent with a minimum ionizing particle in the calorimeter. Such muons are called stub-less muons.

Muon identification cuts. The following variables are used to separate muons from hadrons that penetrate calorimeters, and from cosmic rays [77]:

- The matching distance between the extrapolated track and the track segment in the muon chambers (Δx)
- An energy deposition in the electromagnetic and hadronic calorimeters characteristic of the minimum ionizing particle (E_{em} and E_{had}).
- The distance of the closest approach of the reconstructed track to the beam line (track impact parameter d_0).
- The reconstructed track position in the z-direction (Z_0).
- The isolation defined as an additional transverse energy in a cone of radius $R = 0.4$ around the muon track direction (I).

CHAPTER 5
TRIGGER PATH AND EVENT PRESELECTION

As mentioned in Section it would be an enormous task to try to record and analyze all the events from all 1 million $p\bar{p}$ interactions per second that occur at CDF. The three-level trigger system employed at CDF, allows us to retain the most interesting events and to study them in subsequent analyses. The search for leptoquark pair-production and decay into the $\nu\nu jj$ final state centers on selecting events with large missing-E_{T}, we use the inclusive missing-E_{T} data sample for this search.

5.1 Missing Transverse Energy Trigger

The inclusive missing-E_{T} trigger is designed to select events with a large missing transverse-energy. However, it is desireable to keep the missing-E_{T} trigger threshold as small as possible, while maintaining low enough rate. Below some details are given on how the trigger path is organized and events are collected.

5.1.1 Level-1 Trigger

The Level-1 trigger system uses fast custom electronics to sum the energies of calorimeter towers and to form trigger objects, which are then used for the decision on whether to send the event to Level-2 or to discard it [78]. The calorimeter triggers are divided into two types: object triggers (electrons, photons and jets) and global triggers (missing-E_{T} or $\sum E_{\mathrm{T}}$). The object triggers are formed by applying thresholds to individual calorimeter trigger towers, while thresholds for the global triggers are applied after summing energies from all towers.

Calorimeter trigger tower organization. The trigger system hardware makes use of the projective nature of the calorimeter towers. The physical calorimeter towers are organized into bigger trigger towers, 24 by 24 in $\eta - \phi$ space, for a total

of the 576 towers [79]. One trigger tower covers approximately 15° in $\Delta\phi$ and 0.2 in $\Delta\eta$. Figure 5-1 shows the transverse segmentation of the trigger towers in the plug calorimeter, for example.

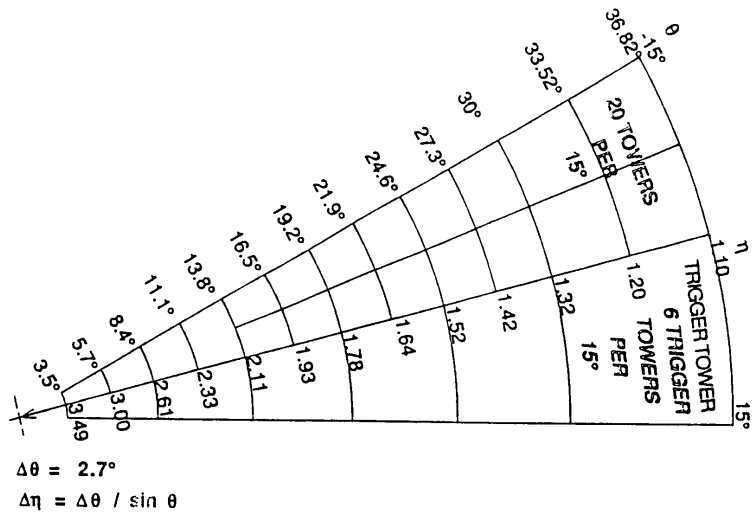

Figure 5-1: Transverse view of two wedges in the plug calorimeter. Physical and trigger tower segmentations are shown.

The calorimeter readout boards, Analog to Digital Converter/Memory cards (ADMEMs) [80], digitize the calorimeter photo-tube signals and determine the trigger tower transverse energy. Since no event vertex information is available at Level-1, $z = 0$ is assumed for the collision vertex.

Online Missing Transverse Energy. All trigger towers with transverse energy above 1 GeV are summed vectorially into an online missing-E_{T} measurement [81]. Then, if the online missing-E_{T} is greater than 25 GeV, the event is accepted by the Level-1 trigger and passed to the Level-2 trigger. Since this calculation is very coarse, the missing-E_{T} could be undermeasured, which would result in trigger inefficiency; therefore, it is desirable to keep the Level-1 threshold as low as possible. On the other hand, overestimation of the missing-E_{T} would result in a higher Level-1 acceptance rate. The missing-E_{T} trigger rate at Level-1 is ~ 6 Hz.

5.1.2 Level-2 Trigger

No improvement is possible for the online missing-E_{T} reconstruction, so events passing the Level-1 trigger automatically accepted by the Level-2. However there is an option to increase the threshold, which would result in the reduction of the total rate. This option is reserved for the very high instantaneous luminosity regime (7×10^{32} cm$^{-2}s^{-1}$), since the rate is expected to scale proportionally to it.

5.1.3 Level-3 Trigger

The full precision of the detector data data is available to the Level-3 trigger. A farm of PC computers, running the same event reconstruction software as in offline, analyzes the event. At Level-3, missing-E_{T} is recalculated as described earlier in section 4.2.1. However, again the nominal vertex position at $z = 0$ is assumed, to avoid possible biases due to vertex reconstruction. Events passing the Level-3 trigger requirement of $\not\!\!E_{\mathrm{T}} > 45$ GeV (`MET45`) are directed to the "E stream" and written to the `ephysr` dataset.

5.2 Data Samples

The data collected during the February 9, 2002 through September 7th, 2003 operating period of the Tevatron is used in this analysis, with a corresponding total integrated luminosity of 224 pb^{-1}. However, slightly smaller sample used for this analysis, after requiring that no detector problems occured during data taking period. The total integrated luminosity recorded by the CDF is shown on Figure 5-2. In addition to the inclusive missing transverse-energy sample, where our signal search is performed, a number of independent data samples are used for the purpose of background normalization and trigger efficiency parametrization. These data samples are described in this section as well.

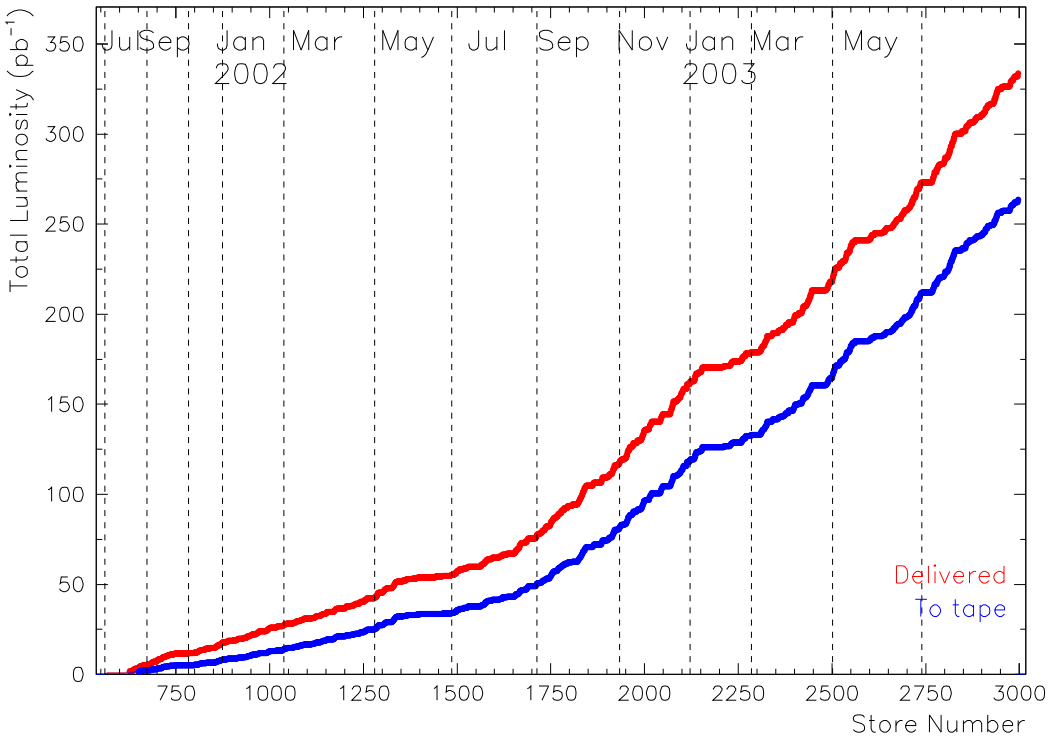

Figure 5-2: Total integrated luminosity recorded by CDF from February 9, 2002 trough September 7th, 2003 of the Tevatron operating period.

5.2.1 Inclusive Missing Transverse Energy Sample

Events from the inclusive `MET45` trigger path are written to the `emetXX`[1] data set from the E stream, after being processed on the offline reconstruction farm. We use data from `emet08` and `emet09` datasets that were originally created with `4.8.4a` and `4.9.1` version of the CDF software respectively.

5.2.2 Inclusive Jet Sample

The inclusive `JET20` and `JET50` samples are used for the QCD multi-jet background normalization (section 8.2). The `JET20` and `JET50` trigger paths require

[1] `XX` corresponds to the version of the reconstruction software.

a single tower in the calorimeter with energy above 5 GeV (ST5) at Level-1 and is prescaled by a factor of 20 (only one out of the twenty events passing Level-1 trigger requirement is selected to be considered by the Level-2 trigger). At Level-2, a calorimeter cluster is required with an energy above 15 GeV and an additional prescale of 25 for the `JET20` trigger path. For the `JET50` trigger path, a calorimeter cluster is required at Level-2 with an energy above 40 GeV and with no additional prescale. The collision vertex for jet reconstruction at Level-3 is at $z = 0$. The jet E_{T} thresholds are 20 and 50 GeV for the `JET20` and `JET50` trigger paths respectively.

5.2.3 Inclusive Lepton Samples

An inclusive high-p_{T} electron sample is used for the electroweak background normalization (section 8.1), and an inclusive high-p_{T} muon sample is used for the `MET45` trigger efficiency parametrization.

The high-p_{T} electron sample. Events from the `ELECTRON_CENTRAL_18` trigger path are used to create the inclusive electron sample. The Level-1 trigger requires a single tower with transverse EM energy above 8 GeV and an XFT track with $p_{\mathrm{T}} > 8$ GeV/c pointing to the tower. At Level-2 a CEM cluster is required of at least 8 GeV. In addition, the hadronic part of the cluster should be less than 0.125 of the EM energy. The XFT track should extrapolate to the seed tower. One electron candidate with $E_{\mathrm{T}}^{em} > 18$ GeV, $E^{had}/E^{em} < 0.125$ and COT track with $p_{\mathrm{T}} > 9$ GeV/c is required at Level-3.

The high p_{T} muon sample. Events from the `MUON_CMUP_18` trigger path are used to create the inclusive muon sample. The central high-p_{T} muon trigger requires a muon stub in the CMU detector with a transverse momentum above 6 GeV/c, a matching XFT track, and the presence of CMP hits associated with this stub. Events passing the Level-1 trigger requirement were automatically

accepted by Level-2. At Level-3 the muon candidate is required to have both CMU and CMP stubs and a COT track with $p_{\mathrm{T}} > 18$ GeV/c.

5.2.4 Standard Ntuple

The data from all samples were reprocessed with the latest version of the CDF software (4.11.1), to take advantage of the latest calibrations and bug fixes in the reconstruction code, and written out to a compressed data format known as `stntuple`, version `dev_240`.

The changes to the calorimeter calibration include:

- Plug calorimeter PMT gain corrections as a function of run number. To monitor gain of the PMTs calorimeter is calibrated periodically with laser or radioactive source. The variation of the measured plug calorimeter energy with time was extracted from the laser/source data.
- The WHA energy scale correction for the period from December 2001 to January 2003, which was lower by about 10%.
- CHA tower-to-tower corrections, which were obtained from muon data and applied to remove a gain variation in ϕ.
- The global energy scale in the CHA, which was increased by 4%.
- CEM tower-to-tower and time dependent corrections, which were derived from electron E/p studies.
- The overall scale of the plug calorimeter, which was adjusted to the energy scale determined from dedicated electron beam tests.

The selected data were processed with older software, when these corrections were not available yet. Therefore, all the objects that rely on calorimetry were dropped and reconstructed using newer CDF software version 4.11.1. Missing transverse-energy and jets were reconstructed using the highest $\sum p_{\mathrm{T}}$ vertex, where the sum is performed over all tracks associated with vertex. Only vertices which have two or more associated COT tracks are considered, since silicon standalone tracks have a higher rate of fake high-p_{T} tracks.

In addition, Layer 00 hit information was removed and tracks were refit with an improved beamline position measurement and tracking detector alignment.

5.2.5 Good Run Requirement

Since we look at the high tails of the missing-E_{T} distribution, special care should be taken that the CDF detector was in a stable working condition during the data collection. Therefore, we require that all the detector components relevant for this search were marked as good by the online and offline data quality operators. A good run list was compiled by requiring that the corresponding online and offline data quality bits were set to one. The total integrated luminosity of the inclusive missing E_{T} sample used for this analysis, after applying the good run list, is 191 pb^{-1}.

5.3 Instrumental Background

Several sources of non-collision backgrounds and detector inefficiencies can spoil the energy measurement in the calorimeter and cause events to appear to have large missing-E_{T}. If the missing-E_{T} is large enough, the event can end up in our sample. Special care needs to be taken to discard such events in searches for new physics in the tails of the missing-E_{T} distribution. Some of these sources are:

- High energy muons (beam halo) traveling parallel to the beam, but outside the beampipe, created by an upstream proton interaction with the beampipe or surrounding material. These muons can radiate a photon in the calorimeter in coincidence with a real $p\bar{p}$ collision.
- Cosmic ray showers in the calorimeter.
- $p\bar{p}$ collisions produced far from the nominal collision point. In this case some of the energy could escape detection.
- QCD multi-jet events where one of the jets falls into a crack in the calorimeter or non-instrumented region.
- Energy response mis-calibration in the calorimeter.
- Two or more $p\bar{p}$ collisions in the same bunch crossing.

Beam halo and cosmic ray events.. Losses from proton and antiproton beams produce a halo of particles accompanying the beams, which may contribute to the missing-E_{T} trigger. Beam halo muons travel parallel to the beam and may produce showers in the calorimeter. The energy deposition associated with such beam halo events has two distinct signatures [82]. In one case, there is a narrow strip of the towers in the central calorimeter, with most of the energy deposited exclusively either in the electromagnetic or hadronic sections of the detector in one wedge at an azimuthal angle $\sim 0°$. Figure 5-3 shows an event display of a beam halo muon showering in the CHA.

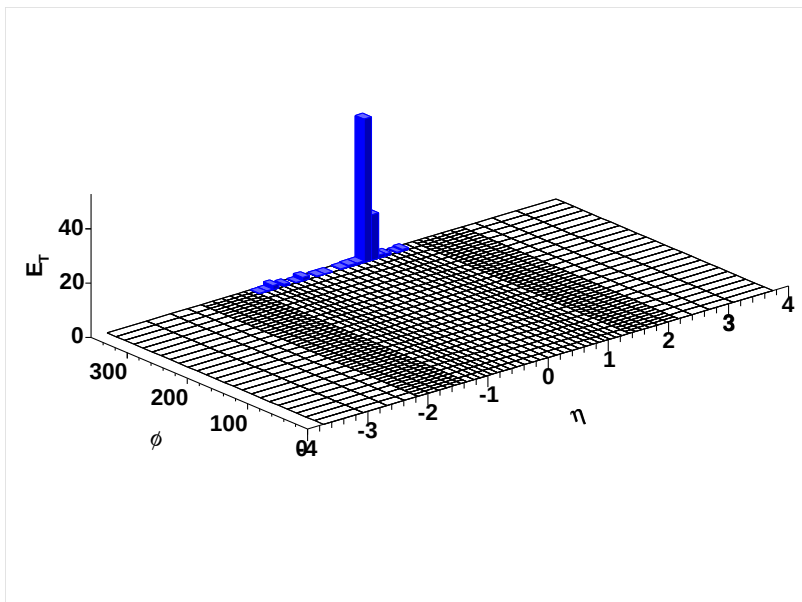

Figure 5-3: Event display of the typical beam halo muon bremsstrahlung in the calorimeter.

Figure 5-4 shows the azimuthal angle distribution of the missing-E_{T} direction from the inclusive `MET45` sample after the good run requirement. The pronounced peak at $\phi = 3.14$ rad is attributed to the events with beam halo particles showering in the calorimeter.

In the other case, a high energy spike is observed in a few towers in the plug calorimeters. These high energetic towers are located roughly at $\sim 90°$ and $\sim 270°$

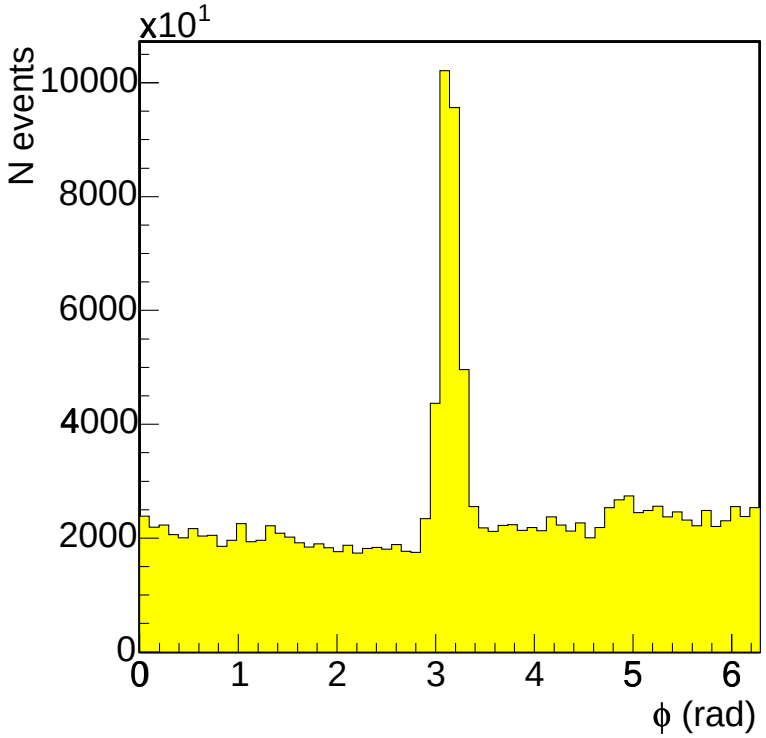

Figure 5-4: Azimuthal angle distribution of the missing-E_{T} in the inclusive `MET45` sample.

in ϕ. The reason for such pattern is that the steel shielding wall of the IMU muon system are split vertically along the beam axis. This split produces a gap between the two halves of the IMU shielding and thus allows some fraction of the beam halo particles to pass on to the plug and end-wall calorimeters in the vertical plane.

As with beam halo particles, cosmic ray particles also may produce showers in the calorimeter, leading to a large $\not\!\!E_{\mathrm{T}}$. Figure 5-5 shows a candidate of the cosmic ray event showering in the calorimeter.

These events coincidentally overlap with a bunch crossing and usually do not have tracks or much energy deposition in other parts of the detector. However, since they are interpreted to have a large energy imbalance, they have large $\not\!\!E_{\mathrm{T}}$ and therefore end up in the data sample.

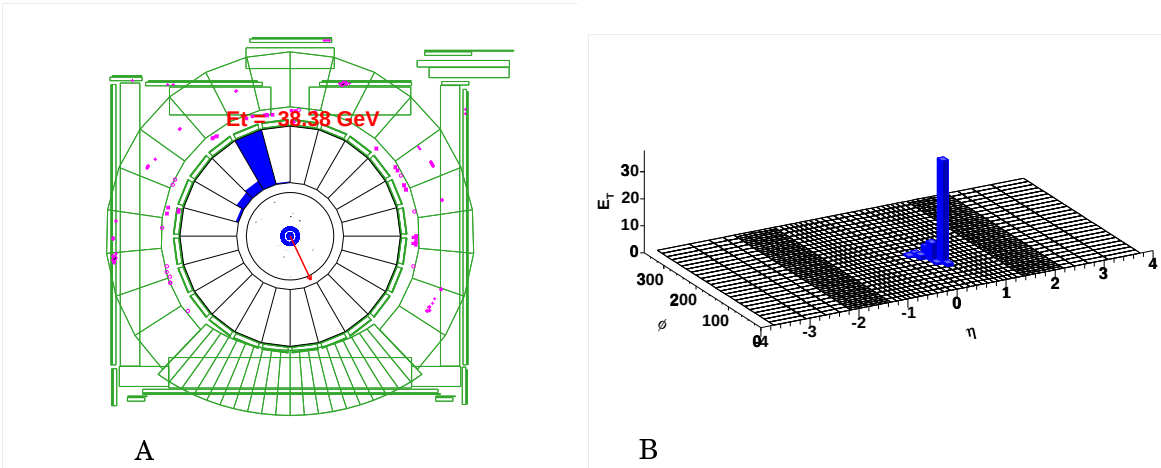

Figure 5-5: Event display of the typical cosmic ray event. A) The COT view. B) Lego plot of energy deposited in CHA.

5.4 Initial Data Selection

A secondary dataset was derived after applying clean-up cuts similar to those of Run I [83]. Theses cuts are designed to significantly reduce the contribution of events with fake missing E_{T} and from non-collision backgrounds. The `JET50` data sample and QCD di-jet Monte Carlo sample (see section 6.2) were used to define and study event pre-selection criteria, which were later applied to the inclusive missing-E_{T} sample. The `JET50` data sample consists predominantly of QCD di-jet events, which do not have large intrinsic missing-E_{T}.

Charged particles, produced in proton-antiproton collisions are reconstructed as tracks in the tracking system. Therefore a $p\bar{p}$ interaction is expected to have a reconstructed vertex. Tracks from non-collision events usually do not form a vertex. This requirement also removes events from satellites' bunch interactions outside the nominal collision region. Figure 5-6 shows distribution of the number of vertices in the `MET45` sample. As can be easily seen, more than half of the events have zero reconstructed vertices, which are mostly from non-collision background.

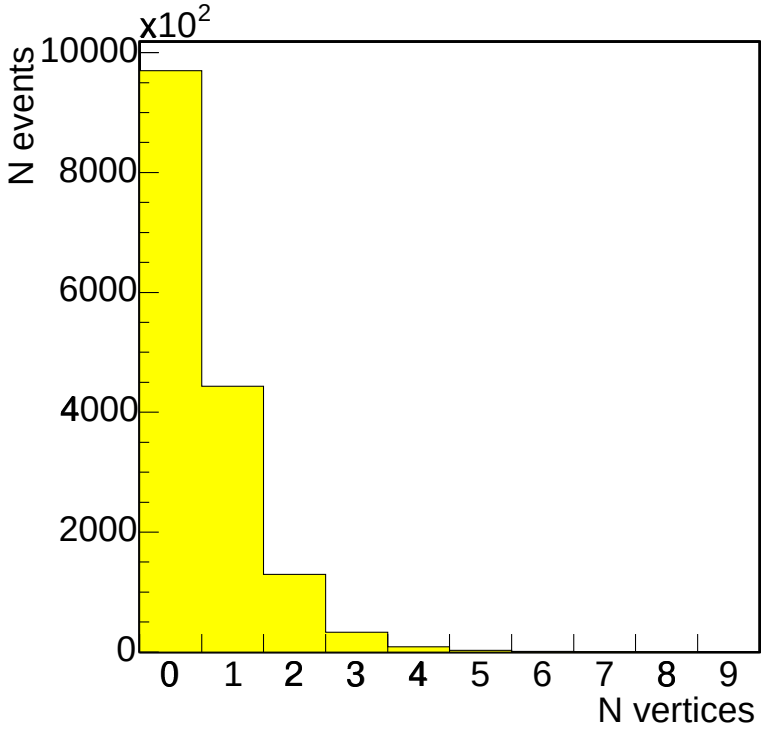

Figure 5-6: Distribution of the number of vertices in the `MET45` sample.

Some of the hadrons in a jet develop showers in the EM section of the calorimeter, therefore, a jet usually has both electromagnetic and hadronic energy components. The electromagnetic fraction (EMF) of a jet is defined as the fraction of the electromagnetic energy to the total jet energy. Beam halo particles deposit energy in either the EM or HAD calorimeters, producing a jet with an EM fraction close to 0 or 1. The Event Electromagnetic Fraction (EEMF) is defined as

$$EEMF = \frac{\sum_{j=1}^{N_{jet}} E_{\mathrm{T}}^{j} \cdot EMF_j}{\sum_{j=1}^{N_{jet}} E_{\mathrm{T}}^{j}}, \tag{5-1}$$

and EMF_j is the electromagnetic fraction of the jet. Only jets with $E_{\mathrm{T}} > 10$ GeV are considered. Figure 5-7 shows the event electromagnetic fraction distribution for QCD Monte Carlo and `JET50` data. Figure 5-8 shows the distribution of the event electromagnetic fraction versus missing-E_{T} in `JET50` data. The correlation between large missing-E_{T} and low EEMF (< 0.1) or high EEMF (> 0.9) can be

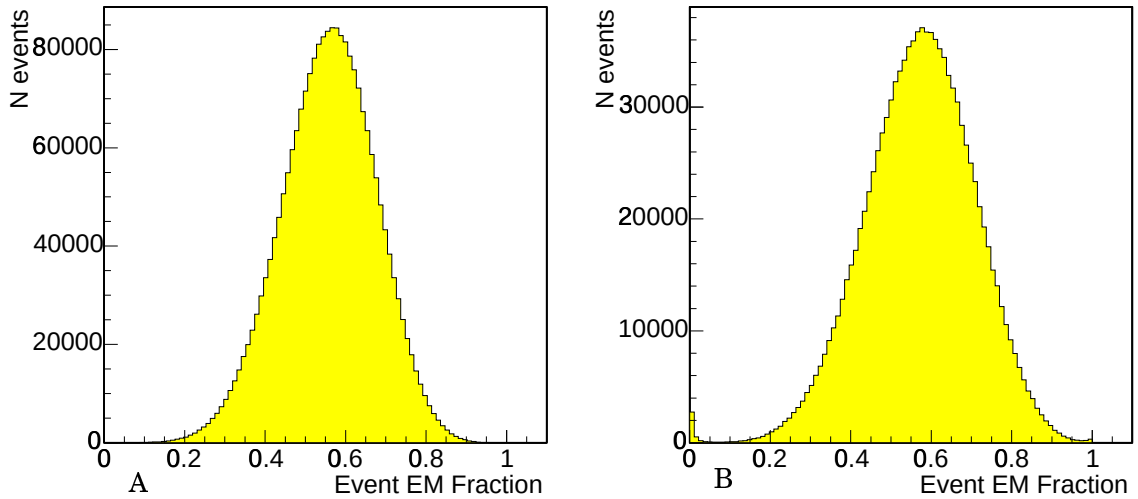

Figure 5-7: Event electromagnetic fraction distribution. Plot on the left shows the EEMF distribution for the QCD di-jet Monte Carlo events, plot on the right shows the EEMF distribution for `JET50` data.

clearly seen. The peak at EEMF< 0.1 for the data distribution is attributed to the non-collision backgrounds. Some of the events with EEMF> 0.9 can result from W or Z boson production, with an electron in the final state, which passes trigger the `JET50` trigger requirement.

Jet consists of both charged and neutral particles, hence there should be some tracks pointing from the event vertex in the jet direction. Tracks containing COT hits, with $P_{\mathrm{T}} > 0.5$ GeV and within 10 cm from the event vertex are associated to the jet by requiring that the track is within an η–ϕ cone of radius 0.4 from the jet centroid. The jet charge fraction is the defined as $CHF = \sum p_{\mathrm{T}}^{j}/E_{\mathrm{T}}^{j}$, where $\sum p_{\mathrm{T}}^{j}$ is the scalar sum of the transverse momenta of the tracks associated with the jet and E_{T}^{j} is transverse energy of the jet. The Event Charge Fraction (ECHF) is defined as:

$$ECHF = \sum_{j=1}^{N_{jet}} \frac{(\sum_{i}^{tracks} P_{\mathrm{T}i})_j}{E_{\mathrm{T}j}} \Big/ N_{jet}. \tag{5-2}$$

Jets with uncorrected $E_{\mathrm{T}} > 10$ and $\eta_d < 0.9$ are considered. Figure 5-9 shows the event charge fraction distribution for QCD Monte Carlo and `JET50` data. Figure

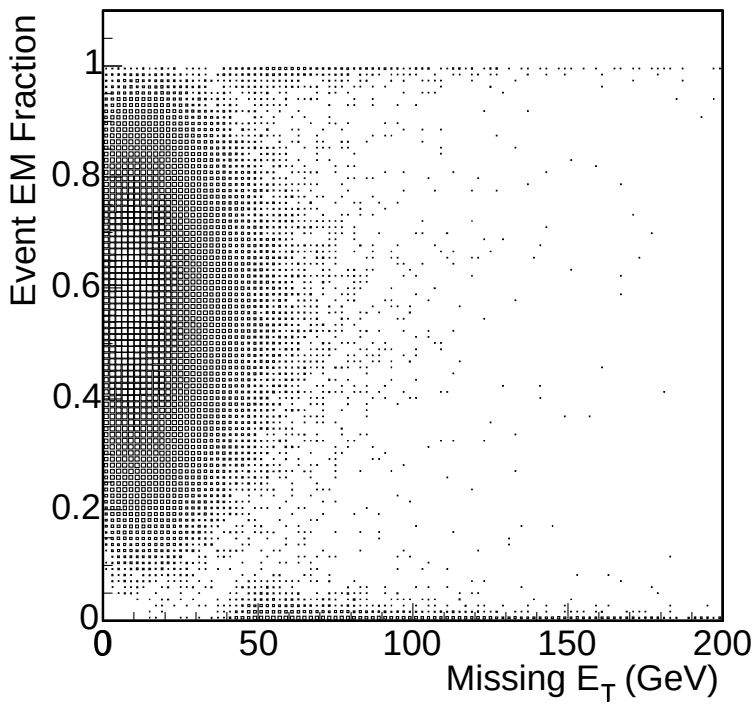

Figure 5-8: Distribution of the event electromagnetic fraction versus missing-E_{T} in `JET50` data.

5-10 shows the distribution of the event charge fraction versus missing-E_{T} in `JET50` data. The correlation between large missing-E_{T} and low ECHF (< 0.1) could be clearly seen. Therefore, the peak at ECHF< 0.1 for the data distribution is attributed to the non-collision backgrounds.

Figure 5-11 shows the event electromagnetic and charge fraction distribution for the inclusive `MET45` data sample. Figure 5-12 shows the distribution of the event charge fraction versus the event electromagnetic fraction for the inclusive `MET45` data sample. The regions with low (EEMF < 0.1) electromagnetic fraction and low charge fraction are attributed to the non-collision background. Smaller peak in the region with EEMF ≈ 1 and ECHF ≈ 1 is attributed to the events with electron in the final state from the W boson production.

Therefore, the following requirements were used as an initial data selection:

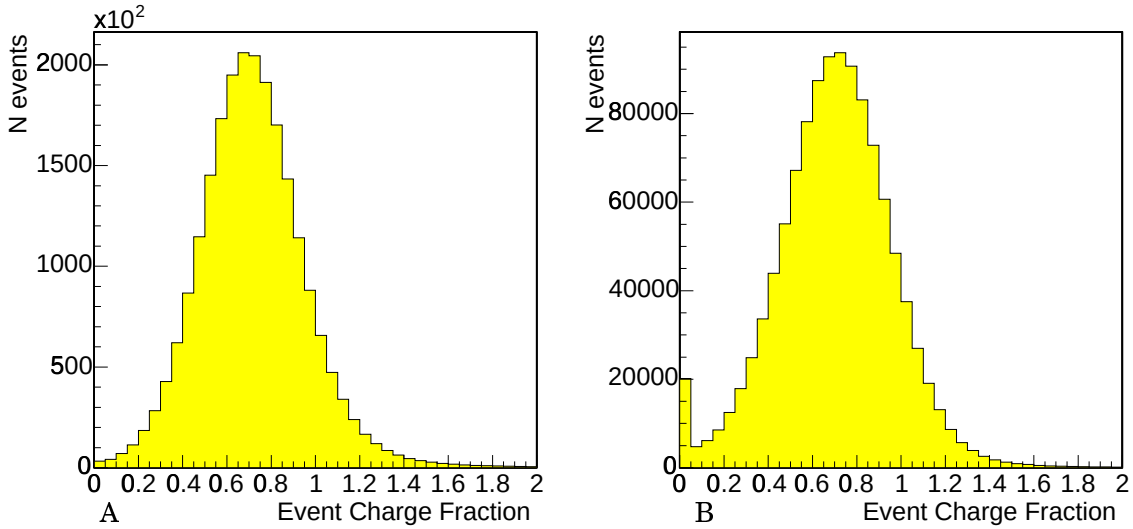

Figure 5-9: Event charge fraction distribution for `JET50` data sample and QCD di-jet Monte Carlo sample. A) Event charge fraction distribution for the QCD di-jet Monte Carlo events. B) Event charge fraction distribution for `JET50` data.

- At least one vertex with two or more COT tracks with $|Z_{vtx}| < 60$ cm is required.
- At least one central jet, $E_{\mathrm{T}} > 10$ GeV, $\eta_d < 0.9$
- The EEMF fraction is greater than 0.1.
- The ECHF fraction is greater than 0.1.
- Total calorimeter energy less than 2 TeV.

In addition, in our analysis dataset, we require that the missing-E_{T} reconstructed with the highest $\sum p_{\mathrm{T}}$ vertex be greater than 45 GeV. Table 5-1 summarizes the clean up cuts used for the initial data selection and shows the number of events surviving after each cut. Figure 5-13 shows the missing-E_{T} distribution for the events from the inclusive `MET45` data sample before and after applying pre-selection cuts (except the missing-$E_{\mathrm{T}} > 45$ GeV requirement). Events with missing-E_{T} below the trigger threshold are attributed to the difference in the calibration constants online and offline and to the corrections of missing-E_{T} for the event vertex position.

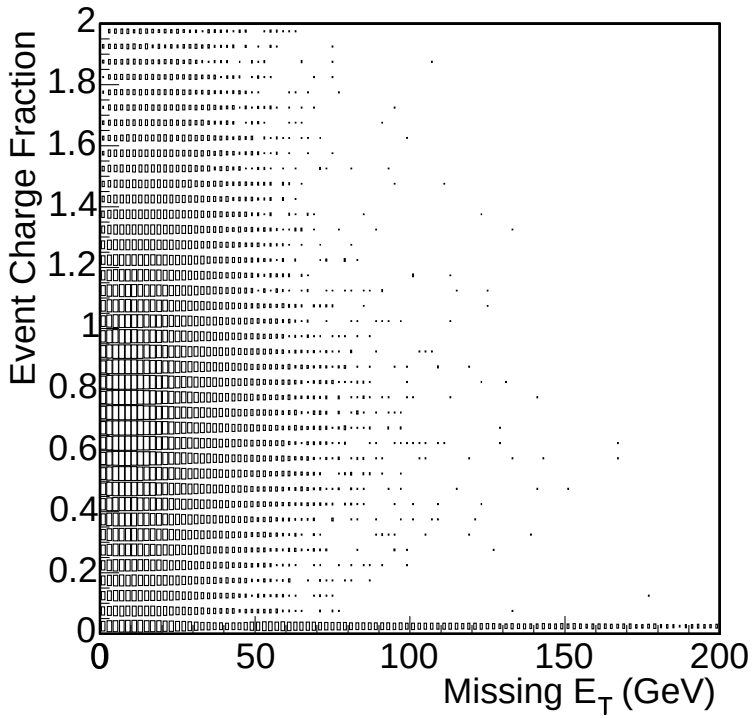

Figure 5-10: Distribution of the event charge fraction versus missing-E_{T} in `JET50` data.

Figure 5-14 shows the total scalar transverse energy distribution for the events from the inclusive `MET45` data sample before and after applying pre-selection cuts.

5.5 Trigger Efficiency

The selection efficiency of events with large missing-E_{T} is dependent on the online trigger. We measure the efficiency of the combined Level-1 and Level-3 trigger directly from the data using events from overlapping triggers. For this purpose, we choose two independent trigger paths, which contain events with a large spread in missing-E_{T} to measure the efficiency across full missing-E_{T} spectrum. The measured trigger efficiency is later applied to Monte Carlo samples to predict the number of background events from the Standard Model and to measure the signal acceptance.

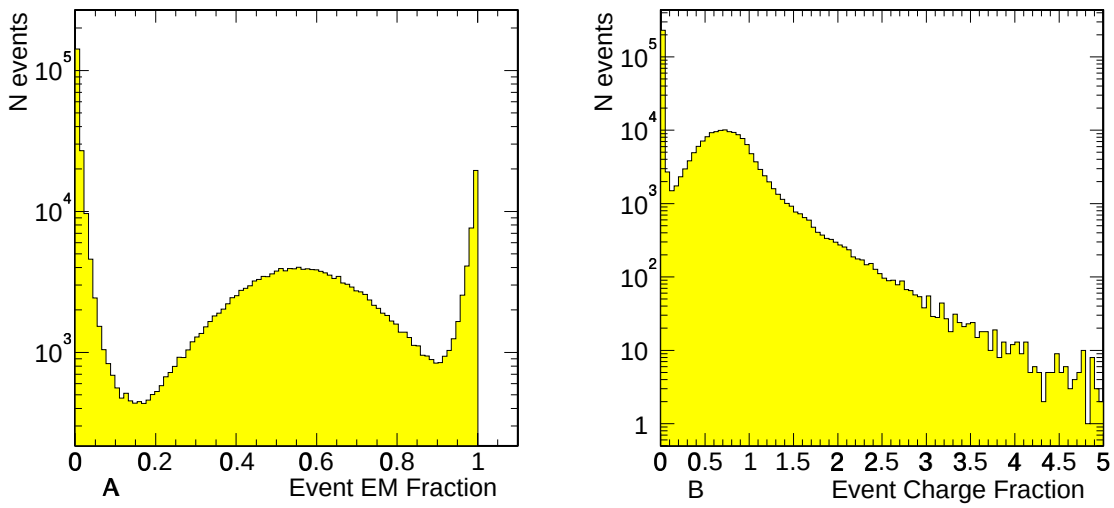

Figure 5-11: Distributions of event electromagnetic fraction and event charge fraction for `MET45` data. A) Event electromagnetic fraction. B) Event charge fraction.

Table 5-1: Event reduction in missing E_T sample.

Cut	# of Events
`MET45` sample	2173563
Good Run	1588592
Vertex requirement	508894
Central jet	382182
EEMF>0.1 and ECHF>0.1	148462
$\not\!\!E_{\mathrm{T}} > 45$ GeV	91525

As was mentioned before, there are two primary sources of large missing-E_{T}: weakly interacting particles and energy mismeasurement in the calorimeter. The efficiency to select events from these two different sources may not be necessarily the same. We use high-p_{T} electron and muon samples to measure the efficiency for missing-E_{T} from weakly interacting particles. A large fraction of events from those samples come from the leptonic decay of the W boson. Therefore, events in these samples have an intrinsic missing-E_{T}. In case of QCD muli-jet events, missing-E_{T} arises due to jet mismeasurements. We estimate the number of background events from QCD multi-jet processes directly from the inclusive `MET45` sample (section

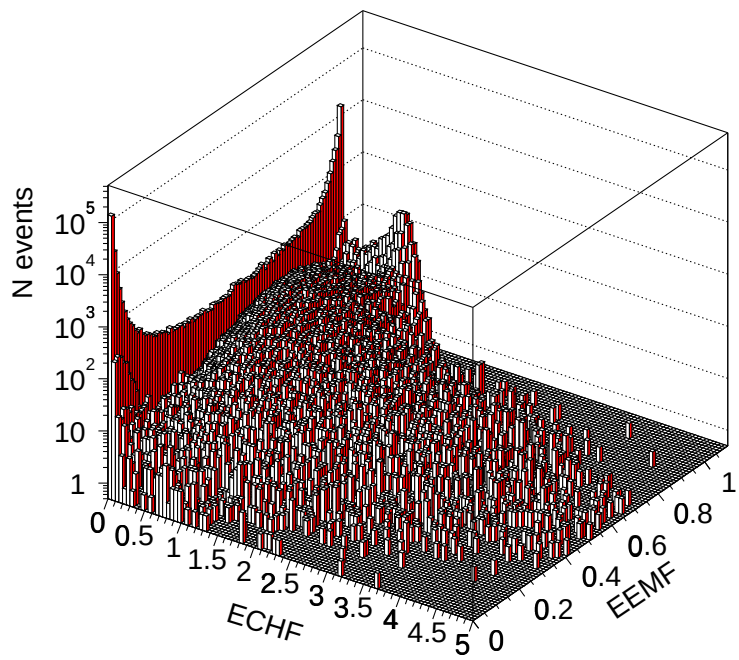

Figure 5-12: Distribution of the event charge fraction versus event electromagnetic fraction in the inclusive `MET45` data sample.

8.2). Events from this sample already have passed trigger requirement by definition and therefore, the trigger efficiency was already taken into account.

The combined Level-1 and Level-3 missing E_T trigger efficiency is defined as:

$$\epsilon(\texttt{MET45}) = \frac{\texttt{\#of events passing MET45 and high-}p_{\mathrm{T}}\texttt{ electron trigger}}{\texttt{\#total events passing high-}p_{\mathrm{T}}\texttt{ electron trigger}}, \quad (5\text{-}3)$$

or, in the case of the muon sample, events are required to pass the muon trigger instead of electron trigger. The trigger efficiency is measured with respect to the offline missing-E_{T} corrected for the vertex and jet energy corrections. We do not correct for missing-E_{T} resulting from muons, since we plan to exclude all events with identified leptons. Figure 5-15 shows the missing-E_{T} distribution in the high-p_{T} electron sample before and after the requirement that the `L3_MET_45` trigger bit was set. Figures 5-16 and 5-17 show the trigger efficiency curves from the high-p_{T}

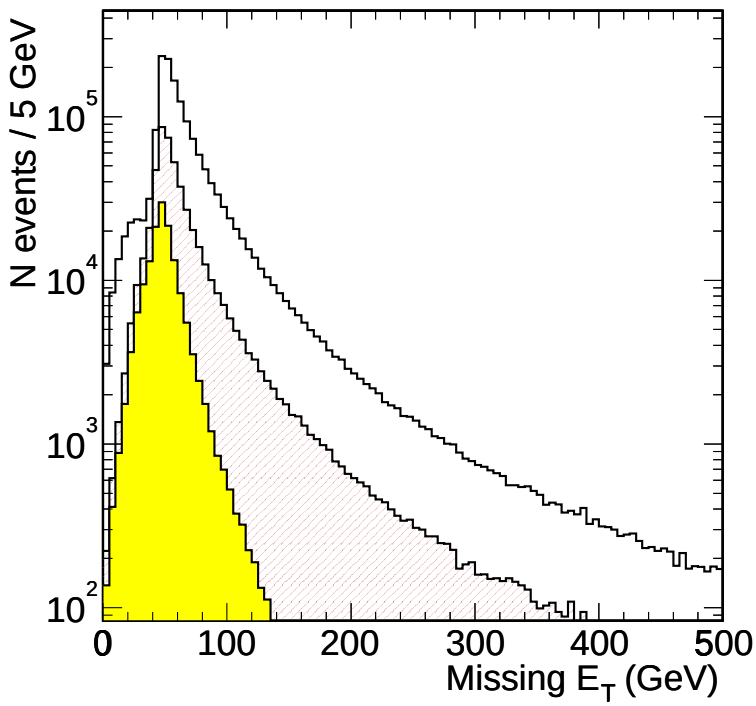

Figure 5-13: The missing-E_{T} distribution for the events from the inclusive `MET45` data sample. Open histogram shows the missing-E_{T} distribution after good run requirement, but before applying pre-selection cuts. Hatched histogram shows the missing-E_{T} distribution after vertex requirement and shaded histogram shows missing-E_{T} after applying all the pre-selection cuts, except the missing-$E_{\mathrm{T}} > 45$ GeV requirement.

electron and the high-p_{T} muon samples respectively. The trigger efficiency curves are fit with the function:

$$\epsilon(\not{E}_{\mathrm{T}}) = \epsilon_o + \frac{1-\epsilon_o}{1+exp(-\frac{\not{E}_{\mathrm{T}}-A_o}{\Delta})}. \tag{5-4}$$

The fit parameters for both samples are listed in Table 5-2. Although, slower turn-on is observed in high-p_{T} electron sample, the trigger turn-on curve reaches a plateau of 100% efficiency at around 60 GeV in both samples. The difference in the trigger turn on is attributed to the fact that muon is registered as a minimum ionizing particle in the calorimeter and thus contributes to the missing-E_{T}.

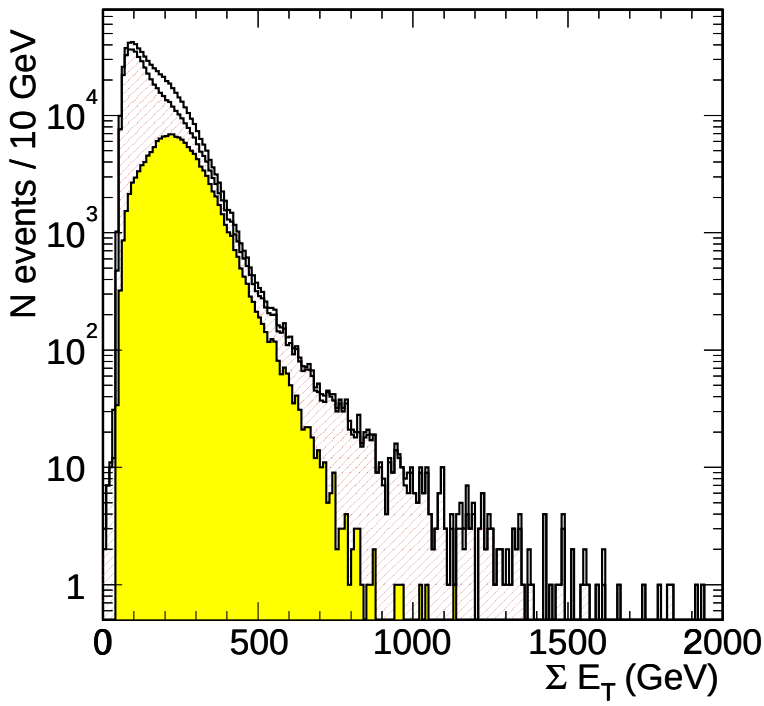

Figure 5-14: The total scalar transverse energy distribution for the events from the inclusive `MET45` data sample after good run requirement (open histogram), after vertex requirement (hatched histogram) and after applying all the pre-selection cuts except the missing-$E_{\mathrm{T}} > 45$ GeV requirement (shaded histogram).

Table 5-2: Parametrization of the missing-E_{T} trigger efficiency.

Sample	ϵ_o	A_o	Δ
`Electron Sample`	0.00006 ± 0.0002	47.5 ± 0.4	3.3 ± 0.2
`Muon Sample`	0.001 ± 0.004	51.4 ± 0.4	1.3 ± 0.2

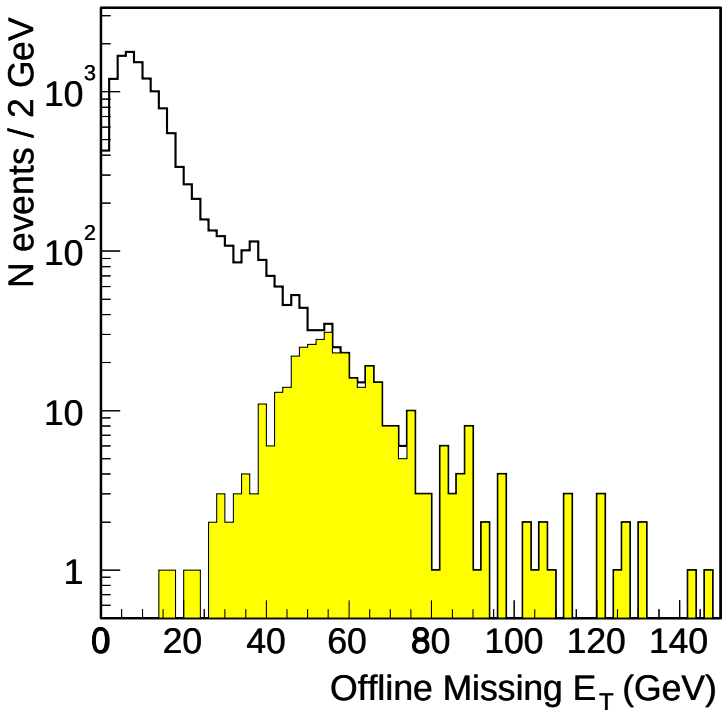

Figure 5-15: Missing-E_{T} distribution in the high-p_{T} electron sample. The empty histogram represents all events, the shaded histogram is after the `MET45` trigger requirement.

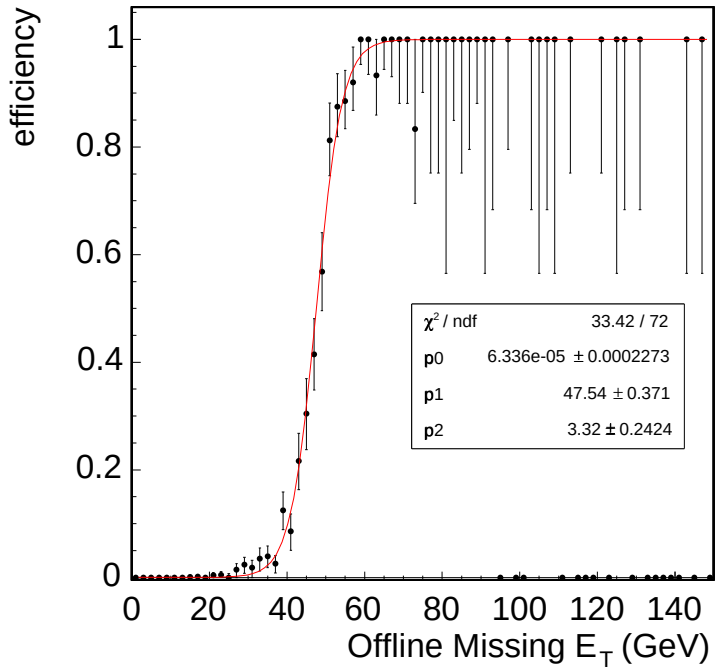

Figure 5-16: Efficiency of the `MET45` trigger as a function of offline missing-E_{T} from the high-p_{T} electron sample.

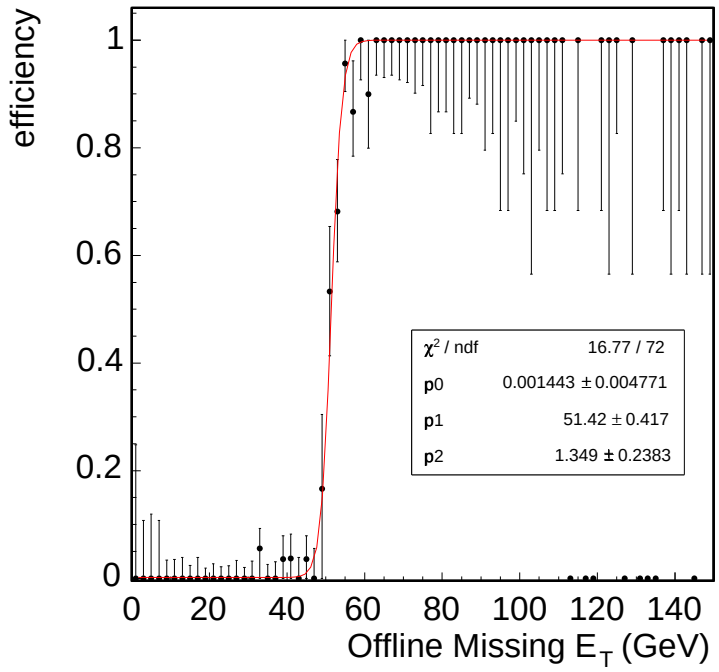

Figure 5-17: Efficiency of the `MET45` trigger as a function of offline missing-E_{T} from the high-p_{T} muon sample.

CHAPTER 6
STANDARD MODEL BACKGROUND

Standard Model processes are the main source of background in the search for new physics with large missing-E_{T} plus jets in the final state. Such processes include vector boson production (W, Z) in association with two or more jets, top pair production and QCD multi-jet production. The Monte Carlo samples used to estimate the Standard Model background are described in this chapter.

6.1 Electroweak Background

In $p\bar{p}$ collisions W and Z bosons can be produced in association with one or more hadronic jets. These jets arise from high energy quarks or gluons radiated of the incoming quarks. Events from the vector boson production in association with two or more jets are expected to be the dominant source of background. Such production results in the missing E_{T} + jets final state, when the boson decays to neutrinos, or when one of the decay products falls into an uninstrumented region or goes unidentified. Such processes include:

- $W^{\pm} \rightarrow \tau^{\pm}\nu + \geq$ 2 jets. Since the tau-lepton could decay hadronicaly it would be counted as a jet, thus this process represents an irreducible background process. In the case when the τ decays leptonically, the final lepton may fail identification cuts and fake the signal signature.
- $W^{\pm} \rightarrow l^{\pm}\nu + \geq$ 2 jets, where $l^{\pm}$ is a muon or electron. In this case the lepton may fall into a non fiducial region of the detector or fail the identification cuts, thus faking the signal.
- $Z \rightarrow \nu\bar{\nu} + \geq$ 2 jets, where the decay products are the same as in the signal, thus this channel represents an irreducible Standard Model background.
- $Z \rightarrow l^{+}l^{-} \geq$ 2 jets, where $l^{\pm}$ is a muon or tau-lepton and fails the identification criteria.

The samples of the W and Z boson plus jets were created using the ALPGEN Monte Carlo event generator [84]. This generators performs an exact calculation of the matrix element to first order in α_s for a large set of parton level process, namely for $W + n$ partons and $Z + n$ partons, where $n = 0, 1, 2, 3, 4$. The generated parton level events have complete quantum mechanical information and can be used later in parton shower development and hadronization programs. The following parameters were used at the parton level generation:

- The renormalization scale $Q^2 = (p_{\mathrm{T}}^{bos})^2 + \sum_i^{N\ partons} (p_{\mathrm{T}i}^{parton})^2$, where p_{T}^{bos} is the transverse momentum of the vector boson and $\sum_i^{N\ partons} p_{\mathrm{T}i}^{parton}$ is the sum of transverse momenta of the outgoing partons.
- The charged lepton (in case of W or Z boson) or neutrino (in case of Z boson) from the boson decay is required to have $p_{\mathrm{T}} > 1$ GeV/c and $|\eta| < 6$
- At least 2 final state partons.
- The final state quark or gluon is required to have $p_{\mathrm{T}} > 8$ GeV/c and $|\eta| < 3$.
- The final state partons are required to be separated by more than 0.2 in η-ϕ space, to avoid 2 partons being reconstructed as one jet.
- The CTEQ5L parton-distribution functions were used.

We generate exclusive samples for each charged lepton generation. The $Z \rightarrow e^+e^- + 1$ parton was generated to normalize the MC background prediction to the $Z \rightarrow e^+e^-$+jets observed data as described in section 8.1. In addition, an exclusive sample with $Z \rightarrow \nu\bar{\nu} + 2$ jets was generated as well. The specific background channels simulated are listed in Table 6-1.

The output from the ALPGEN generator was fed to the Herwig Monte Carlo program [85] for parton showering and hadronization. Herwig is a general-purpose particles physics event generator. It uses the parton-shower model for the initial- and final-state QCD radiation with color coherence effects and azimuthal correlations, and a cluster model for parton hadronization.

Table 6-1: List of MC background samples used, number of events generated, leading-order cross section, and equivalent integrated luminosity.

Background Channel	Number of events	σ(LO) (pb)	Luminosity (pb^{-1})
$W \to e\nu + 2$ jets	187.5K	258.7	538.33
$W \to \mu\nu + 2$ jets	260K	258.7	746.48
$W \to \tau\nu + 2$ jets	127.5K	258.7	366.06
$Z \to ee + 1$ jets	295K	64.23	4593
$Z \to \mu\mu + 2$ jets	161K	23.3	4597
$Z \to \tau\tau + 2$ jets	167.5K	23.3	4785
$Z \to \nu\nu + 2$ jets	170K	139.8	809
$t\bar{t}(m = 175\ GeV)$ inclusive	38K	7	5428

6.2 Multi-Jet QCD Background

Light quark or gluon production are the most dominant processes in $p\bar{p}$ collisions at the Tevatron. Those events usually have two or more jets in the final state and usually no large intrinsic missing-E_{T}. However, one or more jets from these QCD multi-jet process could be mismeasured, and thus create significant missing-E_{T}.

The QCD multi-jet events were generated using the Pythia MC generator [86] with CTEQ5L parton-distribution functions. Pythia uses tree-level matrix element calculations for the parton hard scattering to first order in α_s. We generate $2 \to 2$ QCD processes. [1] Higher jet multiplicities are achieved through initial- and final-state QCD radiation. Quark/anti-quark pairs and gluons from the initial- and final-state radiation are hadronized according to the string fragmentation model. In a typical proton-antiproton collision, in addition to the particles from the hard 2-to-2 parton scattering, there are a number of particles from the breakup of the proton and antiproton (*i.e.* "beam-beam" remnants). The "underlying event" includes beam-beam remnants and contributions from initial- and final-state

[1] option `msel = 1`

radiation and excludes two outgoing hard scattered partons. Pythia models an underlying event in a $p\bar{p}$ collision by including multiple parton interactions. The underlying event in Pythia was tuned to fit the CDF data [87].

Two large samples of 500,000 and 3.3 million QCD-dijet events were produced with hard scattering transverse momentum of the outgoing partons $\hat{p}_{\mathrm{T}}^{min} >$ 60 and 80 GeV. The leading order cross-section for QCD-dijet process with $\hat{p}_{\mathrm{T}}^{min} > 80$ GeV, as reported by Pythia, is 3.95×10^4 pb, and the corresponding luminosity of this sample is 86 pb^{-1}.

6.3 The $t\bar{t}$ Background

Pair production of top quarks is expected to be another source of background events. The top quark decays to a b quark and a W boson, thus it will have a missing-E_{T} + jets signature when one or more W decay products escape detection. An inclusive $t\bar{t}$ sample was produced using the Herwig MC generator (with top mass set to 175 GeV/c^2).

6.4 Detector Simulation

In Run II CDF uses a simulation program based on the GEANT detector simulation package [58]. The GEANT program provides a framework for uniform geometry description for all different detector components. It decays and propagates the generated particles and models their interactions with the detector material. The calorimeter simulation uses GEANT for the detector geometry description and models the detector response based on the fast simulation of electromagnetic and hadronic showers (GFLASH) [88], which allows to reduce significantly the generation time.

The output from the event generators, after parton shower and hadronization, is used as input to the detector simulation program. The simulation program produces raw-data banks as if there were created from the real detector data. At

this point, we use the same reconstruction and analysis software for the Monte Carlo events as for data.

CHAPTER 7
LEPTOQUARK SELECTION CUTS

The cross-section for Standard Model processes in the missing-E_{T} plus jets channel is several orders of magnitude higher than that of the possible signal from new physics. Therefore, some selection mechanism is needed to maximize analysis sensitivity to this signal. Kinematical distribution of the leptoquark signal, generated using Monte Carlo programs, are compared with background distributions. Selection cuts are derived in order to maximize the statistical significance of a possible excess due to the signal events.

7.1 Signal Monte Carlo

A simulation of the first-generation scalar leptoquark signal was done for 9 mass points (60, 75, 80, 90, 100, 110, 115, 125, 150 and GeV/c^2) with the Pythia event generator. The CTEQ5L parton-distribution functions are used and the underlying event is tuned as in the QCD MC generation, described in Section 6.2. We generated 30,000 events for each mass point, except for the leptoquark mass of 60 GeV/c^2, where 78,000 events were generated.

The Pythia output was run through the simulation and reconstruction programs as described in section 6.4.

7.2 Signal and Background Kinematical Distributions

We use the signal and background Monte Carlo samples to compare kinematical distributions. The analysis strategy is to identify such variables that discriminate the signal from the background the most. Then we can place cuts on such variables, with the intention to retain as much signal events as possible while keeping the number of background events small. We use the signal MC sample

generated with a leptoquark mass of 100 GeV/c^2 for these optimization studies, since we would like to extend the current limit of 98 GeV/c^2.

We first look at the kinematical distributions of the leptoquark decay products at the generator level. Figure 7-1 shows the transverse momentum and pseudo-rapidity distributions of the quarks appearing from the decay of pair of leptoquarks. Usually, a heavy particle gets litle boost in the longitudinal direction, since most of the initial parton energy goes into the particle creation. Figure 7-2

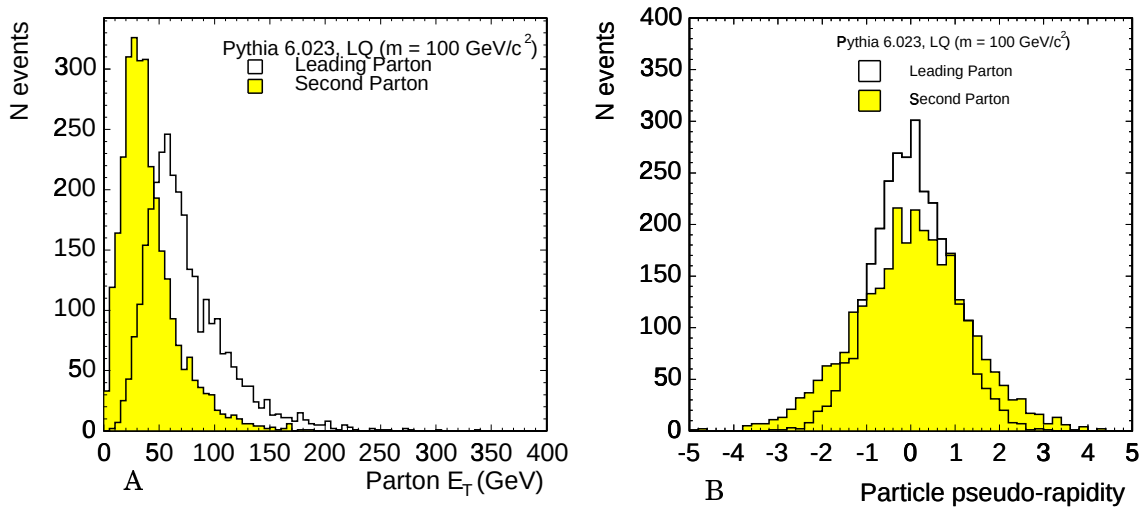

Figure 7-1: Kinematic distribution of quarks from leptoquark decay. The left plot shows the transverse momentum and the plot on the right shows pseudo-rapidity distributions of the quarks appearing from the decay of pair of leptoquarks.

shows the projection in the transverse plane of the vector sum of the momenta from the two neutrinos from the leptoquark decays. It gives an idea of the size of the expected momentum imbalance due to our inability to detect neutrinos.

We next compare the shapes of the distributions for signal and for background for the following variables after detector simulation and reconstruction: missing transverse energy, jet transverse energies, pseudo-rapidity of the jets, the angle between the two most energetic jets, the angle between the highest energetic jet and missing-E_{T} direction, the separation between the missing-E_{T} direction

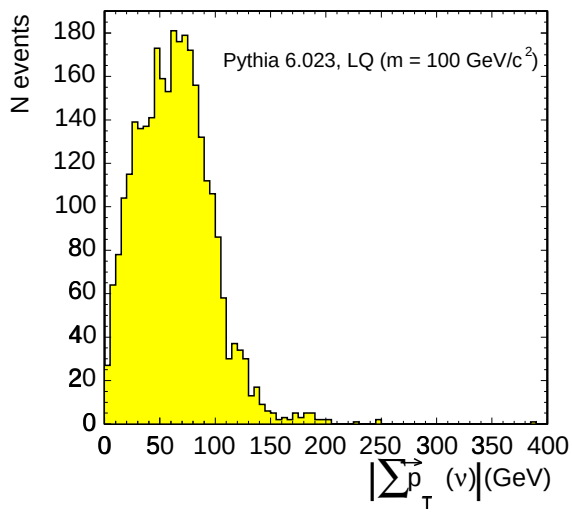

Figure 7-2: Vector sum of the transverse momenta from the two neutrinos from the leptoquark decays.

and direction of any jet in ϕ and the number of tracks associated to the jet. We normalize the distributions for the missing-E_{T} and jet transverse energies to the number of events expected in 191 pb^{-1} of data. The rest of the distributions are normalized to unit area.

Our signal is expected to have large missing-E_{T} since the final state includes two neutrinos that carry away part of the LQ momentum and escape detection. On the other hand, we expect somewhat smaller missing-E_{T} from the electroweak background, since only one neutrino is typically present; and we do not expect large missing-E_{T} for the QCD multi-jet events (however the cross section is much larger). Figure 7-3 compares the missing-E_{T} distribution for signal and background events.

Figures 7-4 and 7-5 show the leading- and second-leading jet E_{T} distribution. The jets in the electroweak processes are mostly due to quark and gluon radiation and thus are not as energetic as from LQ decay or as from $2 \rightarrow 2$ QCD process.

Jets from leading order QCD processes are expected to be back-to-back in ϕ and more boosted in the forward and backward regions than LQ jets due to the color connection of the initial and final state partons. Figures 7-6, 7-7 and 7-8 show

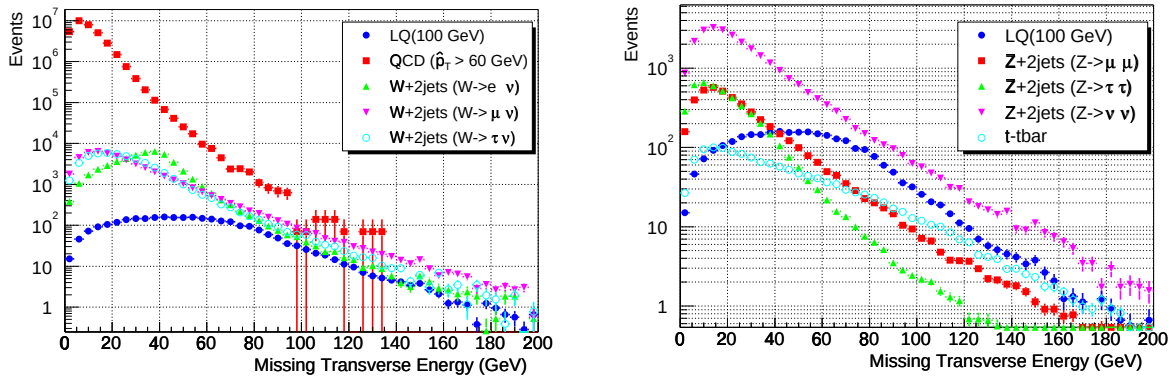

Figure 7-3: Missing-E_{T} distribution for the pair production of first generation leptoquarks ($m_{\mathrm{LQ}} = 100$ GeV/c^2) compared to the missing-E_{T} distributions for the dominant Standard Model background processes.

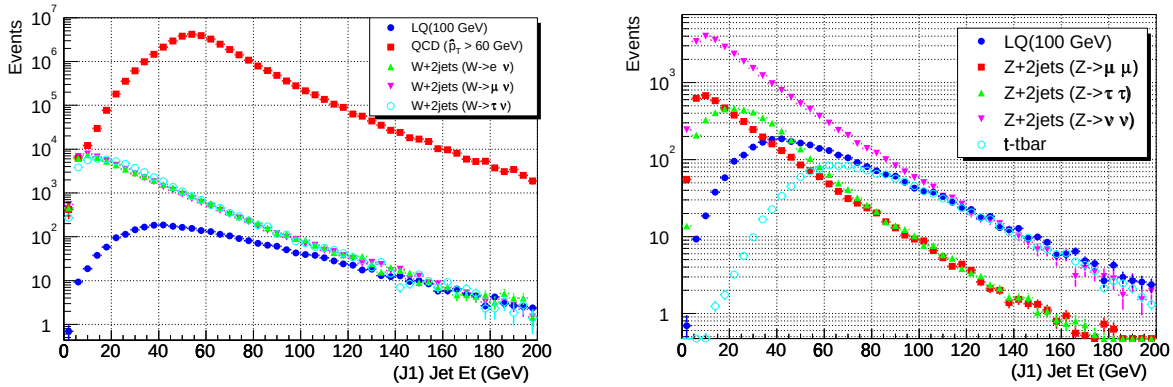

Figure 7-4: Comparison of the E_{T} distributions for the first-leading jet (J1) for leptoquark pair production and for the dominant Standard Model processes.

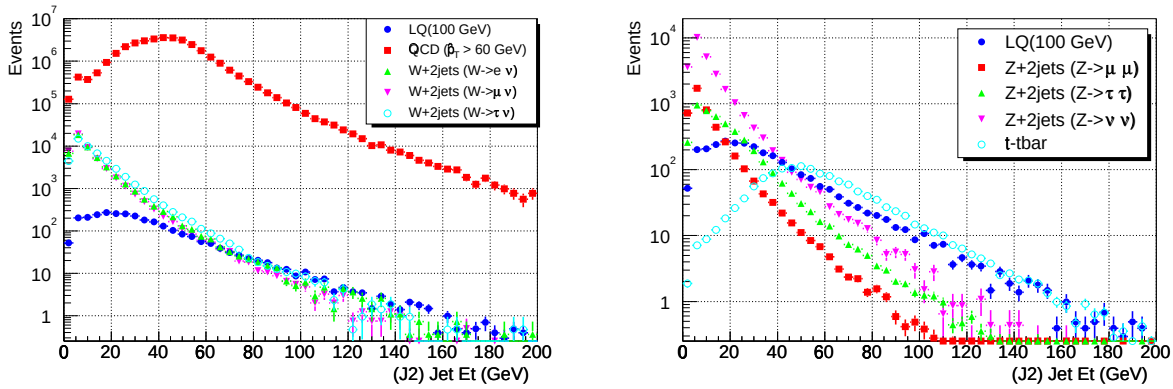

Figure 7-5: Comparison of the E_{T} distributions for the second-leading jet (J2) for the leptoquark pair production and for the dominant Standard Model processes.

the pseudo-rapidity distribution of the two leading jets and opening angle between them in the transverse plane respectively. The peak around 30° on the distributions for the electroweak processes is attributed to gluon splitting into two quark jets.

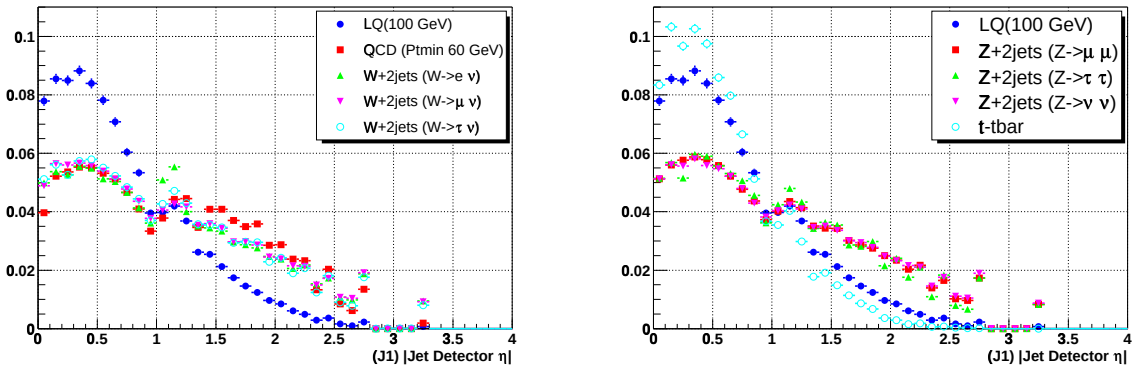

Figure 7-6: Pseudo-rapidity distribution of the first-leading jet (J1) for the leptoquark pair production and for the dominant Standard Model processes. The distributons are normalized to unit area.

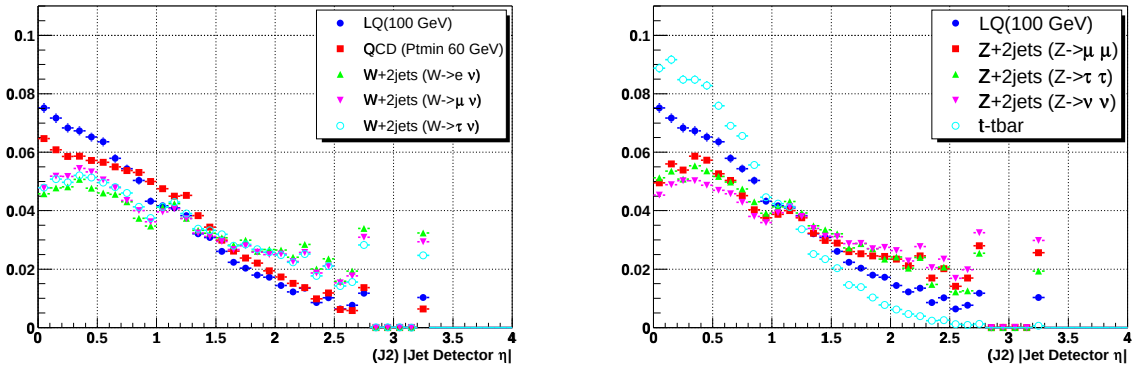

Figure 7-7: Pseudo-rapidity distribution of the second-leading jet (J2) for the leptoquark pair production and for the dominant Standard Model processes. The distributons are normalized to unit area.

In events with no neutrinos, missing-E_{T} appears mostly due to jet mismeasurement. Thus, in the di-jet events, the missing-E_{T} direction will be either parallel to or anti-parallel to the mismeasured jet in the transverse plane. Figure 7-9 shows the difference in azimuth of the highest energetic jet and the missing-E_{T} direction.

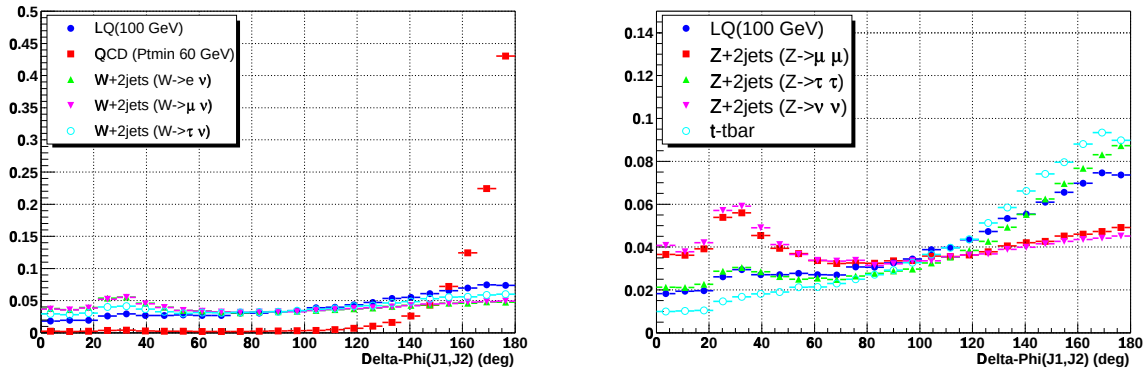

Figure 7-8: The distribution of the azimuthal angular separation between the first- and second-leading jets for the leptoquark pair production and for the dominant Standard Model processes. The distributons are normalized to unit area.

Figure 7-10 shows separation in the azimuthal direction between the missing-E_{T} direction and the closest jet in ϕ for leptoquark pair production and for the dominant Standard Model processes.

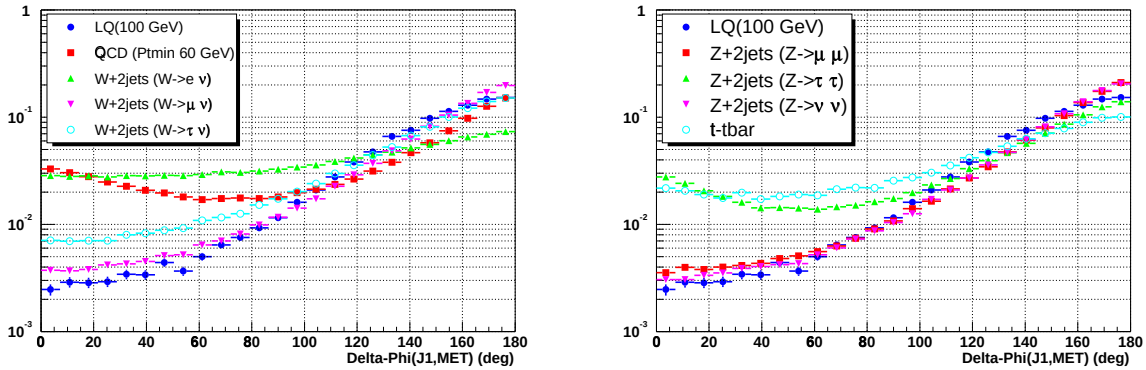

Figure 7-9: The distribution of the azimuthal angular separation between the directions of the first leading jet and the missing-E_{T} for leptoquark pair production and for the dominant Standard Model processes. The distributons are normalized to unit area.

Tau-leptons (arising from the decays of W and Z, for example) that decay hadronicaly are reconstructed as jets in the detector. Electrons that fail identification would also appear as a jet. However jets from misidentified leptons would have fewer tracks on average than a jet originating from a quark or gluon. Figure 7-11

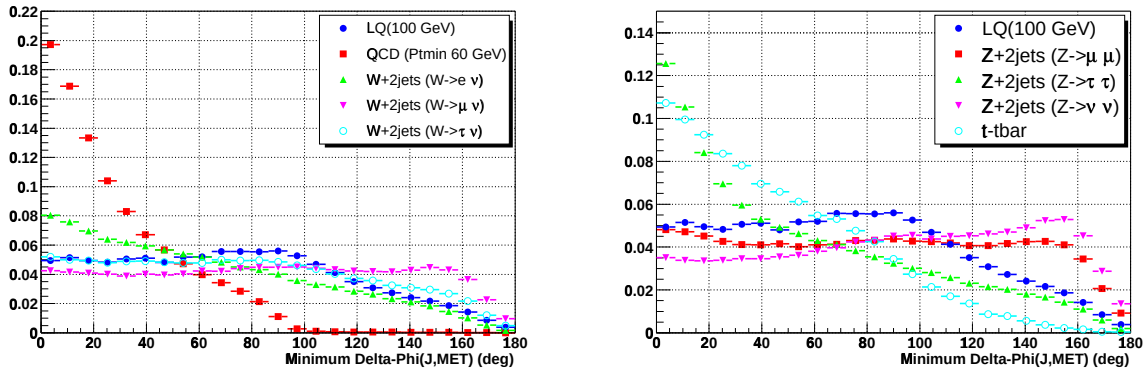

Figure 7-10: The distribution of the minimum azimuthal angular separation between the directions of the jets and the missing-E_{T} direction for the leptoquark pair production and for the dominant Standard Model processes. The distributons are normalized to unit area.

shows the distribution of the number of tracks associated to the jet, for the jets in the event with $|\eta| < 1$ and least tracks, for the signal and background.

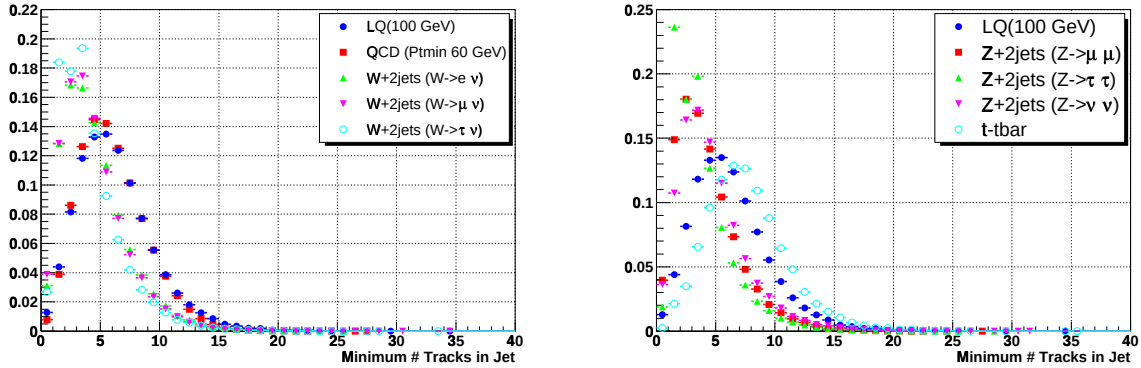

Figure 7-11: The distribution of the number of tracks in central jets for leptoquark pair production and for the dominant Standard Model processes. The distributons are normalized to unit area.

7.3 Acceptance

The number of expected signal or background events after all cuts is given by:

$$N_{\mathrm{exp}} = \sigma_{\mathrm{tot}} \times L \times a, \tag{7-1}$$

where σ_{tot} is the process production cross-section, L is the total luminosity of the data sample and a is the acceptance for the process under consideration after all cuts. The acceptance is defined as:

$$a = \frac{N_{\text{acc}}}{N_{\text{tot}}}, \tag{7-2}$$

where N_{acc} number of the events that pass all the selection cuts and N_{tot} is the total number of events. The acceptances are measured separately for signal and for each background process using our Monte Carlo samples. Therefore, N_{tot} is the total number of the generated events for the given process.

7.4 Cut Optimization

We would like to define a region in a multi-variable space where signal production is dominant over the Standard Model background processes. Therefore, we impose a cut on each variable that we described in the previous section. The selection of threshold values for those variables were determined in the following steps.

First, we select events with large missing-E_{T} and require at least 2 jets. Events with 3 jets are allowed since the jet multiplicity in the signal events could be enhanced due to initial or final state QCD radiation. The cut on the missing-E_{T} is chosen to be at 60 GeV or larger, where the the trigger efficiency turn-on curve reaches the plateau region. We remove events with identified electrons or muons in order to suppress electroweak backgrounds and $t\bar{t}$ pair production. Table 7-1 and 7-2 lists loose electron and muon identification cuts respectively, which are used for lepton veto. In addition, the electromagnetic fraction of the jet is required to be between 0.1 and 0.9 to further suppress fake electrons from jets and cosmic ray background.

At the next step, we choose the cut value for a variable to maximize the significance of the excess that would arise due to the signal events. The significance

Table 7-1: Loose central and plug electron identification cuts used for electron veto.

Variable	Central	Plug
E_{T}	> 10 GeV	> 10 GeV
HAD/EM	< 0.1	< 0.1
E/p	< 2.0	
L_{shr}	< 0.2	
$\lvert\Delta x\rvert$	< 3.0 cm	
$\lvert\Delta z\rvert$	< 3.0 cm	
χ^2_{strip}	< 10	< 10

Table 7-2: Loose central muon identification cuts used for muon veto.

Variable	CMU	CMP	CMU-CMP	CMX	Stub-less Muon
p_{T}	> 10 GeV	> 10 GeV	> 10 GeV	> 10 GeV	> 10 GeV
EM	< 2 GeV	< 2 GeV	< 2 GeV	< 2 GeV	< 2 GeV
HAD	< 6 GeV	< 6 GeV	< 6 GeV	< 6 GeV	< 6 GeV
$EM + HAD$	> 0.1 GeV	> 0.1 GeV	> 0.1 GeV	> 0.1 GeV	> 0.1 GeV
d_0	< 0.5 cm	< 0.5 cm	< 0.5 cm	< 0.5 cm	< 0.5 cm
Z_0	< 60 cm	< 60 cm	< 60 cm	< 60 cm	< 60 cm
$\lvert\Delta x_{CMU}\rvert$	< 3.0 cm		< 3.0 cm		
$\lvert\Delta x_{CMP}\rvert$		< 6.0 cm	< 6.0 cm		
$\lvert\Delta x_{CMX}\rvert$				< 8.0 cm	
I					< 5 GeV

is defined in terms of the number of standard deviations from the number of observed events assuming that the signal and background events are distributed according to Poisson statistics for the variable under consideration:

$$S = \frac{N_{\mathrm{signal}}}{\sqrt{N_{\mathrm{background}} + N_{\mathrm{signal}}}}, \tag{7-3}$$

where N_{signal} and $N_{\mathrm{background}}$ are the number of signal and background events, respectively. This procedure gives us an estimate of the threshold for the variable under consideration, since it does not account for the possible systematic errors in the calculation of the number of background events. For this procedure, we

normalize the luminosity of the signal and the Standard Model samples to the luminosity of the inclusive missing-E_{T} data sample.

To select a maximum (minimum) cut value we integrate the number of events for both signal and the Standard Model histogram from the left (right). The bin where the significance reaches a maximum a good place to cut on. In the following, every cut optimization is done after all previous cuts have been applied already. The arrows in the histograms indicate the cut values and the regions that are kept.

The preselected events are still dominated by the QCD multi-jet events, after requiring large missing-E_{T} and at least 2 jets in the event. Figure 7-12 shows the significance curves for the azimuthal separation between the first-leading jet and the missing-E_{T} direction.

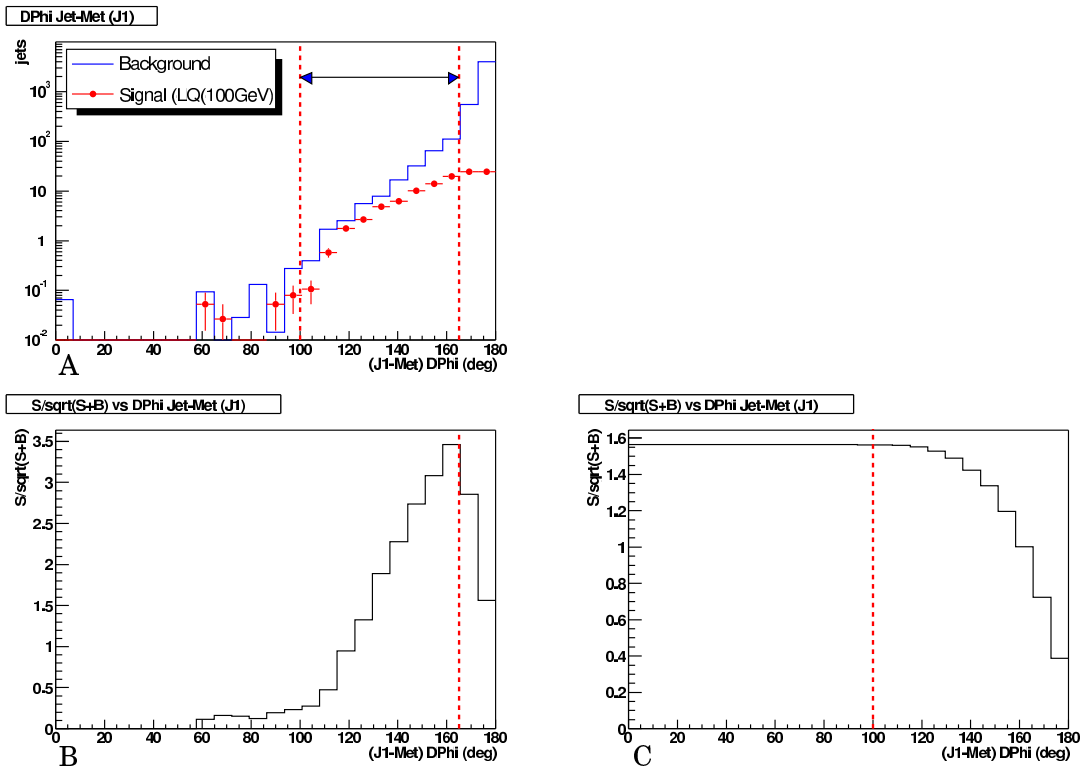

Figure 7-12: Optimization of the cut on the azimuthal angle between the first-leading jet and the missing-E_{T} direction in ϕ. A) The distribution of the azimuthal angle between the first-leading jet and the missing-E_{T} direction in ϕ from lepto-quark pair production, and from Standard Model processes. B), C) These are the $\mathrm{S}/\sqrt{\mathrm{S}+\mathrm{B}}$ distributions of the parameter shown in A).

For the next optimization step, we select events where the two leading jets are not back-to-back in azimuth and the missing-E_{T} is not anti-parallel to the most energetic jet in the event. The significance curves for the azimuthal separation between the first- and second-leading jets are shown on Figure 7-13.

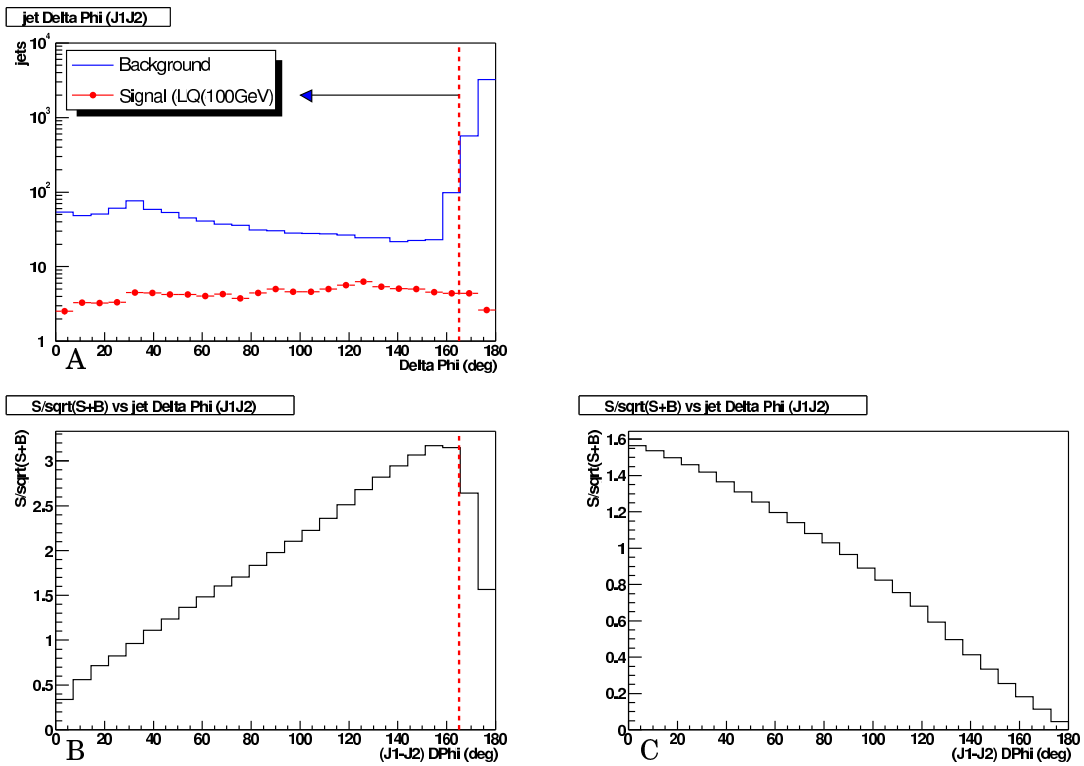

Figure 7-13: Optimization of the cut on the azimuthal angle between the first- and second-leading jets. A) The distribution of the azimuthal angle between the first- and second-leading jets from leptoquark pair production and from Standard Model processes. B), C) These are the $\mathrm{S}/\sqrt{\mathrm{S}+\mathrm{B}}$ distributions of the parameter shown in A).

At the next step, we optimize the selection on the transverse energy of the first two leading jets. Figures 7-14 and 7-15 show the significance optimization curves for those distributions as well as the selected cut values.Figures 7-16 and 7-17 show the significance optimization curves for the pseudo-rapidity of the first- and second-leading jets as well as the selected cut values. Although the cut $|\eta| < 1$ for the first and second jet does not give a maximum in significance, we choose this value in order to reduce the uncertainty on the jet energy measurement in the

crack regions of the calorimeter. Figure 7-18 shows the cut optimization for the requirement on the third jet pseudo-rapidity.

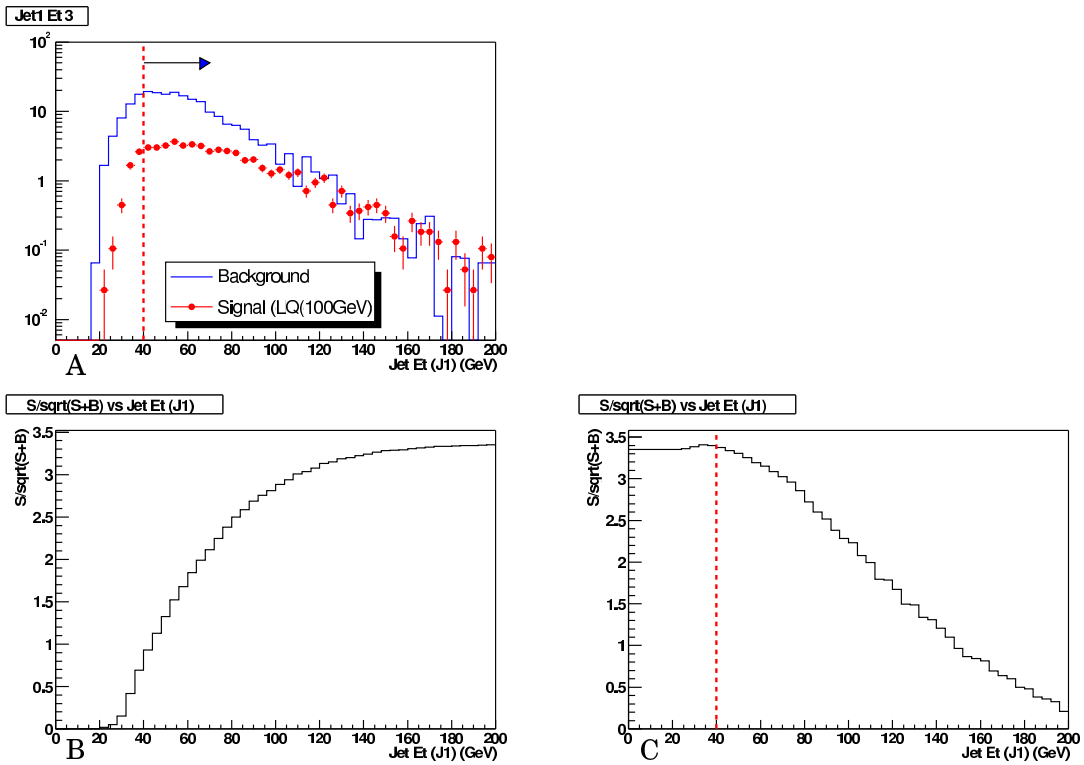

Figure 7-14: Optimization of the cut on the transverse energy of the first-leading jet. A) The distribution of the transverse energy of the first-leading jet from leptoquark pair production and from Standard Model processes. B), C) These are the $S/\sqrt{S+B}$ distributions of the parameter shown in A).

Finally, we require that the missing-E_T direction is not parallel in ϕ to any of the jets, which would indicate a jet energy mismeasurement. Figure 7-19 shows that cut optimization for the azimuthal angle between the missing-E_T direction and closest jet in ϕ for the leptoquark pair production and the Standard Model processes. To further suppress background events from electroweak processes, where W decays to τ-lepton and neutrino, we require that the number of the tracks associated to each jet is greater than 4, as illustrated by the significance curves shown in Figure 7-21.

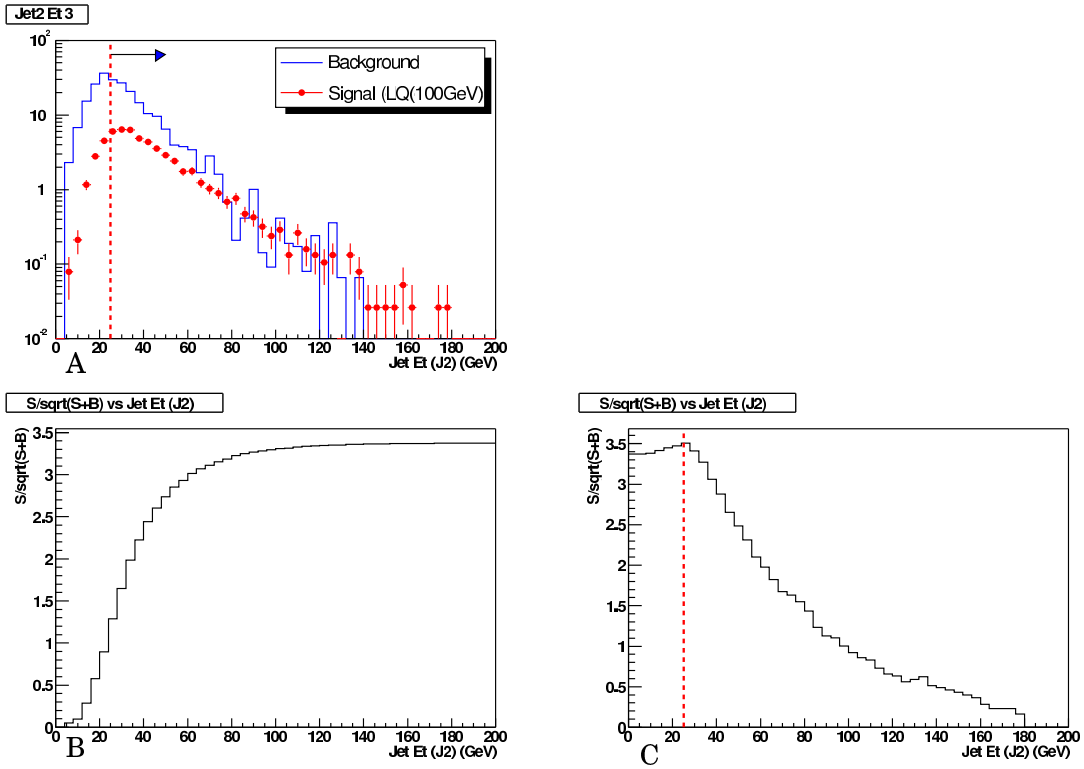

Figure 7-15: Optimization of the cut on the transverse energy of the second-leading jet. A) The distribution of the transverse energy of the second-leading jet from leptoquark pair production and from Standard Model processes. B), C) These are the $S/\sqrt{S+B}$ distributions of the parameter shown in A).

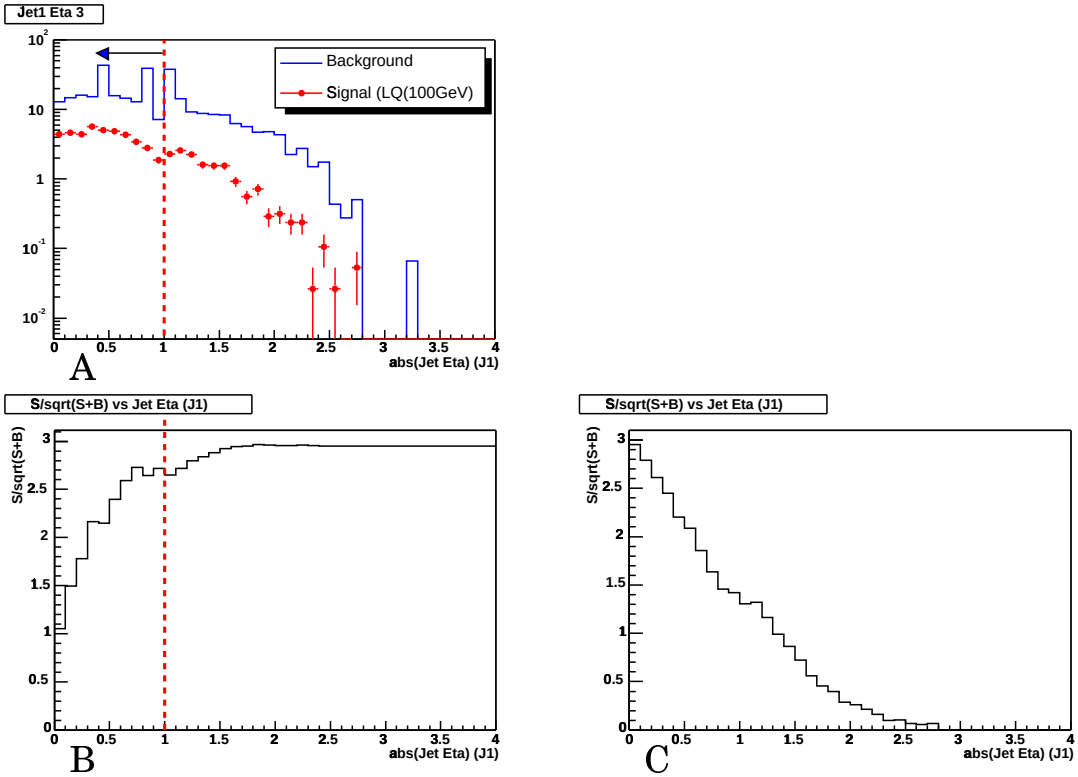

Figure 7-16: Optimization of the cut on the pseudo-rapidity of the first-leading jet. A) The distribution of the pseudo-rapidity of the first-leading jet from lepto-quark pair production and from Standard Model processes. B), C) These are the $S/\sqrt{S+B}$ distributions of the parameter shown in A).

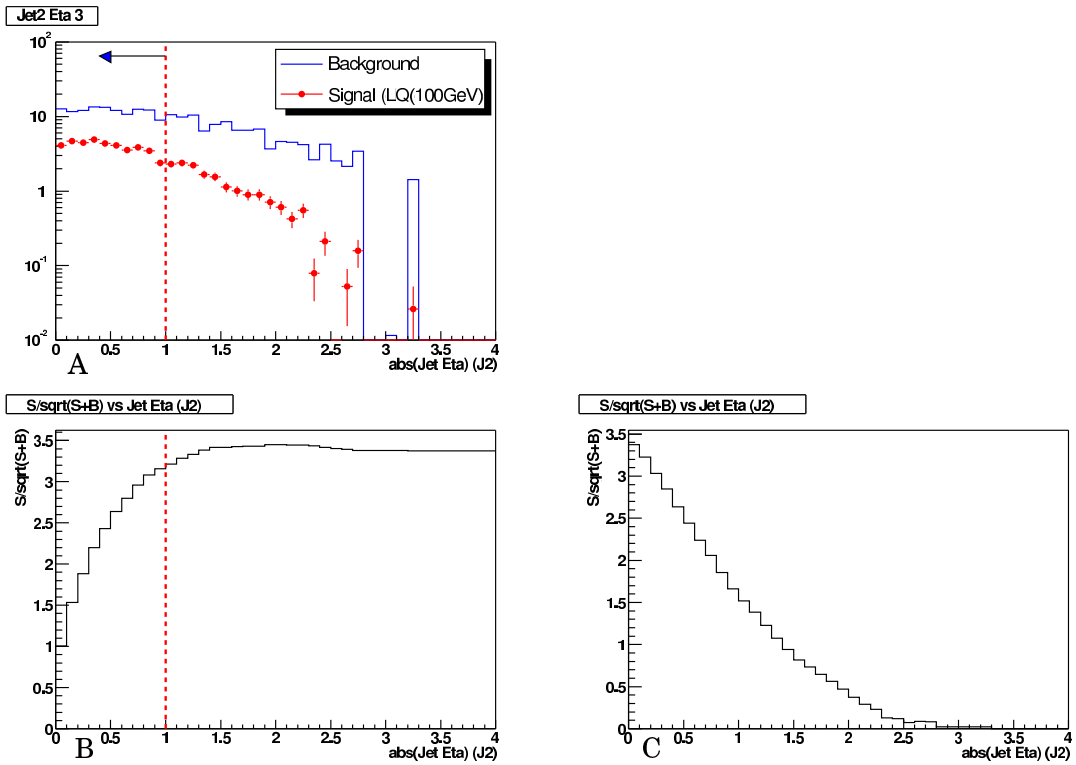

Figure 7-17: Optimization of the cut on the pseudo-rapidity of the second-leading jet. A) The distribution of the pseudo-rapidity of the second-leading jet from leptoquark pair production and from Standard Model processes. B), C) These are the $S/\sqrt{S+B}$ distributions of the parameter shown in A).

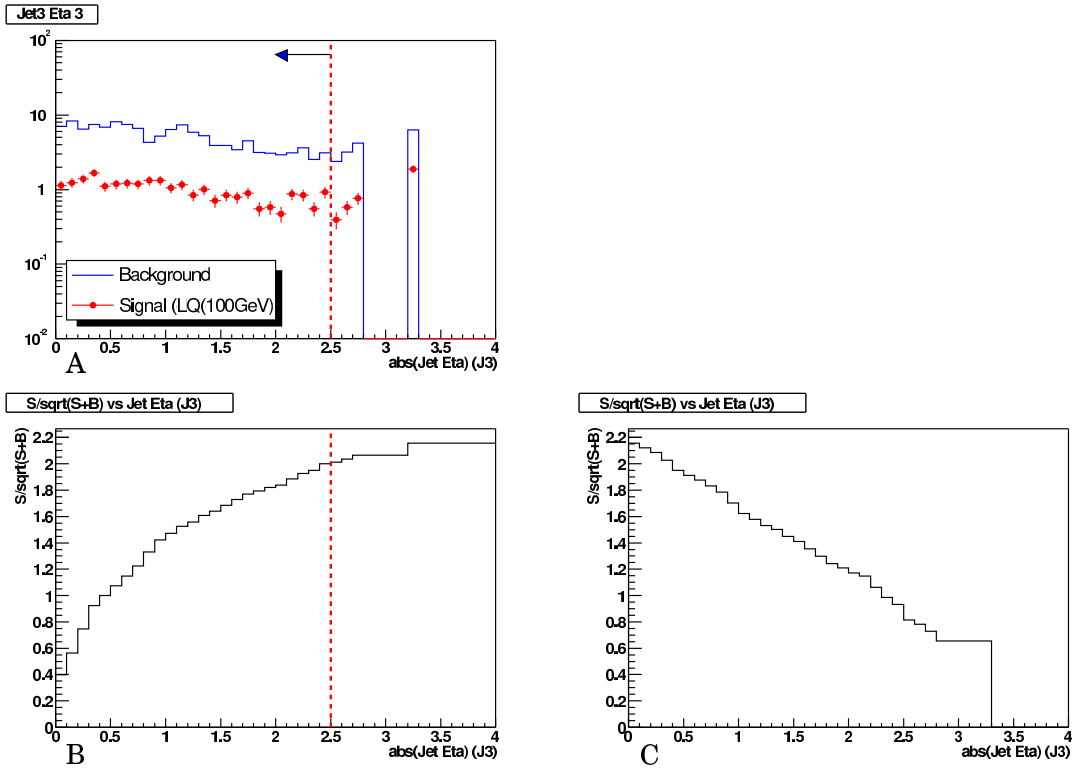

Figure 7-18: Optimization of the cut on the pseudo-rapidity of the third-leading jet. A) The distribution of the pseudo-rapidity of the third-leading jet from lepto-quark pair production and from Standard Model processes. B), C) These are the $S/\sqrt{S+B}$ distributions of the parameter shown in A).

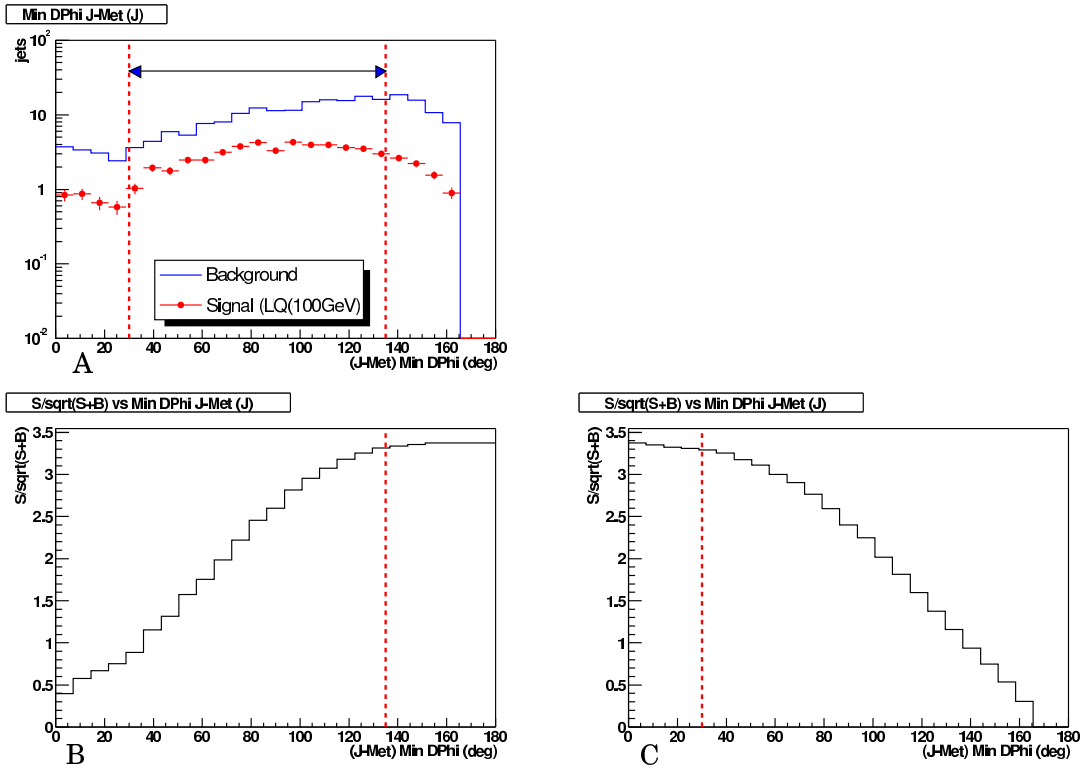

Figure 7-19: Optimization of the cut on the minimum azimuthal separation between any jet and missing-E_{T} direction. A) The distribution of the minimum azimuthal separation between any jet and missing-E_{T} direction from leptoquark pair production, and from Standard Model processes. B), C) These are the $\mathrm{S}/\sqrt{\mathrm{S}+\mathrm{B}}$ distributions of the parameter shown in A).

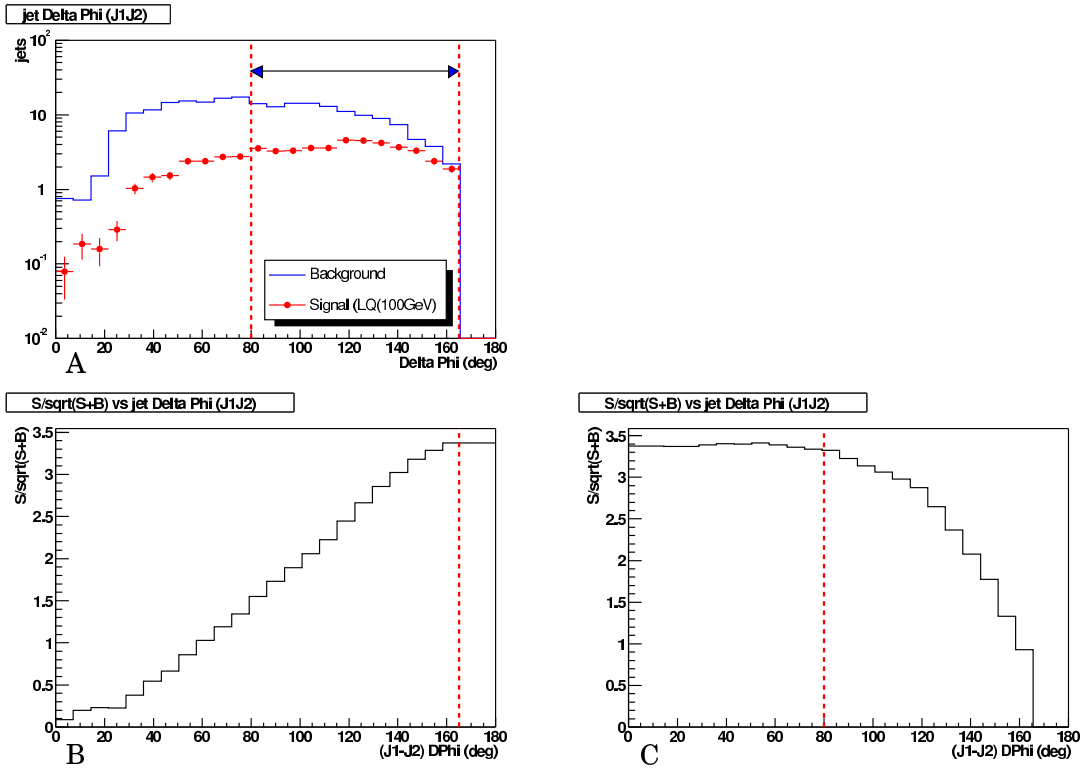

Figure 7-20: Final optimization of the cut on the azimuthal angle between the first- and second-leading jets. A) The distribution of the azimuthal angle between the first- and second-leading jets from leptoquark pair production, and from Standard Model processes. B), C) These are the $S/\sqrt{S+B}$ distributions of the parameter shown in A).

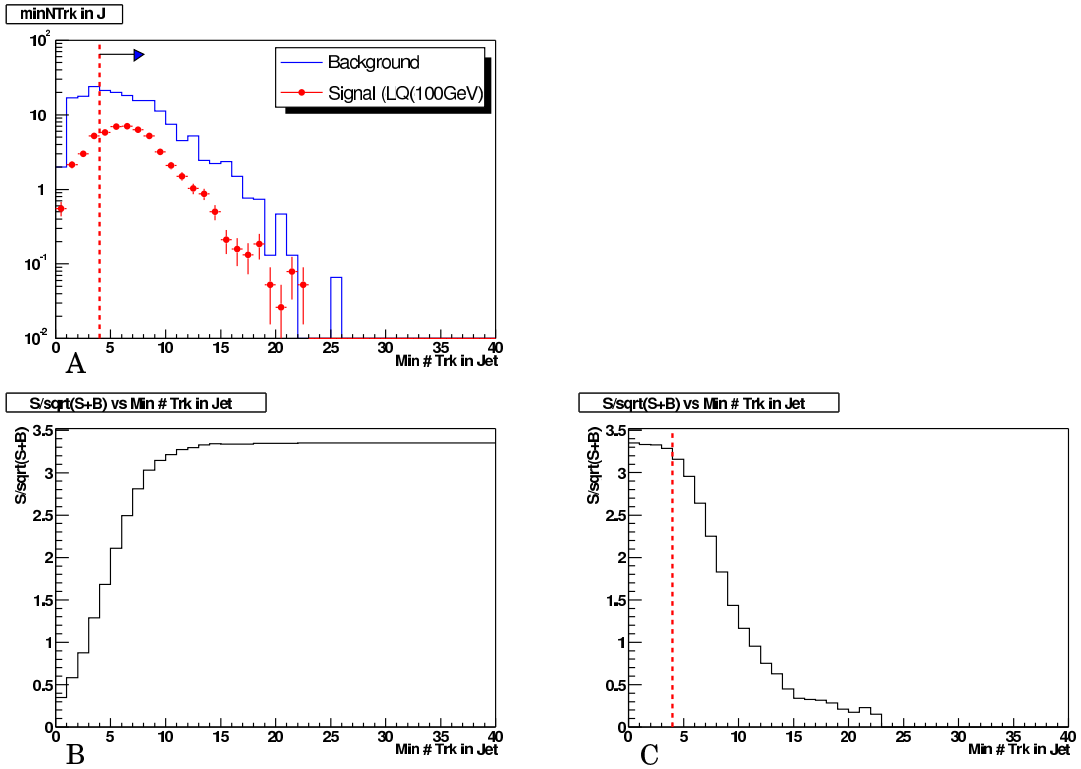

Figure 7-21: Optimization of the cut on the minimum number of tracks in the selected central jets. A) The distribution of the minimum number of tracks in the selected central jets in the from leptoquark pair production, and from Standard Model processes. B), C) These are the $S/\sqrt{S+B}$ distributions of the parameter shown in A).

Therefore, the following selection cuts are chosen to maximize the significance of a possible excess of events from leptoquark pair production over the Standard Model processes:

- Missing- $E_{\mathrm{T}} > 60$ GeV
- Lepton veto
- 2 or 3 jets (cone size 0.4, and electromagnetic fraction of the jet between 0.1 and 0.9) as well as:
  - $E_{\mathrm{T}}(\mathrm{J1}) > 40$ GeV, $E_{\mathrm{T}}(\mathrm{J2}) > 25$ GeV, $E_{\mathrm{T}}(\mathrm{J3}) > 15$ GeV
  - $0.1 <\mid \eta_{\mathrm{J1,J2}} \mid< 1$, $0.1 <\mid \eta_{\mathrm{J3}} \mid< 2.5$
  - Jet does not fall into the chimney region of the central calorimeter.
- No other jet with $E_{\mathrm{T}} > 15$ GeV anywhere in the calorimeter.
- $100^\circ < \Delta\phi(\mathrm{J1}, \not{E}_{\mathrm{T}}) < 165^\circ$
- $80^\circ < \Delta\phi(\mathrm{J1}, \mathrm{J2}) < 165^\circ$
- $30^\circ < \min\Delta\phi(\mathrm{J}, \not{E}_{\mathrm{T}}) < 135^\circ$ (J: any of the 2 or 3 selected jets)
- Minimum number of tracks in jet ≥ 4 (for jets in $\mid \eta \mid< 1$)

CHAPTER 8
BACKGROUND NORMALIZATION, CONTROL REGIONS, SYSTEMATIC UNCERTAINTIES

To estimate the number of the background events from the electroweak processes in the final sample, we apply our leptoquark selection cuts to the relevant MC samples and normalize the MC prediction of those process to the $Z \to e^+e^- + 1$ jet data. We estimate the QCD multi-jet contribution in the signal region directly from the inclusive missing-E_{T} data sample.

In addition to the signal region described in the previous section, several control regions are also defined to check our predictions for the backgrounds. These control regions are formed by relaxing or inverting some of the cuts used to enhance the leptoquark signal.

8.1 Electroweak Background Normalization

The major backgrounds to the LQ production in the missing-E_{T} plus jets channel are expected to be due to $Z \to \nu\bar{\nu} + \geq 2$ jets and $W^{\pm} \to l^{\pm}\nu + \geq 2$ jets. We select the $Z \to e^+e^- + 1$ jet data sample to derive a normalization scale factor for the MC background prediction from electroweak processes. The main advantage of using this sample is that it has a negligible background; however, it is statistically limited when compared, for example, with the $W^{\pm} \to e^{\pm}\nu +$ jets sample. Since we use the ALPGEN event generator with the same parton generation parameters and because of lepton universality, the scale factor is assumed to be the same for all Z and W MC samples. This normalization method allows us to avoid the systematic uncertainties due to the theoretical renormalization/factorization scale factors and choice of PDFs. The systematic effects are then reduced primary to the uncertainty on the luminosity of the inclusive electron data sample and on the jet energy scale.

$Z \to e^+e^- +$jets data and Monte Carlo. First, Z candidates are selected by requiring that at least two electrons are present in an event, one of which must satisfy tight central ($|\eta| < 1.1$) electron selection cuts and the other which should pass either tight or loose central electron selection cuts. The tight and loose central electron selection cuts are listed in table 8-1. In addition, fiducial cuts are imposed on the electromagnetic shower position, as measured in the CES, to ensure that the electron is away from the calorimeter boundary and the energy is well measured.

Table 8-1: Tight and loose central electron selection cuts for $Z \to e^+e^-$ candidate events. Q is electron charge

Variable	Tight selection	Loose selection
E_{T}	> 20 GeV	> 10 GeV
p_{T}	> 10 GeV	> 10 GeV
I	< 0.1	< 0.1
HAD/EM	$< 0.055 + 0.00045 * E$	$< 0.055 + 0.00045 * E$
E/p	< 2.0 (or $p_{\mathrm{T}} > 50$ GeV)	
L_{shr}	< 0.2	
$Q * \Delta x$	> -3.0 cm, < 1.5 cm	
$\lvert\Delta z\rvert$	< 3.0 cm	
χ^2_{strip}	< 10	
$\lvert Z_0\rvert$	< 60 cm	
COT Track quality	3 axial and 3 stereo segments with at least 7 hits each	3 axial and 3 stereo segments with at least 7 hits each
		opposite charge

We require that the invariant mass of the electron pair is within a 30 GeV window from the world average Z boson mass of 91.2 GeV [8]. Events where one of the electrons originates from a photon conversion are removed. Electrons from photon conversions are identified using an algorithm based on tracking information [89]. Electron tracks that have an oppositely charged companion track are considered conversion candidates. The following variables are used to identify and remove photon conversions: the difference of the polar angles ($\Delta \cot\theta_0 < 0.04$); the distance between the two tracks in the r-ϕ plane at the radius R_{conv} where the

tracks a parallel, $\Delta_{sep} < 0.2$ cm. Figure 8-1 shows the invariant mass distribution

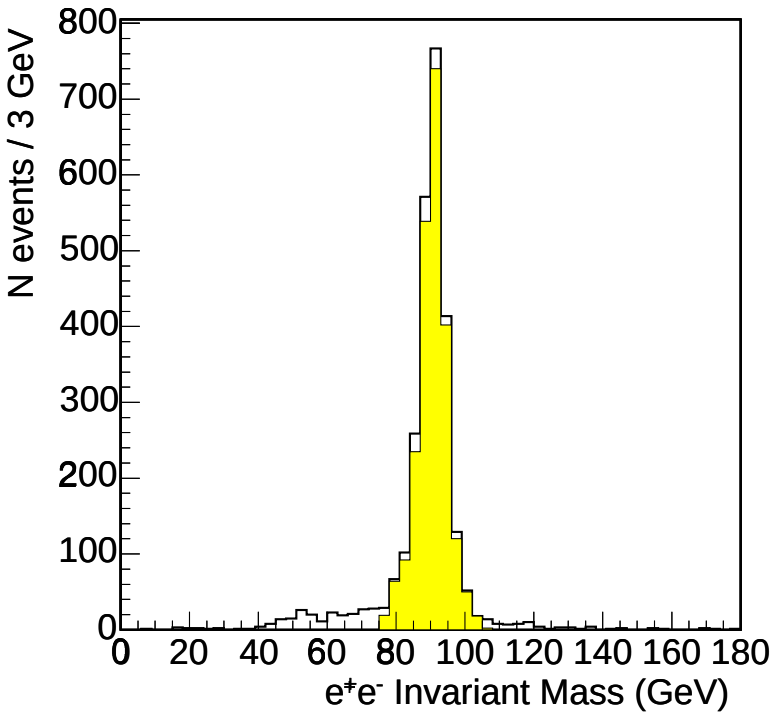

Figure 8-1: The invariant mass distribution of electron pairs. The shaded histogram indicates events selected after the mass window cut and conversion electron removal.

of the electron pairs passing all cuts.

After these cuts, we select an inclusive $Z \to e^+e^- +$ jets sample by requiring, that there is at least one jet in the event with a corrected transverse energy above 15 GeV and $|\eta| < 2$. A total of 316 such events are found in the Z mass window between 76 and 106 GeV in our inclusive high p_{T} electron data sample.

We apply the same selection criteria to the ALPGEN $Z \to ee + 1$ parton MC sample. A total of 8867 of such events are found in this MC sample.

To validate our normalization procedure and Monte Carlo prediction we compare distributions of kinematic variables between data and Monte Carlo. We examine the jet multiplicity distribution, Z boson transverse momentum, the

missing-E_{T} and jet E_{T}. We normalize the MC distributions to the number of events observed in the inclusive $Z \rightarrow e^+e^- +$ jets sample.

Figure 8-2 compares the jet multiplicity distributions in the data and Monte Carlo. The missing-E_{T} in the $Z \rightarrow \nu\bar{\nu} +$ jets process is directly proportional to

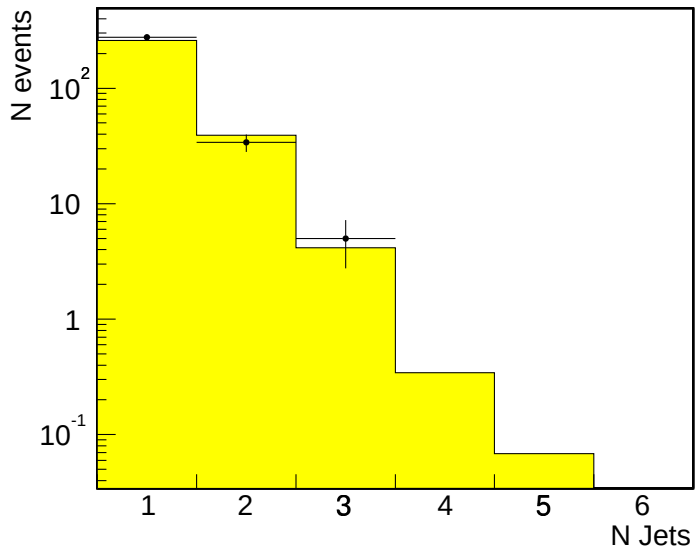

Figure 8-2: Number of jets in inclusive $Z \rightarrow e^+e^- +$ jets sample, dots are data and histogram is MC.

the Z boson transverse momentum. Therefore, we compare the Z boson p_{T}, formed by the vector sum of electrons, between data and Monte Carlo (Fig. 8-3.) In the case of the Z decaying to neutrinos, we can not reconstruct the Z boson transverse momentum, since neutrinos escape detection. However, the Z boson transverse momentum could be measured indirectly through the total momentum of the jet system recoiling against the Z boson. Figure 8-3 shows the transverse momentum of the vector sum of the jet momenta. The missing-E_{T} due to neutrinos in the $Z \rightarrow \nu\bar{\nu} +$ jets process could be simulated from the $Z \rightarrow e^+e^- +$ jets data sample if the electrons from the Z decay are removed in the event. We define the simulated

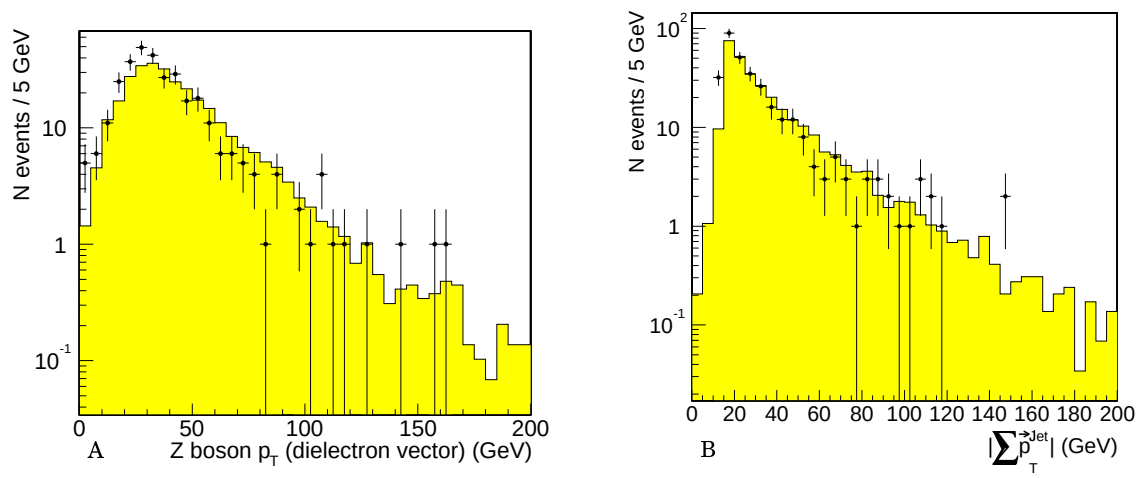

Figure 8-3: Z boson p_{T} distribution in $Z \rightarrow e^+e^- +$ jets sample for data (dots) and Monte Carlo (histogram). A) Z boson p_{T}, formed by the vector sum of electrons. B) The transverse momentum of the vector sum of the jets recoiling against Z boson.

missing-E_{T} as:

$$\vec{\not{E}}_{\mathrm{T}}(sim) = \vec{\not{E}}_{\mathrm{T}}(corr) - \sum_{i=1}^{2} E_{i\ \mathrm{T}}^{electron} \hat{n}_i, \tag{8-1}$$

where $\vec{\not{E}}_{\mathrm{T}}(corr)$ is missing-E_{T} corrected for the jet energy corrections, as defined by Equation 4-23, $E_{i\ \mathrm{T}}^{electron}$ is the electron energy and $\hat{n}$ is a unit vector pointing in the direction of the electron. The missing-E_{T} distributions before applying relative jet energy corrections and the simulated missing-E_{T} distribution for both data and Monte Carlo are shown in Figure 8-4. Figure 8-5 shows the transverse energy distribution for the first and second leading jets in data and Monte Carlo.

Overall good agreement is observed in the kinematical distributions between data and Monte Carlo, therefore we are justified in using our normalization scheme.

We normalize the luminosity of the MC sample to that of data using exclusive $Z \rightarrow e^+e^- + 1$ jet events with following relationship:

$$L_{Z\rightarrow ee+1\ \mathrm{parton}}^{\mathrm{MC}\ norm} = \frac{L_{Z\rightarrow ee+1\ \mathrm{jet}}^{\mathrm{data}} N_Z^{\mathrm{MC}}}{N_Z^{\mathrm{data}}}, \tag{8-2}$$

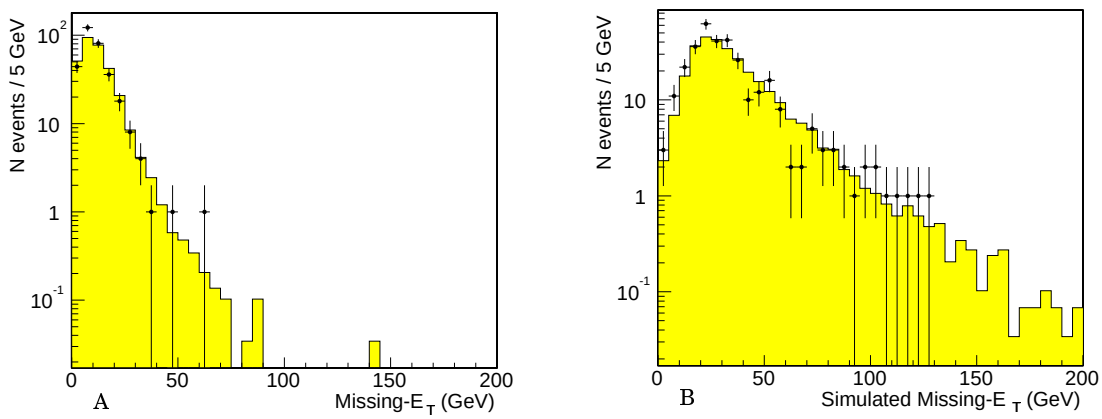

Figure 8-4: Missing-E_{T} distribution in $Z \rightarrow e^+e^- +$ jets sample for data (dots) and Monte Carlo (histogram). A) Uncorrected missing-E_{T}. B) Simulated missing-E_{T}.

where $L^{\mathrm{data}}_{Z\rightarrow ee+1\ \mathrm{jet}}$ is the luminosity of the inclusive electron data sample, and N_Z^{data} and N_Z^{MC} number of exclusive Z bosons plus one jet events in data and Monte Carlo, respectively. Therefore, we select an exclusive $Z \rightarrow e^+e^- + 1$ jet sample by requiring, that there is one and only one jet in the event. A total of 277 such events are found in the data. A total of 7590 of such events are found in our $Z \rightarrow ee + 1$ parton MC sample. However, the electron identification cut efficiencies may not be the same in data and in MC. Therefore, Z boson selection efficiencies should be taken into account for both data and MC. The Z boson selection efficiency is defined as $\epsilon_z = \epsilon_t(2\epsilon_l - \epsilon_t)$, where ϵ_t and ϵ_l are tight and loose electron identification cut efficiencies respectively. The electron identification efficiencies were measured using $Z \rightarrow e^+e^-$ candidate events, selected by requiring one tight central electron and an additional electromagnetic cluster with $E_{\mathrm{T}} > 20$ GeV [90]. So the number of Z events in data and MC is given by $N_Z^{\mathrm{MC}} = N_Z^{\mathrm{MC}\ obs}/\epsilon_z^{\mathrm{MC}}$ and $N_Z^{\mathrm{data}} = N_Z^{\mathrm{data}\ obs}/\epsilon_z^{\mathrm{data}}$. The tight and loose electron identification cut efficiencies for data and Monte Carlo are given in table 8-2. The Z boson selection efficiency in data is 0.88, whereas in MC it is 0.91. The normalized luminosity of the Monte

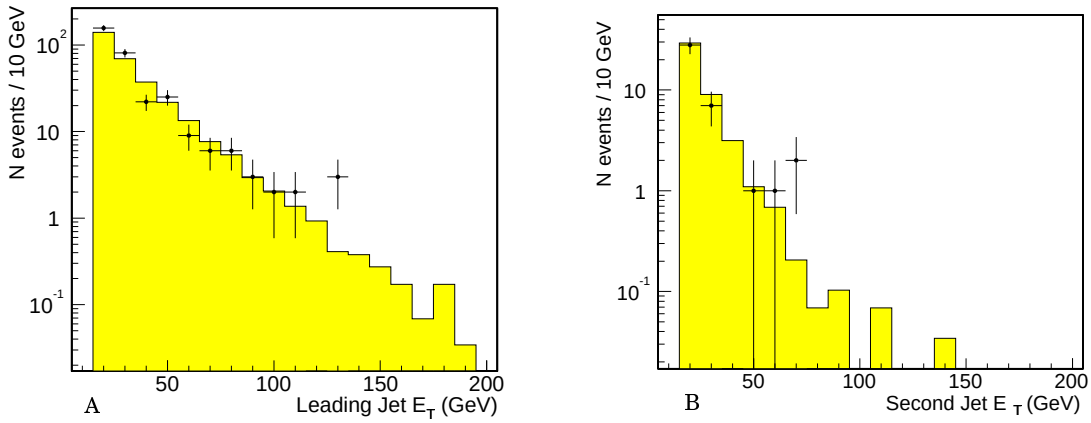

Figure 8-5: Transverse energy distribution for the first and second leading jets in inclusive $Z \rightarrow e^+e^- +$ jets sample for data (dots) and Monte Carlo (histogram). A) Leading jet E_{T} distribution. B) Second jet E_{T} distribution.

Table 8-2: Total efficiency for tight and loose electron identification cuts in data and Monte Carlo

	Data	Monte Carlo
Tight Cuts	83.4 ± 0.6	85.5 ± 0.2
Loose Cuts	94.2 ± 0.4	96.2 ± 0.1

Carlo $Z \rightarrow e^+e^- + 1$ parton sample is then:

$$\begin{aligned} L^{\mathrm{MC}\ norm}_{Z\rightarrow ee+1\ \mathrm{parton}} &= \frac{L^{\mathrm{data}}_{Z\rightarrow ee+\geq 1\ \mathrm{jets}} N^{\mathrm{MC}}_{Z} \times \epsilon_{\mathrm{data}}}{N^{\mathrm{data}}_{Z} \times \epsilon_{\mathrm{MC}}} \\ &= \frac{127.6 \times 7590 \times 0.88}{277 \times 0.91} \\ &= 3381 \pm 203\ \mathrm{pb}^{-1}. \end{aligned} \tag{8-3}$$

The MC to data normalization scale factor for the other electroweak processes is then given by:

$$k = \frac{L^{\mathrm{MC}}_{Z\rightarrow ee+\geq 1\ \mathrm{jets}}}{L^{\mathrm{MC}\ norm}_{Z\rightarrow ee+\geq 1\ \mathrm{jets}}} \tag{8-4}$$

$$= \frac{4593\ \mathrm{pb}^{-1}}{3381\ \mathrm{pb}^{-1}} \tag{8-5}$$

$$= 1.36 \pm 0.08 \tag{8-6}$$

and is found to be 1.36 ± 0.08 (stat). As a cross check, the theoretical leading order to next to leading order cross section scale factor for the vector boson production plus 2-jets was calculated using the MCFM program [91]. The scale factors for $W + 2$ jets and $Z + 2$ jets are 1.34 and 1.35, respectively, which is in good agreement with our normalization scale factor.

8.2 Multi-Jet QCD Background Normalization

We employ two methods to estimate the QCD multi-jet contribution in the signal region directly from the inclusive missing-E_{T} data sample.

Among all the offline analysis selection cuts, most of the QCD multi-jet events are removed by the missing-E_{T} and the azimuthal angular separation cuts ($\Delta\phi(\mathrm{J1}, \not{E}_{\mathrm{T}})$, $\Delta\phi(\mathrm{J1}, \mathrm{J2})$, $\min\Delta\phi(\mathrm{J}, \not{E}_{\mathrm{T}})$). For the first method we reverse and, or, remove these cuts to define regions which are rich in QCD multi-jet events. Based on these regions we try to estimate how much QCD will contribute in the signal region. For the second method, the combined selection cut efficiency is measured as a function of the missing-E_{T} in an independent inclusive jet sample and applied to the high missing-E_{T} subsample, preselected with looser analysis cuts.

8.2.1 Method-1

For this method we investigate four kinematic regions, as illustrated in table 8-3.

Table 8-3: The four kinematic regions of the `MET45` data sample defined by the azimuthal angular separation and missing-E_{T}. Method-1 looks at the events in region (A), (B), and (C) to predict the QCD multi-jet contribution in (D).

QCD-like, low missing-E_{T} (A)	QCD-like, high missing-E_{T} (B)
Non-QCD-like, low missing-E_{T} (C)	Non-QCD-like, high missing-E_{T} (D)

We define "Low missing-E_{T}" and "High missing-E_{T}" regions as follows :

- Low missing-E_{T}: $50 < \not{E}_{\mathrm{T}} < 60$ GeV

- High missing-E_{T}: $\not\!\!E_{\mathrm{T}} > 60$ GeV

The "QCD-like" and "non-QCD-like" regions are defined by the azimuthal angle separation cuts. The "non-QCD-like" region, which uses the same azimuthal angle separation cuts as the signal region ((D) in Table 8-3) described in section 7.4, is defined by:

- non-QCD-like:
  - $80^\circ < \Delta\phi(\mathrm{J1}, \mathrm{J2}) < 165^\circ$
  - $100^\circ < \Delta\phi(\mathrm{J1}, \not\!\!E_{\mathrm{T}}) < 165^\circ$
  - $30^\circ < \mathrm{min}\Delta\phi(\mathrm{J}, \not\!\!E_{\mathrm{T}}) < 135^\circ$

For the "QCD-like" region, we have to choose the azimuthal angle separation cuts such that the missing-E_{T} distribution of the QCD events in this region has the same shape as the missing-E_{T} distribution of the QCD events in the "non-QCD-like" region. Since there are some correlations between the azimuthal angles separating the jet direction and the missing-E_{T} direction, ideally one would apply minimal change to the azimuthal angular separation cuts that are used in the "non-QCD-like" region, to define a kinematic region that is disjoint from the signal region, and yet dominated mainly by QCD multi-jets events. These cuts are obtained from studies on a QCD MC sample (Pythia, $\hat{p}_{\mathrm{T}} > 80$ GeV). Table 8-4 lists the different sets of azimuthal angular separation cuts that define the "QCD-like" regions. The plots in Figure 8-6 are the missing-E_{T} distributions for the "non-QCD-like" region (red histogram) and for the different definitions of the "QCD-like" regions (blue points). All selections cuts were applied except the missing-E_{T} cut and the missing-E_{T} trigger threshold emulation. The distributions are normalized to unit area. The shapes of the missing-E_{T} distributions for "q1" and "q8" are in good agreement with the shape of the "non-QCD-like" region. However both "q1" and "q8" have few events at high missing-E_{T} ($\not\!\!E_{\mathrm{T}} > 60$ GeV). For "q10", although the entire missing-E_{T} shape does not agree well with the shape of the "non-QCD-like", still, for $\not\!\!E_{\mathrm{T}} > 20$ GeV, both distributions show

Table 8-4: Definition of "QCD-like" regions.

QCD-like regions	$\Delta\phi$(J1, J2) (degree)	$\Delta\phi$(J1, $\not\!\!E_T$) (degree)	min$\Delta\phi$(J, $\not\!\!E_T$) (degree)
q1	80-165	100-165	20-30
q2	80-165	100-165	10-30
q3	80-165	100-165	0-30
q4	80-165	165-180	30-135
q5	80-165	0-100	30-135
q6	165-180	100-165	30-135
q7	165-180	0-100	30-135
q8	80-180	100-165	20-30
q9	80-165	100-180	20-30
q10	80-180	100-180	20-30
q11	80-180	100-180	20-27
q12	80-180	100-180	17-27

similar slope at the tail of the distribution. This is seen more clearly in Figure 8-7 (the distributions are normalized to unit area). Regions "q11" and "q12" are slight modification of region "q10". Figure 8-8 shows the ratio of the missing-E_T distribution of "QCD-like" (defined as "q11") to the "non-QCD-like". The ratio is more or less flat within the error. The region "q11" is chosen as the nominal "QCD-like" region, and "q10" and "q12" are used to account for some of the systematic uncertainty with this method.

Table 8-5 lists the number of events in the "QCD-like" and "non-QCD-like" regions from the `MET45` data sample, and from the MC prediction ($W/Z + 2$jets and $t\bar{t}$) at $L = 191$ pb^{-1}. The parameterization of the `MET45` trigger efficiency (section 5.5) has been used on the MC samples to simulate the `MET45` trigger. In table 8-5 one can clearly observe that the data in regions (A) and (B) are predominantly QCD multi-jet since the MC simulation prediction for the contribution from ($W/Z + 2$jets and $t\bar{t}$) processes are much smaller compared to the number of events in the data. The region defined by "q11" is chosen as the nominal "QCD-like"

region, and the missing-E_{T} range $50 < \not{E}_{\mathrm{T}} < 57$ GeV is the nominal low missing-E_{T} region.

In the "low missing-E_{T}" and "non-QCD-like" region (C) the number of events seen in the data is about double the prediction from MC for the ($W/Z + 2$jets and $t\bar{t}$) processes. We assume that this difference is due to QCD multi-jet process that is not accounted for in the MC prediction. The QCD contribution in region (D), the signal region, is estimated from the following formula:

$$\mathrm{N}^{\mathrm{D}}_{\mathrm{QCD}} = \frac{\mathrm{N}^{\mathrm{C}}_{\mathrm{QCD}}}{\mathrm{N}^{\mathrm{A}}_{\mathrm{QCD}}} \cdot \mathrm{N}^{\mathrm{B}}_{\mathrm{QCD}}, \tag{8-7}$$

where $\mathrm{N}^{\mathrm{A}}_{\mathrm{QCD}}$, $\mathrm{N}^{\mathrm{B}}_{\mathrm{QCD}}$ and $\mathrm{N}^{\mathrm{C}}_{\mathrm{QCD}}$ are, respectively, the number of QCD events in the data in regions (A), (B) and (C). The estimated QCD contribution in the signal region (D) from the Equation 8-7 is shown in Table 8-6. Using this method, the estimated QCD events in the signal region is 15.0 ± 4.6 (stat) $^{+6.8}_{-4.3}$ $^{+1.8}_{-4.3}$. The first error is statistical, the second error is due to the different definitions of the low missing-E_{T} region and "QCD-like" region, and the third error is due to the uncertainty in the estimation of the events from $W/Z + 2$jets and $t\bar{t}$ caused by the uncertainty in the jet energy scale.

Method-1 in inclusive jet data.

As a cross check we compare the shapes of the missing-E_{T} distributions for "non-QCD-like" (signal) region to the "QCD-like" region in inclusive jet data. We use the `q8` region (see Table 8-4), since we are not limited by the statistics of the data sample. Figure 8-9 shows the ratio of the number of events in the "non-QCD-like" region to the number of events in the "QCD-like" region as a function of the missing-E_{T} in `JET20` and `JET50` samples. We raised the cut on the leading jet E_{T} to 90 GeV in `JET50` sample to stay away from the trigger turn-on effects. This ratio is not flat in `JET20` data, as was expected from QCD Monte Carlo and is observed in `JET50` data with missing-$E_{\mathrm{T}} > 15$ GeV. This can be caused by the

Table 8-5: The number of events in the four kinematic regions from `MET45` data. The table also includes the MC prediction of the contributions from $W/Z + 2$ jets and $t\bar{t}$ processes for $L = 191$ pb^{-1}. All errors are statistical.

QCD-like		Low $\not\!\!E_T$ (GeV) (A)			High $\not\!\!E_T$(GeV) (B)
		$50 < \not\!\!E_T < 55$	$50 < \not\!\!E_T < 57$ (nominal)	$50 < \not\!\!E_T < 60$	$\not\!\!E_T > 60$
q10	Data	78	108	122	44
	MC ($W/Z/t\bar{t}$)	2.9 ±0.9	3.4 ±1.0	4.7 ±1.2	8.3 ±1.7
	Data - MC	75.1 ±8.9	104.6 ±10.4	117.3 ±11.1	35.7 ±6.9
q11 (nominal)	Data	65	84	103	36
	MC ($W/Z/t\bar{t}$)	1.5 ±0.6	1.5 ±0.6	2.8 ±0.9	4.6 ±1.2
	Data - MC	63.5 ±8.1	82.5 ±9.2	100.2 ±10.2	31.4 ±6.1
q12	Data	102	138	176	81
	MC ($W/Z/t\bar{t}$)	1.9 ±0.6	1.9 ±0.6	3.7 ±1.0	5.8 ±1.3
	Data - MC	100.2 ±10.1	136.1 ±11.8	172.3 ±13.3	75.2 ±9.1
Non-QCD-like		(C)			(D)
	Data	39	62	79	
	MC ($W/Z/t\bar{t}$)	16.4 ±2.2	22.5 ±2.6	32.5 ±3.2	101.6 ±5.6
	Data - MC	22.6 ±6.6	39.5 ±8.3	46.5 ±9.5	

Table 8-6: Estimated number of QCD events in region (D) for different definitions of the low missing-E_{T} region, and the "QCD-like" region. All errors are statistical.

	Low missing-E_{T} (GeV)		
"QCD-like"	50-55	50-57	50-60
q10	16.9 ± 5.7	21.8 ± 5.6	20.3 ± 5.1
q11	11.2 ± 4.2	15.0 ± 4.6	14.5 ± 4.4
q12	10.7 ± 4.0	13.5 ± 4.1	14.1 ± 4.2

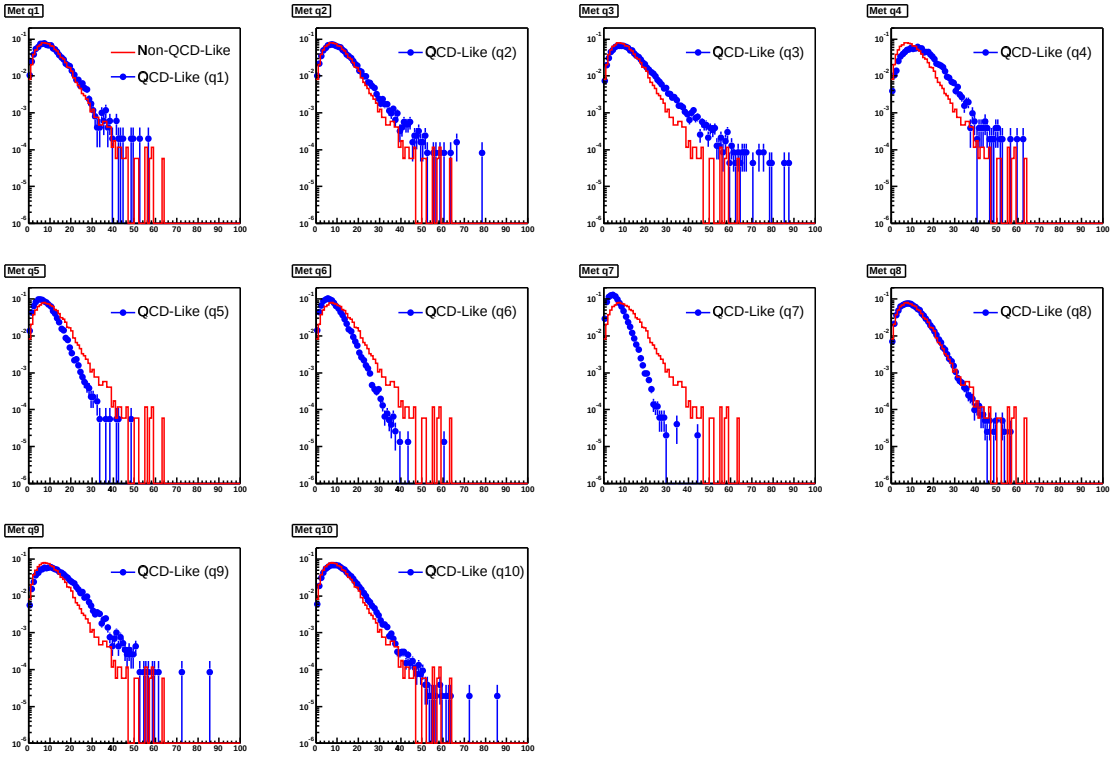

Figure 8-6: Comparison of the shapes of the missing-E_{T} distributions for "non-QCD-like" region to several different definitions of the "QCD-like" regions. These plots are obtained from a QCD MC sample.

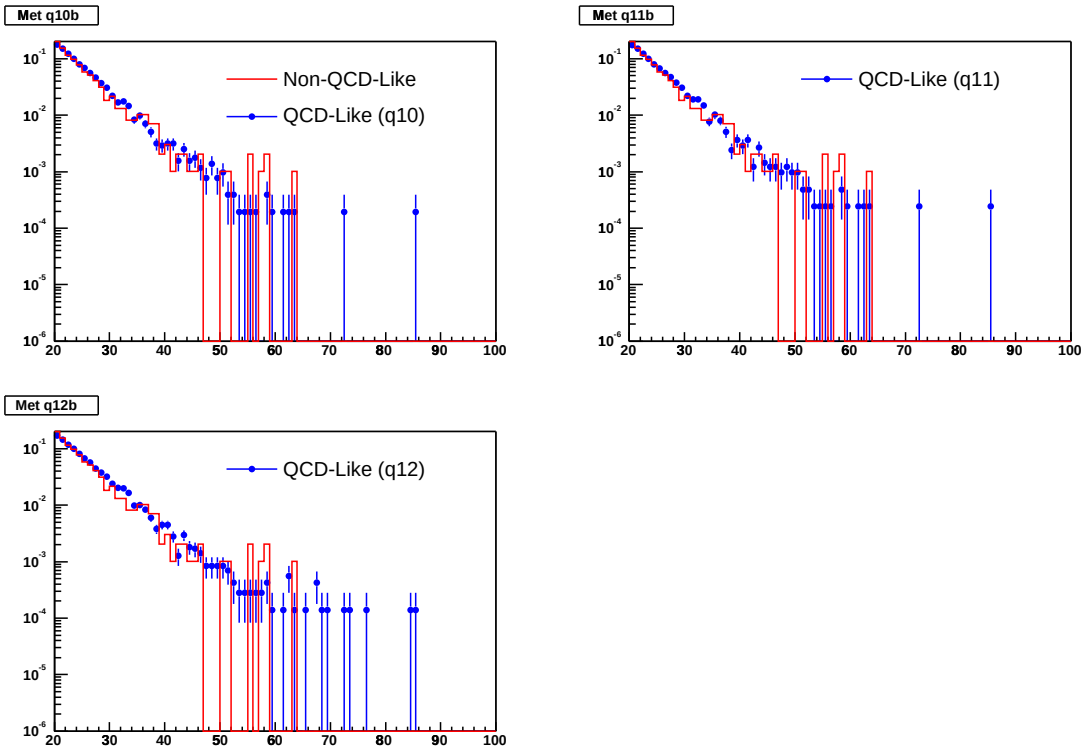

Figure 8-7: Comparison of the shapes of the missing-E_{T} distributions for "non-QCD-like" region to several different definitions of the "QCD-like" regions. These plots are obtained from a MC QCD sample.

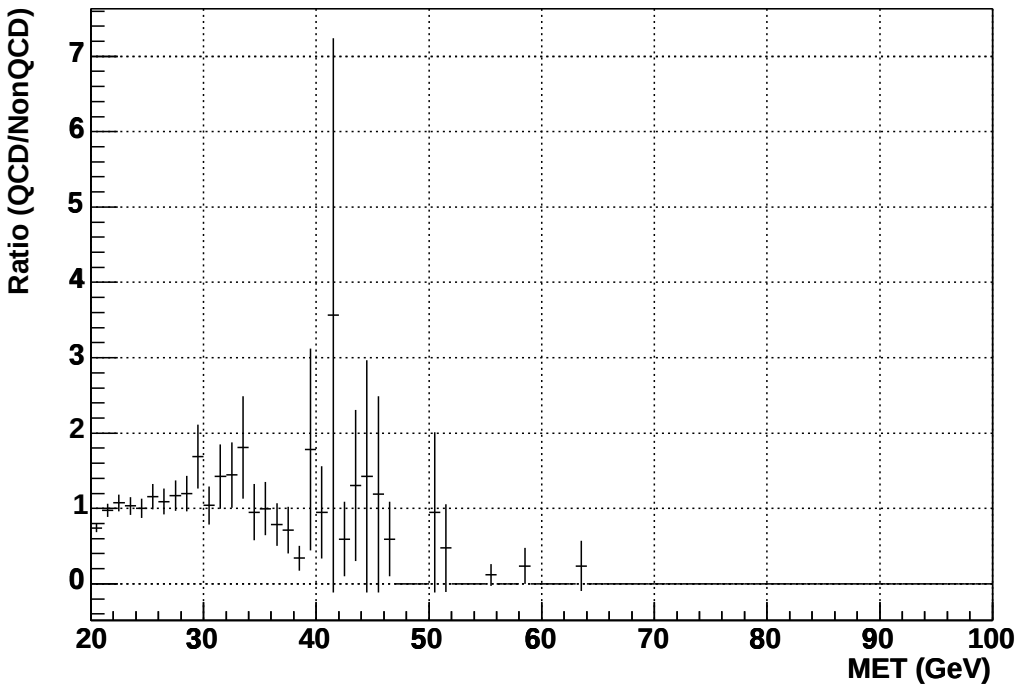

Figure 8-8: Ratio of the missing-E_{T} distribution of "QCD-like" (defined as "q11") to the "non-QCD-like". This plot is obtained from a MC QCD sample.

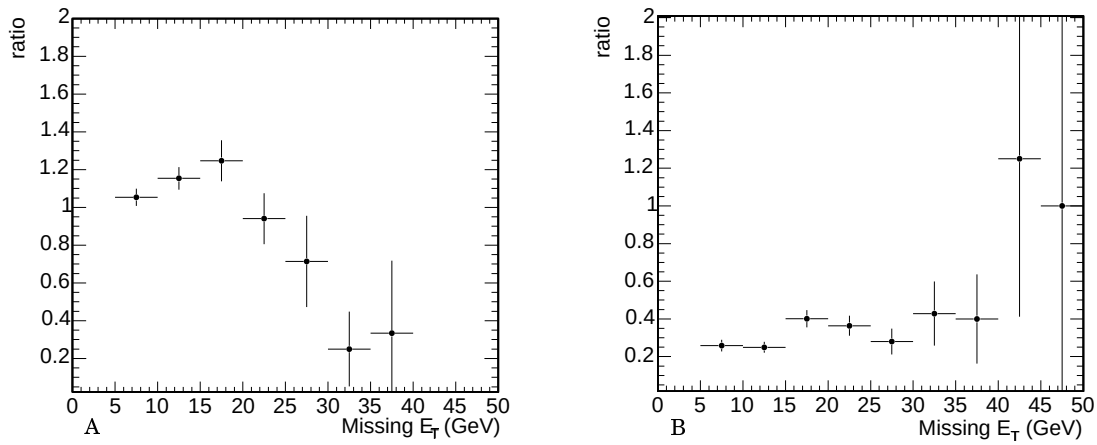

Figure 8-9: Ratio of the number of events in "non-QCD-like" region to the number of events in the "QCD-like" region as a function of the missing-E_{T}. A) Ratio in the JET20 data. B) Ratio in the JET50 data.

additional energy in the calorimeter due to extra interactions in the same bunch crossing. Figure 8-10 shows the number of vertices with 2 or more COT tracks in the JET20 sample. Figure 8-11 compares the missing-E_{T} distribution for the events with one and only one vertex and events with two or more vertices. Figure 8-12 shows the ratio of the number of events in "non-QCD-like" region to the number of events in the "QCD-like" region as a function of the missing-E_{T} in JET20 sample after we require only one vertex. After this requirement the ratio looks reasonably flat.

8.2.2 Method-2

For the second method we measure the efficiency of the azimuthal angle separation cuts as function of the missing-E_{T} in the low missing-E_{T} range ($5 \leq \not{E}_{\mathrm{T}} \leq 50$ GeV) of the QCD sample that has already passed all the signal selection cuts except the cuts from missing-E_{T}, number of jets requirement, azimuthal angle separation cuts, and the MET45 trigger efficiency. This efficiency function is then extrapolated to the high missing-E_{T} region ($\not{E}_{\mathrm{T}} > 60$ GeV) to predict the number of QCD multi-jet events that will survive the azimuthal angular separation cuts.

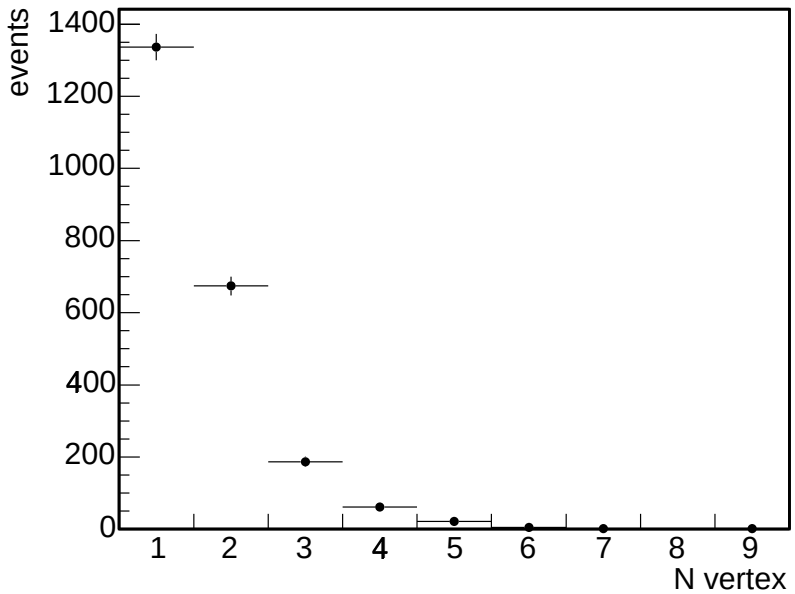

Figure 8-10: Number of vertices of class 12 or higher in JET20 sample.

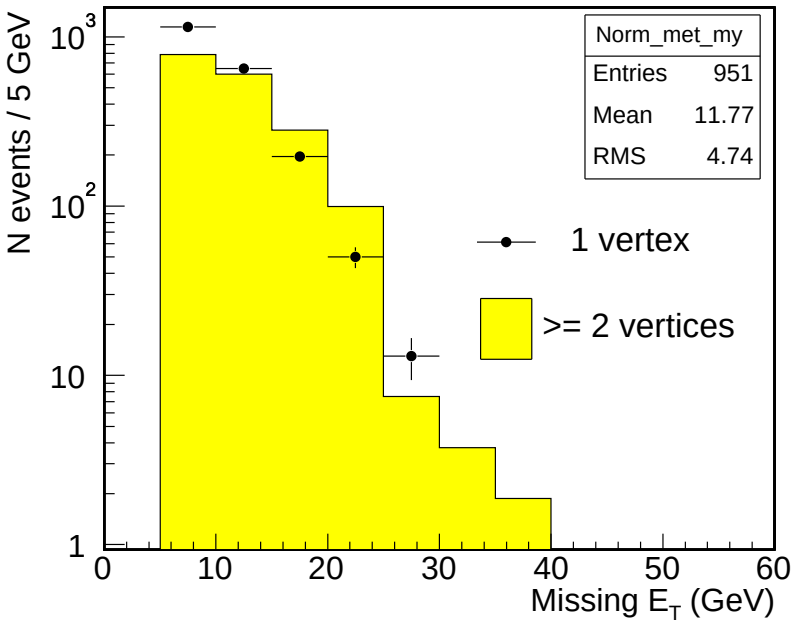

Figure 8-11: Comparison of the missing-E_{T} distributions for the events with one and only one vertex and events with two or more vertices in JET20 sample.

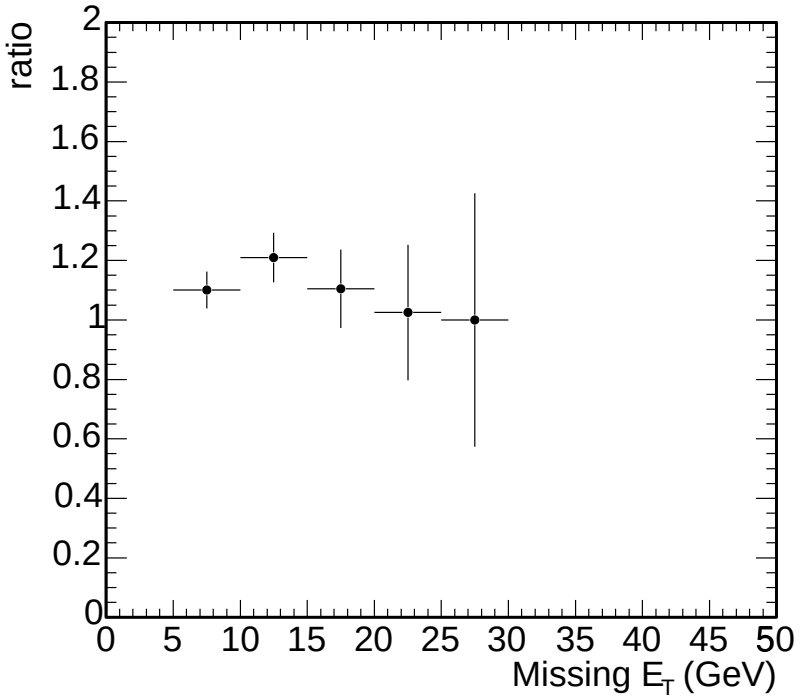

Figure 8-12: Ratio of the number of events in "non-QCD-like" region to the number of events in the "QCD-like" region as a function of the missing-E_{T} in `JET20` for events with only one vertex of class 12 or higher.

We measure the efficiency of our final cuts using the JET20 data sample. This sample consists predominantly of QCD di-jet events and has a low enough jet E_{T} threshold to suit our analysis cuts. First, from the JET20 sample we select events that have at least two central jets ($\eta_{det} < 1$), with the leading jet satisfying $E_{\mathrm{T}} > 40$ GeV and the second jet satisfying $E_{\mathrm{T}} > 25$ GeV. We allow additional jets in the event, however we veto events with jets in the forward region ($E_{\mathrm{T}} > 15$ GeV and $\eta_{det} > 2.5$). In addition, we require that there is only one vertex with 2 or more COT tracks attached to it. Events with loosely identified leptons are vetoed. After that, we apply our LQ selections cuts, except for the missing-E_{T} cut, to the preselected events. Figure 8-13 shows the ratio of the number of events after all selection cuts to the number of preselected events as a function of the missing-E_{T} in JET20 sample. The ratio is fit with an exponential function of the form:

$$f(\not{E}_{\mathrm{T}}) = e^{p0+p1\times\not{E}_{\mathrm{T}}}, \tag{8-8}$$

in the range $10 < \not{E}_{\mathrm{T}} < 45$ GeV, where $p0$ and $p1$ are the fit parameters. As a cross check, we compare the efficiency measured in the JET20 data sample with the efficiency measured in the JET50 data sample. Figure 8-14 shows the ratio of the number of events after all selection cuts to the number of preselected events as a function of the missing-E_{T} in JET50 sample. We raised the cut on the leading jet E_{T} to 90 GeV to stay away from the trigger turn on effects. The slope in the fit function is similar to that in the JET20 data sample. Table 8-7 summarizes the fit parameters obtained from JET20 and JET50 samples.

Table 8-7: Fit parameters for final cut efficiency function from JET20 and JET50 samples.

Data Sample	p0	p1
JET20	-1.6 ± 0.2	-0.05 ± 0.01
JET50	-2.4 ± 0.2	-0.048 ± 0.009

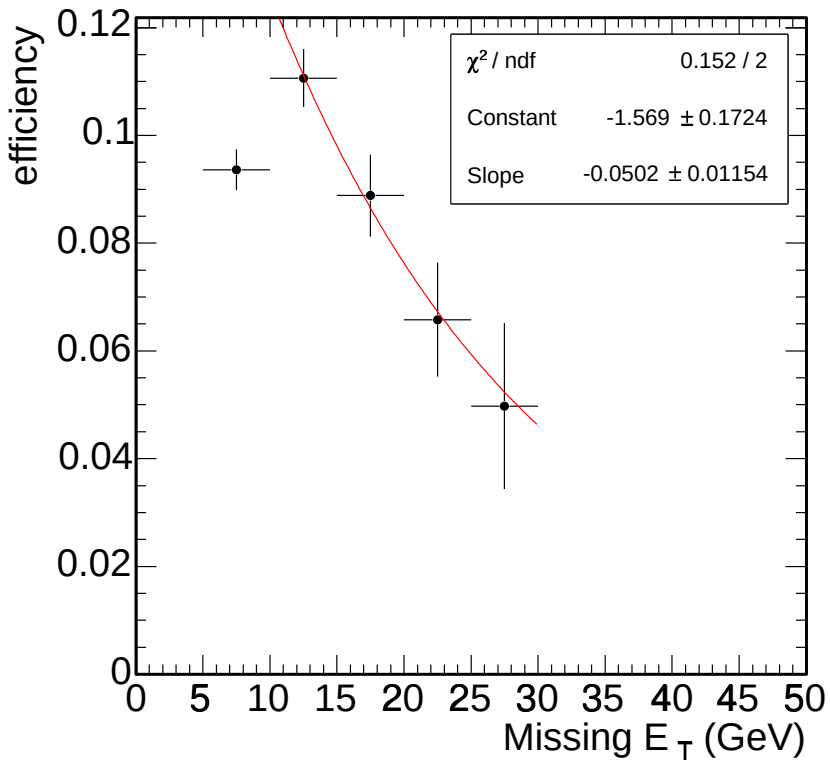

Figure 8-13: Efficiency of the azimuthal angular separation cuts as function of the missing-E_{T} in JET20 sample.

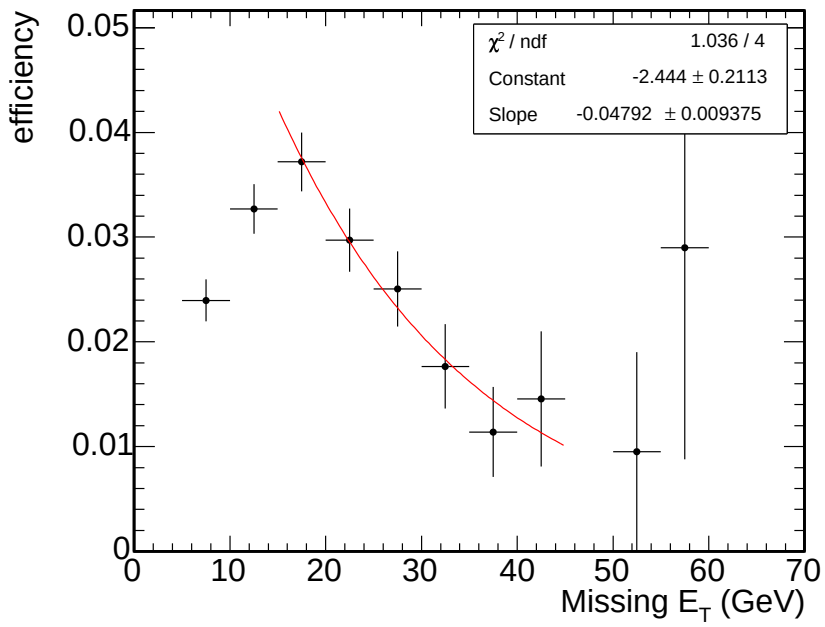

Figure 8-14: Efficiency of the azimuthal angular separation cuts as function of the missing-E_{T} in `JET50` sample.

To check the exponential form of the efficiency function we look at the QCD MC sample (Pythia QCD-dijet, $\hat{p}_{\mathrm{T}} > 80$ GeV). Figure 8-15 shows the ratio of the missing-E_{T} distribution after all LQ selection cuts to the missing-E_{T} distribution after all selection cuts except the cuts from missing-E_{T}, number of jets requirement and azimuthal angular separation. The ratio is fit with an exponential function in the range $15 < \not{E}_{\mathrm{T}} < 65$ GeV. The slope is consistent with data, although not the constant term.

We then apply this parameterized efficiency function, onto events from the inclusive missing-E_{T} data sample, after subtracting contribution due to electroweak background, which passed all selection cuts except the number of jets requirement and the azimuthal angular separation cuts. Figure 8-16 shows the missing-E_{T} distribution from the inclusive missing-E_{T} data sample along with the expected electroweak and $t\bar{t}$ contribution, before applying the angular separation cuts and

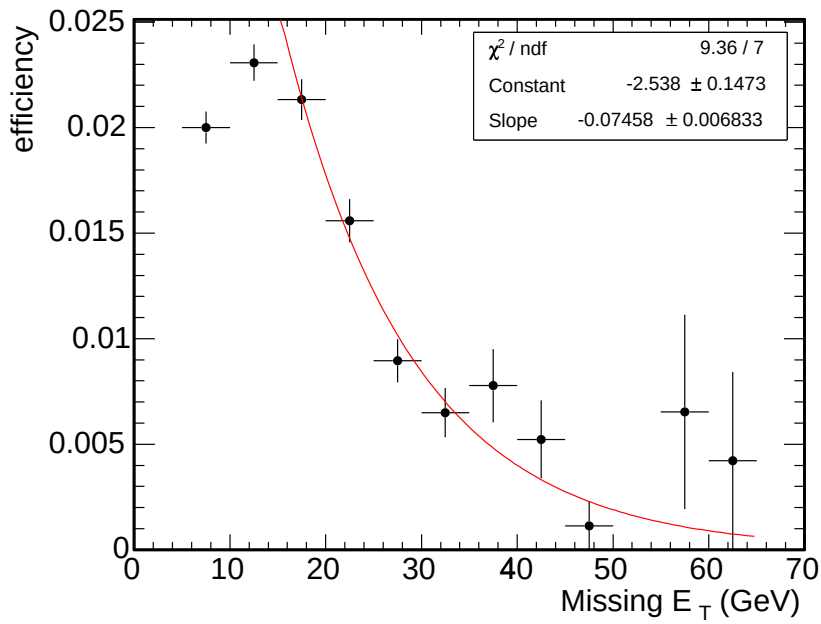

Figure 8-15: Efficiency of the azimuthal angular separation cuts as function of the missing-E_{T} of a QCD MC sample

the number of jets requirement. The predicted number of events with $\not{E}_{\mathrm{T}} > 60$ GeV that will survive the azimuthal angular separation cuts is 21.5. If we use instead fit parameters obtained from the `JET50` sample we predict 10.4 events. We are possibly underestimating the number of QCD events due to the multiple interactions in the same bunch crossing, since the final cut efficiency was measured with a one vertex requirement. All these results are summarized in table 8-8. We also include the variation in the prediction of the QCD contribution due to the uncertainties in the fits. This variation is taken as an uncertainty of the method. We take 21.5 ± 12.4 as an estimated QCD contribution in the signal region from this method.

8.2.3 Multi-jet QCD Background Contribution in the Signal Region

The estimations from Method-1 and Method-2 are consistent with each other. We assume that those measurement are uncorrelated and take weighted average of

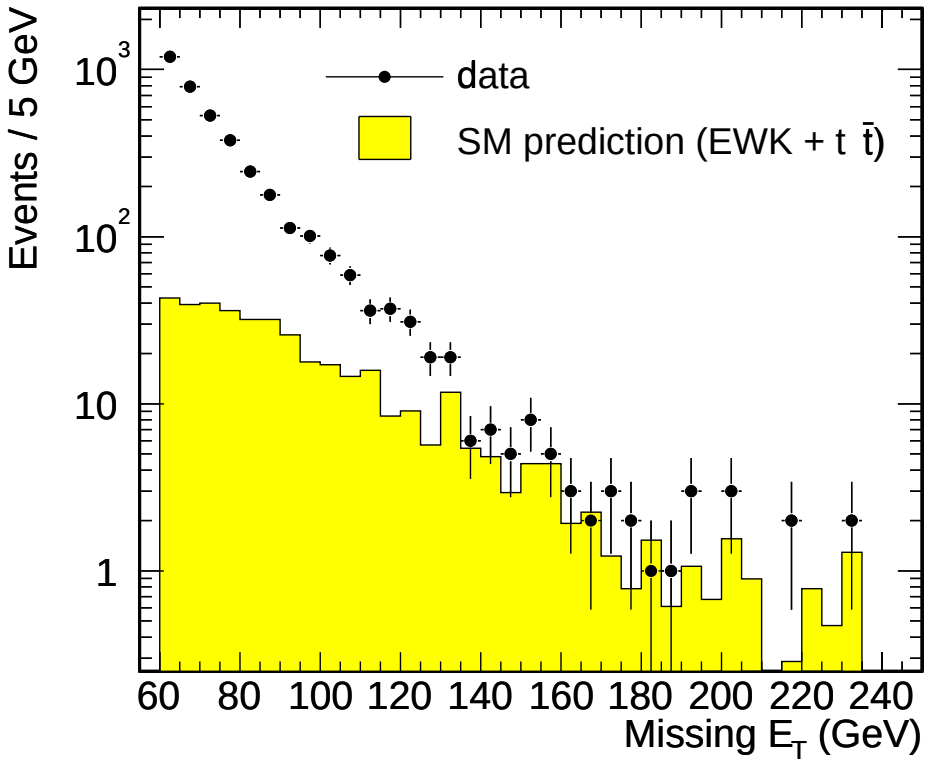

Figure 8-16: Missing-E_{T} distribution from the inclusive missing-E_{T} data sample, all selection cuts are applied, except the number of jets requirement and azimuthal angular separation cuts. The expected contribution from the electroweak and $t\bar{t}$ background is also shown.

Table 8-8: Predicted number of QCD multi-jet events in the signal region by Method-2.

	Number of QCD Events Predicted		
Data Sample	p0 p1 (nominal)	p0 $+1\sigma$	p0 -1σ
JET20	21.5	37	12.3
JET50	10.4	15.4	6.8

2 methods. Therefore the predicted QCD multi-jet contribution in the signal region is 16.7 ± 6.7.

8.3 Control Regions and Background Normalization Cross-Check.

In addition to the signal "box" described in the previous section, several control regions are defined to check the expected QCD multi-jet contribution as well as the normalizations of the other backgrounds.

To increase the statistics of the regions, we relaxed some of the cuts from their values used for the leptoquark search region:

- $0^\circ < \Delta\phi(\mathrm{J1}, \not{E}_\mathrm{T}) < 165^\circ$
- $0^\circ < \Delta\phi(\mathrm{J1}, \mathrm{J2}) < 165^\circ$
- $20^\circ < \min\Delta\phi(\mathrm{J}, \not{E}_\mathrm{T})$ (J: any of the 2 or 3 selected jets)

These control regions are formed by permutation of the missing-E_T cut, the cut on angle between the first two leading jets and the cut on the number of leptons requirement. The definition of the control regions are listed in Tab. 8-9. Before discussing results in the control and signal regions we address systematic

Table 8-9: Definition of 7 control regions with large missing-E_T.

Region definition			
1)	$45 < \not{E}_\mathrm{T} < 60$ GeV,	$\Delta\phi(j_1, j_2) > 165^\circ$,	$N_l = 0$
2)	$45 < \not{E}_\mathrm{T} < 60$ GeV,	$\Delta\phi(j_1, j_2) < 165^\circ$,	$N_l = 0$
3)	$45 < \not{E}_\mathrm{T} < 60$ GeV,	$\Delta\phi(j_1, j_2) > 165^\circ$,	$N_l > 0$
4)	$\not{E}_\mathrm{T} > 60$ GeV,	$\Delta\phi(j_1, j_2) > 165^\circ$,	$N_l = 0$
5)	$\not{E}_\mathrm{T} > 60$ GeV,	$\Delta\phi(j_1, j_2) > 165^\circ$,	$N_l > 0$
6)	$\not{E}_\mathrm{T} > 60$ GeV,	$\Delta\phi(j_1, j_2) < 165^\circ$,	$N_l > 0$
7)	$45 < \not{E}_\mathrm{T} < 60$ GeV,	$\Delta\phi(j_1, j_2) < 165^\circ$,	$N_l > 0$

uncertainties of our predictions.

8.4 Systematic Uncertainties

This section investigates the sources of systematic errors in predicting the number of background events in the signal region and estimating the signal acceptance.

The systematic uncertainty due to a particular source is taken to be the difference in event yield for the case of background events, and the relative difference in the acceptance between the nominal conditions and when the condition for a particular source is varied within its uncertainty for signal events.

The uncertainties on the luminosity and on the jet energy measurement are 100% correlated for the signal acceptance and the number of background events. Below we discuss identified systematic uncertainties.

8.4.1 Luminosity Measurement Uncertainty

The systematic uncertainty on the luminosity measurement was found to be 6% (see Section 3.4.2).

8.4.2 Jet Energy Measurement Uncertainty

An energy cluster in the calorimeter is counted as a jet if it passes a cut above a certain threshold. Therefore, it is expected that the calorimeter energy scale and the jet correction uncertainties will be a significant source of the systematic error in estimating signal and background yields. The systematic uncertainty due to the detector response includes the calorimeter calibration uncertainty and the calorimeter stability. The total systematic uncertainty due to the jet energy scale is given by summing in quadratures the relative uncertainties from individual contributions to the jet corrections [92]. The biggest contribution to the jet energy uncertainty is due to the relative jet energy scale correction and can be as large as 7%. However, it is minimized in this analysis, since the two leading jets are required to be in the central region, where the energy scale is best known.

8.4.3 Initial- and Final-State Radiation Uncertainty

The effect of gluon radiation is studied for a leptoquark mass 100 GeV/c^2 by turning on and off initial- (ISR) and final-state (FSR) radiation using the Pythia event generator. The amount of gluon radiation can change the number of the jets in the final state, and thus change the acceptance. The ISR and FSR are turned

on for the nominal settings in signal generation. The systematic uncertainty on final state radiation is estimated by completely switching off final state radiation (since leptoquarks could hadronize if long-lived). This results in a relatively large acceptance variation of 20%. Similarly, the systematic uncertainty on the initial state radiation is estimated by completely switching it off. The observed difference in the acceptance is 1%. Alternatively, the systematic uncertainty on the initial state radiation model used by Pythia can be estimated from the difference in acceptance between the tunes "A" and "B" of Reference [93], which use different amount of initial state radiation as intput parameters. Half of the maximum difference (10%) in the signal acceptance compared to the nominal value is taken as a systematic uncertainty due to gluon radiation.

8.4.4 Parton Distribution Function Uncertainty

The choice of the parton distribution functions affects the total leptoquark cross-section as well as the development of the parton shower in the initial state radiation. CTEQ5L structure functions are used to generate the leptoquark MC samples. We generated two additional samples with GRV98L ([94]) and MRST (set 72, [95]) structure functions at $m_{\mathrm{LQ}} = 100$ GeV/c^2. The biggest deviation of 4% (with GRB98L) is taken as an uncertainty due to the choice of the parton density functions.

8.4.5 Uncertainties on the Signal Acceptance

Here we summarize the systematic uncertainties on the signal acceptance from the different sources.

The finite statistics of the leptoquark Monte Carlo samples gives a 2-8% statistical error, depending on the leptoquark mass.

Systematics due to the theoretical uncertainties on the renormalization and factorization scales are not included here, since we conservatively choose the NLO

cross section for $\mu = 2m_{\mathrm{LQ}}$, which is found to reduce the cross section by 15% relative to $\mu = m_{\mathrm{LQ}}$.

On the experimental side, the systematic uncertainty on the luminosity is 6%, and the uncertainty on the z-vertex cut is 0.5% [96]. The uncertainty on the `MET45` trigger efficiency (1%) is estimated from the difference in acceptance if the efficiency curve derived from a high-p_{T} muon sample is used in place of the one derived from a high-p_{T} electron sample.

The uncertainty on the calorimeter energy scale is taken as the full difference in acceptance by varying the jet energy corrections by $\pm 1\sigma$ uncertainty about the nominal jet energy scale. This uncertainty makes the biggest contribution to the overall systematic error and is found to be between 4% to 26%, depending on the leptoquark mass.

Overall, the total systematic and statistical uncertainty assigned to the acceptance is between 15% to 32%, depending on the leptoquark mass. Table 8-10 summarizes the systematic uncertainties on the acceptance for leptoquark mass of 100 GeV.

Table 8-10: Systematic uncertainties on the acceptance of the first-generation scalar leptoquark signal (for leptoquark mass of 100 GeV).

Systematic	Value
PDF	4%
ISR/FSR	10%
MC Statistics	3%
Luminosity	6%
Vertex Cut	0.5%
Trigger Efficiency	1%
Energy Scale	17%
Total	20%

8.4.6 Uncertainties on Background Prediction in Signal and Control Regions

The systematic uncertainties on the background predictions in the leptoquark signal region, as well as in the various control regions, have been determined. The systematic uncertainty on the luminosity is taken to be 6%.

The uncertainty on the electroweak background prediction is reduced to the uncertainty due to the jet energy scale and the statistical uncertainty of the small $Z \to e^+e^- +$ jets data sample (6%).

In order to estimate the systematic uncertainty due to the calorimeter energy scale and jet corrections, we change the jet energy by $\pm 1\sigma$ of the jet energy correction uncertainty and recalculate the number of events passing the selection cuts. Since we normalize the electroweak background prediction in exclusive $Z \to +1$ jet events, we take the ratio of events in the signal region from electroweak processes to the number of exclusive $Z \to e^+e^- + 1$ jet events. The difference in this ratio for $\pm 1\sigma$ of the jet energy correction uncertainty from the nominal energy scale is taken as a systematic uncertainty and is found to be $\sim 8\%$.

The statistical error on the contributions from each Monte Carlo sample are also included, and can be as large as 24% for $W \to e\nu +$ jets. But when combined with other background sources, the total statistical uncertainty is only 5% in the leptoquark signal region.

The uncertainty on the `MET45` trigger efficiency in the signal region is taken to be 1% However, a larger uncertainty on the trigger efficiency is expected in the low missing-E_{T} regions. It is estimated from the difference in the event yield if the efficiency curve derived from a high-p_{T} muon sample is used in place of the one derived from a high-p_{T} electron sample, and can be as large as 20% (control region 2, for example).

Overall, the total systematic and statistical uncertainty on the background contribution to the leptoquark signal region is 12%.

CHAPTER 9
RESULTS

9.1 Control Regions

The seven control regions with large missing-E_{T} defined in Tab. 8-9 were examined before "opening the box" that contains the leptoquark signal. The total background expected from the Monte Carlo simulation, with the statistical and systematic uncertainties listed separately, and the number of events observed in the data are listed in Tab. 9-1 and shown in Fig. 9-1. The cross section for the vector boson production plus 2-jets has been scaled up from the LO cross section of ALPGEN by the scale factor derived in Chapter 8.1. As stated earlier, the QCD multi-jet production has been estimated from the data by applying efficiency curve to the set of events preselected with our analysis cuts, except the number of jet requirement and cuts on angular separation.

The Poisson probability to observe the number of events seen in data or more has been computed based on the Monte Carlo expectation, and is shown in Tab. 9-1. The total uncertainty on the expectation is accounted for by smearing the mean number of expected events by a Gaussian whose width is given by the uncertainty and performing 100,000 pseudo-experiments. As can be seen, most regions are within one standard deviation from the expected number ($0.16 < \mathcal{P} < 0.84$), except for bin 4 which has a 94% probability (2σ).

To further validate the Standard Model expectation the shapes, of the kinematical distributions from Monte Carlo are compared with those from data for control region 6, for it is required that the missing-E_{T} is 60 GeV or larger, that there are two leading jets are not back-to-back in ϕ and that there is at least one lepton (electron or muon). The distributions shown include missing-E_{T} (Fig. 9-2),

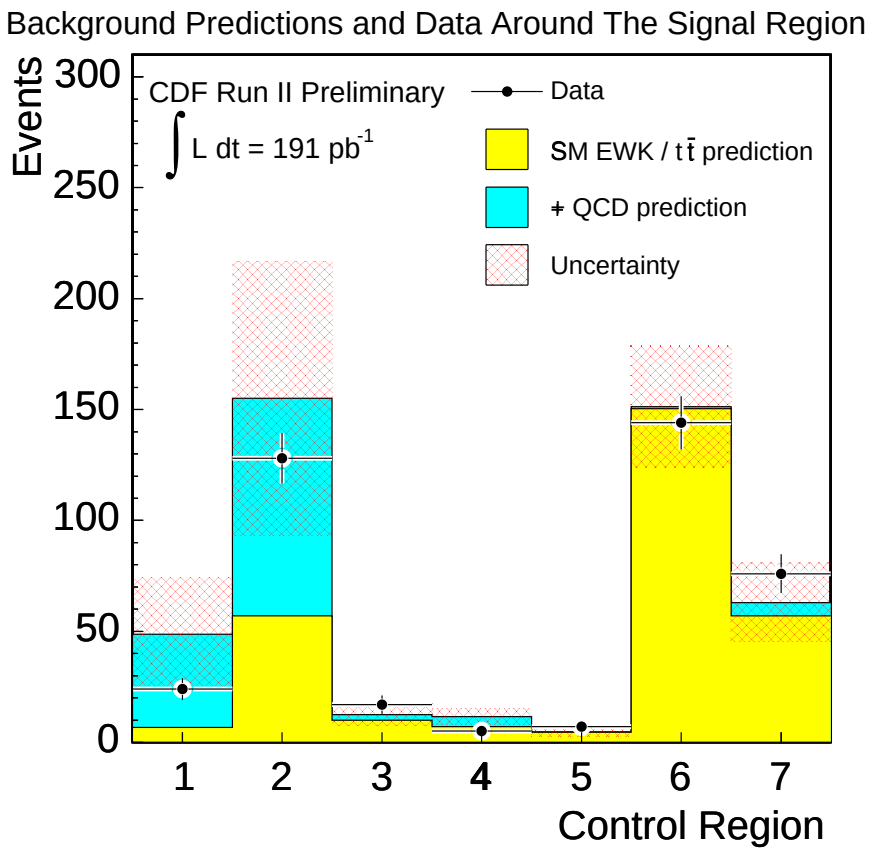

Figure 9-1: Comparison of the number of events observed in data (solid points) with the number expected from Standard Model sources (histogram) for the control regions defined in Tab. 8-9. The electroweak and top pair production contributions are shown separately from the contribution due to QCD multi-jet production. The total uncertainty on the predicted background is shown by the hatched region.

Table 9-1: Comparison of the number of expected events from Monte Carlo with the number observed in data for the seven control regions. The Monte Carlo statistical error is the first uncertainty shown, and the systematic error from other sources is the second. The probability $\mathcal{P}$ to observe the number of events in data or more is shown.

Region	1	2	3	4	5	6	7
QCD	42.0	98.0	2.6	4.5	0.2	1.0	6.0
$W \to e\nu + 2$ jets	0.7	5.3	6.7	0.7	1.8	37.2	24.2
$W \to \mu\nu + 2$ jets	1.3	13.7	1.0	1.3	1.	66.7	19.5
$W \to \tau\nu + 2$ jets	2.6	19.1	1.0	3.6	0.5	20.6	6.7
$Z \to \mu\mu + 2$ jets	0.04	0.6	0.1	0.0	0.1	9.2	2.4
$Z \to \tau\tau + 2$ jets	0.14	1.0	0.1	0.0	0.1	1.4	0.4
$Z \to \nu\nu + 2$ jets	1.7	15.9	0	1.3	0.0	0.	0.
$t\bar{t}$	0.4	1.6	1.0	0.3	1.0	15.1	3.9
Total Events	48.9	156.2	12.7	11.7	4.8	154.3	64.2
Uncertainty	$\pm1.5\pm25.5$	$\pm4.4\pm61.8$	$\pm1.8\pm4.6$	$\pm1.7\pm3.1$	$\pm1.1\pm2.0$	$\pm6.6\pm27.1$	$\pm4.2\pm17.7$
Data	24	128	17	5	7	144	76
$\mathcal{P}(\%)$	83	67	25	94	27	63	28

jet multiplicity (Fig. 9-3), leading-jet E_{T} (Fig. 9-4), second-leading jet E_{T} (Fig. 9-5), third-leading jet E_{T} (Fig. 9-6), the ϕ difference between the two highest E_{T} jets (Fig. 9-7), the ϕ difference between the leading-jet and the missing-E_{T} direction (Fig. 9-8), and the minimum ϕ difference between any jet and the missing-E_{T} direction (Fig. 9-9). The contribution from QCD multi-jet production is not shown.

9.2 Leptoquark Acceptance and Background Prediction in the Signal Region

Table 9-2 shows the acceptance of first-generation scalar leptoquarks (with $\beta = 0$) as a function of mass after the final selection cuts. Also shown is the number of events expected in 191 pb^{-1} using the NLO cross section of T. Plehn [32]. The total systematic uncertainty on the leptoquark acceptance is between 15%-32% (depending on the leptoquark mass), as described in Section 8.4.5.

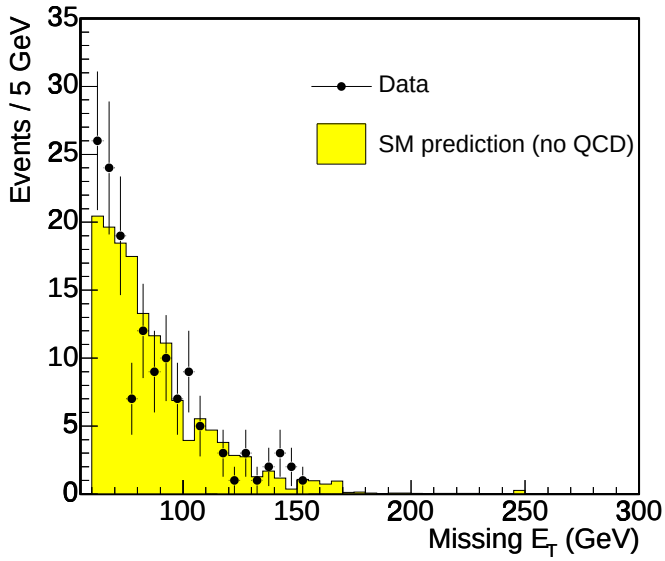

Figure 9-2: Missing-E_{T} distribution in the electroweak-like control region for data (solid points) compared to Standard Model expectation (shaded histogram).

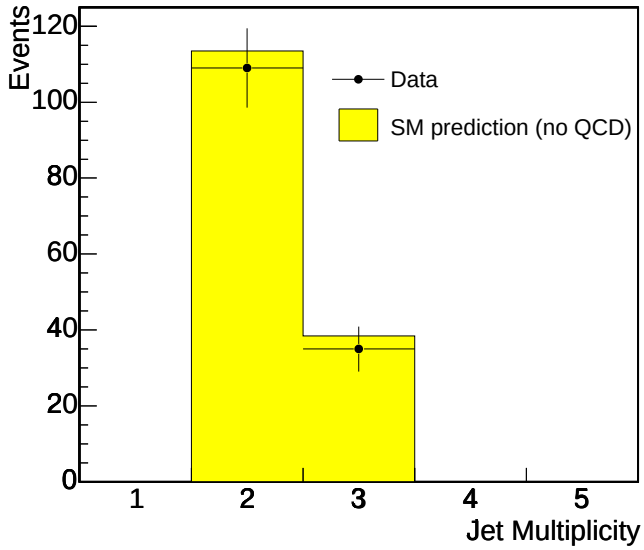

Figure 9-3: Jet multiplicity distribution in the electroweak-like control region for data (solid points) compared to Standard Model expectation (shaded histogram).

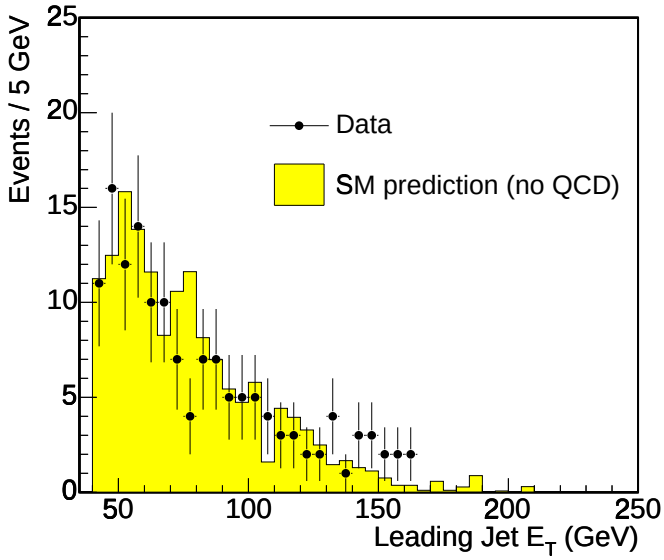

Figure 9-4: The leading-jet E_{T} distribution in the electroweak-like control region for data (solid points) compared to Standard Model expectation (shaded histogram).

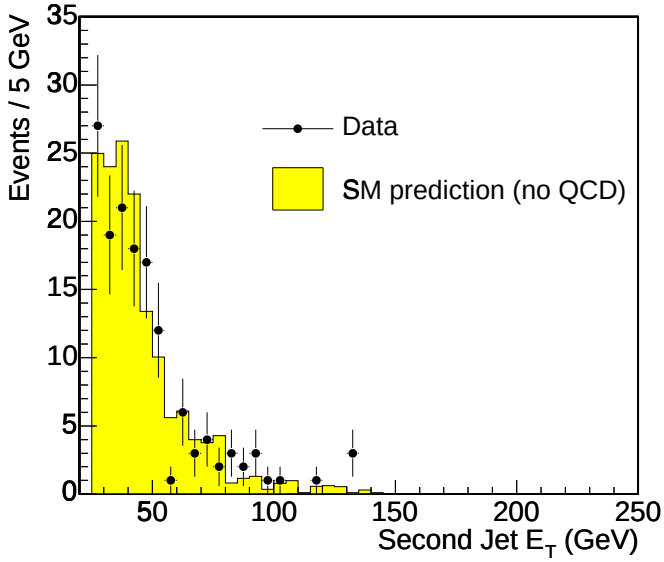

Figure 9-5: The second-leading jet E_{T} distribution in the electroweak-like control region for data (solid points) compared to Standard Model expectation (shaded histogram).

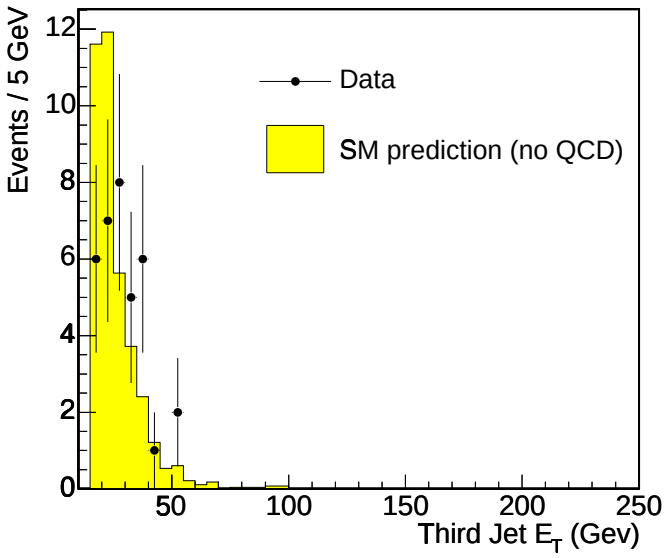

Figure 9-6: The third-leading jet E_{T} distribution in the electroweak-like control region for data (solid points) compared to Standard Model expectation (shaded histogram).

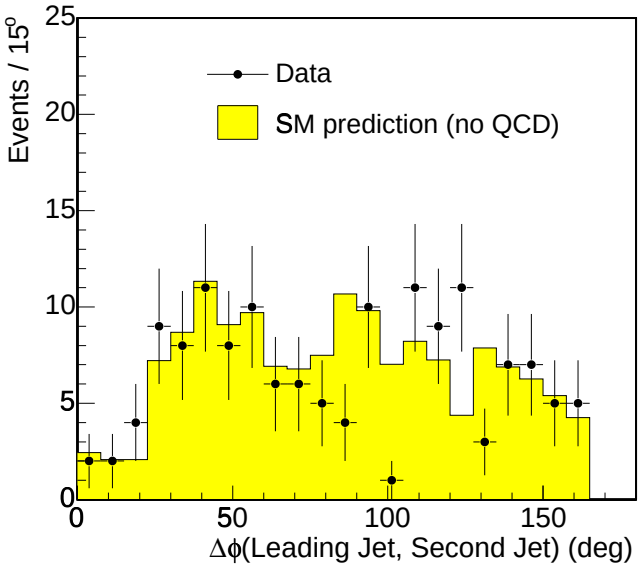

Figure 9-7: The ϕ difference between the two highest E_{T} jets in the electroweak-like control region for data (solid points) compared to Standard Model expectation (shaded histogram).

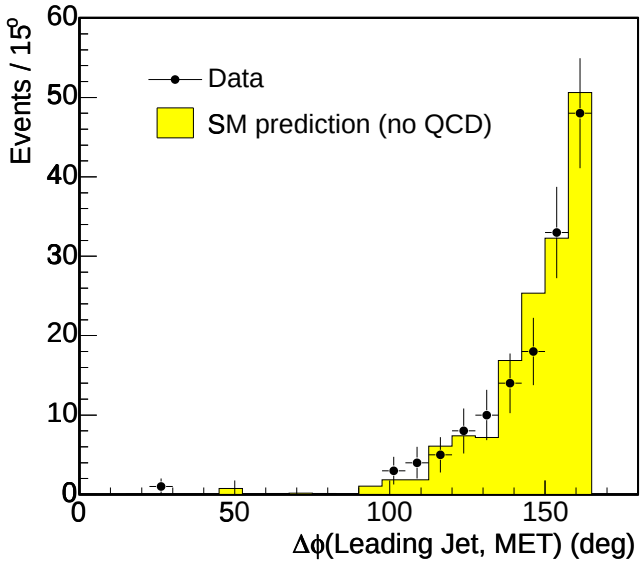

Figure 9-8: The ϕ difference between the leading-jet and the missing-E_{T} direction in the electroweak-like control region for data (solid points) compared to Standard Model expectation (shaded histogram).

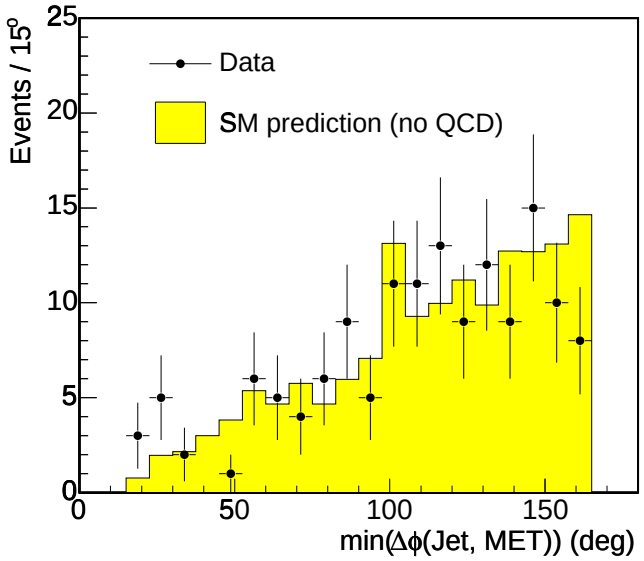

Figure 9-9: The minimum ϕ difference between any jet and the missing-E_{T} direction in the electroweak-like control region for data (solid points) compared to Standard Model expectation (shaded histogram).

Table 9-2: Acceptance of the first-generation scalar leptoquark signal as a function of mass, as well as the number of events expected in 191 pb^{-1}.

LQ Mass (GeV/c^2)	Acceptance	Number Expected
60	0.0017	72.0
75	0.0073	97.6
80	0.0113	106.5
90	0.0187	93.1
100	0.0300	83.8
110	0.0431	70.7
115	0.0482	64.4
125	0.0590	47.3
150	0.0828	22.1

The total background to the leptoquark signal region is predicted to be 118.3 ± 14.5, where the breakdown according to each Standard Model source is listed in Tab. 9-3.

Table 9-3: The number of expected events from various Standard Model sources in the leptoquark signal region. The Monte Carlo statistical error is the first uncertainty shown, and the systematic error from other sources is the second.

Source	Events expected
QCD	16.7 ± 6.7 (total)
$W \to e\nu + 2$ jets	$6.1 \pm 1.4 \pm 1.5$
$W \to \mu\nu + 2$ jets	$21.7 \pm 2.3 \pm 2.8$
$W \to \tau\nu + 2$ jets	$28.4 \pm 3.8 \pm 4.1$
$Z \to \mu\mu + 2$ jets	$1.1 \pm 0.2 \pm 0.2$
$Z \to \tau\tau + 2$ jets	$0.9 \pm 0.2 \pm 0.2$
$Z \to \nu\nu + 2$ jets	$39.1 \pm 2.8 \pm 3.6$
$t\bar{t}$	$4.3 \pm 0.4 \pm 0.3$
Total Events	118.3 ± 5.6(stat) ± 13.4(syst)

9.3 Projected Limits

Assuming that there is no leptoquark signal, and that the number of observed events in data would equal the expected background, we can derive an expected cross section upper limit using the acceptances in Tab. 9-2 and the systematic uncertainties for the signal and background. To determine the upper limit on the

possible number of signal events at the 95% confidence level we use a Bayesian likelihood method [8].

An upper limit on the production cross-section for leptoquarks could be derived from the observed number of events if no excess is found over the expected number of background events from the following relation:

$$\sigma_{\text{U.L.}} \leq \frac{N_{\text{obs}}}{L \times a}, \tag{9-1}$$

where N_{obs} is the number of the observed events in the data after all selection cuts, L is the total integrated luminosity and a is signal acceptance. However, this relation should be modified to reflect the fact that an assumption was made that in the number of events observed, none were attributed to the signal. Moreover, the number of observed events is described by Poisson statistics and can fluctuate up or down from the expected number. Therefore, the upper limit on the cross-section will be defined in some confidence interval, which is constructed to exclude the true number of the signal events with a probability ϵ greater than a specified value (5%). Then a cross section outside this confidence interval could be excluded at a $1 - \epsilon$ confidence level (CL).

The expected number of events is given by:

$$\mu = L\sigma_{sig}a + \mu_B, \tag{9-2}$$

where L is the integrated luminosity, σ_{sig} is the signal cross section, a is the signal acceptance and μ_B is the expected number of of background events. The likelihood function for Poisson distributed number of observed events n is given by:

$$L(n|\sigma_{sig}, \mu_B, a) = \frac{\mu^n e^{-\mu}}{n!}. \tag{9-3}$$

A posterior probability density as a function of the signal cross section is derived from the Bayes' theorem:

$$\mathcal{P}(\sigma_{sig}|n,\mu_B,a) = \frac{L(n|\sigma_{sig},\mu_B,a)P(\sigma_{sig})}{\int_0^\infty L(n|\sigma'_{sig},\mu_B,a)P(\sigma'_{sig})d\sigma'_{sig}}, \tag{9-4}$$

where $P(\sigma_{sig})$ is the the prior probability density for the signal cross section and is taken to be:

$$P(\sigma_{sig}) = \begin{cases} 0, & \sigma_{sig} < 0 \\ 1, & \sigma_{sig} > 0 \end{cases} \tag{9-5}$$

The systematic uncertainties are assumed to be distributed according to a Gaussian and can be convoluted with the Poisson likelihood as in:

$$L(n|\sigma_{sig},\mu_B,a) = \frac{1}{\sqrt{2\pi\sigma_a^2}}\int_0^\infty \frac{\mu'^n e^{-\mu'}}{n!} e^{-(a'-a)^2/2\sigma_a^2} da', \tag{9-6}$$

for the uncertain acceptance. This can be extended to include systematic uncertainties on the number of background events in the same way. The 95% confidence level upper limit can be obtained then by solving the following equation:

$$\int_0^{\sigma_{95\%CL}} \mathcal{P}(\sigma'_{sig}|n,\mu_B,a)d\sigma'_{sig} = 0.95 \tag{9-7}$$

for $\sigma_{95\%CL}$. This is done by a Monte Carlo technique [97].

Figure 9-10 shows the projected 95%CL upper limit on the leptoquark production cross-section as a function of a leptoquark mass for $n = \mu_{\mathrm{B}}$. We compare the obtained limit with prediction from the theoretical cross-section calculation and exclude the mass region where our cross-section is less or equal to the theoretical one. If we conservatively choose the theoretical cross section calculated with $\mu = 2m_{\mathrm{LQ}}$, we expect to exclude the mass interval between about 78 and 121 GeV/c^2. Also shown in the plot are the expected limits if we were to observe a $\pm 1\sigma$ fluctuation in the data, where σ includes both the statistical and

systematic errors added in quadrature. For a positive fluctuation of one standard deviation or larger, we may not be able to exclude any mass interval.

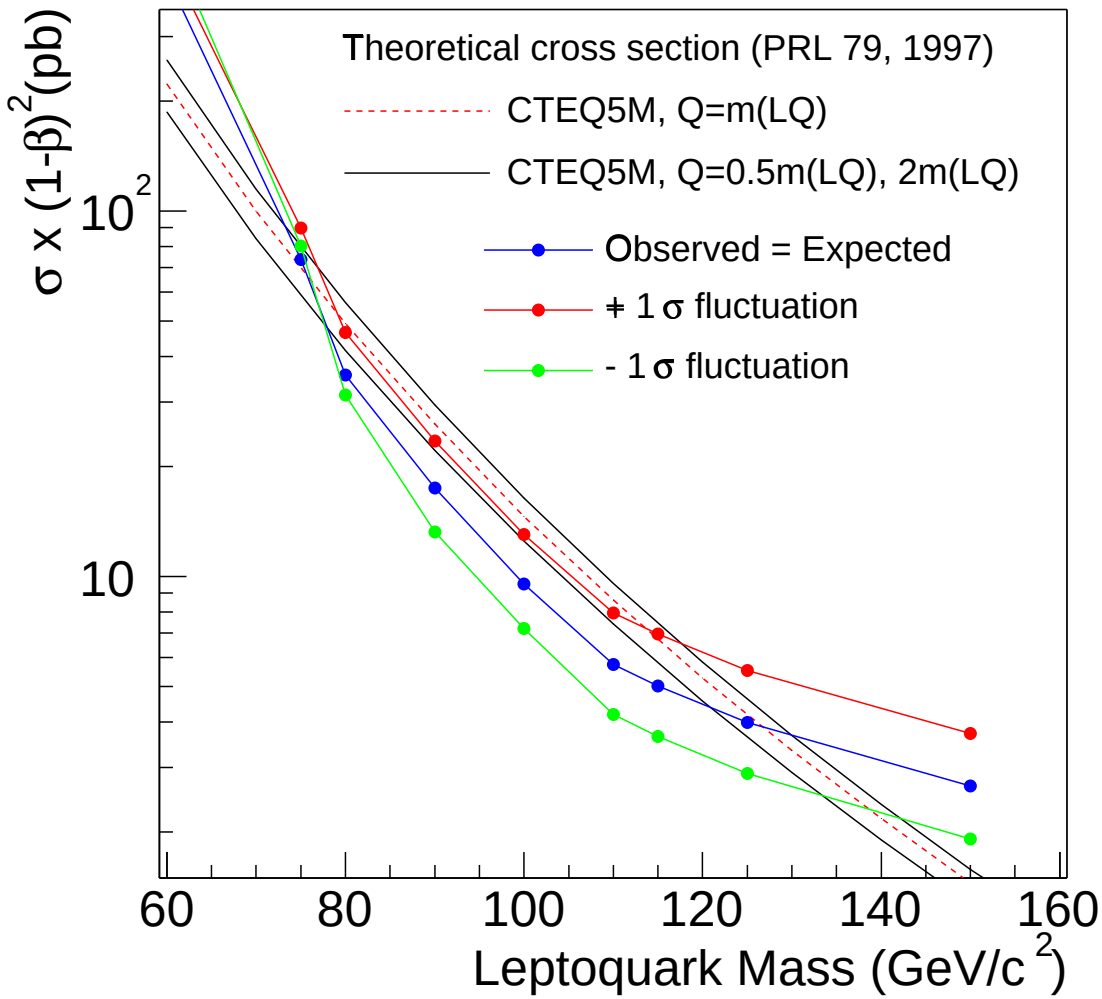

Figure 9-10: The expected cross section upper limit for scalar leptoquark production ($\beta = 0$) assuming that no leptoquark events are observed and that the data will yield exactly the Monte Carlo expectation for the Standard Model background. Also shown are the limits that would be obtained if we observe a $\pm 1\sigma$ fluctuation in the expected background.

9.4 Signal Region

The number of events observed in the data for the leptoquark signal region is 124, in agreement with the number predicted.

Figure 9-11 shows the missing-E_{T} distribution for the data (solid points) compared to the Monte Carlo expectations from $W/Z + 2$ jets and top quark pair production (yellow histogram), and QCD expectations (blue histogram) estimated from the data. Very good agreement between SM expectations and data is found. Also shown is the expected distribution arising from leptoquark production at a mass of 125 GeV/c^2 (hatched histograms).

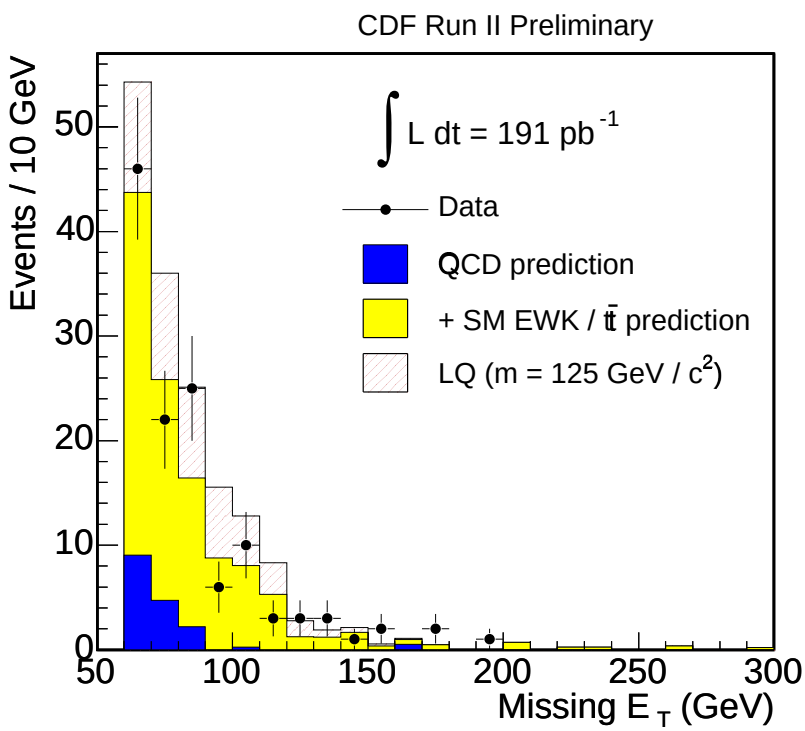

Figure 9-11: Missing-E_{T} distribution in the leptoquark signal region for data (solid points) compared to Standard Model background (yellow histogram). Also shown is the expected distribution arising from leptoquark production and decay at a mass of 125 GeV/c^2 (hatched histograms).

The following histograms show the distributions of several principal kinematic quantities for data (solid points) compared to the Monte Carlo expectations from $W/Z + 2$ jets and top quark pair production (shaded histograms). The contribution from QCD multi-jet production is not shown. The distributions shown include leading-jet E_{T} (Fig. 9-12), second-leading jet E_{T} (Fig. 9-13), third-leading jet E_{T}

(Fig. 9-14), the ϕ difference between the two highest E_{T} jets (Fig. 9-15), the ϕ difference between the leading-jet and the missing-E_{T} direction (Fig. 9-16), and the minimum ϕ difference between any jet and the missing-E_{T} direction (Fig. 9-17).

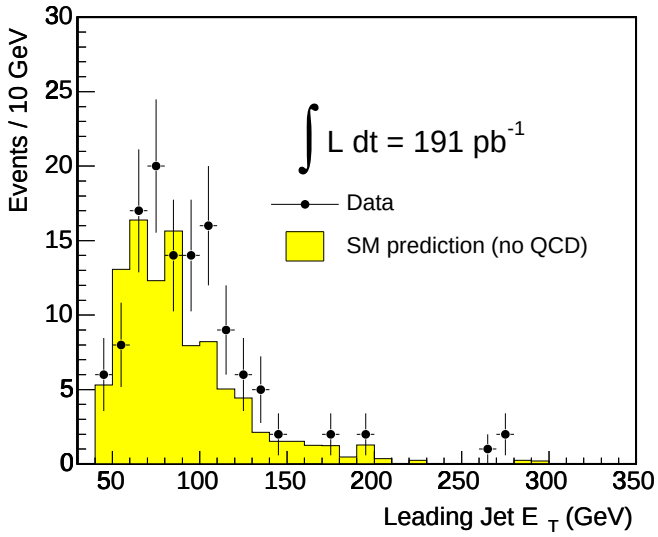

Figure 9-12: The leading-jet E_{T} distribution in the leptoquark signal region for data (solid points) compared to Standard Model background (yellow histogram).

9.5 Search Limits

The number of events observed in data for the leptoquark signal region is 124, in good agreement with the 118.3 $\pm$ 14.5 expected from Standard Model backgrounds. Unfortunately, no evidence for leptoquark production is observed, and an upper limit can be set on the cross section times squared branching ratio. This is shown in Fig. 9-18, where we have used the Bayesian likelihood method described above to determine the upper limit on the possible number of signal events at the 95% confidence level using a 15-32% systematic uncertainty on the signal acceptance and a 12% systematic uncertainty on the background yield. If we conservatively choose the theoretical cross section calculated with $\mu = 2m_{\mathrm{LQ}}$, we exclude the mass interval between 78 and 117 GeV/c^2 for 100% branching ratio into neutrino plus quark.

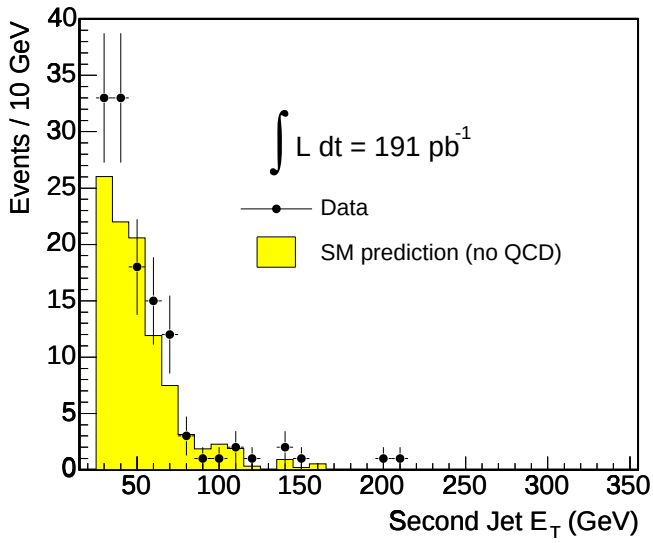

Figure 9-13: The second leading jet E_{T} distribution in the leptoquark signal region for data (solid points) compared to Standard Model background (yellow histogram).

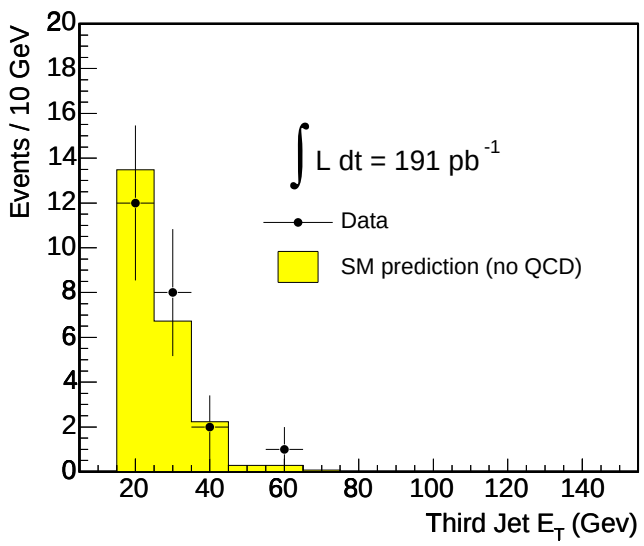

Figure 9-14: The third leading-jet E_{T} distribution in the leptoquark signal region for data (solid points) compared to Standard Model background (yellow histogram).

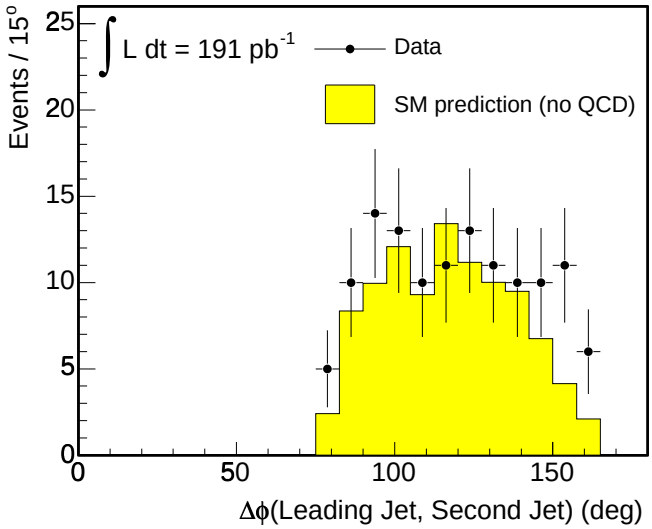

Figure 9-15: The ϕ difference between the two highest E_{T} jets in the leptoquark signal region for data (solid points) compared to Standard Model background (yellow histogram).

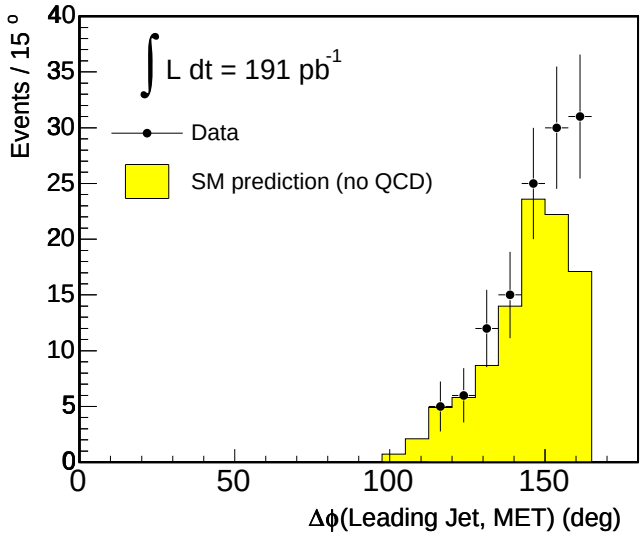

Figure 9-16: The ϕ difference between the leading-jet and the MET direction in the leptoquark signal region for data (solid points) compared to Standard Model background (yellow histogram).

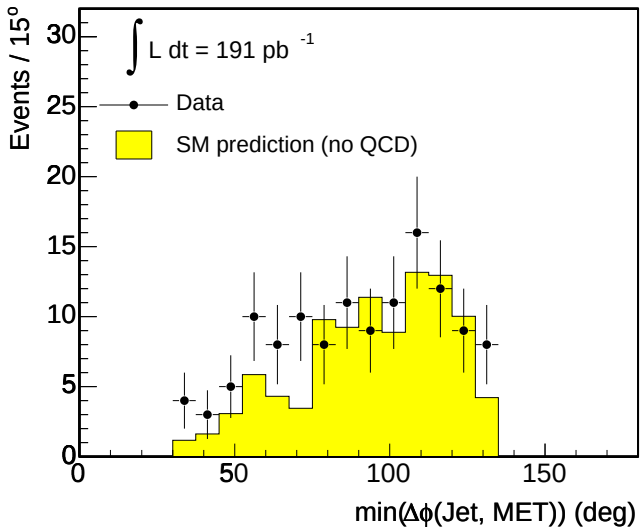

Figure 9-17: The minimum ϕ difference between any jet and the MET direction in the leptoquark signal region for data (solid points) compared to Standard Model background (yellow histogram).

9.6 Conclusion

We have performed a search for first-generation leptoquarks in the missing-E_{T} plus jets channel in the first 191 pb^{-1} of Run II data. We saw no evidence for leptoquarks in the data; therefore, we set an upper limit on the production cross section at 95% CL. We exclude the corresponding mass interval from 78 to 117 GeV/c^2 for leptoquark decays into neutrino and quark with 100% branching ratio. This limit is the highest mass limit to date for the first-generation leptoquarks in the missing-E_{T} plus jets topology. The previous limit of 98 GeV was set by DØ [44] in Run I.

This result is complementary to the searches for first-generation leptoquarks, where leptoquark decays into electron and quark. This result can be combined with results from other searches to set a mass limit independent of the branching ratio of the leptoquark to charged lepton.

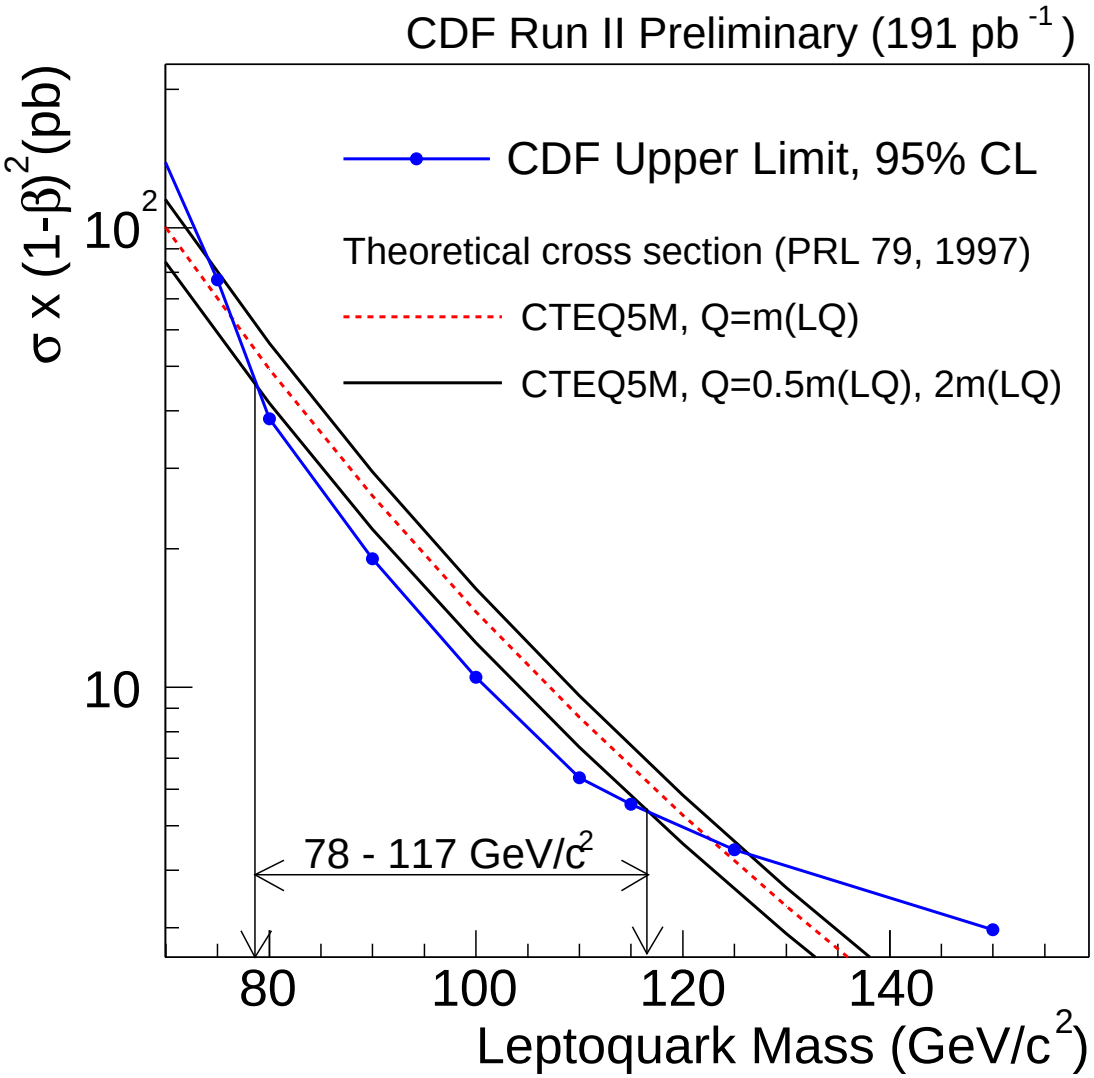

Figure 9-18: The upper limit on the cross section times squared branching ratio for scalar leptoquark production in missing-E_{T} plus jets signature. Also shown is the NLO cross section for $\beta = 0$ for 3 choices of the factorization/renormalization scale: $\mu = m_{\mathrm{LQ}}$, $\mu = 2\ m_{\mathrm{LQ}}$, and $\mu = 0.5\ m_{\mathrm{LQ}}$.

The biggest limitation in this analysis was the current understanding of the jet energy scale in CDF calorimeter, which resulted in relatively large systematic uncertainty. This uncertainty would limit further searches in larger data sample. The mass limit set in this search can be improved by as much as 10%, if the systematic uncertainty associated with the jet energy scale can be reduced by half. Therefore, this analysis would greatly benefit from improved systematic uncertainty associated with the jet energy scale.

The multi-jet and missing E_{T} signature, especially when combined with heavy-flavor tagging, is very interesting for many other new particle searches, such as second- and third-generation leptoquarks, Supersymmetry particles (scalar top and bottom) and Higgs.

The stop quark could be the lightest supersymmetric quark, due to the large mass splitting between the left- and right-handed stop eigenstate induced by the large mass of the Standard Model top quark. The stop quark would predominantly decay to the bottom quark and a chargino, with a subsequent decay of the chargino to a charged lepton and a neutralino. However, if the chargino is heavier than the stop quark, this decay mode will be closed and stop will decay to a charm quark and a neutralino. In the latter scenario, the experimental signature will be two heavy-flavor jets and missing transverse energy. On the other hand the large splitting can also appear in the sbottom sector, if the ratio of the vacuum expectation values of two supersymmetric higgs fields is large. The dominant decay mode then would be similar to that of stop: heavy-flavor jets and missing transverse energy. This final state is also relevant for associated Higgs production Zh, where Z boson decays to neutrinos and Higgs decay to b quark-antiquark pair. The missing transverse energy plus multi-jet final state is also very promising for the search for the Extra Dimensions.

REFERENCES

[1] F. Halzen, A. D. Martin, "Quarks and Leptons: An Introductory Course in Modern Particle Physics", John Wiley & Sons, Inc. (1984).

[2] I. J. R. Aitchison, A. J. G. Hey, "Gauge Theories in Particle Physics: A Practical Introduction" Adam Hilger, Bristol and Philadelphia, 2nd edition (1989).

[3] G. Arnison *et al.*, *Phys. Rev. Lett.* **122** 103 (1983).

[4] M. Banner *et al.*, *Phys. Rev. Lett.* **122** 476 (1983).

[5] G. Arnison *et al.*, *Phys. Rev. Lett.* **126** 398 (1983).

[6] P. Bagnaia *et al.*, *Phys. Rev. Lett.* **129** 130 (1983).

[7] F. Abe *et al.*, *Phys. Rev. Lett.* **74** 2626 (1995).

[8] Particle Data Group, *Phys. Rev.* **D66** 010001 (2002); http://pdg.lbl.gov.

[9] S. L. Glashow, *Nucl. Phys.* **22** 579 (1961).

[10] S. Weinberg, *Phys. Rev. Lett.* **19** 1264 (1967).

[11] A. Salam, "Elementary Particle Theory", N. Svartholm (1969).

[12] P. W. Higgs, *Phys. Rev. Lett.* **13** 508 (1964);
P. W. Higgs, *Phys. Lett.* **12** 132 (1964).

[13] G. 't Hooft *Nucl. Phys.* **B33** 173 (1967).

[14] H. Georgi, S. L. Glashow, *Phys. Rev. Lett.* **32** 438 (1974).

[15] S. Dawson, "The MSSM and Why it Works", hep-ph/9712464.

[16] J. C. Pati, A. Salam, *Phys. Rev.* **D19** 275 (1974).

[17] N. Cabibbo, *Phys. Rev. Lett.* **10** 531 (1963).

[18] M. Kobayashi and T. Maskawa, *Prog. Theor. Phys.* **49** 652 (1973).

[19] Y. A. Golfand and E. P. Likhtman, *JETP Lett.* **13** 452 (1971).

[20] D. V. Volkov and V. P. Akulov, *JETP Lett.* **16** 621 (1972).

[21] J. Wess and B. Zumino, *Phys. Lett.* **B49** 52 (1974).

[22] M. B. Green, J. H. Schwarz and E. Witten, "Superstring Theory", Cambridge Univ. Press (1987).

[23] S. P. Martin, "A Supersymmetry Primer", hep-ph/9709356.

[24] W. Buchmüller, R. Rückl, and D. Wyler, *Phys. Lett.* **B191** 442 (1987) and Erratum **B448** 320 (1999).

[25] J. Blümlein, R. Rückl, *Phys. Lett.* **B304** 337 (1993).

[26] J. Blümlein, E. Boos, A. Pukhov, *Mod. Phys. Lett.* **A9** 3007 (1994).

[27] D. Castaño, S. Martin, *Phys. Lett.* **B340** 67 (1994).

[28] J. Blümlein, E. Boos, A. Kryukov, *Z. Phys.* **C76** 137 (1997).

[29] M. Krämer, T. Plehn, M. Spira, and P.M. Zerwas, *Phys. Rev. Lett.* **79** 341 (1997).

[30] H. L. Lai *et al.* (CTEQ Collab.), *Phys. Rev.* **D55** 1280 (1997).

[31] H. L. Lai *et al.* (CTEQ Collab.), *Eur. Phys. J.* **C12** 375 (2000);

[32] M. Krämer and T. Plehn, private communications.

[33] D.E. Acosta and S.K. Blessing, *Annu. Rev. Nucl. Part. Sci.* **49**, 389 (1999).

[34] C. Adloff *et al.* (H1 Collab.), *Z. Phys.* **C74** 191 (1997).

[35] J. Breitweg *et al.* (ZEUS Collab.), *Z. Phys.* **C74** 207 (1997).

[36] C. Adloff *et al.* (H1 Collab.), *Eur. Phys. J.* **C11** 447 (1999); [Erratum-ibid. **C11** 553 (1999)];
hep-ex/9907002.

[37] J. Breitweg *et al.* (ZEUS Collab.), *Eur. Phys. J.* **C16** 253 (2000);
hep-ex/0002038.

[38] S. Chekanov *et al.* (ZEUS Collab.), *Phys. Rev.* **D68** 052004 (2003).

[39] G. Abbiendi *et al.* (OPAL Collab.), *Phys. Lett.* **B526** 233 (2002).

[40] G. Abbiendi *et al.* (OPAL Collab.), hep-ex/0305053.

[41] F. Abe *et al.* (CDF Collab.) *Phys. Rev. Lett.* **79** 4327 (1997).

[42] B. Abbott *et al.* (DØ Collab.) *Phys. Rev. Lett.* **79** 4321 (1997).

[43] C. Grosso-Pilcher and G. Landsberg, CDF Note 4575.

[44] V.M. Abazov *et al.* (DØCollab.) *Phys. Rev. Lett.* **88** 191801 (2002).

[45] T. Affolder *et al.* (CDF Collab.) *Phys. Rev. Lett.* **85** 2056 (2000).

[46] F. Strumia, A. Clark, L. Moneta, X. Wu, and C. Grosso-Pilcher, CDF Note 4873.

[47] C. Holck, R. Demina, and A. Nomerotski, CDF Note 4958.

[48] "Tevatron Run II Handbook," http://www-bd.fnal.gov/lug/runII_handbook/RunII_index.html.

[49] CDF Collaboration, "A Time-Of-Flight System For CDF," Fermilab preprint, FERMILAB-PROPOSAL-0830-3 (1995).

[50] D. Acosta *et al.*, *Nucl. Instrum. Meth.* **A461** 540 (2001).

[51] A. Bhatti *et al.*, "The Beam Shower Counters for Run II," CDF Note 5247 (2000).

[52] R. Blair *et al.*, (CDF Collab.), Fermilab preprint, FERMILAB-PUB-96-390-E (1996).

[53] F. Abe *et al.*, *Nucl. Instrum. Methods Phys. Res.* **271** 387 (1998).

[54] R. Wigmans, "Calorimetry Energy Measurement in Particle Physics," Claredon Press, Oxford (2000).

[55] S. Lami, (CDF Collab.), Pub. Proceedings 10th International Workshop on Deep Inelastic Scattering, Cracow, Poland, April 30-May 4, 2002; Fermilab preprint, FERMILAB-CONF-02/127-E (2002).

[56] T.K. Nelson for the CDF II Collaboration, "The CDF Layer 00 Detector," Fermilab preprint, FERMILAB-CONF-01-357-E (2001).

[57] E.J. Thomson *et al.*, *IEEE Trans. Nucl. Sci.* **49** 1063 (2002).

[58] R. Brun, F. Carninati, "GEANT Detector Description and Simulation Tool," CERN Programming Library Long Writeup, **W5013** (1993).

[59] D. Acosta *et al.*, "Geant Simulation of the CLC," CDF Note 5398 (2000).

[60] E. Gerchtein, D. Acosta, D. Tsybychev, "CLC simulation user's guide," CDF Note 6034 (2002).

[61] A. Bhatti, M.E. Convery, K. Goulianos, "User's guide and update of the MBR minimum-bias event generator," CDF Note 5371 (2001).

[62] D. Acosta *et al.*, "The CLC Minimum Bias Trigger," CDF Note 5861 (2002).

[63] S. Klimenko, J. Konigsberg, T. Liss, "Average cross-section of the inelastic $p\bar{p}$ scattering at 1800 GeV.," CDF Note 6314.

[64] F. Abe *et al.*, *Phys. Rev.* **D50** 5550 (1994).

[65] C. Avilla *et al.*, (E-811 Collab.) *Phys. Lett.* **445** 419 (1999).

[66] F. Abe *et al.*, *Phys. Rev.* **D45** 1448 (1992).

[67] J.–F. Arguin *et al.*, "Jet Corrections for Summer 2003 Analyses," CDF Note 6565.

[68] G. Latino, "Comparing Run I and Run II Central Jet Energy Scale," CDF Note 6537.

[69] A. Baden *et al.*, "The Missing-E_{T} resolution for 87 run data," CDF Note 715.

[70] P. Gatti, "Performance of the New Tracking System at CDF II," Ph. D. Thesis, University of Padova, Padova, Italy, (2001).

[71] D. Glenzinski *et al.*, "Run IIa COT Tracking Efficiency," CDF Note 5973.

[72] M. Bishai *et al.*, "COT and SVXII Tracking Performance", CDF Note 5931.

[73] J.- F. Arguin, B. Heinemann, "Underlying Event Corrections in Run II," CDF Note 6239.

[74] R. G. Wagner, "Electron Identification for Run II: Algorithms," CDF Note 5456 (2003).

[75] G. Manca, Ph. D. Thesis, University of Oxford, Oxford, UK (2003).

[76] J. Bellinger *et al.*, "A Guide to Muon Reconstruction for Run 2," CDF note 5870 (2002).

[77] D. Amidei *et al.*, "Measurements of $W \to \mu\nu$ and $Z \to \mu\mu$ production cross sections and R using CDF Run II Data," CDF note 6711 (2003).

[78] H. J. Frish *et al.*, "Conceptual Design of the L1 Calorimeter Trigger for the Run II Upgrade," CDF Note 2909 (1994).

[79] H. J. Frish, P. J. Wilson, "Trigger Tower Organization and Summing in η-ϕ Space for Run II and beyond," CDF Note 2045 (1993).

[80] T. Shaw, "Specification for ADC/Memory Module (ADMEM)," CDF Note 4685 (1997).

[81] P. J. Wilson, "Specification for Trigger Tower Summing and E_{T} Weighting for ADMEM Board," CDF Note 4781 (2002).

[82] M. Albrow *et al.*, "Missing- E_{T} and Beam Related Backgrounds at CDF," CDF Note 5926.

[83] M. Spiropolu "A Blind Search for Supersymmetry in $p\bar{p}$ Collision at $sqrts =$ 1.8 TeV using the Missing Energy plus Multijet channel,"Ph.D thesis, Harvard University, Cambridge, Massachusetts (2000).

[84] M.L. Mangano, M. Moretti, F. Piccinini, R. Pittau, and A. Polosa, hep-ph/0206293; http://mlm.home.cern.ch/mlm/alpgen/.

[85] G. Corcella, I.G. Knowles, G. Marchesini, S. Moretti, K. Odagiri, P. Richardson, M.H. Seymour and B.R. Webber, *JHEP* 0101 (2001) 010 (hep-ph/0011363); hep-ph/0210213.

[86] T. Sjostrand, P. Eden, C. Friberg, L. Lonnblad, G. Miu, S. Mrenna, E. Norrbin, *Comput. Phys. Commun.*, **135** 238 (2001); hep-ph/0010017.

[87] T. Affolder *et al.*, (CDF Collab.), *Phys. Rev* **D65** 092002 (2002).

[88] G. Grindhammer, M. Rudowicz, S. Peters, *Nucl. Instrum. Meth.* **A290** 469 (1990).

[89] E. Halkiadakis *et al.*, "A Conversion Removal Algorithm for the 2003 Winter Conferences," CDF Note 6250 (2003).

[90] M. Coca, E. Halkiadakis, S. Lockwitz, "Central Electron Identification Efficiencies for Summer 2003 Conferences," CDF Note 6580 (2003).

[91] J. Campbell, R.K. Ellis, *Phys. Rev.* **D65** 113007 (2002); http://mcfm.fnal.gov.

[92] J.-F. Arguin, *et al.*, "Systematic uncertainties Associated with Jet Corrections for Winter 2003 Conferences," CDF Note 6419 (2003).

[93] R. Field, http://www.phys.ufl.edu/~rfield/cdf/tunes/rdf_tunes.html

[94] M. Glück, E. Reya, A. Vogt, *Eur. Phys. J.* **C5** 461 (1998);

[95] A.D. Martin, R.G. Roberts, W.J. Stirling and R.S. Thorne *Eur. Phys. J.* **C4** 463 (1998);

[96] W.K. Sakumoto and A. Hocker, "Event $|Z_{vtx}| < 60$ cm Cut Acceptance for Run II," CDF Note 6660 (2003).

[97] J. Conway, "Calculation of Cross Section Upper Limits Combining Channels Incorporating Correlated and Uncorrelated Systematic Uncertainties," CDF Note 6428 (2003).